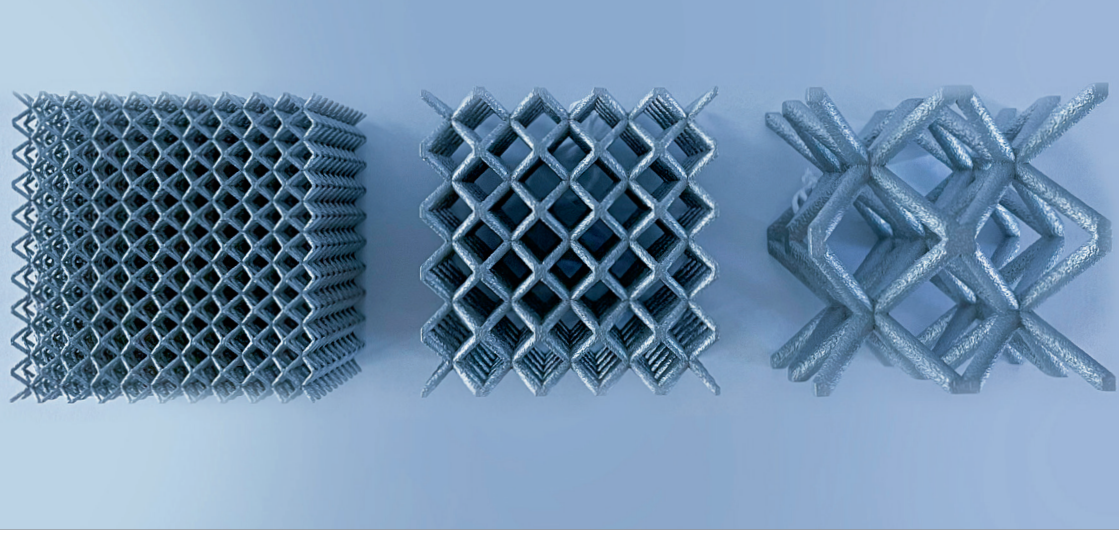

Aachener Berichte aus dem Leichtbau

Characterisation and Optimisation of Lattice Structures Embedded with Phase Change Materials

Stefano Piacquadio

Institut für Strukturmechanik und Leichtbau

RWTH AACHEN UNIVERSITY

Characterisation and Optimisation of Lattice Structures Embedded with Phase Change Materials

Charakterisierung und Optimierung von in Phasenwechselmaterialien eingebetteten Gitterstrukturen

Von der Fakultät für Maschinenwesen der Rheinisch-Westfälischen Technischen Hochschule Aachen zur Erlangung des akademischen Grades eines Doktors der Ingenieurwissenschaften genehmigte Dissertation

vorgelegt von

Stefano Piacquadio

Berichter: Univ.-Prof. Dr.-Ing. Kai-Uwe Schröder
Prof. Dr. Ing. Sauro Filippeschi

Tag der mündlichen Prüfung: 05. September 2024

Diese Dissertation ist auf den Internetseiten der Universitätsbibliothek online verfügbar.

Aachener Berichte aus dem Leichtbau
herausgegeben von Univ.-Prof. Dr.-Ing. Kai-Uwe Schröder

Band 5/2024

Stefano Piacquadio

Characterisation and Optimisation of Lattice Structures Embedded with Phase Change Materials

Shaker Verlag
Düren 2025

Bibliographic information published by the Deutsche Nationalbibliothek
The Deutsche Nationalbibliothek lists this publication in the Deutsche Nationalbibliografie; detailed bibliographic data are available in the Internet at http://dnb.d-nb.de.

Zugl.: D 82 (Diss. RWTH Aachen University, 2024)

Printed in Germany.

Print-ISBN 978-3-8440-9795-5
PDF-ISBN 978-3-8440-9889-1
ISSN 2509-663X
eISSN 2944-702X
https://doi.org/10.2370/9783844098891

Shaker Verlag GmbH • Am Langen Graben 15a • 52353 Düren
Phone: 0049/2421/99011-0 • Telefax: 0049/2421/99011-9
Internet: www.shaker.de • e-mail: info@shaker.de

Preface

This thesis is the result of four years of research at the Institute of Structural Mechanics and Lightweight Design (SLA) at the RWTH Aachen University. I would like to express my gratitude to Prof. Schröder for his inspiring guidance. His motivating leadership was fundamental in unlocking a critical scientific creativity, keeping the passion for research work alive. I am also extremely grateful to Prof. Filippeschi for his insights throughout the course of this work and my academic career. His support, both scientific and personal, was invaluable.

I would like to thank my former students Dominik Wagner, David Behnke, Laura Hernandez, and Samuel Hayden, for their support in my research activities, which also contributed to this dissertation. I hope our collaboration was mutually beneficial.
A big thank you goes to my former colleagues at the institute, especially Jannik Bühring and Maximilian Schirp, for their support and the fun we had together. I cherish our continuing friendship. I am also grateful to Jannik Zimmermann, Dominik Pridöhl, Martin Schubert, and the many other colleagues of the institute, for the many fruitful discussions and for contributing to a lighter daily life at the institute. I would like to thank Dr. Thanos Dafnis, for giving me the possibility to work on fascinating projects, and for the many teaching moments he provided.
My sincere thanks also go to Ulrich Höbel, Lara Kurzhals, Claudia Kerres, Werner Just, Verena Maas, and Lars Moosdorf who not only supported any time they could, but also warmly welcomed me at the institute and always had a good word for me. A special thanks goes to my friend and colleague Laura Babetto, with whom I shared the highs and lows of life abroad, making it much easier to endure.
I owe a special debt of gratitude to Tobias Meinert, who inspired me to move abroad, an experience that profoundly changed my perspective on life. His friendship and his pragmatic help make him a key person in my life.
I extend my heartfelt gratitude to my dear parents, my sister, and especially my grandpa, Nonno Giulio, for instilling in me a lifelong curiosity about that which surrounds us. Their continuous support and encouragement throughout my life helped me even amidst the challenges and anxieties of the pandemic.
Finally, the biggest thank you goes to my wife Aliaksandra. Her unwavering support throughout the challenges of completing this work, especially after the birth of our daughter Laura, was a beacon in the dark. I am deeply grateful for her active support, her experienced suggestions, and her always understanding patience. Completing this work required immense dedication and was undeniably stressful, but it was also a teaching moment in my life. I dedicate this work to Laura, wishing her to always be able to pursue her passions, hoping that they will be many and drive her personal and professional growth.

Abstract

In engineering fields where mass is a design-driving parameter, holistic mass reduction via multi-functionality is seen as a key enabler for further improvement of systems' performance. This research addresses the upcoming need for multi-functional structures capable of concurrently managing thermal control, energy storage, and load-bearing requirements.
An investigation on the thermal and mechanical properties of lattice structures incorporating Phase Change Materials (PCMs) is described throughout this thesis.
The work commences with an analytical description of the geometry of lattice structures. Then, it delves into the exploration of the effective thermophysical properties of the homogenised composite material, followed by meticulous validation through experimental methodologies. The impact of natural convection on the expansion of the melting front within the medium is considered as well.
To elucidate how the presence of the PCM influences the structural integrity of the lattice, numerical and experimental analyses are performed for the PCM-infused lattice structures, focusing on the stability of the struts when the PCM is frozen.
Furthermore, the thesis introduces a multi-variate optimisation framework designed to offer novel pathways for topology optimisation of lattice structures. This framework enables the exploration of optimal configurations by considering multiple variables simultaneously, providing a comprehensive approach to tailor the performance of such composites.
The findings of this research contribute to a deeper understanding of the thermal and mechanical behaviour of cellular solids embedded with PCMs, providing valuable insights for applications in thermal energy storage, thermal management systems, and other related fields.
In summary, this research contributes significantly to the advancement of multi-functional structures, offering a holistic perspective to address the complex demands of aerospace and other applications where mass is a constraint.

Keywords: Lattice Structures; Phase Change Materials; Topology Optimisation; Homogenisation Approach; Natural Convection;

Kurzfassung

In Bereichen der Ingenieurwissenschaften, in denen die Masse ein konstruktionsbestimmender Parameter ist, wird eine ganzheitliche Massenreduzierung durch Multifunktionalität als Schlüsselfaktor für die weitere Verbesserung der Leistung von Systemen angesehen. Diese Forschung befasst sich mit dem aufkommenden Bedarf an multifunktionalen Strukturen, die in der Lage sind, gleichzeitig thermische Kontrolle, Energiespeicherung und Lasttragende Anforderungen zu erfüllen.
Eine Untersuchung der thermischen und mechanischen Eigenschaften von Gitterstrukturen, die Phasenwechselmaterialien (PCMs) enthalten, wird in dieser Arbeit beschrieben.
Die Arbeit beginnt mit einer analytischen Beschreibung der Geometrie von Gitterstrukturen. Anschließend werden die effektiven thermophysikalischen Eigenschaften des homogenisierten Verbundwerkstoffs erforscht, gefolgt von einer sorgfältigen Validierung durch experimentelle Methoden. Darüber hinaus werden die Auswirkungen der natürlichen Konvektion auf die Ausdehnung der Schmelzfront innerhalb des Mediums untersucht.
Es werden numerische und experimentelle Analysen für die mit PCM infundierten Gitterstrukturen durchgeführt, wobei der Schwerpunkt auf der Stabilität der Streben liegt, wenn das PCM gefroren ist. Die Studie soll klären, wie die Anwesenheit des Phasenwechselmaterials die strukturelle Integrität des Gitters beeinflusst.
Darüber hinaus wird in dieser Arbeit ein multivariater Optimierungsansatz vorgestellt, der neue Wege für die Topologieoptimierung von Gitterstrukturen bietet. Dieser Rahmen ermöglicht die Erforschung optimaler Konfigurationen durch die gleichzeitige Berücksichtigung mehrerer Variablen und bietet so einen umfassenden Ansatz zur Anpassung der Leistung solcher Verbundwerkstoffe.
Die Ergebnisse dieser Forschung tragen zu einem tieferen Verständnis des thermischen und mechanischen Verhaltens von zellulären Festkörpern bei, die mit PCM eingebettet sind, und liefern wertvolle Erkenntnisse für Anwendungen in der thermischen Energiespeicherung, in Wärmemanagementsystemen und in anderen verwandten Bereichen.

Zusammenfassend trägt diese Forschung wesentlich zur Weiterentwicklung von multifunktionalen Strukturen bei und bietet eine holistische Perspektive, um die komplexen Anforderungen der Luft- und Raumfahrt und anderer Anwendungen zu erfüllen, bei denen die Masse eine Einschränkung darstellt.

Contents

1 Introduction **1**

2 State of the Art **5**
2.1 Cellular solids . . . 6
2.2 Phase Change Materials . . . 20
2.3 Heat transfer in porous media . . . 24
2.4 Stability of beams on elastic foundations . . . 34
2.5 Fundamentals of topology optimisation . . . 39

3 Lattice structures geometry **49**
3.1 Derivation of the Porosity . . . 50

4 Thermal characterisation **57**
4.1 Derivation of the effective thermal conductivity . . . 57
4.2 Experimental investigation and validation . . . 77
4.3 Analysis of natural convection . . . 91
4.4 Conclusion . . . 116

5 Stability of lattice structures embedded with PCM **119**
5.1 Numerical investigation of the stability behaviour of PCM-lattice composites . 119
5.2 Experimental verification of the stability behaviour . . . 144
5.3 Conclusion . . . 153

6 Multivariate Topology Optimisation **157**
6.1 Single functional optimisations . . . 158
6.2 Multi-functional optimisation . . . 165
6.3 Results and Discussion . . . 169

7 Conclusions and Outlook **179**

Bibliography **182**

A Non-dimensional numbers for heat transfer **205**

B Material properties considered **207**

C Effective Thermal Conductivity Formulae **209**

D Experimental setup of the thermal experiments **221**

E Temperature profiles and Infrared frames **225**

F Algorithm Implementation Natural Convection **237**

G Derivations of the equations for the stability of beams **243**

H Fundamentals on the modelling of beams on elastic foundations **253**

I Beam elements model implementation for embedded lattices **265**
I.1 Analytical solution for unit cells 267

J Analysis of a lattice component **271**

K Automatic Differentiation **281**

L Calculation of the Phase Change sensitivity **285**

Nomenclature

Abbreviations

bc	body centered
fc	face centered
bcc	body centered cubic
fcc	face centered cubic
f_2cc	face centered cubic with double diagonal
bccz	body centered cubic with vertical strut
f_2ccz	face centered cubic with double diagonal and vertical strut
f_2bcc	f_2cc combined with *bcc*
f_2bccz	f_2bcc with vertical strut
GWI	Global Warming Impact
ELVs	Expendable Launch Vehicles
RLVs	Reusable Launch Vehicles
MFS	Multifunctional Structure
LVs	Launch Vehicles
EVs	Electric Vehicles
CSP	Concentrated Solar Power
BTMS	Battery thermal Management Systems
PCMs	Phase Change Materials
FEM	Finite Element Method
FVM	Finite Volume Method
SLM	Selective Laser Melting
ETC	Effective thermal Conductivity
LHTES	Latent Heat thermal Energy Storage
SHTES	Sensible Heat thermal Energy Storage
PPI	Pores Per Inch

LTE	Local thermal Equilibrium
LTNE	Local thermal Non-Equilibrium
IHTC	Interstitial Heat Transfer Coefficient
SIMP	Solid isotropic material with penalization
GOCM	Generalised Optimality Criteria Method
OCM	Optimality Criteria Method
TPMS	Triply Periodic Minimal Surface
PWM	Pulse Width Modulation
CAD	Computer-Aided Design
RMSE	Root Mean Squared Error
IR	Infrared
PTFE	Polytetrafluoroethylene
STP	Specific thermal Performance
SIMPLE	Semi-Implicit Method for Pressure Linked Equations
ANA	analytical results
NUM	numerical results
LPBF	Laser Powder Bed Fusion
BEAM	beam elements
VOL	volumetric elements
PLC	Portevin-Le Chatelier
AD	Automatic Differentiation

Non-dimensional variables in thermal characterisation:

Fo	Fourier number
Ste	Stefan number
Ra	Rayleigh number
Nu	Nusselt number
Re	Reynolds number
Pr	Prandtl number
Gr	Grashof number

List of variables

Due to vast and multidisciplinary topic, variables with same symbol were used in different contexts. Here y are appropriately separated.

Unit cell geometry and effective properties:

χ	volume fraction (or relative density) of cellular solid
ε	porosity of cellular solid
A_0	cell cross-section
A_t	node cross-section
A_l	cross-section area of strut
α	ratio of node area to cross-section area of strut
t	edge length of node
L	strut length
e	ratio between edge length of node and strut length
ω_z	fitting parameter for complex intersection
V_{tot}	volume of unit cell
V_s	volume of struts
t_1 and t_2	side lengths of cubes
ω_ε	additional fitting parameter
ρ^*	relative density of cellular solid
ρ_s	density of bulk material of which cellular solid is made
ρ_f	density of filler material
ρ_{eff}	effective density of composite
E^*	effective Young's modulus of cellular solid
E_s	Young's modulus of bulk material
σ^*	effective yield stress of cellular solid
σ_{y_s}	yield stress of bulk material
$C_{p_{eff}}$	effective specific heat capacity of composite
C_{p_f}	specific heat capacity of filler
C_{p_s}	specific heat capacity of cellular solid bulk material
λ_{eff}	effective thermal conductivity
$\lambda_{\|\|}$	parallel model: upper bound
$\lambda_\perp$	series model: lower bound

λ_f	conductivity of raw filling material
λ_s	conductivity of raw solid material
Q_s	heat flux over solid phase
Q_f	heat flux over filler
ΔT	temperature difference
$H(s)$	distances of material through layer
$A_L(s)$	surface of conducting material at position s
H_c	cell height
A_f	surface of filling material

thermo-fluidic variables:

$\mathbf{u}$	velocity vector
ρ	density
p	pressure
$\boldsymbol{\tau}$	deviatoric stress tensor
g	gravitational acceleration
α	thermal diffusivity of medium
C_p	specific heat capacity at constant pressure
Ξ	heat source term
T_0	reference temperature
ρ_0	density at reference temperature T_0
β	coefficient of thermal expansion of fluid
$\mathbf{u_D}$	Darcy velocity vector
$\mathbf{K}$	permeability tensor
μ	dynamic viscosity of fluid
B	tortuosity
μ_{eff}	effective viscosity of porous medium in Darcy-Brinkman equation
T	temperature
S	source term
$(\rho C_p)_*$	heat capacity of fluid (f) or solid (s)
$(\rho C_p)_{eff}$	effective heat capacity of homogenised medium
λ_*	thermal conductivity

h_{if}	interstitial heat transfer coefficient
T_*	temperature of fluid or solid
Δh	change in enthalpy
ξ	position of interface between two phases, melting front position
n	normal vector to interface
t	time
ρ_{PCM}	density of PCM
H_f	heat of fusion of PCM
Φ	liquid fraction within domain
T_m	melting temperature of PCM
T_s	solidus temperature
T_l	liquidus temperature
$T(x=0,t)$	wall temperature
$H_{f,eff}$	effective latent heat of fusion
$H_{f,PCM}$	latent heat of PCM
D_H	hydraulic diameter

Structural variables:

σ	compressive stress
σ_{cr}	critical buckling stress
P	load
P_{cr}	critical buckling load of a slender beam
L_{eff}	effective length of slender beam
A	cross-section area of a slender beam
E	Young's modulus of material
I	second moment of area of cross-section
w	buckling shape
λ	eigenvalue
k	spring stiffness
y	spring deflection
q	spring reaction force
G_P	shear stiffness of spring bed

k_{Vesic}	foundation modulus based on Vesic's model
$k_{Herrmann}$	Herrmann foundation modulus
G_f	shear modulus of foundation
$K_0()$ and $K_1()$	modified Bessel functions of second kind for orders 0 and 1
EI	bending stiffness of beam
D	beam's diameter
b	foundation width
ΔU_1	strain energy of bending of beam
ΔU_2	bending strain energy resulting from elastic foundation
m	buckling mode
a_m	wave function
m_{cr}	critical mode

Optimisation variables:

$\mathbf{u}$	vector of unknowns
$\mathbf{K}$	stiffness matrix
$\mathbf{f}$	forcing array
D_e	element material tensor
c	compliance
D_0	actual material tensor
D_e	penalised material tensor
z	penalisation parameter
Ω	domain
r	filter radius
$\mathscr{L}$	Lagrangian
f	volume fraction of domain
V_0	total volume of domain
λ	Lagrange multiplier
B_e	scale factor
η	power parameter for scale factor
g_i	constraint
s_i	slack variable

$\mathbf{T}$	temperature matrix
k_e	stiffness matrix of a single element
$\mathbf{K}_h$	convection matrix
$\mathbf{K}_c$	conductivity matrix
$\mathbf{R}$	rotation matrix
$\mathbf{C}$	material tensor
τ_{xy}	shear stress
σ_x	principal stress in x-direction
σ_y	principal stress in y-direction
θ_p	rotation angle of principal axis
θ	rotation angle
J	goal function
w_i	weights of multifunctional optimisation
p	penalisation coefficient

Operators:

$\nabla\cdot$	divergence operator
∇	gradient operator
∇^2	Laplacian operator

1 Introduction

Background and Motivation of Research

Human-induced climate change is compelling society to undergo a paradigm shift. In the realm of emerging energy production and storage technologies, there is a crucial demand for innovative approaches to conceptualizing systems and subsystems. The significance of lightweight design is escalating, particularly in the context of mobile systems. Reductions in mass and volume not only enhance the performance of a mobile system but also positively influence its economic and ecological footprint. Specifically, direct emission reductions can be realized through mass savings, and the emissions stemming from the production process can be curtailed through lightweight design. The Life Cycle Assessment of mobile systems is significantly impacted by their mass. For instance, recent research has shown that Reusable Launch Vehicles (RLVs) consistently exhibit a higher Global Warming Impact (GWI) compared to Expendable Launch Vehicles (ELVs), irrespective of the number of reuses [1]. This discrepancy is attributable to the additional mass required for re-entry and landing during launch. Likewise, Electric Vehicles (EVs), grappling with the low energy density of Li-ion batteries, are attaining unsustainable mass levels, potentially jeopardizing the transition to a decarbonized electricity grid [2].

In light of these considerations, it is imperative to explore solutions that target mass reduction across the entire system. Within this context, the multifunctionality of load-bearing structures emerges as a critical enabler. A Multifunctional Structure (MFS) is achieved by integrating functional components into a structure, typically resembling a sandwich panel [3]. The integration of functional components into the load-bearing structure diminishes the need for secondary structures and joints, facilitating holistic mass reductions at the system level. Although the mass of structural components may increase, overall system mass reductions can be achieved.

As demonstrated by Son et al. [4], thermal control functionalities can be efficiently incorporated into structural components. In the context of climate change mitigation efforts, there is a growing interest in thermal control and management systems, as well as thermal energy storage [5, 6]. On one hand, thermal management systems are indispensable for the safe operation of widespread electro-chemical energy storage systems. Similarly, thermal control is becoming a concern for increasingly power-dense electronics, essential for autonomous driving, advanced avionics, and on-board electronics operating in harsh environments, such as spacecraft and Launch Vehicles (LVs).

On the other hand, thermal energy storage is anticipated to constitute a significant portion of energy storage technologies aimed at achieving climate change mitigation goals [7, 8]. Therefore, leveraging thermal energy storage and thermal control is pivotal for attaining the necessary technological progress. The confluence of these two aspects— the imperative for lightweight, mul-

tifunctional structural components and the escalating requirements for thermal control—forms the motivation for this research.

In particular, the recent years saw a sharp increase in research and industrial efforts to make use of latent heat to achieve efficient thermal energy storage or thermal management. So-called Phase Change Materials (PCMs), i.e. materials which exhibit a high latent heat of fusion, are intensively investigated for applications where heat sinks or thermal buffers are needed, but mass and volume constraints impose strict energy density requirements, i.e. in automotive and aerospace applications [9]. At the same time PCMs are proposed for energy storage in Concentrated Solar Power (CSP) plants [10] or for the built environment [11]. PCMs are commonly employed in applications where lightweight is a design driver, e.g. in the thermal control of spacecrafts. The rise of Electric Vehicles (EVs) and the requirements of an efficient Thermal Management for Li-ion battery packs brought to an exponential increase in investigations aiming to the exploitation of such materials for Battery Thermal Management Systems (BTMS) [12]. As also indicated by Shi et al. [12], a key to enable the efficient use of PCMs for BTMS and other thermal control systems in non-stationary applications lies in the structural integration. A comprehensively efficient thermal control system can be achieved by embedding the PCM within the load bearing structure of the controlled system. In this perspective, several synergies can be found to holistically improve both the thermal performance of the system and achieve mass reductions via multifunctionality.

In particular, the widespread use of PCMs for room-temperature thermal management is hindered by their poor thermal conductivity. Excluding metallic eutectic alloys, which are used for high temperature applications, most PCMs exhibit a low thermal conductivity, typically ranging between 10^{-1} and $10^{0}\frac{W}{mK}$ [13]. Several mitigation techniques are proposed in the literature to both address the encapsulation issues and the improvement of the thermal conductivity. In particular, embedding the PCM within cellular solids with open-cell morphology and a high thermal conductivity, is a method that increasingly gained popularity thanks to the advancement of manufacturing techniques. This way, composite materials are obtained, which exhibit an effective thermal conductivity that is orders of magnitude higher than the one of a PCM. Such composites are of interest for lightweight applications. In particular, novel porous structures obtained via additive manufacturing offer a high flexibility in controlling the effective properties of the composite. Additive manufacturing enables designing locally tailored lattice structures with different technical goals, i.e. mass reduction, stiffness improvement, or high surface area for heat exchange. Lattice structures were recently introduced as cores for lightweight sandwich structural panels, where mass and resource savings are a design driver. Being open-celled and having the possibility to efficiently tailor the geometry, such structural elements have been recently investigated for the multi-functional purpose of enhancing the thermal conductivity of a PCM while obtaining enclosures that can act as lightweight primary structures of different kinds of vehicles. If one considers that secondary structures, i.e. thermal control modules, can be removed, a holistic mass reduction potential can be achieved when considering such a composite primary structure, leading to energy and cost savings. While for static applications, mass savings are not as relevant for the performance of the system, resource savings are becoming increasingly important. Thus, a similar approach could become interesting for applications in

the energy sector, e.g. for high temperature salt-based latent-heat storage systems, which face challenges connected to the PCM encapsulation and the thermal and mechanical stresses acting on the containers. However, the thermal and mechanical behaviour of such composites is still poorly understood. Only few authors investigated the topic within the literature, and often, with attention to the thermal performance only. Thus, this work, sets the goal of introducing multi-functional structures based on architected lattice structures embedding Phase Change Materials. A multidisciplinary analysis and characterisation of the thermal and mechanical behaviour of composites made of metallic lattice core sandwich structures embedded with PCMs is proposed to cover such literature gap.

Research objectives

This work aims to characterise the thermal behaviour of PCMs embedded within metallic periodic lattices. Similarly, the effect of the presence of a PCM within the core of a sandwich panel on the effective mechanical properties is investigated. The obtained correlations are discussed and semi-analytical formulae are obtained. Within the frame of these activities, three research hypotheses are formulated, which are then validated or disproved throughout the following chapters of this work. These are:

1. The effective thermal conductivity tensor can be derived in the form of an analytical function of generic unit cell geometric parameters and material properties.
2. The topology influences only the effective thermal conductivity, while effective density and effective specific heat are obtainable via volume mixture rule (i.e. they only depend on the cell porosity). These combined are sufficient to describe the transient thermal behaviour of the composite.
3. The presence of a solid PCM acts as an elastic bed for the lattice struts. The critical buckling load of both the lattice struts, and the structure as a whole is increased.
4. Optimal geometries for thermal and structural functionality can have opposing design drivers. With help of a multivariate topology optimisation, and Pareto optimality evaluations, the appropriate geometry for any boundary condition can be found.

Structure of the Thesis

Chapter 2 delivers insights on the relevant works in the fields of cellular solids for the considered applications, i.e. thermal and structural purposes. An overview is given on both latent heat thermal energy storage and mechanical and thermal properties of different kinds of cellular solids.
The fundamental equations for the thermal and mechanical behaviour of the composites are introduced. In particular, the methods to calculate the effective properties of similar cellular solids are described. The fundamentals as well as the state of the art on fluid flow in porous media are described in order to introduce the methods to characterise natural convective motions in the composite, and its effect on the thermal behaviour.

Fundamental theories regarding the stability of lattice struts embedded within elastic media are introduced.
Finally, the fundamentals of topology optimisation are introduced to allow a detailed approach to the multi-variate optimisation of the lattice structure.
It is worth mentioning here that, due to the very broad and multidisciplinary nature of this work, detailed discussions of the state of the art are included in the following chapters, where the relevant topics are introduced.
Chapter 3 describes the methods to analytically describe the geometrical properties of the lattice structures. In particular a univoque relation between the porosity of the unit cell and all other geometrical parameters is derived. While synthetic, this Chapter is necessary to introduce the analytical description of the thermal behaviour of the composites, as well as allow the multivariate topology optimisation.
Chapter 4 introduces the characterisation of the thermal behaviour of the composites. In particular, semi-analytical methods to describe the effective thermophysical properties of the composite are derived. Numerical and experimental validations are proposed. A variety of geometrical parameters are included in order to be able to deliver a description of the thermal behaviour which is applicable for a periodic lattice structure with generic geometrical arrangement of the struts in the unit cell. Additionally, evaluations of the effect of natural convection on the melting process are introduced.
Chapter 5 sheds light on the effect of PCMs presence within an enclosed lattice structure. A treatment of the PCM as an elastic medium is introduced. In particular, the effect of the PCM on the stability of lattice structures is numerically investigated. A brief experimental validation is presented as well.
With the information obtained by the characterisations described in chapters 4 and 5, **Chapter 6** delivers an approach to perform a multivariate optimisation of such components. The main target functions considered are mechanical stiffness and wall temperature, while the mass is fixed as a constraint.
Chapter 7 summarises the findings and indicates additional activities to be performed in future works to increase the maturity of this technology.

2 State of the Art

Due to the multidisciplinary goals, this work draws from two fundamental fields of engineering, namely structural mechanics and heat transfer. To appropriately treat the analytical, numerical and experimental methods implemented in this thesis, the relevant theoretical background for both engineering fields is introduced in separate successive sections. Additionally, a brief introduction about the fundamentals of topology optimisation is given. For sake of brevity, only the relevant theoretical frameworks necessary to develop this work, are introduced. The reader can refer to the book of Incropera et al. [14] for a fundamental description of the basic principles of heat transfer. Similarly, for structural mechanics and lightweight design fundamentals, the reader can refer to the work of Megson [15] or Wiedemann [16]. Both the Finite Element Method (FEM) and the Finite Volume Method (FVM) are employed throughout this work to numerically solve the equations which describe the analysed phenomena. The reader can refer to the book from Prathap [17] to have a description of the FEM with a focus on structural mechanics, including the formulation of elements useful throughout this work, i.e. Timoshenko beam elements. For the FVM with focus on heat transfer, the reader is referred to Reddy et al. [18]. The main reference for topology optimisation fundamentals is instead the book of Bensøe and Sigmund [19]. This work also refers to the text of Kochenderfer and Wheeler [20] for optimisation algorithms.
The lattice structures treated in this work are additively manufactured. The manufacturing process is based on the Selective Laser Melting (SLM) technology. This is however not the scope of this work. The reader can refer to the work of DebRoy et al. [21] for a comprehensive review of the SLM process. The work of Mines et al. [22] instead gives a review of the state of the art of the manufacturing of metallic lattice structures. The reader might want to refer also to recent work which obtained such structures also via investment casting, with a variety of alloys [23].

The focus of this work is the description of the thermal and mechanical behaviour of lattice structures with embedded Phase Change Materials. The lattice structures can be treated as porous media. As such, the characterisation is first approached via obtaining effective thermophysical, and mechanical properties of the composite with help of volume averaging methods. Chapter 6 of Shyy's book [24] efficiently illustrates the rigorous approach to obtain volume averaged equations, and thus properties, from the microscopic ones.
First a literature review of cellular solids, of which lattice structures are a sub-branch, is made. Fundamental methods and correlations to obtain effective properties are described. Then, the fundamental theory and state of the art necessary to describe transport phenomena in porous media is described. This is a preamble for the aimed description of the thermal behaviour of a PCM within such porous media. Finally, a review of the literature on latent heat thermal energy

storage and the use of Phase Change Materials is done. In particular, the literature regarding the use of high thermal conductivity cellular solids to improve the thermal conductivity of PCMs is analysed. Finally, the fundamental background to describe the effect of PCMs on the mechanical behaviour of the lattice structure is illustrated to describe the basic theory applied to investigate the phenomenon.

2.1 Cellular solids

The definition of cellular solid used in this work is consequent with Gibson and Ashby [25]. Cellular solids are employed in a variety of engineering applications, the main ones being thermal insulation, lightweight structures, heat exchangers, energy absorption, vibration damping, sound insulation, filtering, catalysis [25, 26, 27, 28, 29]. Cellular solids can be found in nature in the form of wood, cork or sponge, whereas foams are the most common man-made cellular materials. They are usually made by foaming polymers. However, it is also possible to foam ceramics, glasses and metals.

2.1.1 Topology

The most general description of a cellular solid is that of a conglomerate of enclosed spaces (cells) with solid edges or faces, which are packed together to fill up a space domain. Solids composed of two-dimensional arrays of regular or irregular polygons are typically named *honeycombs*. One refers instead to *foams* when considering a three-dimensional packaging of cells constituted by polyhedra. Not all polyhedra are suited to fill space in their undistorted form. Only the triangular, hexagonal and rhombic prisms, as well as the rhombic dodecahedron and the tetrakaidecahedron (also known as Kelvin cell) are. Foams exhibit an usually stochastic arrangement of non-identical unit-cells, with different sizes, shapes, number of edges and faces. However, idealisations of a foam geometry can be based on the above mentioned polyhedra. Foams can be either open-celled, if the polyhedra connect via open faces, or close-celled otherwise (see Figure 2.1).

With recent advancements in manufacturing technologies, i.e. metal additive manufacturing, so-called *lattice structures* with different kinds of unit cells were introduced [30]. Their peculiarity is having a three-dimensional periodicity (differently from the two-dimensional one of honeycombs), and are generally open-celled [22]. Lattice structures can be seen as a particular kind of foam with a non-stochastic arrangement and can be divided in strut-based and surface-based lattices. The first have morphologies inspired to the Bravais cells and are denominated as such. The surface-based lattices are represented by periodic arrangement of unit cells defined as different Triply Periodic Minimal Surfaces [31]. Figure 2.2 schematically shows this subdivision of cellular solids, while Figure 2.3 shows the most relevant strut lattices analysed in the

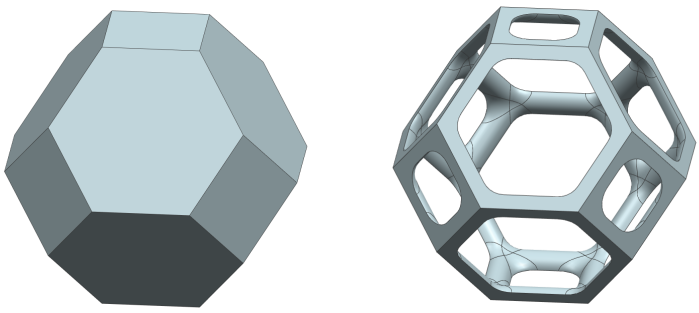

Fig. 2.1: Closed and open Kelvin Cell.

literature, and which are the focus of this work.

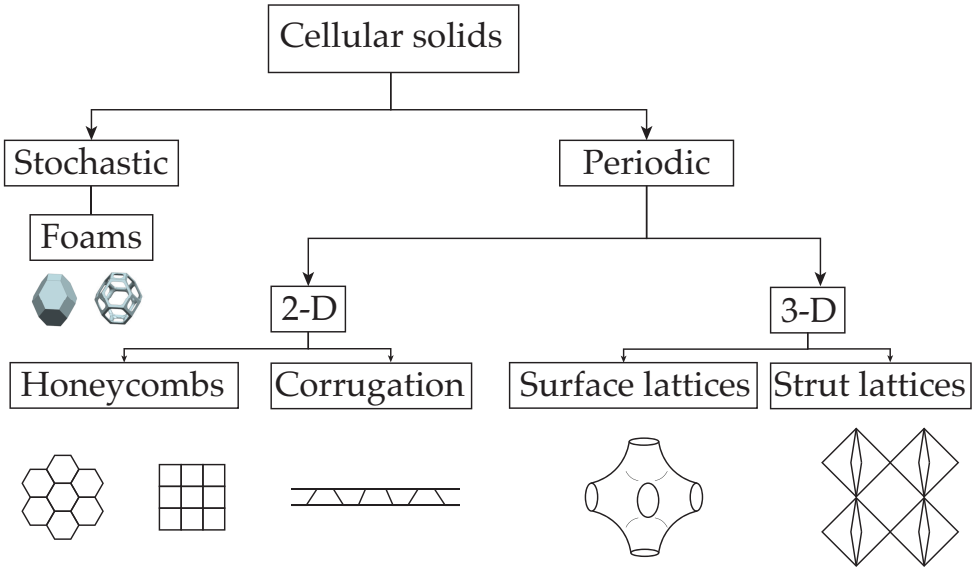

Fig. 2.2: Schematic description of the various cellular solid categories.

Three fundamental rules characterise the geometry of cellular solids, namely the Euler's law, the Aboav-Weaire law and Lewis's rule. These help define critical topological parameters, such as the relative density (or porosity), that drive the effective physical properties of cellular solids. The **Euler's law** helps quantify the amount of faces, edges and vertices a space-filling cellular solid can have. Indeed, one can idealise any cellular structure via a number of *vertices* V connected to each other via *edges* E. Edges surround *faces* F which enclose *cells* C. The number of edges which meet at a vertex is defined as edge-connectivity, while the number of faces meeting at an edge is the face-connectivity. The Euler's law states that

$$-C+F-E+V=1 \tag{2.1}$$

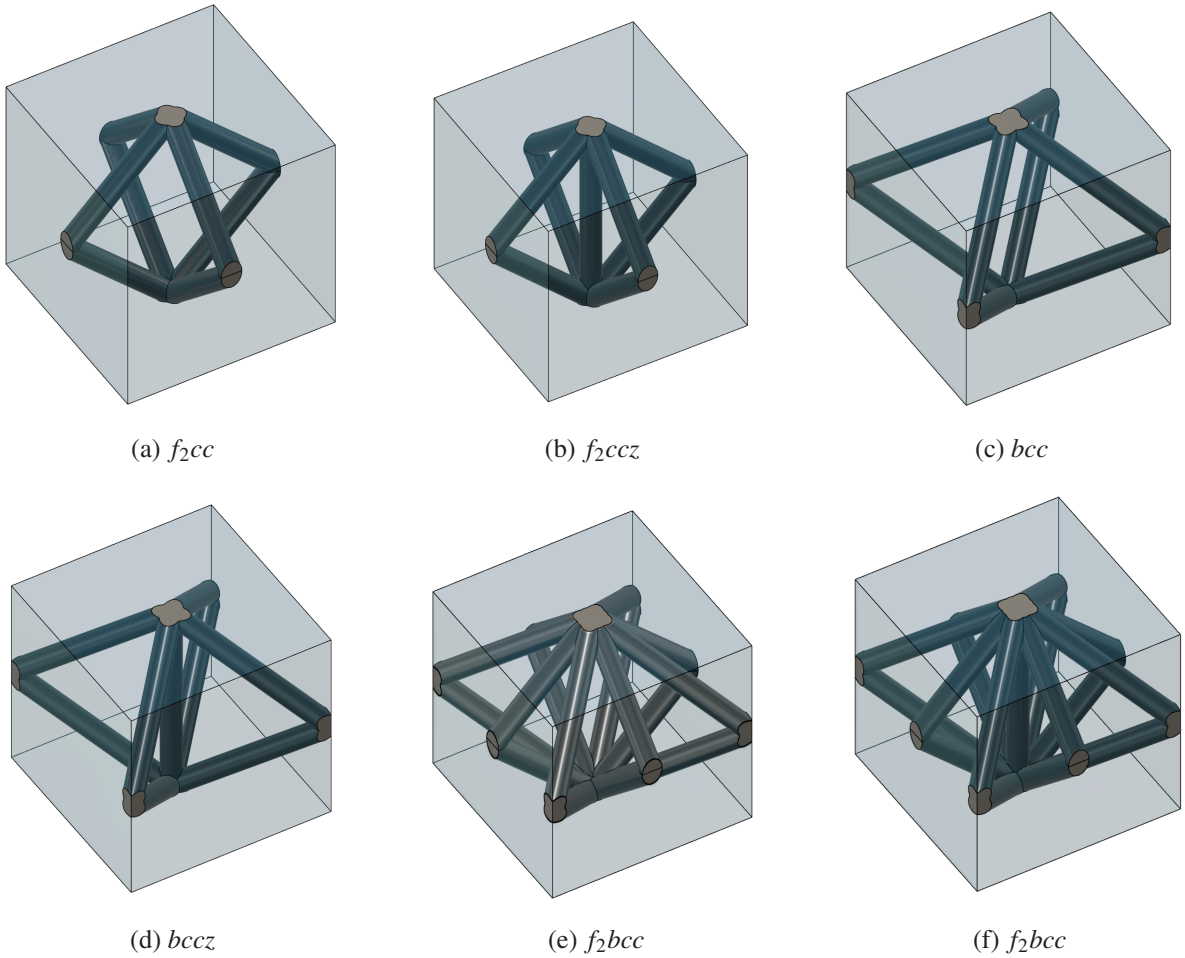

(a) f_2cc (b) f_2ccz (c) bcc

(d) $bccz$ (e) f_2bcc (f) f_2bcc

Fig. 2.3: The investigated cuboid unit cells.

or, in a two dimensional case (honeycomb),

$$F - E + V = 1 \tag{2.2}$$

The consequence of this law is that even *irregular* cellular solids have, on average, a fixed amount of sides per face. In three dimensions, i.e. for foams and lattices, the number of sides per face $\bar{n}$, is given by

$$\bar{n} = \frac{Z_e Z_f}{Z_e - 2}\left(1 - \frac{2}{F}\right) \tag{2.3}$$

where Z_e is the edge-connectivity and Z_f is the face connectivity. The Euler's law hints that if a cell has a higher than average number of edges, the neighbours shall have a lower than average one.

2.1.2 Properties

The mechanical, thermal and electrical properties of cellular solids are not only dependent on the properties of the bulk material, but rather they strongly depend on their relative density. Many properties such as the thermal and electrical conductivity or the Young's modulus roughly adhere to power laws in dependence of the volume fraction χ (or relative density) of the cellular solid [25]. This dependence can be generically described by the following equation.

$$\frac{K^*}{K_{solid}} = C\chi^n \tag{2.4}$$

where K^* is a generic property of the cellular solid, K_{solid} is the property of the bulk material under the same conditions, C and n are empirically determined coefficients. The theoretical explanation for this is provided by the so-called *percolation theory* [32]. The theory deals with the forming of network-like clusters in grids or arrays of squares called square lattices. If there is some probability P^* that a square is occupied by a dot, depending on the probability, clusters of neighbouring squares with dots will form. Above a certain probability a continuous cluster

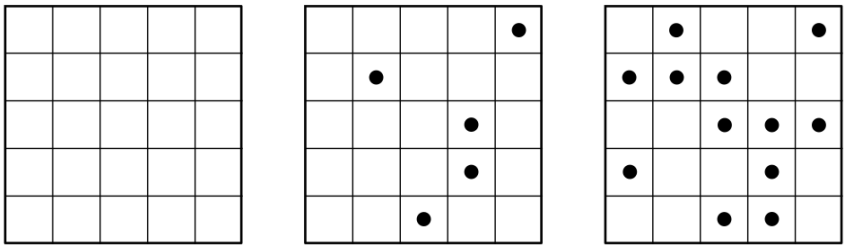

Fig. 2.4: From left to right: empty square lattice, square lattice with randomly distributed dots, square lattice with continuous cluster of dots. [32]

that connects all boundaries of the array is formed. That probability is called the percolation threshold P_c^*. It can be shown that above the percolation threshold many geometrical and statistical properties of the network adhere to power laws of the kind expressed in the following equation [32].

$$K^* \sim \left(P^* - P_c^*\right)^n \tag{2.5}$$

In the case of cellular solids P_c^* can be set to zero, since all regions of the solid have to be connected, otherwise it would not be one body. The probability is analogous to the volume fraction, since the fraction of occupied squares in a large lattice is equal to the probability. Hence, one obtains Equation 2.4. The most relevant properties for this work are static-mechanical (i.e. effective stiffness and strength) and thermofluidic (i.e. effective thermal conductivity, diffusivity and permeability). These are discussed in detail.

2.1.3 Mechanical properties

The most widely accepted description of the mechanical behaviour of cellular solids, including lattice structures, is the Gibson-Ashby model [25]. According to such model, the behaviour of a unit-cell when mechanically loaded can be either *stretching-dominated* or *bending-dominated* [25, 33, 34, 35]. A generalised deformation behaviour of cellular solids is shown in Figure 2.5. Three different stages exist: linear-elastic, plastic deformation and densification [33, 35]. In the elastic part of the deformation, the structure deforms following a linear relationship with the bulk Young Modulus of the material. However, as possible to see in Figure2.5, the effective Young Modulus of a stretching dominated cell is typically higher than the one of a bending dominated one. Once the elastic limit (yield stress) is reached, plastic deformation takes place. Here the differences between stretching and bending-dominated cellular solids become more evident. Indeed, a bending dominated behaviour is characterised by a so-called plateau stress, i.e. deformation continues with an almost constant stress. The stress required for further plastic deformation in a stretching dominated unit cell is variable [35]. The last stage, named densification, occurs when components of the unit cell deform so much that they contact each other. Further deformation is constrained by newly tightly packed cell components and the associated stress increases exponentially. Foams exhibit an isotropic bending dominated behaviour[36].

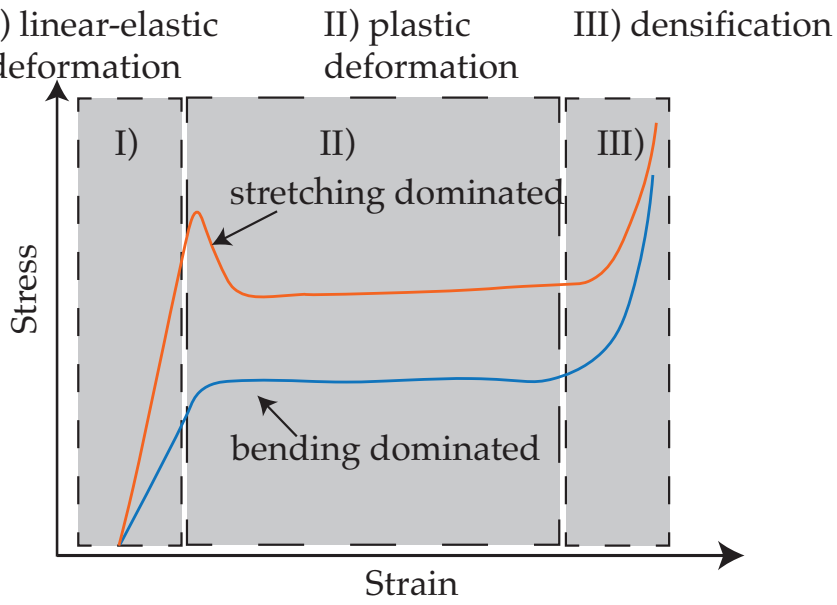

Fig. 2.5: Schematic description of the two different deformation behaviours for a stretching dominated and a bending dominated unit cell.

The isotropicity was already described in Sec.2.1.1. The bending dominated behaviour is the result of the struts usually meeting at an obtuse angle (see e.g. Figure2.1). Lattice structures, instead, are usually anisotropic although some topology, e.g. the cubic *bcc* is isotropic. A generalised determination of their mechanical behaviour is not immediate. In an effort to establish a generalised criterion to distinguish a stretch-dominated cellular solid from a bending-dominated

one based on its geometry, Deshpande et al. first [36] and Ashby et al. [33] later, made use of the Maxwell's stability criterion [37] described in Equation 2.6 and Equation 2.7.

$$M = b - 2j + 3 = 0 \tag{2.6}$$

$$M = b - 3j + 6 = 0 \tag{2.7}$$

where M is the number of degrees of freedom, j is the number of joints, b the number of struts. If $M < 0$ the structure is a mechanism. If the joints are locked, as it is the case for cellular solids, where the unit-cell struts are connected to adjacent struts of other unit-cells, the struts bend under loading (bending dominated). If $M = 0$, the struts are loaded as trusses, i.e. under tension or compression only (stretching dominated). Slender structures like the struts of an open celled cellular solid are much more structurally efficient when stretched than under bending. Thus, as shown schematically in Figure2.5, a stretching dominated cellular solid has a higher structural efficiency than a bending dominated one with the same relative density. Looking at Figure 2.6 one can notice that an additional condition, corresponding to the case of $M > 0$ exists. If the horizontal strut is shortened, the other struts will be put into compression, balancing the tension it carries. The struts carry stress even though the structure carries no external loads (self-stress). Equation 2.6 and Equation 2.7 represent a necessary but not-sufficient condition for rigidity, as they do not account for states of self-stress or mechanisms. A generalised version of the Maxwell criterion can be found in Equation 2.8.

$$M = b - 3j + 6 = s - m \tag{2.8}$$

where s is the number of states of self-stress (overconstraining) and m the number of mechanisms. The insufficiency of the Maxwell criterion as a condition for the definition of the behaviour of a cellular solid is evident as M=0 can be obtained by any combination of s and m that subtracted from each other yields 0. Gibson and Ashby [25, 33] established a model for the description of mechanical properties based on bending or stretching dominated behaviour. The model is based on different power laws, with empirical coefficients and exponents. These laws are summed up in Table 2.1. Here the exponents are fixed according to [25]. However, they may also be derived from experimental data.

Lattice structures Important studies like the one from Leary et al.[38] evidenced that, as expected according to the Maxwell criterion, the response to uniaxial compression of bcc and $f_2$cc-based lattice structures fits the one of a bending dominated unit cell. The addition of a vertical strut (parallel to the direction of the compressive load), yields bccz and $f_2$ccz unit cells which according to the Maxwell criterion shall be stretching dominated. The study from Leary et al. also indicated a mechanical response compatible with it, however they noticed an oscillative behaviour of the stress as a function of strain in the plastic deformation (II) in Figure2.5) part of the stress-strain curve. In a relevant and extensive review, Maconachie et al. [35] related the experimental data available in the literature with the Gibson-Ashby model.

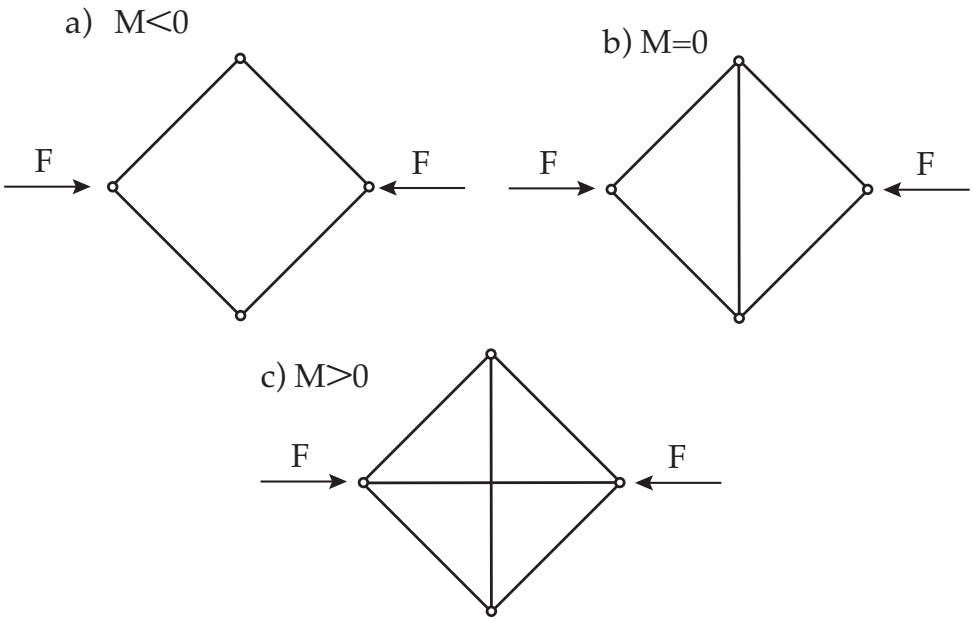

Fig. 2.6: Schematic description of the possible cases related to the Maxwell criterion for: a) a cellular solid which has a bending dominated behaviour, b) one with stretching dominated behaviour and c) an overconstrained one which gives origin to self-stress and does not directly identify in one of the two previous categories. Here F is the external force, and M is the number of degrees of freedom.

Property	Bending dominated	Stretching dominated
Relative modulus (E^*)	$\frac{E^*}{E_s} = C\left(\frac{\rho^*}{\rho_s}\right)^2$	$\frac{E^*}{E_s} = C\left(\frac{\rho^*}{\rho_s}\right)$
Relative strength (σ^*)	$\frac{\sigma^*}{\sigma_{y_s}} = C\left(\frac{\rho^*}{\rho_s}\right)^{\frac{3}{2}}$	$\frac{\sigma^*}{\sigma_{y_s}} = C\left(\frac{\rho^*}{\rho_s}\right)$

Table 2.1: Power laws for bending and stretching dominated behaviours according to [25]. C is an empirically obtained coefficient, ρ^* is the relative density of the cellular solid, ρ_s is the density of the bulk material of which the cellular solid is made, E^* is the effective Young's modulus of the cellular solid, E_s is the Young's modulus of the bulk material, σ^* is the effective yield stress of the cellular solid and σ_{y_s} is the yield stress of the bulk material.

They found that most lattice structures exhibit a bending dominated behaviour and that their coefficients C vary in a range between 0.1 and 4 for the relative modulus and between 0.1 and 1 for the relative strength. However, the authors themselves indicate that the applicability of such a generalised model is limited and several factors hinder its quantitative reliability. Indeed, as indicated also by Zadpoor [39], the orientation of the cell of an anisotropic lattice structure with respect to the load strongly affect the mechanical response. Zadpoor additionally evidenced that the lack of reliable models for the estimation of the relative density can also be misleading. Bühring et al. [40] developed and validated a semi-analytical model for the description of the axial stiffness of lattice structures based on bcc and $f_2$ccz unit cells. Interestingly enough and in counter-tendency with respect to what reported by Leary et al. [38], the relationship between the relative modulus and the relative density was reported to be linear for both bcc and $f_2$ccz, thus coherent with a stretching dominated structure. Bühring et al. [40] additionally showed how the effective mechanical properties of the considered lattice structures strongly depend on other geometrical parameters and boundary conditions, indicating that an unequivocal description of the mechanical behaviour of such structures via power laws is not feasible.

2.1.4 Thermophysical properties

Cellular solids and in particular foams found application as insulation and fire retardant materials. Recent literature intensively investigated the exploitation of the typically low thermal conductivity, with respect to the bulk material, of sandwich cores based on cellular solids, in particular corrugated and lattice cores, for high temperature applications, i.e. so-called Thermal Protection Systems. In other applications, exploiting the high surface area, material flows through foams using the cellular solid as heat exchangers [41]. For the combination of cellular solids with a filler, e.g. a PCM embedded in a metallic foam or a metallic lattice structure, effective thermophysical properties are used and the component can be treated as a composite material. Properties such as the effective density or the effective specific heat capacity can be determined via mixing laws [42] and depend only on the porosity ε via the following equations.

$$\varepsilon = 1 - \chi \tag{2.9}$$

where χ is the volume fraction of the cellular solid, often also described as the relative density with respect to the bulk material of which it is made ($\frac{\rho^*}{\rho_s}$). The effective density of the composite is then

$$\rho_{\text{eff}} = \varepsilon \rho_f + \chi \rho_s \tag{2.10}$$

where ρ_{eff} is the effective density of the composite, ρ_f is the density of the filler material, ρ_s the density of the bulk material of the cellular solid. Similarly, the effective specific heat capacity is given by

$$C_{p_{\text{eff}}} = \varepsilon \frac{\rho_f}{\rho_{\text{eff}}} C_{p_f} + \chi \frac{\rho_s}{\rho_{\text{eff}}} C_{p_s} \tag{2.11}$$

where $C_{p_{\text{eff}}}$ is the effective specific heat capacity of the composite, C_{p_f} is the specific heat capacity of the filler and C_{p_s} is the specific heat capacity of the cellular solid bulk material. The mixing law cannot as simply be applied to the effective thermal conductivity (ETC). To determine the ETC, the morphology of the cellular solid is of fundamental importance [42]. In the most general case, the ETC is represented by a tensor with nine different terms.

$$\bar{\bar{\lambda}}_{\text{eff}} = \begin{bmatrix} \lambda_{xx} & \lambda_{xy} & \lambda_{xz} \\ \lambda_{yx} & \lambda_{yy} & \lambda_{yz} \\ \lambda_{zx} & \lambda_{zy} & \lambda_{zz} \end{bmatrix} \tag{2.12}$$

Different methods to determine the ETC of a cellular solid were presented in the literature. Models such as the upper and lower bounds established by Maxwell [37] were transferred to the calculation of effective properties of porous media by Hashin and Shtrikman [43]. Analytical approaches such as those of Dul'Nev et al. [44] are still used in research decades later, for example in Paek's et al. [45] experimental investigations. At the turn of the century, many works appeared on calculating the ETC of porous media. Till the end of the first decade of the 21$^{\text{st}}$ century, mainly metallic and ceramic foams were investigated. Fu et al. [46] used the thermal circuit method to approximate the ETC of porous ceramics by means of standard cubic cells. In the thermal circuit method, different layers of a specific resistance are stacked, resulting in a serial system [14]. The investigations performed by Lu and Chen show that, if the filler is a fluid, the conductivity of the fluid phase can often be neglected. For small closed cells, such as honeycombs, convection has a negligible influence. Kaviany [42] and Ranut et al. [47] give a summary of methods for calculating the ETC of porous media. Especially Maxwell's upper and lower bound theory is used. These methods are also called asymptotic solutions. However, the results of this method are very inaccurate [47]. With the help of empirical fits, the accuracy of the models was greatly improved [48, 49, 47]. In addition to the density and the material properties of both materials, fit factors are necessary to balance the asymptotic solutions, which sometimes differ strongly for different foams. The deviation in the geometry of different foams is strongly dependent on the manufacturing process and parameters, and is often so high that a generalisation of the parameters is often not successful. Ashby et al. [33] us the percolation theory of Stauffer et al. [32] to estimate the ETC by means of fitted power laws as a function of the relative density of the foam.

A different approach is used by Calmidi et al. [48], who approximates the appearance of the porous cell structures by means of hexagons and determines the ETC in two-dimensional space using the the circuit method. Subsequently, the first three-dimensional models for the description of metallic foams were developed by Boomsma et al. [50]. Kelvin cells described in 2.1.1 are used as a reference geometry for the estimation of the ETC.

The different approaches to derive the ETC of metallic foams can be divided into three different methods [47]. Figure 2.7 gives an overview of the approaches. The *asymptotic* approach uses the porosity to set up a thermal network model. It calculates the upper or lower bounds of the conductivity of the cells. The parallel model $\lambda_{||}$ (Equation 2.13) of the ETC calculates

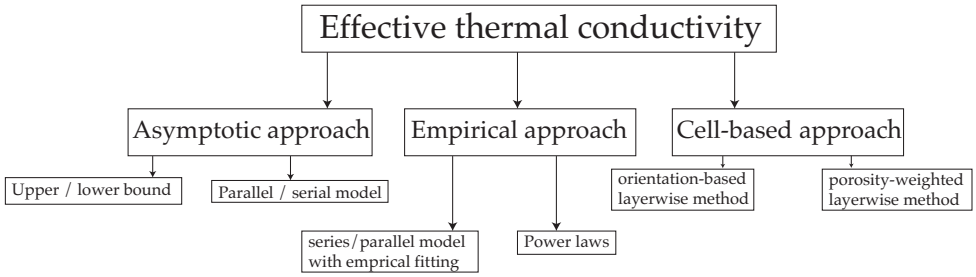

Fig. 2.7: Methods to derive the ETC of a cellular solid, in particular of a foam.

the upper bound, i.e. the maximum achievable conductivity through the arithmetic mean of the conductivity of the two materials (i.e. filler λ_f and cellular solid λ_s). The lower bound $\lambda_\perp$ is achieved in the series model (Equation 2.14)[47]. This method to approximate the ETC was used by Maxwell [37] and is referred to as upper and lower bound method.

$$\lambda_{||} = \varepsilon\lambda_f + \chi\lambda_s \tag{2.13}$$

$$\lambda_\perp = \left(\frac{\varepsilon}{\lambda_f} + \frac{\chi}{\lambda_s}\right)^{-1} \tag{2.14}$$

Due to the aforementioned low accuracy of the asymptotic approach, *empirical* descriptions were developed. In Calmidi et al. [48], the parallel model (Equation 2.13) is fitted to experimental results via a power law. Bhattachaeya et al. [49] used both the parallel and serial models (Equations 2.13 and 2.14) and determined a proportion of how much the two models contribute to the ETC. One third of the upper bound and two thirds of the lower bound yielded a good approximation of the ETC for the cases considered. Mendes [51] examined different methods for calculating the upper bound and lower bound, such as the Hashin-Shtrikman bounds or the effective medium theory, and combined them. He obtained good results with some combinations of the different bound-methods. The described empirical models show high accuracy in estimating the ETC of foams with fillers. However, the models have a small flexibility. For small changes in the morphology of the foam, or even for when considering honeycombs or lattices, new empirical coefficients have to be determined to make the models fit the experimental results.

The *cell-based* approach, aims at addressing the issues of the previously discussed models. Here, the unit cell of a foam is approximated by an ordered structure, usually the tetracaidecahedron, the dodecahedron or other unit cells. Using this method, the basic geometry of the foam is appropriately taken into account. However, due to the difficulty to model the nodes at which struts of the unit cell meet, empirical factors still must to be used to adapt the models to the experimental or numerical results. Furthermore the random distribution and size of the unit cells introduces further variability that can only be taken into account via empirical coefficients. The circuit method is often used to calculate the conductivity of different layers in series. The conductivity can be determined with a porosity-weighted approach [48, 50].

Calmidi et al. [48] determine the ETC of foams by assuming the cells to be two-dimensional

hexagons. The intersections of the struts are considered as square nodes. The square nodes do not intend to represent the real shape of the intersections, but the intersection area. The cell is divided into different layers. Figure 2.8 shows the different layers of one eighth of the hexagonal cell. The thermal conductivity of one layer is calculated weighting the fraction of the metallic phase (black area) and the filler (white area) as in Equation 2.13 and the total thermal resistance of all layers can be calculated according to the Equation 2.14 for serial systems. Using an empirical correlation factor, the model agrees well with the experimental data. However, the model has unrealistically large nodes (22 times larger than the strut diameter). A correction is made in Bhattacharya et al. [49] by assuming circular nodes instead of square nodes. The size of the nodes is reduced, but it is still unrealistically large in this model. This indicates that the two-dimensional modelling does not realistically represent the real case. Boomsma et

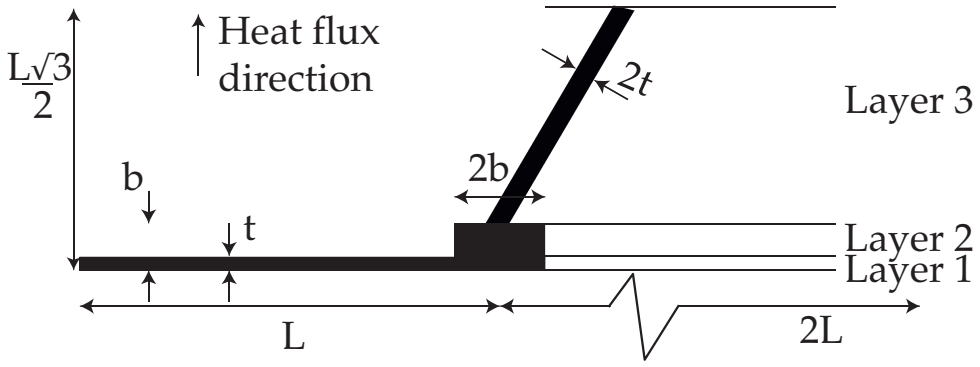

Fig. 2.8: One eighth of the two-dimensional hexagonal cells used by Calmidi et al. [48]. The structure is separated into three layers, and b is the node size, t - strut thickness, L - strut length.

al. [50] established a three-dimensional approach in which the porous cells are approximated as tetracaidecahedral cells. For derivation, 1/16 of the cell is used. This fraction is chosen to contain all the geometrical properties of the cell. The intersections are represented by cubes. The cell is then divided into layers and, similar to Calmidi et al. [48], the conductivity of the layers is calculated on a porosity-weighted basis according to Equation 2.14. Dai et al. [52] reveal three significant errors of the model of Boomsma et al. [50], which addresses misrepresentations of results and faulty equations. It also draws attention to the fact that the orientation of the struts is of importance and thus the porosity-based approach is an inadequate representation of reality. This is especially true when the conductivity of the filler is significantly smaller than that of the foam. Moreover, Dai et al. [52] question the tetracaidecahedral cell as an appropriate approximation of the foam. Even the corrected equations in Dai et al. [52] lead to physically unrealistic models. The size of the nodes decreases as the porosity of the foam decreases, which is reversed in reality and results in the strut diameters becoming larger than the nodes. Yang et al. [53] exposes the error of setting the parameter describing the ratio of nodal edge length to nodal spacing constant. They proposed a fitted parameter and thus solved the problem of mismatched node sizes. Yang et al. in [54] presented an alternative approach that determines the ETC via integrating over the cell from Fourier's Law. Tetracaidecahedral cells are assumed. By transforming Fourier's law and integrating, Equation 2.15 is obtained for the solid phase. Q_s

is the heat flux over the solid phase due to the temperature gradient ΔT. λ_s is the conductivity of the raw solid material, $H(s)$ represents the distances of the material through the layer and $A_L(s)$ the surface of the conducting material at the position s.

$$Q_s = \frac{\lambda_S \Delta T}{\int_0^{H(s)} \frac{1}{A_L(s)} ds} \tag{2.15}$$

For the heat flow of the filler Q_f, Equation 2.16 is assumed according to Fourier's Law. λ_f is the conductivity of the raw filling material, H_c represents the cell height and A_f the surface of the filling material.

$$Q_f = \lambda_f A_f \frac{\Delta T}{H_c} \tag{2.16}$$

After inserting the two Equations 2.15 and 2.16 into Equation 2.17, and after transforming the equation, Equation 2.18 is obtained.

$$Q_f + Q_s = \lambda_{\text{eff}} A_0 \frac{\Delta T}{H_c} \tag{2.17}$$

$$\frac{\lambda_{\text{eff}}}{\lambda_s} = \frac{\left(\frac{H_C}{A_0}\right)}{\left(\int_0^{H(s)} \frac{1}{A_L(s)} ds\right)} + \frac{\lambda_f}{\lambda_s}\varepsilon \tag{2.18}$$

where λ_{eff} is the ETC, ΔT the temperature gradient over the cell, A_0 the cell surface orthogonal to the interested direction and ε the porosity. Topological parameters are used to solve the integral. The ratio of the node area A_t to the cross section area of the strut A_L is defined as $\alpha = A_t / A_L$ and the edge length of the node t is compared to the strut length L with $e = t/L$. For the detailed solution of the integral, the reader is referred to the appendix of Yang et al. [54]. The result is shown in Equation 2.19.

$$\frac{\lambda_{\text{eff}}}{\lambda_s} = \frac{1-\varepsilon}{\left(1 - e + \frac{3e}{2\alpha}\right)\left(3(1-e) + \frac{3}{2}\alpha e\right)} + \frac{\lambda_f}{\lambda_s} \tag{2.19}$$

The topological parameters are found optimal with the help of a fit to experimental data and yield $\alpha = 1.5$ and $e = 0.3$. If the conductivity of the fluid is neglected ($\lambda_f / \lambda_s << 1$), the Equation 2.19 can be simplified to the first right term.

Yang et al. [54] further investigate to what extent the decoupling of lattice and filler influences the result. For $\lambda_s / \lambda_f > 8000$, the fluid phase is completely negligible as it is not noticeable in the ETC. For $\lambda_s / \lambda_f = 538$ the thermal conductivity increases by 10% due to the fluid phase. However, this value only applies to the foams investigated by Yang et al. [54] and differs for other cell architectures and porosities.

A wide literature regarding models to determine the ETC of foams, and in particular metal foams, exists. While the estimation of the ETC is relevant to this work and cell-based approaches similar to the ones of foams are used in this work, a full description of the models present in the literature is out of scope. The reader can found an extensive review on the mod-

els for the estimation of the ETC of foams in [47]. The following paragraph focuses on the available models for the description of the ETC of lattices and discusses their limits.

Lattice structures The cell-based approach is particularly useful to describe the ETC of periodic lattice structures, which are the focus of this dissertation. Indeed, the periodicity allows to reduce the amount of empirical factors needed, making the models presented in the literature more reliable and flexible. This far, only few authors proposed models to describe the ETC of lattice structures [55, 56]. The semi-analytical model presented by Hubert et al. [55] represents the most reliable and accurate one present in the literature at the time of writing. Their work consisted in the adaptation of the method previously derived by Yang et al. in [54] for foams. The following assumptions apply for modelling the ETC:

- Uniform lattices
- No convection and radiation
- Constant physical properties
- Thermal equilibrium

If radiation and convection are neglected, the pore size has no influence on the ETC [51, 54]. Thus, the ETC of the lattice structures can be considered scale invariant under these assumptions, i.e. unit cells with different cell size but same porosity yield the same thermal conductivity.
Hubert et al. [55] investigated the cubic unit cells f_2cc, f_2ccz, bcc and $bccz$. To allow a simplified treatment of the nodes at which different struts meet, the unit cells geometry was approximated by assuming that the region in which the struts of the unit cell meet, a cube is formed, as schematically shown in Figure 2.9. Neighbouring cells also lead to nodes, which are accounted as a cube of half the size of the central node. Fit factors are introduced to model the complex intersection between struts and nodes. Such factors were determined from experimental data. Topological parameters defining the relations of the different sizes in the unit cell, i.e.

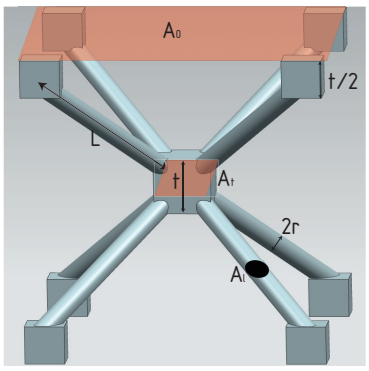

Fig. 2.9: Schematic description of the unit cell geometrical model proposed by Hubert et al. [55], whereas A_0 is the cell cross-section, A_l - strut cross-section, and A_t - node cross-section.

$\alpha = A_t/A_l$ and $e = t/L$, were inspired by Yang et al. in [54]. Due to the different intersections and thus the different node sizes of each different unit cell, different topological parameters (α_1 and α_2, or e_1 and e_2) were used. For the cell f_2cc, the integral from Equation 2.18 results in Equation 2.20.

$$\frac{\frac{H_C}{A_0}}{\int_0^{H_c} \frac{1}{A_l(s)} ds} = \frac{A_l}{L^2}\left[1 - \omega_z \frac{e_1+e_2}{2} + 2\left(\frac{e_1}{\alpha_1} + \frac{e_2}{2\alpha_2}\right)\right] \tag{2.20}$$

where ω_z is an additional fitting parameter needed to consider the complex intersection. This parameter was fitted using numerical simulations.
The porosity was derived as follows. The volume of the unit cell V_{tot} is shown in Equation 2.21 as a function of strut length L. A strut angle of $\varphi = 45°$ was assumed.

$$V_{tot} = 2\sqrt{2}L^3 \tag{2.21}$$

The volume of the struts in a f_2cc cell is given in Equation 2.22. t_1 and t_2 are the side lengths of the cubes that approximate the strut intersections. In the cell bcc, only one intersection type appears, thus $t_1 = t_2$. In the cells f_2cc, $bccz$ and f_2ccz, two different intersection types appear due to the different number of intersecting struts.

$$V_s = 8\left(L - \omega_\varepsilon \frac{t_1+t_2}{2}\right) + t_1 A_{t,1} + 2t_2 A_{t,2} \tag{2.22}$$

ω_ε is as well an additional fitting parameter. The porosity is thus given by $\varepsilon = \frac{V_{tot}-V_S}{V_{tot}}$, resulting in Equation 2.23.

$$\varepsilon = 1 - \frac{A_l}{L^2}\sqrt{2}\left(2\left(1 - \omega_\varepsilon \frac{e_1+e_2}{2}\right) + \frac{\alpha_1 e_1 + 2\alpha_2 e_2}{4}\right) \tag{2.23}$$

Substituted into Equation 2.18, Equation 2.24 calculates the ETC in relation to the conductivity of the solid. The first term on the right hand side of the equation corresponds to the thermal conductivity of the lattice, the second part corresponds to that of the PCM.

$$\begin{aligned}\frac{\lambda_{\text{eff}}}{\lambda_s} = {} & \frac{A_l}{L^2}\left[1 - \omega_z \frac{e_1+e_2}{2} + 2\left(\frac{e_1}{\alpha_1} + \frac{e_2}{2\alpha_2}\right)\right] \\ & + \frac{\lambda_f}{\lambda_s}\left[1 - \frac{A_l}{L^2}\sqrt{2}\left(2\left(1 - \omega_\varepsilon \frac{e_1+e_2}{2}\right) + \frac{\alpha_1 e_1 + 2\alpha_2 e_2}{4}\right)\right]\end{aligned} \tag{2.24}$$

The equations derived by Hubert et al. [55] agree exactly with the numerical results. In addition, they investigate the thermal constriction resistance that arises at the interface of the heat-spreader to the struts. An envelope is needed to close the volume filled by the PCM to keep the PCM inside the matrix when it is melted. Additionally, the envelope can be used to conduct the heat into the PCM and is thus called heat spreader. This resistance is mainly caused by the curvature of the heat flux lines. Above a certain number of cells, however, this extra

resistance is negligible. The model is thus able to take the following topology parameters into account for a cell characterisation:

- Cell topology (*bcc*, *bccz*, f_2cc, f_2ccz)
- Porosity
- Number of cells

This model can only be used for the cell characterisation and topology optimisation to a limited extent. On the one hand, the number of investigated cell types is relatively small with respect to the ones available both via additive manufacturing or hybrid manufacturing methods. There is a large number of cell topologies and new cell shapes, such as the hexagonal ones. Furthermore, the model only applies to cubic cells, i.e. the aspect ratio between the cell sizes is 1. However, the same cell topologies can be manufactured in a prismatic fashion where cell sizes differ. The only limit in terms of manufacturability is the minimum angle at which a strut can be manufactured with respect to the horizontal, without needing additional support structures. Varying the aspect ratios leads to different strut angles and thus to significant changes in the ETC. This is especially interesting for multifunctional use cases. An additional parameter enables more flexibility in tailoring the material properties.
An additional limit of the presented literature lies in the description of the geometry, i.e. the porosity ε, which is heavily reliant on empirical factors. Because of the complicated geometry of as-manufactured nodes in lattice structures, a reliable model for the evaluation of the porosity, and thus of all the physical properties of the lattice, is hardly separated from empirical factors. However, an attempt to extend the reliability and improve the independence of analytical models from empirical factors shall be made to reduce the effort of future design activities. Reducing the error performed by estimating the effective properties of lattices via analytical formulae allows to reduce the need for expensive and time consuming fitting of empirical data. In this perspective, Chapter 3 of this work describes a novel approach to estimate the porosity of lattice structures with more generic topology as well as an improved calculation of the thermophysical properties.

2.2 Phase Change Materials

This far, the described state of the art and theoretical background did not considere the presence of a Phase Change Material. In the following a generalised description of PCMs, their challenges and the mathematical formulations used to describe their thermofluidic behaviour are introduced.
Latent heat thermal energy storage (LHTES) is a promising technology for the efficient storage of thermal energy, which has the potential to reduce energy waste and increase the utilization of renewable energy sources[8]. LHTES systems store thermal energy by absorbing or releasing latent heat during phase change processes, such as melting or solidification, rather than

through changes in temperature alone, as shown in Figure 2.10. Working close to the melting point, LHTES shows much higher gravimetric energy density than sensible thermal energy storage. This makes such systems attractive also for mobile applications, i.e. automotive [57] or aerospace [58], where mass is a concern. The state of the art on LHTES has been rapidly

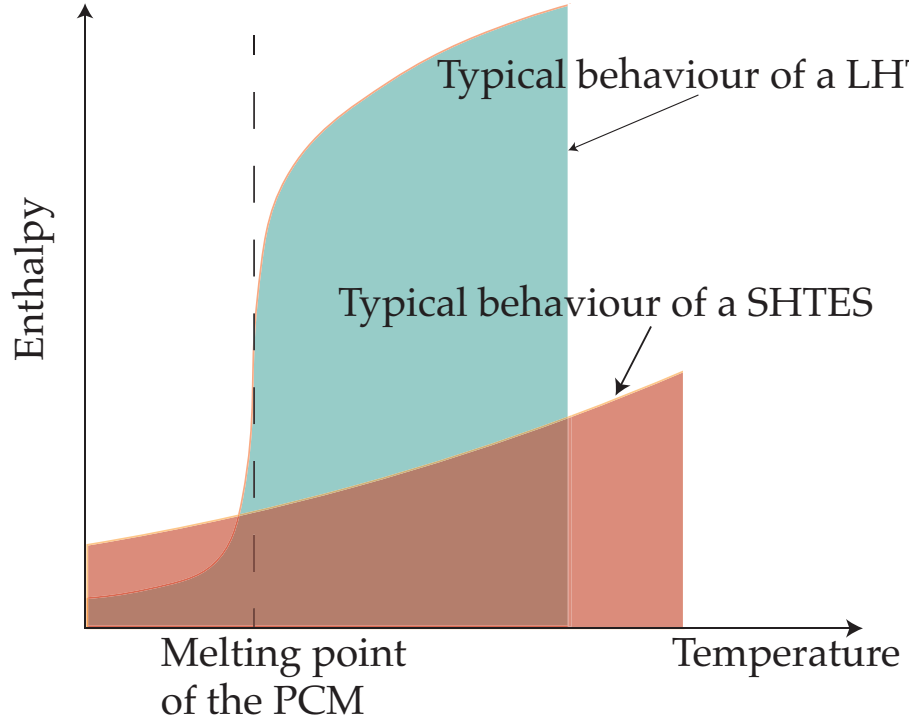

Fig. 2.10: Schematic description of the difference between latent heat thermal energy storage (LHTES) and sensible heat thermal energy storage (SHTES). The areas under the respective curves represent the stored energy.

advancing in recent years due to increasing demand for renewable energy storage solutions. The development of advanced materials and technologies has led to improvements in LHTES system efficiency, reliability, and cost-effectiveness. One of the major challenges in LHTES research is to find suitable phase change materials (PCMs) that have a high latent heat of fusion, good thermal stability, and appropriate thermal conductivity [59]. In addition, there is a need to optimise the design and operation of LHTES systems to ensure efficient energy transfer and minimize system losses. Recent research efforts have focused on the development of novel PCMs and LHTES systems, such as encapsulated PCMs, composite materials, and hybrid systems [13]. In addition, new approaches for characterizing and modeling LHTES systems have been developed to provide a better understanding of the underlying physical and chemical processes.

2.2.1 Encapsulation methods

Encapsulation is a method of incorporating phase change materials (PCMs) into a matrix to form a composite material, which can be used for thermal energy storage. The encapsulation process can help to improve the stability, thermal conductivity, and durability of the PCM, as well as reduce the problem of PCM leakage and phase separation [60].
There are several methods for encapsulating PCMs, including:

- Physical encapsulation: In this method, the PCM is coated with a thin layer of a matrix material, such as polymer, silica, or carbon. The PCM can be encapsulated by spray drying, coacervation, or electrostatic spinning. The matrix material acts as a barrier to prevent the PCM from leaking or solidifying during the melting or solidification process.
- Microencapsulation: In this method, the PCM is encapsulated in microspheres or microparticles made of a matrix material. The matrix material can be a polymer, such as polyethylene glycol, polystyrene, or polyurethane. The microcapsules are typically between 1 and 100 microns in diameter and can be dispersed in a matrix material to form a composite material. Microencapsulation can provide a high surface area to volume ratio, which can improve the heat transfer properties of the composite material.
- Nanoencapsulation: In this method, the PCM is encapsulated in nanoparticles made of a matrix material, such as silica or carbon. The nanoparticles are typically between 10 and 100 nanometers in diameter and can be dispersed in a matrix material to form a composite material. Nanoencapsulation can provide a large surface area and high thermal conductivity, which can enhance the heat transfer properties of the composite material.
- Macroencapsulation: In this method, the PCM is encapsulated in large containers or tubes made of a matrix material, such as metal or plastic. Macroencapsulation is typically used for high-temperature applications, such as solar thermal energy storage.

The selection of the encapsulation method depends on several factors, including the properties of the PCM, the required thermal performance, and the intended application. Encapsulation methods can be combined to create hybrid encapsulation systems that provide the advantages of multiple encapsulation methods.
Macroencapsulation methods offer several advantages, including easy installation, flexibility in design, and compatibility with a wide range of PCMs. However, they may also have limitations, such as low thermal conductivity, which can affect their thermal performance. To address such issues extensive research has been performed in enhancing the thermal performance of macronecapsulated PCMs via use of metallic or carbon fins [61]. Optimal designs of fins can effectively tackle issues related to the the low thermal conductivity of the PCMs. However, they generally constitute a discontinuous domain. This reduces their applicability in the aimed multifunctional approach of this work. Alternatively, metallic or carbon foams have been extensively researched [62]. As previously described, these are a sub-branch of cellular solids. The research on the use of **metallic foams** for PCM thermal performance enhancement is thus

the fundamental research on which this work builds up.
Depending on the bulk material of the foam, a wide variety of experimental and numerical quantitative results have been obtained [63, 64, 65, 66, 67, 68]. The thermal performance increase is often measured in terms of the wall temperature of the considered samples. The foam geometry is a fundamental parameter, which affects such performance. The parameters which most affect the foam geometry are its porosity and the pore sizes. Due to the stochastic nature of metal foams, the pore sizes are not constant. However, the average pore size, expressed in terms of Pores Per Inch (PPI) is commonly employed. Performing experiments on a variety of foams with different porosities and PPIs, Diani and Campanale [69] achieved a power-law based correlation for the wall temperature as a function of the product of the Stefan and the Fourier numbers. The geometry information is contained within this product, as the effective thermal diffusivity and specific heat constitute these numbers. Similarly, Righetti et al.[70] attempted the same for *bcc* lattice structures with different cell sizes.
The authors assumed a purely conductive regime within the domain, i.e. no convection and radiation were considered when describing the thermal behaviour of the composite. As several authors noted, especially when analysing foams with high porosity and low number of PPIs, natural convection can play a significant role in the heat transfer process [71, 72, 66, 73, 74]. Thus, depending on the inclination with respect to the volume forces (e.g. gravity) the heat transfer process can be enhanced or reduced. When the heat source acts in direction parallel to local gravity vector (i.e. top heating), the effects of convection are negligible. When the heat source is either perpendicular or opposite to the local gravity vector (i.e. side heating or bottom heating), the effects of convection are significant. Additionally, as evidenced by Filippeschi et al.[75], the value of the volume force itself is of importance. As this work focuses on mobile systems, which in general are in an accelerated condition, this is also of importance.
Based on the scaling theory proposed for a pure PCM by Jany and Bejan [76], the Rayleigh number can be used to describe the onset of convection. The Rayleigh number is defined in Appendix (Equation A.5). Azad, Groulx et al. in two recent papers [77, 78] revised the scaling theory and extended it to other non-dimensional numbers of interest (defined in Appendix A). Particularly interesting is the existence of critical Rayleigh and Stefan-Fourier numbers for the onset of convection.
These results are of fundamental importance as they consitute a guideline for the design of PCM based systems. However, the results are valid for a pure PCM. Nield and Bejan [79] extended the scaling theory to porous media. However their treatment assumes an isotropic porous medium, which is, in general, not the case for the lattices considered in this work. This work will concentrate on obtaining critical values of the relevant non-dimensional numbers for the onset of convection for the lattices considered in this work.
Considering the above, it is essential to be able to describe the heat transfer phenomena within a porous medium, such as a foam or a lattice structure, in the presence of a phase change material. The following section describes the mathematical formulation of the heat transfer phenomena in porous media.

2.3 Heat transfer in porous media

The fundamental equations for heat transfer can be generalised by making use of the energy conservation equation, in combination with the momentum and mass conservation. These equations are valid for an incompressible, newtonian fluid, which is in general a valid assumption for PCMs treated in this work, in their liquid state. For solids, i.e., in this work the lattice structure or the PCM in its solid state, the equations reduce to the energy equation only, with negligible convective terms. The equations are reported in their strong form.

$$\nabla(\mathbf{u}) = 0 \tag{2.25}$$

where $\mathbf{u}$ is the velocity vector.

$$\rho\left(\frac{\partial \mathbf{u}}{\partial t} + \mathbf{u}\nabla\mathbf{u}\right) = -\nabla p + \nabla\boldsymbol{\tau} + \rho\mathbf{g} \tag{2.26}$$

where ρ is the density of the medium, p is the pressure, $\boldsymbol{\tau}$ is the deviatoric stress tensor and $\mathbf{g}$ is the gravitational acceleration vector.

$$\frac{\partial T}{\partial t} + (\mathbf{u}\nabla)T = -\frac{1}{\rho(T)C_p(T)}\nabla\dot{\mathbf{q}} = -\frac{1}{\rho(T)C_p(T)}\nabla\left(-\lambda\nabla T\right) + \Xi = \alpha\nabla^2 T + \Xi \tag{2.27}$$

where T is the temperature, C_p is the specific heat capacity of the medium, $\mathbf{q}$ is the heat flux vector,λ is the thermal conductivity, α is the thermal diffusivity of the medium, ∇^2 is the Laplacian operator, ρ is the density, C_p is the specific heat capacity at constant pressure, ∇ is the divergence operator and Ξ is the heat source term.
These coupled equations can be solved via a wide variety of numerical schemes. The most common are the Finite Element Method (FEM) and the Finite Volume Method (FVM). The former is based on the discretisation of the domain into a mesh of elements, while the latter is based on the discretisation of the domain into a mesh of control volumes. The FEM is more flexible and can be used for complex geometries, while the FVM is more robust and can be used for complex boundary conditions. In this work, both FVM based and FEM based solvers are used.
To treat the phenomena relevant in this work, some approximations can be made, which are added to the conservation equations. In particular, when dealing with natural convection, the **Boussinesq approximation** is often used. This approximation assumes that the density of the fluid is constant, except in the buoyancy term. This approximation is valid for small temperature differences. The Boussinesq approximation is reported in the following.

$$\rho(T) = \rho_0\left(1 - \beta(T - T_0)\right) \tag{2.28}$$

where ρ_0 is the density at the reference temperature T_0 and β is the coefficient of thermal expansion of the fluid.

2.3.1 Porous medium models

Darcy's law is the fundamental equation to describe the fluid flow in porous media [80]. It is based on the assumption of a creeping flow, i.e. a flow with a very low Reynolds number (Re«1). The equation is reported in the following.

$$\varepsilon \mathbf{u_D} = -\frac{\mathbf{K}}{\mu}(\nabla p - \rho \mathbf{g}) \tag{2.29}$$

where ε is the porosity of the medium, $\mathbf{u_D}$ is the so-called Darcy velocity vector, $\mathbf{K}$ is the permeability tensor, μ is the dynamic viscosity of the fluid. The Darcy velocity represents an average pore velocity. The permeability tensor is a second order tensor, which describes the fluid-flow resistance of the porous medium. It is a purely geometrical property, i.e. it does not depend on the fluid properties.
The validity of Darcy's law is limited to creeping flows. For higher flow rates, several extension of Equation 2.29 were presented. They all take into account the inertial effects of the fluid. The most common extension is the Forchheimer's law, while recently Brinkman's and Richards's models are being investigated, especially with the purpose of an accurate numerical prediction of the fluid flow in porous media. The three models are reported in the following.
Forchheimer's law assumes the Darcy's law can be extended via the addition of a quadratic term. The coefficient of the quadratic term can be expressed in several ways. As reported by Ehlers [81], recent literature, like Markert [82], suggests that such coefficient is a tortuosity parameter with dimensions m. With some modification, Ehlers [81] reports the Forchheimer's law as

$$\mathbf{u_D} = -\frac{\mathbf{K}}{\mu}\left(\frac{1}{2} + \sqrt{\frac{1}{4} + \left(\frac{\mathbf{K}}{\mu}\right)^2 \frac{\rho}{B}|\nabla p + \rho \mathbf{g}|}\right)^{-1} (\nabla p + \rho \mathbf{g}) \tag{2.30}$$

where B is the tortuosity.
The **Darcy-Brinkman** equation corrects Darcy's law by adding a term proportional to the laplacian of the velocity. Neglecting the volume forces, the equation is reported in the following.

$$\nabla p = -\varepsilon \frac{\mu}{\mathbf{K}} \mathbf{u_D} - \mu_{\text{eff}} \nabla^2 \mathbf{u_D} \tag{2.31}$$

where μ_{eff} is the so-called effective viscosity of the fluid, while the other symbols have the same meaning as in Equation 2.29. μ_{eff} can be obtained from a volume averaging of the microscopic transport equations [24]. Regarding the actual definition of the effective viscosity several authors still assume it to be equal to the pure fluid viscosity, also when considering a phase change problem with moving interface [83, 84, 73, 85]. However, already several decades ago, it was evidenced that, in general, $\mu_{\text{eff}} > \mu$ [86, 87, 88]. As expressed in the recent review from Habibishandiz et al. [89]. The most common models are the Einstein's model and the Brinkman's one. The former is based on the assumption that the fluid is composed of spherical particles, while the latter is based on the assumption that the fluid is composed of cylindrical

particles. The two models are reported in the following.
Einstein's model:

$$\mu_{\text{eff}} = \mu\,(1+2.5\varepsilon) \tag{2.32}$$

Brinkman's model:

$$\mu_{\text{eff}} = \mu\frac{1}{(1-\varepsilon)^{2.5}} \tag{2.33}$$

Habibishandiz et al. [89] report other models, proposed for a variety of porous media, also considering the presence of nanoparticles. To the author's knowledge, no generally valid formulation was proposed this far. This is especially critical if one considers the moving boundary of a PCM. This criticality is discussed in detail in Chapter 4.
According to Habibishandiz et al. [89] another open aspect regarding the modelling of the fluid flow in porous media is the use of Local Thermal Equilibrium (LTE) or Local Thermal Non-Equilibrium (LTNE) to treat the energy equation of the two phases within the porous domain. The LTE assumes that the two phases are at the same temperature, while the LTNE assumes that the two phases are at different temperatures. Thus, to be able to use two coupled energy-equations, when LTNE is assumed, an Interstitial Heat Transfer Coefficient (IHTC) must be included to couple the two equations. This coefficient cannot be trivially found. Pati et al. [90] performed a critical review regarding the applicability of one or the other assumption. While no quantitative values were reported, they report that for porous media with small pores LTE can be assumed.
The generalised governing equations for flow and heat transfer in porous media are

$$\nabla(\mathbf{u}) = 0 \tag{2.34}$$

$$\rho_{\text{eff}}\left(\frac{\partial \mathbf{u}}{\partial t}+\mathbf{u}\nabla\mathbf{u}\right) = -\nabla p-\mu_{\text{eff}}\nabla^2\mathbf{u}-\frac{\mu}{\mathbf{K}}\mathbf{u}+\rho\mathbf{g}\beta\,(T-T_0)+S \tag{2.35}$$

where ρ_{eff} is the effective density of the fluid, μ_{eff} is the effective viscosity of the fluid, $\mathbf{K}$ is the permeability tensor, μ is the dynamic viscosity of the fluid, $\mathbf{u}$ is the velocity vector, p is the pressure, ρ is the density of the fluid, $\mathbf{g}$ is the gravitational acceleration, β is the coefficient of thermal expansion of the fluid, T is the temperature of the fluid, T_0 is the reference temperature of the fluid and S is the source term.
If LTNE is assumed, the energy equations are

$$(\rho C_p)_f(\varepsilon\frac{\partial T_f}{\partial t}+\mathbf{u}\nabla T_f) = \varepsilon\lambda_f\nabla^2 T_f+h_{if}(T_s-T_f)+\Xi_f \tag{2.36}$$

$$(\rho C_p)_s((1-\varepsilon)\frac{\partial T_s}{\partial t}+\mathbf{u}\nabla T_s) = (1-\varepsilon)\lambda_s\nabla^2 T_s+h_{if}(T_f-T_s)+\Xi_s \tag{2.37}$$

where $(\rho C_p)_*$ is the heat capacity of the fluid (f) or the solid (s), λ_* is the thermal conductivity, h_{if} is the interstitial heat transfer coefficient, T_* is the temperature of the fluid or the solid, Ξ_*

is the heat source term.
In the case that LTE is valid, the energy equation reduces to[79]

$$(\rho C_p)_{\text{eff}} \frac{\partial T}{\partial t} + (\rho C_p)_f \mathbf{u} \nabla T = \lambda_{\text{eff}} \nabla^2 T + \Xi_{\text{eff}} \tag{2.38}$$

where $(\rho C_p)_{\text{eff}}$ is the effective heat capacity of the homogenised medium, λ_{eff} is the effective thermal conductivity, and Ξ_{eff} is the effective heat source term.

Addition of phase change phenomena

To the Equations 2.34 to 2.38 the following equations must be added to describe the phase change phenomena within the porous medium.
The mathematical modelling of phase change materials is a complex task, which requires the description of the heat transfer phenomena in the solid and liquid phases, as well as the moving interface between the two phases. The fundamental work in this regard was performed by Stefan [91], who derived the analytical solution for the moving interface between two phases. His work fundamentally consisted of adding the following relationship to the heat diffusion equation.

$$\lambda \frac{\partial T}{\partial n} = \rho \Delta h \frac{\partial \xi}{\partial t} \tag{2.39}$$

where Δh is the latent heat of fusion, ξ is the position of the interface between the two phases, n is the normal vector to the interface, and t is the time.
The Stefan problem is a mathematical model for the heat transfer in a phase change material. It is based on the assumption that the phase change happens instantaneously, i.e. the temperature of the material is equal to the melting temperature at the interface between the two phases. The Stefan problem can be solved analytically for a semi-infinite domain, i.e. a domain with infinite length in one direction and finite length in the other two directions.
For a generic domain, considering a porous medium, the energy equation under LTE assumption is reformulated by substituting the source term in Equation 2.38.

$$\begin{aligned}(\rho C_p)_{\text{eff}} \frac{\partial T}{\partial t} + (\rho C_p)_{PCM} \mathbf{u} \nabla T = \lambda_{\text{eff}} \nabla^2 T - \\ \varepsilon \rho_{PCM} H_f \left(\frac{\partial \Phi}{\partial t} + \mathbf{u} \nabla \Phi\right) + T_m \left(\frac{\partial (\rho C_p)_{\text{eff}}}{\partial t} + \mathbf{u} \nabla (\rho C_p)_{\text{eff}}\right)\end{aligned} \tag{2.40}$$

where the subscript $_f$ was substituted by $_{PCM}$, i.e. ρ_{PCM} is the density of the PCM; H_f is the heat of fusion of the PCM, Φ is the liquid fraction within the domain, T_m is the melting temperature of the PCM. The last term is caused by the change of material properties within the mushy zone,

and is zero outside of such region.
The liquid fraction function is defined as

$$\Phi(T) = \begin{cases} 0 & \text{if } T < T_s \\ \dfrac{T - T_m}{T_s - T_l} & \text{if } T_s < T < T_l \\ 1 & \text{if } T > T_l \end{cases} \tag{2.41}$$

where T_m is the melting temperature of the PCM. T_s is the solidus temperature and T_l is the liquidus temperature. The value of $T_s - T_l$ is strongly related to the stability of numerical schemes used to simulate the behaviour of a PCM.
The source term S in Equation 2.35 is substituted by

$$S = A\frac{(1-\Phi)^2}{b+\Phi^3} \tag{2.42}$$

which is known as the Carman-Kozeny term [79]. The parameters A and b are empirical parameters. In general b is chosen to be a small number 10^{-3} so that division by zero is avoided. The parameter A is chosen to be a large number, so that the source term is negligible in the solid phase. The value of A strongly affects the shape of the mushy zone.
The equations described this far constitute the basis for the so-called *enthalpy-porosity method*. Other methods can be applied to numerically solve the problem. These are extensively described by the review of Zeneli et al. as well other authors [92, 93, 94].
Further details on the implementation of numerical schemes for the solution of the problem are given in Chapter 4.

Simplified conductive model

This far, the methods to describe the behaviour of a PCM embedded within a porous medium were illustrated. At this point, it is useful to introduce Stefan's analytical solution to describe, in a simplified fashion, the effect of a metallic cellular solid on the melting and thermal behaviour of the composite.
Considering a homogeneous medium based on the composite of a metallic foam and a PCM, a one-dimensional semi-infinite wall, as shown in Figure 2.11, is considered. The assumption is made that the wall temperature $T(x = 0, t)$ is constant and above the melting point. The temperature at any distance from the melting front in the solid domain is assumed to be equal to the initial temperature. Different thermophysical properties are assumed for the two phases (liquid and solid). The effect of convection is neglected. The phase transition happens instantaneously once the melting temperature is reached. The position ξ of the point, where the melting temperature is reached, is a function of time, since the melting front is moving through the wall as time goes on. It is assumed that the temperature distributions both in the solid (θ_S) and the

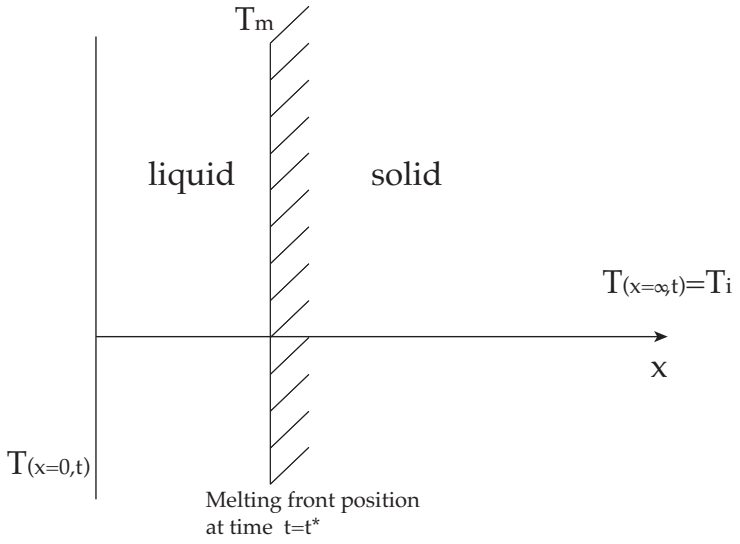

Fig. 2.11: Schematic of the semi-infinite wall with boundary conditions and depiction of the melting front position at a generic time t=t*, whereas $T(x=0,t)$ is the wall temperature, T_i - reference temperature, and T_m - the melting point.

liquid phase (θ_L) have the form of the general solution of the heat equation for a semi-infinite wall without a phase change.

$$\theta_L = A + Berf\frac{x}{2\sqrt{\alpha_L t}} \tag{2.43}$$

$$\theta_S = C + Derf\frac{x}{2\sqrt{\alpha_S t}} \tag{2.44}$$

A,B,C and D are constant coefficients. α_S and α_L are the thermal diffusivities of the solid phase and liquid phase, respectively. The excess temperature θ is the difference between the absolute temperature T and a reference temperature T_i, which in this case is chosen to be the initial temperature:

$$\theta = T - T_i \tag{2.45}$$

Since the phase transition happens instantaneously, the heat of fusion H_f can be treated as a sink term in an energy balance around the melting front. Thus, there are five initial and boundary conditions in total, with Δh being the change in enthalpy.

$$\theta_L(0,t) = \theta_0 \tag{2.46}$$

$$\theta_S(+\infty,t) = \theta_S(x,0) = 0 \tag{2.47}$$

$$\theta_L(\xi,t) = \theta_\xi \tag{2.48}$$

$$\theta_S(\xi,t) = \theta_\xi \tag{2.49}$$

$$\lambda_S \frac{\partial \theta_S}{\partial x}\bigg|_\xi - \lambda_L \frac{\partial \theta_L}{\partial x}\bigg|_\xi = \rho_S \Delta h \frac{d\xi}{dt} \tag{2.50}$$

Imposing the initial and boundary conditions on the general excess temperature profiles yields the following equations.

$$\theta_L(0,t) = \theta_0 \Rightarrow A = \theta_0 \tag{2.51}$$

$$\theta_S(+\infty,t) = \theta_S(x,0) = 0 \Rightarrow C + D = 0 \tag{2.52}$$

$$\theta_L(\xi,t) = \theta_\xi \Rightarrow A + Berf\frac{\xi}{2\sqrt{\alpha_L t}} = \theta_\xi \tag{2.53}$$

$$\theta_S(\xi,t) = \theta_\xi \Rightarrow C + Derf\frac{\xi}{2\sqrt{\alpha_S t}} = \theta_\xi \tag{2.54}$$

Since the temperature at the melting front is independent of time t, it follows that t needs to be canceled out in Equations 2.53 and 2.54. This is only possible if ξ is proportional to the square root of t.

$$\xi = \beta\sqrt{t} \tag{2.55}$$

Inserting Equations 2.53,2.54 and 2.55 into Equation 2.50 yields

$$\lambda_S D\frac{e^{\frac{-\beta^2}{4\alpha_S}}}{\sqrt{\pi\alpha_S t}} - \lambda_L B\frac{e^{\frac{-\beta^2}{4\alpha_L}}}{\sqrt{\pi\alpha_L t}} = \rho_S \Delta h\frac{\beta}{2\sqrt{t}} \tag{2.56}$$

Therefore, in total there are five unknown variables (A,B,C,D, β) and five equations. Through some transformations one can obtain the following equation, which is only dependent on β.

$$\lambda_S\frac{\theta_\xi}{erf\frac{\beta}{2\sqrt{\alpha_S}} - 1}\frac{e^{\frac{-\beta^2}{4\alpha_S}}}{\sqrt{\pi\alpha_S}} - \lambda_L\frac{\theta_\xi - \theta_0}{erf\frac{\beta}{2\sqrt{\alpha_L}}}\frac{e^{\frac{-\beta^2}{4\alpha_L}}}{\sqrt{\pi\alpha_L}} = \rho_S\Delta h\frac{\beta}{2} \tag{2.57}$$

Equation 2.57 is transcendent, so it cannot be solved analytically. However, it is easily solved numerically by using the bisection method. Thus, the melting front position ξ can be calculated for every point in time and the coefficients A, B, C and D can be determined. Due to the homogenisation (volume averaging), the effective thermal conductivities and diffusivities for the solid and the liquid phase need to be determined. The Singh-Ranut-model [47] is used to obtain an estimate for the effective thermal conductivities.

The effective heat capacities and densities are determined by calculating the weighted average of the properties of the PCM and the matrix as in 2.10 and 2.11. Additionally, the latent heat is corrected to account for the metallic matrix as well, with the effective latent heat of fusion $H_{f,\text{eff}}$ derived from latent heat of PCM $H_{f,PCM}$.

$$H_{f,\text{eff}} = \varepsilon\frac{\rho_{PCM}}{\rho_{\text{eff}}}H_{f,PCM} \tag{2.58}$$

The thermophysical properties described in Table B.3 are considered.
A parametric study is conducted by varying the volume fraction χ and solving for the analytical solution of the Stefan problem with effective properties. The volume fraction χ is varied

between 0 and 0.2, where 0 represents a pure PCM material. Figure 2.12 shows the advancement of the melting front position, with reference to the semi-infinite wall shown in Figure 2.11, plotted against a total time of 300s. As expected, a clear acceleration of the melting front expansion can be noticed with increasing volume fraction. On the other hand, one can notice diminishing returns when increasing the volume fraction above a certain amount. With increasing volume fraction, the curves tend to get closer, indicating a limited effect of the effective thermal conductivity with respect to the other thermophysical properties. This is more evident in Figure 2.13 where the relative increment of the melting front position between one volume fraction step and the other is plotted against the volume fraction itself. It is thus clear that due to the introduction of a metallic matrix, the melting front expansion is strongly accelerated. However, the effect tends to decrease above a critical value due to the effect that the metallic matrix has on other thermophysical properties. Figure 2.14 shows such an effect. An increase in volume fraction of the cellular solid leads to a reduction of the effective latent heat, thus reducing the energy that can be stored latently. This is also evident in Figure 2.15.

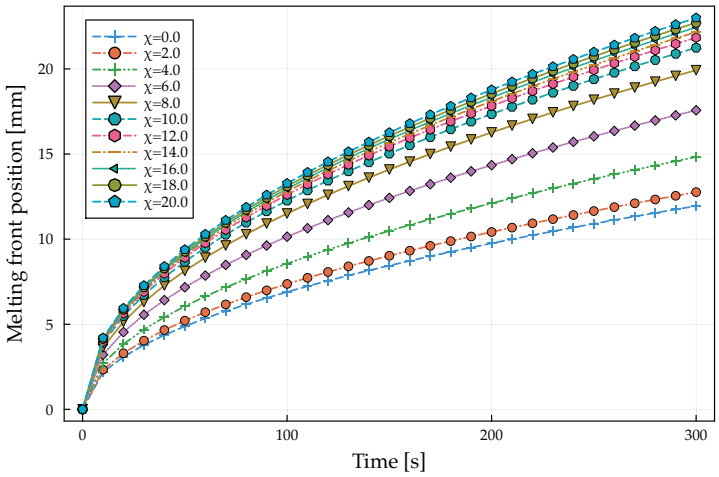

Fig. 2.12: Analytical solution of the Stefan Problem for different volume fractions χ. the effective thermal conductivity is calculated with use of the Ranut model [47]

The purpose of this introductory study is to indicate that the application of metallic cellular solids to increase the overall thermal conductivity of a PCM does not come without drawbacks. Since the effective latent heat is reduced by the porous medium, an optimal balance needs to be achieved. No trivial optimum exists. Moreover, in lightweight applications, such as those considered in this research, the mass requirements play a crucial role, and the increasing volume fraction of metallic cellular solids must be carefully evaluated against the overall system performance.

While the results indicate a general plausible trend, the quantitative validity of these findings is limited. First of all, the conductivity model was developed for metal foams. Furthermore, the model proposed by Ranut et al.[47] is only applicable for volume fractions up to 15%. In

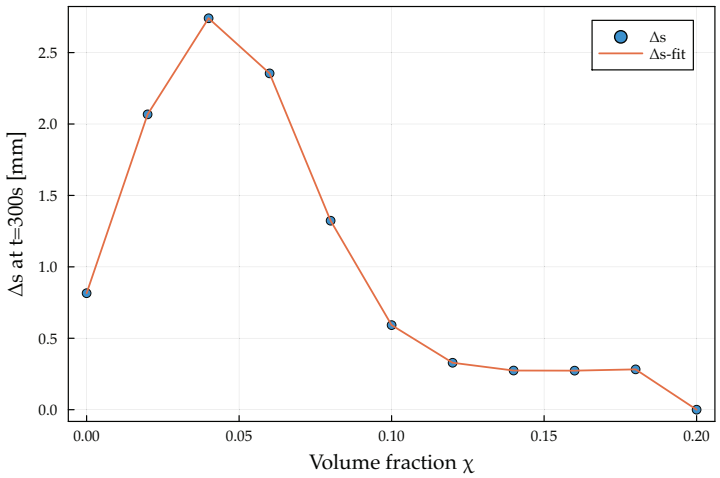

Fig. 2.13: The relative increment of the melting front position at time t=300s when varying the volume fraction of the cellular solid.

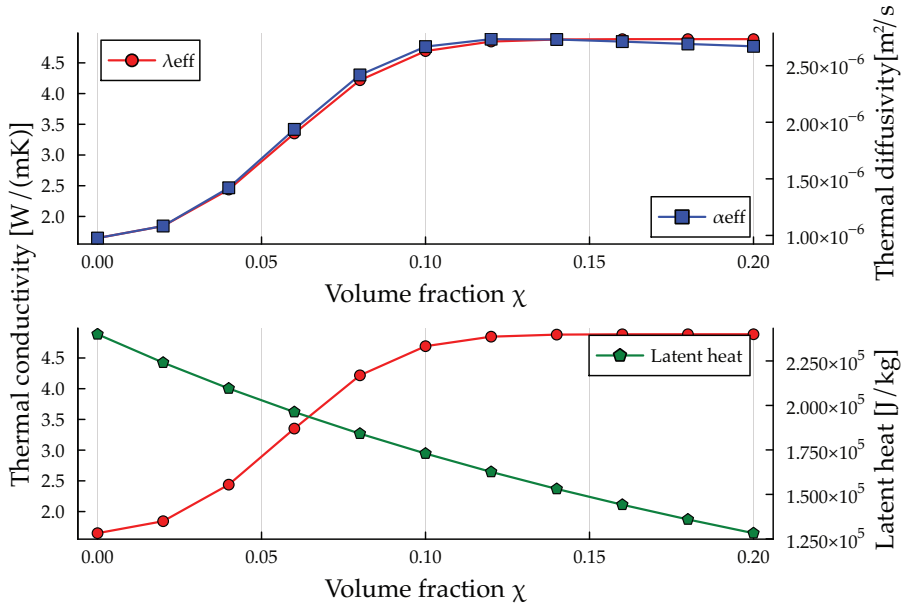

Fig. 2.14: Variation of the effective thermophysical properties with increasing volume fraction. The effective thermal conductivity saturates to a maximum value due to the assumptions of the Ranut model [47].

contrast, this study aims to establish reliable analytical relationships for describing the effective thermophysical properties of composites comprising metallic lattices and PCMs. To achieve this, a thorough treatment of the lattice structure's geometry is indispensable, and this aspect is elaborated in Chapter 3.

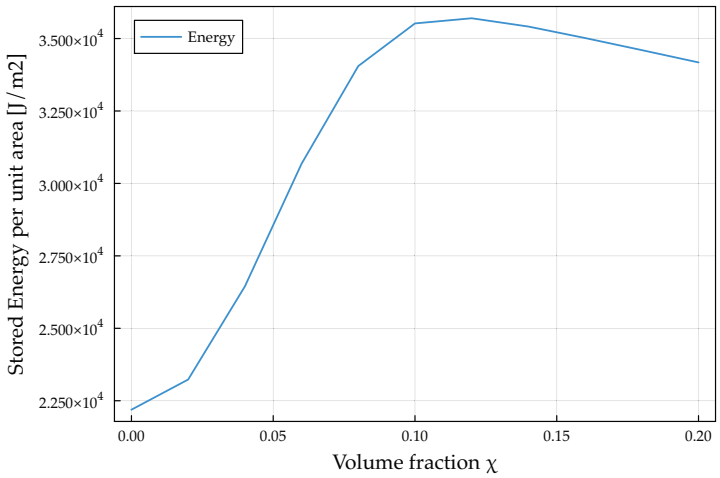

Fig. 2.15: Variation of the latently stored energy with increasing volume fraction. The peak indicates that an optimum value exists.

2.3.2 Summary

This section presented the state of the art relevant for the thermal characterisation of the lattice structure / PCM composite. It is useful to summarise the main open points of this section, which will be investigated in Chapter 4.

- The effective thermal conductivity λ_{eff} of the lattice structures is an intricate function of its geometry and the bulk material λ_{bulk}: $\lambda_{\text{eff}} = f(\lambda_{bulk}, \varepsilon, r, h, \text{unit cell topology})$. Thus, a new model is needed. The existing models for the ETC of metal foams are not appropriate to describe such function. The geometrical parameters are discussed in Chapter 3. Building up on it, a model to describe the ETC of lattice structures is proposed in Section 4.1.

- Even in a purely conductive regime, it is clear that the enhancement of the ETC is not the only relevant aspect, as the addition of material to the highly conductive cellular solid reduces the effective latent heat. Thus, a trade-off between the two aspects must be found. This is discussed in Section 4.1.3.

- The recent literature on metal foam / PCM composites evidenced how the onset of natural convection within the PCM melt affects the thermal behaviour of the composite. It is to be assumed that the same is valid with lattice structures. Additionally, lattice structures are, in general, orthotropic, which complicates the description of the fluid flow within the porous medium. Thus experimental and numerical investigations are reported in Chapter 4 to delve into this aspect.

- This literature review also evidenced that no generally accepted value of the effective viscosity of the fluid within the porous medium exists. This is especially critical when considering the moving boundary of a PCM. This criticality is discussed in detail in Section 4.3.

2.4 Stability of beams on elastic foundations

The goal of this work is to investigate possible novel cores of sandwich structures, which, if soft and/or slender, can buckle [95]. Here, the fundamental difference with respect to conventional structures is the presence of the PCM. While most room temperature PCM are rather soft materials, e.g. paraffin wax, and thus poorly contribute to the effective stiffness of the structure, they can still affect the buckling behaviour of the structure. In particular in their solid phase, they can represent an elastic foundation on which the lattice struts rest. In the liquid phase, such effect vanishes. However, more complex aspect shall be considered. In general, a positive volume change is associated with melting, which induces inner pressure, which can have a stabilising effect. This work focuses on the effect on stability of the lattice structures given by a PCM in its solid phase.
The following section aims to provide the necessary theoretical background to analyse the critical buckling loads of individual beams. To take into account the addition of an elastic medium to the lattice structure, the modelling of elastic foundations is discussed. Afterwards, the analytical solution for the critical buckling loads of individual struts on elastic foundations is derived. In the last section, an introduction into stiffness matrices of beams on elastic foundations is given, as the stiffness matrices are necessary to derive analytical solutions for interconnected struts.

The most common type of buckling is Euler buckling, which is a global instability of a slender structure under compression. The critical buckling load P_{cr} of a slender beam with effective length L_{eff} and cross-section area A is given by

$$P_{cr} = \frac{\pi^2 EI}{L^2} \tag{2.59}$$

where E is the Young's modulus of the material and I is the second moment of area of the cross-section. The value of the effective length L_{eff} depends on the boundary conditions of the beam. For a beam with both ends pinned, $L_{\text{eff}} = L$. For a beam with one end pinned and one end free, $L_{\text{eff}} = 2L$. For a beam with both ends fixed, $L_{\text{eff}} = 0.5L$.
The buckling shape is associated with the lowest eigenvalue of the eigenvalue problem

$$\frac{\partial^2 w}{\partial x^2} + \lambda w = 0 \tag{2.60}$$

where w is the buckling shape and λ is the eigenvalue. The boundary conditions are

$$\begin{aligned} \frac{\partial w}{\partial x} &= 0 \text{ at } x = 0 \\ \frac{\partial w}{\partial x} &= 0 \text{ at } x = L_{\text{eff}} \end{aligned} \tag{2.61}$$

The solution of the eigenvalue problem is

$$\lambda_n = \frac{n^2 \pi^2}{L_{\text{eff}}^2} \tag{2.62}$$

where n is the mode number. The buckling shape is

$$w_n = sin\left(\frac{n\pi x}{L_{\text{eff}}}\right) \tag{2.63}$$

The critical buckling load is obtained by inserting the solution of the eigenvalue problem into the Euler buckling equation

$$P_{cr} = \frac{\pi^2 EI}{L_{\text{eff}}^2} = \frac{\pi^2 EI}{L^2}\frac{L^2}{L_{\text{eff}}^2} = \frac{\pi^2 EI}{L^2}\frac{L_{\text{eff}}^2}{L^2} = \frac{\pi^2 EI}{L^2}\frac{n^2\pi^2}{L_{\text{eff}}^2} = \frac{\pi^4 EI}{L^2}n^2 \tag{2.64}$$

The critical buckling load is thus proportional to the Young's modulus and the second moment of area of the cross-section. It is inversely proportional to the square of the length of the beam. The critical buckling load is proportional to the mode number squared. This means that the higher the mode number, the higher the critical buckling load. This last information is of fundamental importance, as the effect of an elastic foundation is to increase the buckling mode number, thus increasing the critical buckling load.
The modelling of the elastic foundation's effective properties is thus relevant to model the buckling phenomenon. The following section aims to provide the necessary theoretical background to model the elastic foundation.

2.4.1 Elastic foundation

Several authors dealt with the description of the structural behaviour of beams resting on elastic foundations. In particular, fundamental theories were developed by Winkler [96], Pasternak [97], Vesic [98], and Herrmann [99]. They focused on obtaining several levels of abstractions capable to accurately describe the behaviour of the elastic medium on which the beam rest. Winkler's model, which is also the simplest, describes the elastic medium via means of a series

of springs connected in parallel to the beam. The spring stiffness k, obtained from the foundation modulus, is related to the deflection y via

$$q = ky \tag{2.65}$$

where q is the reaction force.
The spacing of the springs and the foundation modulus determine the stiffness of each spring. As highlighted in the review conducted by Younesian et al. [100], a limitation of the Winkler model lies in the assumption that the springs are independent, whereas in reality, the deflection at a specific point is influenced not only by the pressure at that point but also by the pressure in adjacent points. More advanced theories like the one Pasternak assume the additional existence of a shear layer (Figure H.2c). This layer is related to the second derivative of the deflection via the shear stiffness G_P

$$q = ky - G_P \frac{\mathrm{d}^2 y}{\mathrm{d}x^2} \tag{2.66}$$

Herrmann proposed a definition of the foundation modulus for circular beams embedded in a three-dimensional foundation.

$$k_{\text{Herrmann}} = \frac{16\pi G_f (1-\nu_f)}{2(3-4\nu_f)K_0(\psi) + \psi K_1(\psi)} \tag{2.67}$$

where G_f represents the shear modulus of the foundation, and the factor ψ is defined as $\psi = m\pi D/(2L)$. The functions $K_0()$ and $K_1()$ denote the modified Bessel functions of the second kind for orders 0 and 1, respectively. Vesic proposed a simplified solution for k.

$$k_{\text{Vesic}} = \frac{0.65 E_f}{1-\nu_f^2} \sqrt[12]{\frac{E_f b^4}{EI}} \tag{2.68}$$

where EI represents the bending stiffness of the beam, and b denotes the width of the contact between the beam and the foundation. It is noteworthy that the beam's diameter D can be employed as the foundation width b.
In the following, the Herrmann's and Vesic's formulae are used to obtain the critical buckling load of the embedded beam. The details regarding the derivation of the here presented formulae are given in Appendix H.

2.4.2 Critical buckling load of a beam on an elastic foundation

Timoshenko and Gere [101] presented a solution for the critical buckling load of a beam on an elastic foundation using the Winkler model. The computation of the critical buckling load involves applying the energy method. It is assumed, once again, that the deflection curve can be represented by the trigonometric series outlined in Equation G.17. In this context, the strain

energy of bending arises from two sources: the beam itself and the elastic foundation. For the strain energy of bending of the beam, denoted as ΔU_1, an alternative equation to G.19 is employed.

$$\Delta U_1 = \frac{EI}{2} \int_0^L \frac{\mathrm{d}^2 y}{\mathrm{d}x^2} \mathrm{d}x \tag{2.69}$$

The inclusion of Equation G.17 allows for the representation of the integral as a summation with the mode m and wave function a_m.

$$\Delta U_1 = \frac{\pi^4 EI}{4L^3} \sum_{m=1}^{m=\infty} m^4 a_m^2 \tag{2.70}$$

To determine the bending strain energy resulting from the elastic foundation, denoted as ΔU_2, the analysis focuses on the strain energy associated with an infinitesimal beam element. Considering a 2D beam element with a length of $\mathrm{d}x$, the lateral reaction can be expressed as $q\,\mathrm{d}x = ky\,\mathrm{d}x$. Consequently, the strain energy of this infinitesimal element is calculated as follows.

$$\mathrm{d}U_2 = \frac{yq\,\mathrm{d}x}{2} = \frac{k}{2} y^2 \mathrm{d}x \tag{2.71}$$

$$\Delta U_2 = \frac{k}{2} \int_0^L y^2 \mathrm{d}x \tag{2.72}$$

After substituting the trigonometric series for y, Equation 2.72 can be rewritten as

$$\Delta U_2 = \frac{kL}{4} \sum_{m=1}^{m=\infty} a_m^2 \tag{2.73}$$

Utilizing the expression ΔW as provided in G.22 with the load P, and incorporating 2.70 and 2.73 into the equation $\Delta U_1 + \Delta U_2 = \Delta W$, the following relationship is derived

$$\frac{\pi^4 EI}{4L^3} \sum_{m=1}^{m=\infty} m^4 a_m^2 + \frac{kL}{4} \sum_{m=1}^{m=\infty} a_m^2 = \frac{\pi^2 P}{4L} \sum_{m=1}^{m=\infty} m^2 a_m^2 \tag{2.74}$$

Solving for P,

$$P = \frac{\pi^2 EI}{L^2} \frac{\sum_{m=1}^{m=\infty} m^4 a_m^2 + \frac{kL^4}{\pi^4 EI} \sum_{m=1}^{m=\infty} a_m^2}{\sum_{m=1}^{m=\infty} m^2 a_m^2} \tag{2.75}$$

Following a methodology akin to the one outlined in Section G.0.2, the expression attains minimal values when all coefficients a_m are zero, with the exception of one. This condition results in the critical load P_{cr}

$$P_{cr} = \frac{\pi^2 EI}{L^2}\left(m^2 + \frac{kL^4}{m^2\pi^4 EI}\right) \tag{2.76}$$

The trigonometric series represented by G.17 simplifies to a basic sine curve.

$$y = a_m \sin\frac{m\pi x}{L} \tag{2.77}$$

In contrast to the hinged beam without an elastic bed, the number of half-sine waves, denoted as m, is not restricted to being equal to 1. To ascertain the value of m that minimizes the critical load P_{cr}, it is necessary to compute the local minimum of P_{cr} by equating the derivative with respect to m to zero.

$$\frac{\mathrm{d}P_{cr}}{\mathrm{d}m} = \frac{\pi^2 EI}{L^2}\left(2m - \frac{2kL^4}{m^3\pi^4 EI}\right) = 0 \tag{2.78}$$

Thus, solving for m_{cr},

$$m_{cr} = \sqrt[4]{\frac{kL^4}{\pi^4 EI}} = \frac{L}{\pi}\sqrt[4]{\frac{k}{EI}}. \tag{2.79}$$

Demonstrably, the second derivative $\frac{\mathrm{d}^2 P_{cr}}{\mathrm{d}m^2}$ is positive for m_{cr}, indicating the presence of a local minimum. Given the requirement for m to be an integer, the appropriate value for m_{cr} is the nearest integer to the value determined using Equation 2.79, as elucidated by Hetényi [102]. Equation 2.79 reveals that m_{cr} is contingent upon the ratio of the materials' elasticity k/E. An increase in the stiffness of the elastic medium results in a higher number of half-sine waves in the buckled shape. This trend is similarly observed when the slenderness $\lambda = L/D$ of the strut increases, particularly in the case of a circular section with $I = \frac{\pi D^4}{64}$.

$$m_{cr} \sim \frac{L}{\sqrt[4]{I}} \sim \frac{L}{D} \tag{2.80}$$

The solution for a Pasternak foundation can be derived analogously, as shown by El Naschie [103]. For this, the effects of shear deformation are included in the energy terms ΔU_1, ΔU_2 and ΔW. The derivation will not be shown here as it is quite extensive. The solution is [103]

$$P_{cr} = \frac{\pi^2 EI}{L^2}\left(m^2 + \frac{kL^4}{m^2\pi^4 EI} + \frac{G_P L^2}{\pi^2 EI}\right) \tag{2.81}$$

As evident, the solution for a Winkler foundation is derived by setting G_P to zero. Since the term involving G_P is independent of m, the derivative remains consistent with Equation 2.78, resulting in the same value for m_{cr}. This implies that the inclusion of the shear layer has no impact on the number of half-sine waves.

2.5 Fundamentals of topology optimisation

Topology optimization represents a method for optimizing domains, wherein an optimal structure is automatically generated based on a given set of boundary conditions. The process involves the judicious distribution of material within a specified domain, focusing on areas where it is essential. In the realm of structural mechanics, this approach yields structures resembling trusses, while thermal considerations lead to the formation of branch tree-like structures.
To initiate topology optimization, it is imperative to define the boundary conditions. The volume V plays a crucial role in determining the permissible distribution of material. Additionally, the specification of solid or void regions is possible, imposing either full or empty sections within the domain. This feature is particularly relevant, for instance, in establishing locations for screws. Beyond these parameters, the specific shape and connectivity of the resulting structure remain unknown, as highlighted by Bendsøe [19].

2.5.1 SIMP method

To optimise the given domain, the minimisation of a relevant function is performed, and the prevalent approach involves iteratively minimizing the compliance, denoted as c. In the context of a structural problem, this minimisation process seeks to maximise stiffness. Utilizing the FEM, the discrete representation of this optimization problem is expressed in Equation 2.82 [19]. In this equation, $\mathbf{f}$ represents the forcing array or the right-hand side derived from the discretized system of equations, $\mathbf{u}$ is the vector of unknowns, $\mathbf{K}$ is the stiffness matrix obtained from the system of equations, and D_e is the element material tensor, which could be a conductivity or strain matrix.
The compliance c serves as a fundamental measure of the objective, establishing a connection between the displacements or temperature at a boundary condition and the force or flux applied to that boundary. Through the minimisation of compliance, the displacement or temperature on the specified boundary is effectively reduced.

$$\begin{aligned} &\min \qquad c = \mathbf{f}^T \mathbf{u} \\ &\text{such that:} \mathbf{K}(D_e)\mathbf{u} = \mathbf{f} \end{aligned} \tag{2.82}$$

A challenge with the presented formulation lies in its non-differentiability attributed to the binary characteristics of materials. This limitation can be alleviated by incorporating an interpolation function that facilitates a smoother transition. Among the widely adopted interpolation functions, the *'Solid isotropic material with penalization (SIMP)'* stands out as particularly popular [19], as depicted in Equation 2.83. Here, D_0 represents the actual material tensor, and D_e signifies the penalised material tensor.

$$D_e(x) = \rho(x)^z D_0, \quad z > 1 \tag{2.83}$$

Equation 2.83 introduces the element relative density $\rho(x) \in [0,1]$, serving as an interpolation parameter that transitions between the presence of material ($\rho = 1$) and void ($\rho = 0$). The equation incorporates the penalisation parameter z, employed to penalise intermediate densities. This penalisation ensures that densities between solid and void states are discouraged, compelling them to adopt either a solid or void configuration [19]. Typically, a value of $z \geq 3$ is chosen to sufficiently penalize intermediate densities. Consequently, Equation 2.82 can be subtly reformulated, as presented in Equation 2.84. The second constraint pertains to the volume, ensuring that the final volume remains at or below the pre-defined maximum volume specified by the user over the domain Ω.

$$\begin{aligned} \min \quad & c(\rho(\mathbf{x})) = \mathbf{f}^T \mathbf{u} \\ s.t \quad & \mathbf{K}(D_e(\mathbf{x}))\mathbf{u} = \mathbf{f} \\ & \int_\Omega \rho(x)\, d\Omega \leq V \end{aligned} \tag{2.84}$$

Checkerboard issue

While this formulation allows for the generation of a structure, it comes with several complications, with a prominent challenge known as the *'checkerboard'* problem [19]. These problems arise due to inadequacies in numerical modeling, leading to an overestimation of stiffness [19]. The consequence of the checkerboard pattern is the generation of an optimised structure that lacks physical plausibility.

To address this issue, filtering techniques can be employed. Numerous filters have been proposed, with those explored by Sigmund being noteworthy [104]. Among the various options, density and sensitivity filters are particularly favoured for their simplicity of implementation and efficiency [104]. These filters operate akin to low-pass filters, effectively smoothing sensitivities within local regions. Equation 2.85b outlines the structure of a sensitivity filter [105], while Equation 2.85c illustrates the structure of a density filter [106]. Both utilise a filter matrix, such as the one described in Equation 2.85a, where the filter radius is denoted as r. Importantly, the use of these suggested filter matrices has the additional advantage of rendering the results independent of the mesh employed.

$$H_{ij} = \max(r - \|x_i - x_j\|, 0) \tag{2.85a}$$

$$\frac{\widetilde{\partial c_i}}{\partial \rho_e} = \frac{1}{\rho_i \sum_{j=1}^{N} H_{ij}} \sum_{j=1}^{N} H_{ij} \rho_j \frac{\partial c_i}{\partial \rho_j} \tag{2.85b}$$

$$\widetilde{\rho}_i = \frac{\sum_{j=1}^{N} H_{ij} v_j \rho_j}{\sum_{j=1}^{N} H_{ij} v_j} \tag{2.85c}$$

Figure 2.16 illustrates an optimized structure without the application of any filtering. The image reveals the presence of checkerboarding, along with struts featuring elements that connect at only one node. This topology is not feasibly realisable.

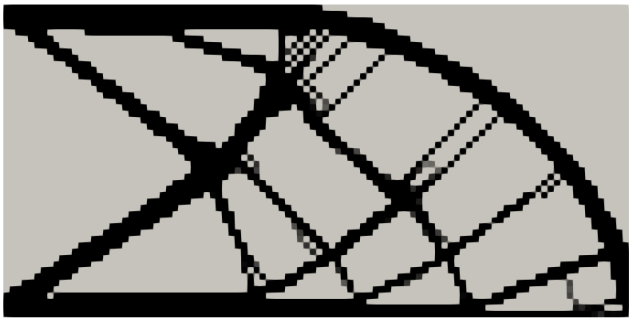

Fig. 2.16: Checkerboard pattern and non-physical regions resulting from no filter

An additional issue with topology optimisation is that local- and not global- minima can be found for the same given set of boundary conditions [19]. Some methods have been used to overcome this problem, but one simple approach is to gradually increase the penalization parameter from 1 to the desired value. Another method is to start with a large filter radius, and gradually decrease it [19].

Update Criterion

To complete the process of topology optimization, the incremental updating of element relative densities is necessary until a converged structure is achieved. Various methods have been employed for updating design variables, including the method of moving asymptotes [107] and the so-called *'optimality criteria method'* [19]. In this work, both the optimality criteria method and the generalized optimality criteria method, as proposed by Kim et al. [108], are considered. For a topology optimization problem, a Lagrangian $\mathscr{L}$ can be formulated as expressed in Equation 2.86 [19]. It is important to highlight that f denotes the volume fraction of the domain, and V_0 represents the total volume of the domain, equivalent to the user-defined final volume. The Lagrange multiplier λ is used to enforce the volume constraint. The volume V is calculated as the integral of the element relative densities ρ over the domain Ω.

$$\begin{aligned} \mathscr{L}(\rho(\mathbf{x}),\lambda) &= c(\rho(\mathbf{x})) + \lambda(V(\rho(\mathbf{x})) - fV_0) \\ \text{where: } V(\rho(\mathbf{x})) &= \int_\Omega \rho(\mathbf{x})\, d\Omega \end{aligned} \tag{2.86}$$

A critical point is found when the following conditions, in Equation 2.87, are met.

$$\begin{aligned} \frac{\partial \mathscr{L}}{\partial \rho(\mathbf{x})} &= \frac{\partial c(\rho(\mathbf{x}))}{\partial \rho(\mathbf{x})} + \lambda \frac{\partial V(\rho(\mathbf{x}))}{\partial \rho(\mathbf{x})} = 0 \\ \frac{\partial \mathscr{L}}{\partial \lambda} &= V(\rho(\mathbf{x})) - fV_0 = 0 \end{aligned} \tag{2.87}$$

To ascertain the Lagrange multiplier, denoted as λ, the rearrangement of the first constraint is presented in Equation 2.88 for each element. The variable B_e is termed the scale factor, and the optimal solution is achieved when it equals one. The determination of the optimal Lagrange multiplier can be accomplished through methods such as bisection or similar techniques.

$$B_e = -\frac{\frac{\partial c(\rho(\mathbf{x}))}{\partial \rho(x_e)}}{\lambda \frac{\partial V(\rho(\mathbf{x}))}{\partial \rho(x_e)}} \tag{2.88}$$

Consequently, each element can undergo an update of its relative density based on Equation 2.89. This methodology constrains the extent of the update for each element by regulating the move parameter, denoted as m. The power parameter η, typically set to 0.5, plays a crucial role in governing the speed and stability of the solution convergence [19].

$$\rho_{k+1} = \begin{cases} \max\left((1-m)\rho_k,\ \rho_{min}\right) & \text{if } \rho_k B_k^\eta \leq \max\left((1-m)\rho_k,\ \rho_{min}\right) \\ \min\left((1+m)\rho_k,\ \rho_{max}\right) & \text{if } \rho_k B_k^\eta \geq \max\left((1+m)\rho_k,\ \rho_{max}\right) \\ \rho_k B_k^\eta & \text{otherwise} \end{cases} \tag{2.89}$$

The Generalised Optimality Criteria Method (GOCM) proposed by Kim et al.[108] is an extension of the standard OCM. It allows multiple inequality constraints with improved computational efficiency. For the GOCM, a general formulation of the Lagrangian is used (see Equation 2.90), which includes a constraint g_i and a slack variable s_i. This variable is non-zero when the constraint is inactive.

$$\mathscr{L}(\rho(\mathbf{x}),\lambda,\mathbf{s}) = c(\rho(\mathbf{x})) + \sum_{i=1}^{N} \lambda_i (g_i(\rho(\mathbf{x})) + s_i^2) \tag{2.90}$$

The critical point is attained by setting the gradient of the Lagrangian to zero, as described by Equation 2.91 [108]. Because of the third condition, only the active constraints need to be considered [108].

$$\begin{aligned} &\nabla_{\rho(\mathbf{x})} c(\rho(\mathbf{x})) + \sum_{i=1}^{N} \lambda_i \nabla_{\rho(\mathbf{x})} g_i = 0 \\ &g_i(\rho(\mathbf{x})) + s_i^2 = 0,\ i \in [1,N] \\ &\nabla_i s_i = 0 \end{aligned} \tag{2.91}$$

An innovative concept introduced by Kim et al. suggests that the Lagrange multipliers need not be satisfied at every iteration, requiring minimal computational resources for their determination in each cycle until convergence is achieved [108]. Patnaik et al. [109] proposed several alternatives for this purpose, two of which are presented in Equation 2.92. The third option, suggested by Kim et al. [108], focuses on controlling the rate at which the Lagrange multiplier is determined. Subsequently, the relative densities can be updated in accordance with Equation 2.89.

$$\begin{aligned} &\lambda_i^{k+1} = \lambda_i^k (1 + \alpha^k p_0 g_i) && \text{Linear form} \\ &\lambda_i^{k+1} = \lambda_i^k (g_i)^{\alpha^k p_0} && \text{Exponential form} \\ &\lambda_i^{k+1} = \lambda_i^k (1 + p_0 (g_i^k + \Delta g_i^k)) && \text{Kim et al., (2023)} \end{aligned} \tag{2.92}$$

Structural optimisation In a structural the minimisation of the compliance, shown in Equation 2.93 has the effect of maximizing stiffness for a given domain volume fraction.

$$\begin{aligned} \min \quad & c(\rho) = \mathbf{u}^T \mathbf{f} \\ s.t \quad & \mathbf{K}(D_e(\mathbf{x}))\mathbf{u} = \mathbf{f} \\ & \int_\Omega \rho(x)\, d\Omega \leq V \end{aligned} \tag{2.93}$$

The gradient of the compliance is shown in Equation 2.94. Its derivation can be found in the text from Bendsøe [19]. The reader should that this only considers the theory of small displacements, i.e. only linear problems are considered.

$$\frac{\partial c}{\partial \rho_e} = -\mathbf{u}^T \frac{\partial \mathbf{K_e}}{\partial \rho_e} \mathbf{u} \tag{2.94}$$

Thermal optimisation Thermal topology optimisation has become a well-researched topic with many methods now existing [19], [110]. By minimising the thermal compliance, shown in Equation 2.95, the temperature at the heat flux boundary is minimised, with **T** being the tem-

perature matrix, and k_e being the stiffness matrix of a single element.

$$\begin{aligned} \min \quad & c(\rho) = \mathbf{T}^T \mathbf{f} \\ s.t \quad & \mathbf{K}(k_e(\mathbf{x}))\mathbf{T} = \mathbf{f} \\ & \int_\Omega \rho(x)\, d\Omega \leq V \end{aligned} \tag{2.95}$$

The gradient of the compliance, as given by Joo et al. [111] is reported in Equation 2.96. They found the derivative of the convection matrix $\mathbf{K}_h$ to be negligible, and the derivative of the forcing array is known to be zero. As a result, only the conductivity matrix $\mathbf{K}_c$ has an impact on the total gradient.

$$\frac{\partial c}{\partial \rho_e} = 2\mathbf{T}^T \frac{\partial \mathbf{f}_e}{\partial \rho_e} - \mathbf{T}^T \left(\frac{\partial \mathbf{K}_{e,h}}{\partial \rho_e} + \frac{\partial \mathbf{K}_{e,c}}{\partial \rho_e} \right) \mathbf{T} = -\mathbf{T}^T \frac{\partial \mathbf{K}_{e,c}}{\partial \rho_e} \mathbf{T} \tag{2.96}$$

In this work, domains are considered to be purely conductive. Convective effects are neglected. This is an acceptable assumption in several cases, i.e. for spacecraft systems or for media with a high domain volume fraction.

2.5.2 Optimisation of Lattice Structures

Optimisation of lattice structures requires the consideration of orthotropic material properties. Within the optimization loop, the orientation of the cells is taken into account to enhance stiffness. This is accomplished by aligning the unit cells along the principal stress axes, as indicated by Groen and Sigmund [112]. A rotation matrix $\mathbf{R}$, as exemplified in Equation 2.97b, can be employed to rotate the material tensor $\mathbf{C}$ to the angle θ, as demonstrated in Equation 2.97a.

$$\mathbf{C}(x,\theta) = \mathbf{R}^T(\theta)\mathbf{C}(x)\mathbf{R}(\theta) \tag{2.97a}$$

$$\mathbf{R}(\theta) = \begin{bmatrix} \cos\theta & -\sin\theta \\ \sin\theta & \cos\theta \end{bmatrix} \tag{2.97b}$$

The optimisation loop is similar to a typical topology optimisation, but during each iteration, the principal stresses σ_x and σ_y need to be determined as well as the rotation angle of the principal axis θ_p. The material tensor can then be rotated and recomputed until the change in angle is below a tolerance. The principle axis can be computed using Equation 2.98, where τ_{xy} is the shear stress.

$$\tan(2\theta_p) = \frac{2\tau_{xy}}{\sigma_x - \sigma_y} \tag{2.98}$$

After the optimal relative density distribution is generated, a post-processing step, consisting of a de-homogenisation, is needed. Many methods have been proposed for this [112, 113, 114]. The de-homogenisation returns a physical lattice structure, with variable geometrical parameters throughout the domain, from the finite element mesh. The de-homogenisation is performed by mapping the relative density of each element to the thickness of the struts.

2.5.3 Multifunctional topology optimisation of lattice structures

Topology optimisation has been successfully applied to a variety of lattice structures. The multifaceted features offered by cellular solids, and, in particular, additively manufactured lattice structures, attracted the attention of researchers from different engineering fields. Many authors employed topology optimisation in order to achieve optimal unit cell topologies for a given goal function. For instance, Kazemi et al. [115] proposed based on a density-based technique, which makes use of geometry projection, in order to achieve several lattice multi-material unit cells. They demonstrated the capability to obtain two- and three-material lattices with maximal bulk modulus, maximal shear modulus and minimal Poisson's ratio subject to a mass constraint.
Cheng et al.[116] introduced a method to optimise the topology of lattice structures based on homogenisation approaches, with a minimum structural compliance goal function. They first empirically described the effective stiffness of a simple cubic unit-cell in relationship to its relative density with help of power laws. Then, they used homogenised properties to perform a SIMP based topology optimisation. They then reconstructed the lattice structure by de-homogenising it. A mapping of the element of the relative density of each element to the thickness of the struts was chosen in order to perform this procedure.
Several methods have evolved for optimising lattice unit cells with a multifunctional purpose. Torquato et al. [117, 118] presented a method to achieve three-dimensional composite microstructures with multifunctional characteristics: the simultaneous transport of heat and electricity in three-dimensional, two-phase composites. The objective functions that they considered consisted of different combinations of the dimensionless effective thermal and electrical conductivities. When the sum of the effective thermal and electrical conductivities is maximized, their finding showed that the optimal three-dimensional microstructures are triply periodic bicontinuous composites with interfaces that are the Schwartz primitive P and diamond D minimal surfaces. In a similar publication, Torquato and Donev [119] demonstrated that triply periodic minimal surfaces resemble optimal geometries also when considering the maximisation of the bulk modulus.
De Kruijf et al. [120] described a method to achieve optimal structures with maximum stiffness and maximum thermal conductivity. The two phases for the material design problem were ill ordered. The microstructures were required to be isotropic with respect to conductivity but only square-symmetric with respect to elasticity.
Challis et al. [121] expanded the work of De Kruijf et al. to a third dimension, while imposing isotropicity. This was justified by the will to achieve a unit cell which can be applied in fields

where the loading direction can be unknown.
A wide combination of weights were used to calibrate the multifunctional optimisation. The results resembled a variety of microstructures which are common lattice structures, i.e. *bcc* truss lattices or Schwartz P Triply Periodic Minimal Surface (TPMS).
Aside from the research intended to achieving optimal unit cells, as described above, several authors approached the optimisation of a domain filled with pre-defined unit cells [122, 123, 124]. Venugopal et al. [125] presented a multi-material topology optimisation with stiffness and thermal conductivity goal functions. They employed pre-defined simple cubic unit cells. Recent research focuses on optimizing a domain given an already homogenized unit cell, so a similar approach to Venugopal et al. [125] can be found in many recent works, e.g. Pejman and Najafi [126] and Takezawa, et al. [127]. They also developed a method for structural optimisation using stress and conduction constraints. Their results indicate an interesting pathway for the purpose of this work.

Pareto optimality The multifunctional purpose of this work imposes the consideration of pareto optimality. To generate a Pareto front, the weight method has been used, similar to what Challis et al. [121] described. Here, the value of the goal function J in Equation 2.99 is minimised.

$$J = -\left(w_1 c_1 + w_2 c_2\right) \tag{2.99}$$

where w_i are weights that sum to one of the relative importance of each separate function c_i.
The Pareto front is obtained by first computing the single field problems, i.e. finding the optimal topology for the structural and the thermal problem, separately, in order to determine the bounds. The compliance of the single functions can then be normalised, and a Pareto front can be generated by incrementing the weights from 0 to 1. The gradient of the objective function ends up being a sum of the gradients of the single functional components with a weight on each.

Summary

The here presented chapter provided an overview of the fundamentals theories and recent literature works necessary for the development of this work. The first section introduced the reader to the theory of cellular solids, with a focus on their effective mechanical and thermophysical properties. Section 2.2 briefly introduced Phase Change Materials and their properties. In particular, methods of macro-encapsulation such as embedding in metal foams are delved into. With the informations obtained from such section, a review of the fundamental governing equations for heat and mass transfer in porous media is given in Section 2.3. Further on, Section 2.4

presents the fundamentals necessary to mathematically describe the stability of the lattice structures' slender struts when embedded within a PCM. Finally, Section 2.5 introduces the reader to the theory of topology optimisation, with a focus on the SIMP method and the optimisation of lattice structures. Present literature on multi-functional topology optimisation is also introduced.
In the following chapters, the presented theory and literature are used to first characterise the thermal and mechanical stability behaviours of the lattice structure / PCM composites. Then a multi-functional topology optimisation tool is developed and presented.

3 Lattice structures geometry

When attempting to deduce effective thermophysical and mechanical properties for the composites proposed in this work, the principal challenge resides in the precise formulation of the unit cell's geometry. The model described in Chapter 2, which is based on Hubert et al.'s research [55], opted for a simplified treatment of the unit cell geometry, specifically restricting it to cubic unit cells with an aspect ratio of 1. As highlighted in the earlier discussion in Chapter 2, their equations provided a reasonably accurate approximation of Effective Thermal Conductivity (ETC) but constrained the permissible variations in cell topology and porosity within defined limits.
In order to facilitate the characterisation of diverse cell topologies and promote meaningful comparisons between cells, it becomes imperative to augment the number of variables in the analytical model, all while upholding the model's precision. Figure 3.1 schematically describes the geometric variables considered. The relevant variables include:

- strut radius r,
- cell topology,
- cell height H,
- aspect ratio of cell height H to cell width W, expressed by the angle $\gamma = \arctan \frac{H}{W}$ (see Figure 3.1).

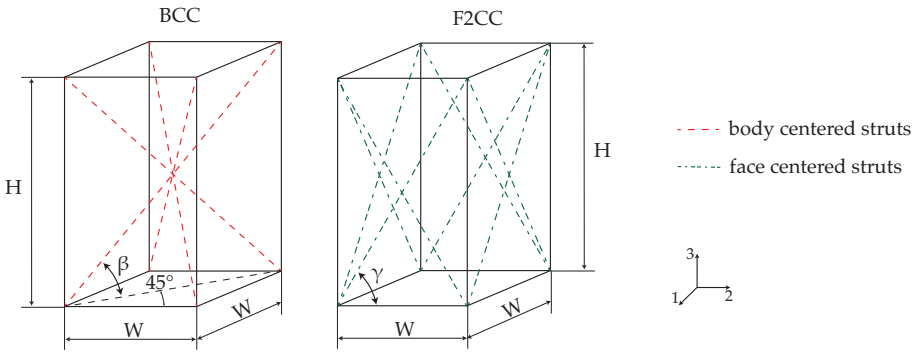

Fig. 3.1: Schematic description of basic cell geometries. In a generic cuboid cell, space-diagonals have an angle β with the face diagonal of the base-square. Face diagonals on the lateral faces make give origin to an angle γ with the base-square edge.

For face-centered struts, the strut angle to the horizontal is the angle γ. For body-centered struts in cuboid cells, this is the angle β. The relationship between the aspect-ratio angle γ and β is given by

$$\beta = \arctan\left(\frac{\tan(\gamma)}{\sqrt{2}}\right) \tag{3.1}$$

The following cell topologies are investigated: f_2cc, f_2ccz, bcc, $bccz$, f_2bcc, $f2bccz$. The unit-cells are shown in Figure 2.3.

3.1 Derivation of the Porosity

In delineating the geometry of these lattice structures, precision in calculating their **volume**, and thus their porosity and volume fraction, is of paramount importance. While determining the volume of the struts is straightforwardly linked to that of a cylinder, the computation of the volume at their intersections is intricate. Historically, empirical models have been employed for this purpose [55, 48], wherein the nodes where struts intersect are treated as cubes, and the side length is empirically estimated.
A more comprehensive model necessitates a nuanced treatment of the lattice strut intersections. In this context, Steinmetz's solids are incorporated in this study to model these intersections. A Steinmetz solid delineates the volume resulting from the intersection of two or more cylinders, as depicted in Figure 3.2.

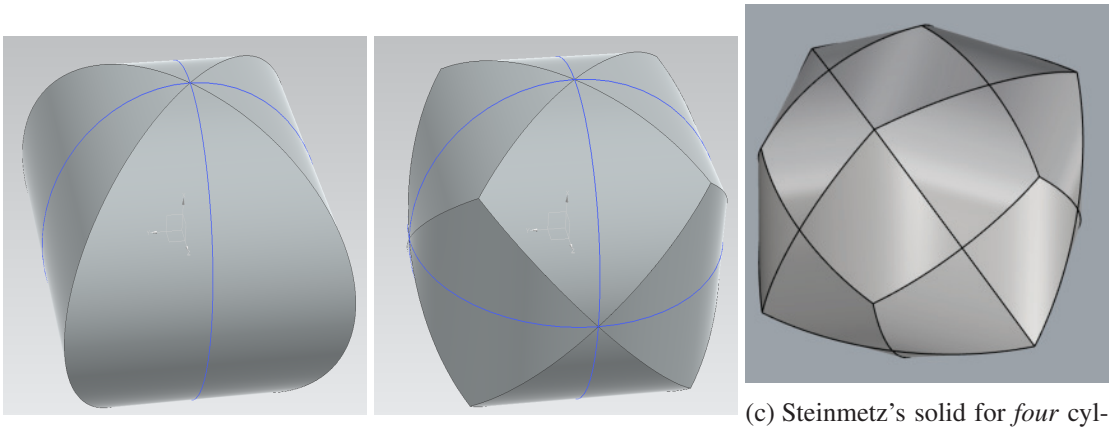

(a) Steinmetz's solid for *two* cylinders. *Four* facets are generated.

(b) Steinmetz's solid for *three* cylinders. *Twelve* facets are generated.

(c) Steinmetz's solid for *four* cylinders, i.e. the bisection axes of a tetrahedron. *Twenty-four* facets are generated.

Fig. 3.2: Steinmetz's solids for cylinders crossing at regular angles. The circles which give origin to the crossing cylinders are evidenced via blue lines.

As mentioned by Angell and Moore [128], with increasing number of cylinders, the Steinmetz's solid converges rapidly towards a sphere. For six cylinders, only a 2.6 % difference is present between the volume of a sphere and the volume of the Steinmetz's solid. This allows simplifying assumptions in the further development of this work.
Within lattice structures, various types of intersections are discernible. Referring to Figure 2.3, at the lateral edges, unit cells featuring body-centered struts manifest a four-fold intersection, denoting the crossing of four struts. In contrast, face-centered struts reduce this count to two. Nodes situated on the upper and lower faces of the unit cell present a diverse array of intersecting struts. In the case of simple *bcc* and f_2cc cells, only four struts intersect at these nodes. However, with the introduction of a z-strut, this count increases to five. Cells such as f_2bcc and f_2bccz display eight and nine intersecting struts, respectively.
For two struts crossing at an arbitrary angle ω, analytical solutions exist [129]. The generic volume of the Steinmetz's solid for cylinders with two different radii is given by

$$V(r_1,r_2,\omega) = \int_{-r_1}^{r_1} 2(r_2^2-x^2)^{0.5} \cdot \frac{2(r_1^2-x^2)^{0.5}}{sin(\omega)}\,dx = \frac{8}{sin(\omega)} \int_0^{r_1} (r_2^2-x^2)^{0.5} \cdot 2(r_1^2-x^2)^{0.5}\,dx \tag{3.2}$$

where r_1 and r_2 are the two different radii, ω is the angle between the axes of the two struts. The term $2(r_2^2-x^2)^{0.5} \cdot \frac{2(r_1^2-x^2)^{0.5}}{sin(\omega)}$ represents the cross-section parallel to the cylinder axes, at a distance x from them. It describes a parallelogram whose height is the left term of the multiplication, while the base is the right one. If the radii are equal, as assumed in this work, the volume is given by Equation 3.3.

$$V(r,\omega) = \frac{8}{sin(\omega)} \int_0^{r} (r^2-x^2)\,dx = \frac{16}{3\sin(\omega)} r^3 \tag{3.3}$$

This also represents the volume of the Steinmetz solid representative of a f_2cc node.
In the general case, each Steinmetz's solid is made of a variable number of cylindrical sectors as shown in Figure 3.3 where the points exhibit generic coordinates: O(0,0,0), A(R,0,0), B(R,Θ,0), C(R,Θ,Z).

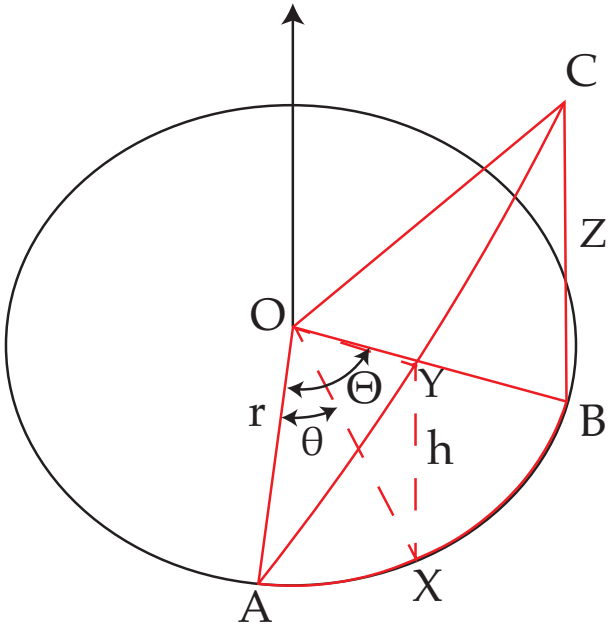

Fig. 3.3: Schematic view of a generic cylindrical sector generated by the crossing of two or more struts.

The height h of the elementary segment XY is related to the one of the segment BC by

$$\frac{h}{Z} = \frac{R\sin\theta}{R\sin\Theta} \tag{3.4}$$

The area of the surface ABC and the volume of OABC are then

$$A = \int_0^{\Theta} hRd\theta = RZ(cosec(\Theta) - \cot\Theta) \tag{3.5}$$

$$V = AR/3 \tag{3.6}$$

Thus, considering for example, the Steinmetz solid for three cylinders shown in Figure 3.2b, each of the 12 rhombic facets can be divided in 4 cylindrical sectors with vertices A=(R,0,0), B=(R,$\pi/4$,0), C=(R,$\pi/4$,R/2). To calculate the area A, $\Theta = \pi/4$ and $Z = R/\sqrt{2}$. The volume is then 48 times the volume of the considered cylindrical sector.

$$V = 48 \cdot (\frac{R^2}{3})(\sqrt{2}-1)\frac{R}{\sqrt{2}} = 8R^3(2-\sqrt{2}) \tag{3.7}$$

Lattice structures exhibit specific kinds of crossings. With reference to Figure 3.1 and Equation 3.1, *bcc* nodes which exhibit the intersection of four struts have Steinmetz solids with 24 facets

which can be divided in 4 cylindrical sectors, each. Thus, the volume of a *bcc* intersection at a generic angle is given by

$$V_{bcc} = 96\frac{r^3}{3}\sin(\pi-\beta)(cosec(\pi-\beta)-\cot(\pi-\beta)) \tag{3.8}$$

To calculate the amount of facets that the Steinmetz solid possess the following formula can be used.

$$N = 2n(n-1) \tag{3.9}$$

where N is the number of facets generated by the crossing of n struts. Then, the volume can be calculated as above, knowing the amount of facets that must be multiplied by the volume of the elementary cylindrical sector.

When z struts are present, the solution is not trivial anymore as the struts cross at different angles. The same is valid for nodes where *bcc* and f_2cc struts cross.

To simplify the calculation process, it is useful to remind that the volume of the Steinmetz solid rapidly converges to the one of a sphere when the number of struts increases. Thus, in the following, crossings involving z struts or the ones of f_2bcc cells are considered as spheres and corrected via empirical factors. Furthermore, the use of empirical factors is advantageous when considering manufacturing tolerances. At the nodes, material accumulation can take place during the manufacturing process, so that roundings are present there where the cylinder intersection lines should lie. The resulting solid thus deviates from a pure Steinmetz solid. The use of empirical factors for each kind of node can thus correct these deviations.

The volume of several lattices at different angles and with various geometric parameters is calculated via CAD and the empirical factors are fitted to these. The porosity ε can be thus calculated with the following generalised formula.

$$\varepsilon = 1 - \frac{\tan\gamma}{W^3}\left[\pi r^2 H\left(\frac{n_{bc}}{\sin\gamma}+\frac{n_{fc}}{\sin\gamma}+n_z\right) - C\cdot V_{\text{Steinmetz}}\right] \tag{3.10}$$

where γ is the aspect ratio angle, W is the size of the cuboid base, H is its height, r is the radius. n_{bc} is the number of body-centered struts in a unit cell, n_{fc} is the number of face-centered struts, n_z is the number of vertical (z) struts, C is the empirical factor and $V_{Steinmetz}$ is the analytical volume of all the nodes. This last variable is different for each lattice. The formulae for the considered lattices and the respective empirical factor C are listed in Table 3.1.

Table 3.1: Formulae for the calculation of the volume of the Steinmetz volumes for each lattice unit cell

Unit cell	Formula for $V_{Steinmetz}$	Empirical factor C
f_2cc	$\frac{16}{3}r^3\frac{2}{\sin(\pi-2\gamma)}+\frac{96}{3}r^3\sin(\pi-2\gamma)(cosec(\pi-2\gamma)-\cot(\pi-2\gamma))$	0.728
bcc	$\frac{96}{3}r^3\sin(\pi-2\beta)(cosec(\pi-2\beta)-\cot(\pi-2\beta)))$	0.908
f_2ccz	$\frac{16}{3}r^3\frac{2}{\sin(\pi-2\gamma)}+\frac{160}{3}r^3\sin(\pi-2\gamma)(cosec(\pi-2\gamma)-\cot(\pi-2\gamma))$	1.015
$bccz$	$\frac{96}{3}r^3\sin(\pi-2\beta)(cosec(\pi-2\beta)-\cot(\pi-2\beta))+V_{sphere}/(\sin(\pi/2-\beta))$	1.044
f_2bcc	$\frac{96}{3}r^3\sin(\pi-2\beta)(cosec(\pi-2\beta)-\cot(\pi-2\beta))+\frac{16}{3}r^3\frac{2}{\sin(\pi-2\gamma)}+V_{sphere}$	1.778
f_2bccz	$\frac{96}{3}r^3\sin(\pi-2\beta)(cosec(\pi-2\beta)-\cot(\pi-2\beta))+\frac{16}{3}r^3\frac{2}{\sin(\pi-2\gamma)}+V_{sphere}$	0.753

To verify the present results, numerical data obtained from a CAD of the unit cell are compared to the semi-analytical results. One should notice that the numerical data used for the verification vary from the ones used for the calculation of the empirical factor C, i.e. different geometries were used to verify the accuracy of the formulae, with respect to the ones used to achieve them. Figure 3.4 shows the verification for a f_2cc unit cell. An additional curve is plotted, named "analytical". This represents the porosity function if one neglects the Steinmetz's solid. For high porosities, the intersection of the struts is minimal and thus contributes minimally to the overall volume fraction. However, its value becomes rapidly relevant, as shown in Figure 3.4 where the results for other cells are shown.

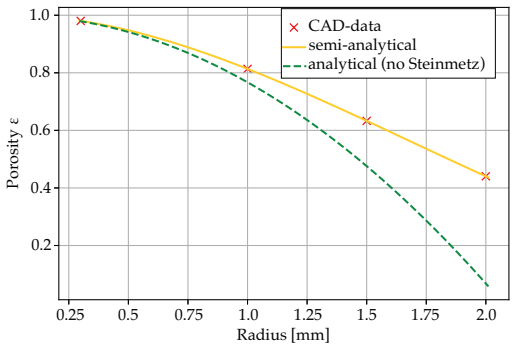

(a) Verification of the porosity analytical function plotted against increasing strut radius.

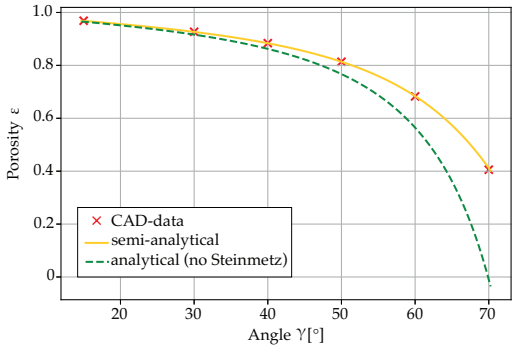

(b) Verification of the porosity analytical function plotted against increasing aspect ratio angles γ.

Fig. 3.4: Verification of the results for the porosity semi-analytical function.

Equation 3.10 delivers fundamental information for the upcoming work. Indeed, the thermophysical and mechanical properties of the lattice depend, in different ways, on the porosity, the cell size, the strut radius,the aspect ratio, and the unit-cell topology. Having obtained a unified

formulation that connects all geometric variables to the porosity, it can be used to control the material properties of each single unit-cell.
This represents a decisive step to be able to setup the optimisation algorithm presented in Chapter 6.

4 Thermal characterisation

Problem statement This chapter tries to elucidate the thermal characterisation of composites incorporating Phase Change Materials (PCMs), such as paraffin waxes, in conjunction with metallic lattice structures exhibiting diverse topologies. Initially, the assumption posited is that the dominant heat transfer regime is purely conductive. Despite the evident limitation in reliability associated with this assumption, it serves as a constructive means to incrementally introduce complexity into the investigation of the thermal behaviour.
Specifically, the primary focus in the initial section of this chapter is the acquisition of reliable descriptions of the composite's effective thermophysical properties. A semi-analytical model is formulated to delineate the effective thermal conductivity of lattice structures featuring generic topologies. The model undergoes numerical verification through the implementation of finite element models, as well as experimental validation. Additionally, a particular emphasis is placed on the model's scale variance, elucidating the variation in thermal behaviour concerning varying sizes of unit cells while maintaining consistent porosity.
Then, an experimental investigation is described. This is used to validate the semi-analytical formulae developed. The experiments also investigate the effect of natural convection within the melt of such composites on the thermal behaviour.
In the subsequent sections of this chapter, a numerical model is introduced to explicate the influence of natural convection on the thermal behavior of the composite. This model is substantiated by experimental outcomes. The experimental investigation reveals that the impact of natural convection on the thermal efficacy of the composite is negligible solely for lattice structures characterized by low porosity, where conduction consistently prevails.

4.1 Derivation of the effective thermal conductivity

The formulae derived for the porosity in Chapter 3 are used in the procedure to calculate the Effective Thermal Conductivity (ETC). Lattice structures strongly differ from other cellular solids like metal foams. Indeed, for metal foams, due to their random geometry, the ETC depends only on the porosity. For lattice structures, it depends on the porosity of the unit cell, on the cell size, the aspect ratio, the strut radius, and the cell topology. In general, the ETC of

a lattice structure is orthotropic. Thus, the effective thermal conductivity is described by the tensor

$$\bar{\bar{\lambda}}_{\text{eff}} = \begin{bmatrix} \lambda_{x,y} & 0 & 0 \\ 0 & \lambda_{x,y} & 0 \\ 0 & 0 & \lambda_z \end{bmatrix} \tag{4.1}$$

where the coordinates X,Y,Z are described in Figure 4.1, i.e. the Z-direction is the direction of z-struts, if present, and the X,Y plane is a simmetry plane.

To ascertain the ETC of the lattice structure, a methodological choice aligns with an orientation-

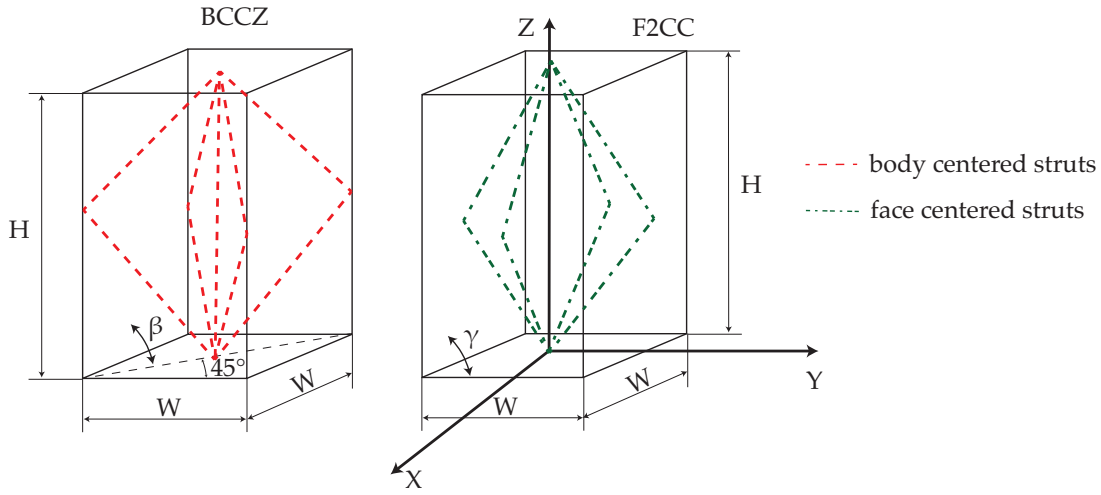

Fig. 4.1: Schematic description of a unit cell equivalent to the one of Figure 3.1, but where the unit cell is centered about the z-strut if present, i.e. the unit cell is displaced by half a cell with respect to Figure 3.1.

based layerwise approach, as illustrated in Figure 2.7. This approach is particularly apt due to the pronounced regularity in the geometry of the unit cell. All unit-cells exhibit symmetry across all three spatial directions. Exploiting this inherent symmetry facilitates a streamlined calculation process. The procedural steps for deriving the ETC are outlined schematically in Figure 4.2 and are described in the following.

The unit-cell topology and geometry, encompassing parameters such as strut radius, aspect ratio, and cell size, uniquely identify the quantity of struts and their associated characteristics (step "1." in Figure 4.2). Modeling the intersections of these struts as cuboid nodes ("2." in Figure 4.2) becomes imperative to efficiently calculate the thermal resistance at such nodes. The dimensions of these cuboid nodes vary based on the direction considered for the calculation of the effective thermal conductivity. Equations 4.2 and 4.3 are employed for calculating the ETC in the Z-direction and in the X,Y-direction, respectively. Notably, the cuboid specifications

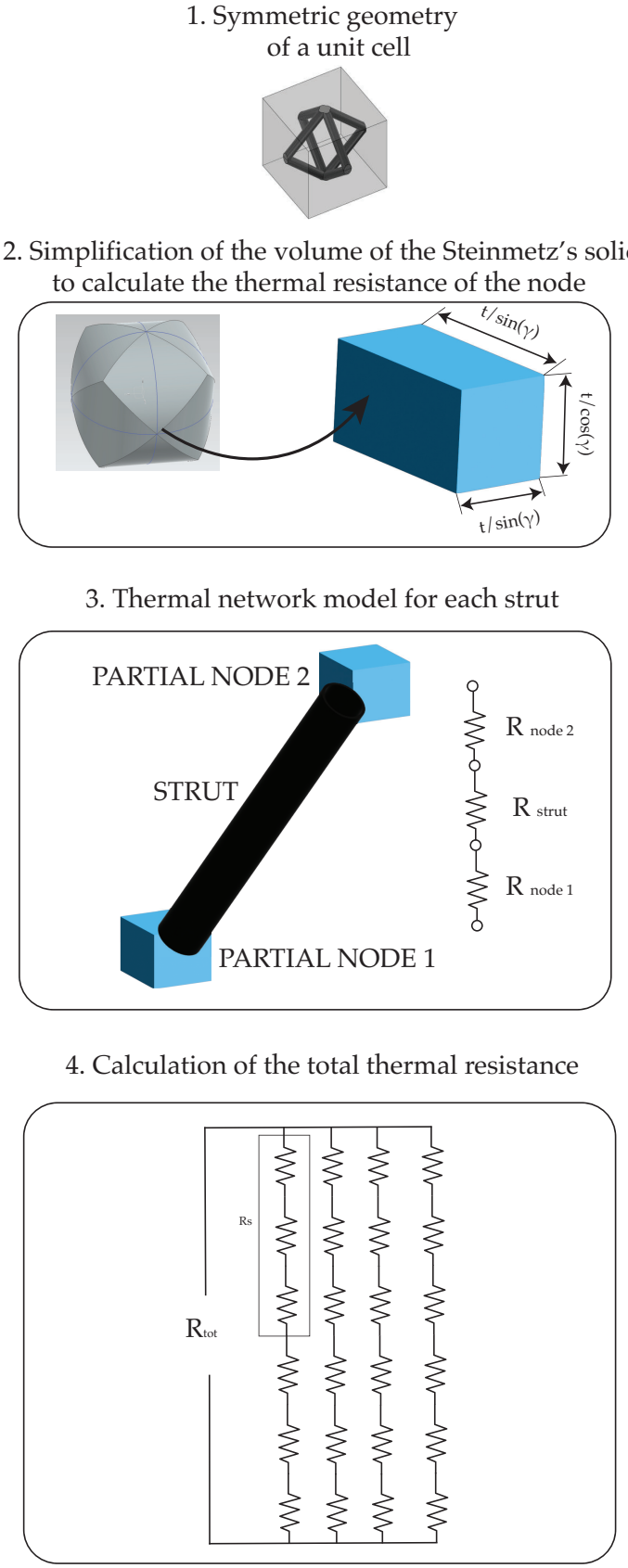

Fig. 4.2: Workflow to obtain the effective thermal conductivity. t represents the thickness of the cuboid defining the Steinmetz volume, while R is the thermal resistance.

differ for each strut type, even when multiple struts converge at the same intersection. Thus, the thickness t of the cuboid defining the Steinmetz volume is given by

$$t_z(\gamma, V_{\text{Steinmetz}}) = \left(V_{\text{Steinmetz}}(\gamma)\sin^2(\gamma)\cos(\gamma)\right)^{1/3} \tag{4.2}$$

$$t_{x,y}(\gamma, V_{\text{Steinmetz}}) = \left(V_{\text{Steinmetz}}(\gamma)\sin(\gamma)\cos^2(\gamma)\right)^{1/3} \tag{4.3}$$

where $V_{\text{Steinmetz}}$ represents the volume of the considered Steinmetz's solid.
A thermal network serves as the computational framework for determining the ETC of each strut and the associated partial node, as depicted in point 3 of Figure 4.2. The thermal network calculation is structured into three layers. The initial layer encompasses the node situated at the top or bottom cell interface. The second layer involves the strut connecting the two nodes. The third layer accommodates the second node at the intersection point of the struts, positioned midway through the cell. In the evaluation of conductivity, the thermal resistance of each layer is initially established, with exclusive consideration given to the lattice structure. The filler material, i.e., the Phase Change Material (PCM), is incorporated as a parallel resistance.
Point 3 in Figure 4.2 illustrates three thermal resistances connected in series to the one corresponding to the symmetrical strut. These series are then interconnected in parallel with the existing strut series. This configuration is schematically represented in point 4 of Figure 4.2, specifically for a f_2cc unit cell (as denoted in point 1).

Z-Direction The thermal resistance R_1 of the first node, considering the thermal resistance of a cuboid and the thermal conductivity λ, is expressed by Equation 4.4.

$$R_1(n,\gamma) = \frac{t}{\lambda A} = \frac{n\,t_n/(2\cos(\gamma))}{\sigma_1 t_n^2/\sin^2(\gamma)\lambda_s} = \frac{1}{\sigma_1}\frac{n\sin^2(\gamma)}{2\,t_n\cos(\gamma)\lambda_s} \tag{4.4}$$

In the provided equation, n denotes the number of struts participating in the intersection, with the exclusion of the z-strut. The parameter σ serves as an empirical factor introduced to accommodate the intricate intersections at the nodes, presuming that resistance diminishes due to material accumulation. λ_s represents the conductivity of the strut material. The analogous procedure is applicable to the third layer, where Equation 4.5 computes the resistance for the third layer situated at half cell height.

$$R_3(n,\gamma) = \frac{1}{\sigma_3}\frac{n\sin^2(\gamma)}{2t_n\cos(\gamma)\lambda_s} \tag{4.5}$$

In the case of the second layer, corresponding to the strut, a distinct methodology is employed. Here, the longitudinal thermal resistance of a cylinder is utilised. However, the effective length of the strut deviates from the theoretical length, which can be obtained from conventional geometric formulae if the Steinmetz's solids are neglected. To derive the modified strut length, the

distance from the center of the node to the vertex of the node is subtracted from the original strut length. Equation 4.6 is formulated to express this new strut length, denoted as L_{str}.

$$L_{str}(\gamma, n_1, n_3) = \frac{H}{2\sin(\gamma)} - \frac{t_{n_1}(\gamma, V_{\text{Steinmetz}_1}) + t_{n_3}(\gamma, V_{\text{Steinmetz}_3})}{2} \left(\frac{1}{\cos^2(\gamma)} + \frac{2}{\sin^2(\gamma)} \right)^{0.5} \tag{4.6}$$

To the determination of L_{str} follows Equation 4.7 for the resistance of the strut.

$$R_2(\gamma, n_1, n_3) = \frac{L_{str}(\gamma, n_1, n_3)}{\pi r^2 \lambda_s} \tag{4.7}$$

In totality, the resistance traversing the entire cell for a single strut is derived as a series system comprising the individual layer resistances, as specified in Equation 4.8. Considering that each strut possesses a symmetrical counterpart in each of the two considered directions (Z and X,Y), the equivalent resistance of each strut is consistently arranged in series with an identical resistance. Consequently, R_1, R_2, and R_3 are each multiplied by two to ascertain the resistance of a strut spanning the entirety of the cell, as illustrated in point 4 of Figure 4.2.

$$R_{str}(\gamma, n_1, n_3) = 2\left(R_1(\gamma, n_1) + R_2(\gamma, n_1, n_3) + R_3(\gamma, n_3)\right) \tag{4.8}$$

For the z-strut, a simpler model is employed, as it spans the entire height of the cell. The impact of material accumulation in the nodes is considered through the empirical factors σ associated with the other diagonal struts. The collective resistance of the lattice can be computed based on the number of struts, in conjunction with R_{str}. Equation 4.9 delineates the overall resistance of the struts.

$$R_{tot} = \left[\frac{\delta_{bc}}{R_{str,bc}(\gamma, n_1, n_3)} + \frac{\delta_{fc}}{R_{str,fc}(\gamma, n_1, n_3)} + \frac{\delta_z}{R_z} \right]^{-1} \tag{4.9}$$

with δ_{bc} representing the number of body-centered struts (i.e. four for a *bcc* unit-cell), δ_{fc} the number of face-centered ones, and δ_z the number of z-struts, which for cuboid cells is always one.

X, Y - Direction An identical methodology is applied for determining the ETC in the x,y-direction. The cell undergoes a 90° rotation around one of the horizontal axes, and the layers are segregated along the scrutinized direction (x- or y-direction). Figure 4.3 illustrates the cells stacked in different orientations, with the example of a rotation around the y-axis. The volume of the prism at the intersections of the struts (nodes) undergoes alterations compared to the modeling in the z-direction. In the x,y-direction, the edge length of the prism becomes $t/\sin(\gamma)$. The cross-section of the prism corresponds to $(t/\cos(\gamma))^2$. Consequently, Equation 4.3 is obtained to represent the edge length parameter t. Given that the parameter t is defined differently with respect to the z-direction, the resistances of the nodes also deviate from Equations 4.4 and

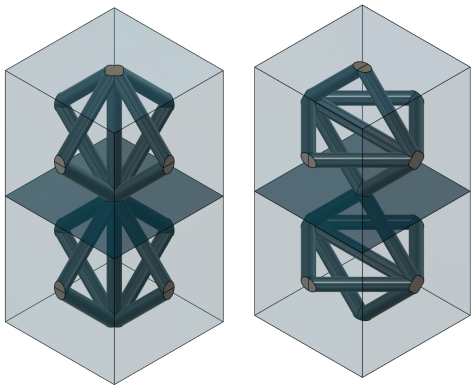

(a) z-direction (b) x,y-direction

Fig. 4.3: Two f_2ccz cells stacked in different directions.

4.5. Consequently, Equation 4.10 is derived for the node of the first layer, and Equation 4.11 is formulated for the node of the third layer in this context.

$$R_1(n,\gamma) = \frac{1}{\sigma_1}\frac{n\cos^2(\gamma)}{2\,t_n\sin(\gamma)\lambda_s} \tag{4.10}$$

$$R_3(n,\gamma) = \frac{1}{\sigma_3}\frac{n\cos^2(\gamma)}{2\,t_n\sin(\gamma)\lambda_s} \tag{4.11}$$

Owing to the rotation, not all struts effectively contribute to the conductivity. For instance, the z strut in Figure 4.3b no longer connects the bottom and top interfaces of the cell. Nonetheless, these struts still enhance the conductivity of the cells by thickening the intersections of the nodes. The additional material augments the cross-section of the node, thereby reducing the path length and lowering the resistance. This influence is incorporated into the model through the empirical parameter σ in Equation 4.12.

$$\sigma_i = \sigma\tan(\gamma) \tag{4.12}$$

The conductivity of layer two is computed using the same equations as those applied in the z-direction (Equations 4.6 and 4.7), but incorporating the new strut length from Equation 4.3. Consequently, the lattice's conductivity can be determined through Equations 4.13-4.14. For a f_2bccz cell, it follows that there are two face-centered (fc) struts ($\delta_{fc} = 2$), as the remaining struts do not contribute directly to the conductivity. There are four body-centered (bc) struts ($\delta_{bc} = 4$) and zero z-struts ($\delta_z = 0$) per unit cell.

$$R_{str}(\gamma,n_1,n_3) = 2\left(R_1(\gamma,n_1) + R_2(\gamma,n_1,n_3) + R_3(\gamma,n_3)\right) \tag{4.13}$$

$$R_{tot} = \left[\frac{\delta_{bc}}{R_{str,bc}(\gamma,n_1,n_3)} + \frac{\delta_{fc}}{R_{str,fc}(\gamma,n_1,n_3)}\right]^{-1} \tag{4.14}$$

Effective Thermal Conductivity The outlined methodology is applicable to a diverse range of cuboid unit cells. An illustrative example is provided below, elucidating the determination of the Effective Thermal Conductivity (ETC) for an f_2bccz unit cell—a composite comprising all possible struts. This specific unit cell features four face-centered (fc) struts ($\delta_{fc} = 4$), four body-centered (bc) struts ($\delta_{bc} = 4$), and one z-strut ($\delta_z = 1$) per unit-cell. The resistance of the body-centered strut, $R_{str,bc}$, involves an eight-fold strut-intersection in the first layer and a four-fold one in the third layer. Consequently, $R_{str,bc}(\gamma, n_1 = 8, n_3 = 4)$ is employed. Conversely, the face-centered struts exhibit an eight-fold intersection in the first layer and a two-fold intersection in the third layer, leading to the use of $R_{str,fc}(\gamma, 8, 2)$. The empirical coefficients are determined through numerical optimisation, employing a gradient descent algorithm to achieve accurate values. Tables 4.1 and 4.2 present the coefficients and values for σ to be utilized.

Table 4.1: Coefficients to calculate the ETC in z-direction. The Root Mean Squared Error (RMSE) is calculated varying all geometric parameters.

cell type	δ_{fc}	δ_{bc}	δ_z	$n_{1,fc}$	$n_{3,fc}$	$n_{1,bc}$	$n_{3,bc}$	$\sigma_{1,fc}$	$\sigma_{3,fc}$	$\sigma_{1,bc}$	$\sigma_{3,bc}$	RMSE [%]
f_2cc	4	0	0	4	2	-	-	2.024	1.793	-	-	2.09
f_2ccz	4	0	1	4	2	-	-	1.448	1.168	-	-	1.65
bcc	0	4	0	-	-	4	4	-	-	1.903	1.903	1.59
$bccz$	0	4	1	-	-	4	4	-	-	1.537	1.537	1.85
f_2bcc	4	4	0	8	2	8	4	2.145	1.311	2.145	1.311	1.01
f_2bccz	4	4	1	8	2	8	4	1.654	1.185	1.654	1.133	1.00

Table 4.2: Coefficients to calculate the ETC in x,y-direction. The * indicates, that the factor is multiplied by $\tan\gamma$ as in Equation 4.12.

cell type	δ_{fc}	δ_{bc}	$n_{1,fc}$	$n_{3,fc}$	$n_{1,bc}$	$n_{3,bc}$	$\sigma_{1,fc}$	$\sigma_{3,fc}$	$\sigma_{1,bc}$	$\sigma_{3,bc}$	RMSE [%]
f_2cc	2	0	4	2	-	-	2.618	3.316	-	-	1.14
f_2ccz	2	0	4	2	-	-	1.732	2.836	-	-	1.54
bcc	0	4	-	-	4	4	-	-	4.277	4.277	1.52
$bccz$	0	4	-	-	4	4	-	-	10.95*	4.073	1.61
f_2bcc	4	4	8	2	8	4	10.86*	2.420	10.86*	3.840	1.87
f_2bccz	4	4	8	2	8	4	9.576*	3.468	9.576*	4.564	2.38

In the z-direction, the empirical factors σ decrease with the addition of a z-strut, as clear comparing f_2cc and f_2ccz unit-cells in the tables above. A decrease in σ corresponds to an increase in the resistance of the strut. Thus, this result is logical, as the z-strut occupies a portion of the node in the first layer, resulting in less conducting surface for the diagonal struts. Once the resistance R_{tot} of the lattice is determined, the ETC can be calculated using Equations 4.15

and 4.16. The necessary inputs include the cell type, radius r, cell height H, and angle γ. The conductivity of the filler, λ_f, is also considered, weighted by the porosity ε.

$$\lambda_{\text{eff}_z}(\gamma, r, h) = \frac{\tan^2(\gamma)}{H\, R_{tot}} + \varepsilon\lambda_f \tag{4.15}$$

$$\lambda_{\text{eff}_{x,y}}(\gamma, r, h) = \frac{1}{H\, R_{tot}} + \varepsilon\lambda_f \tag{4.16}$$

The detailed expressions for the ETC of each unit-cell are given in Appendix C.

4.1.1 Verification

To validate the formulated equations, a comprehensive approach is employed, encompassing numerical simulations, comparison with existing literature—especially the work by Hubert et al. [55]— and experimental investigations detailed in Section 4.2. The experimental data serve a dual purpose, providing immediate validation and potential input for further explorations. Numerical models are constructed utilizing the commercial software COMSOL Multiphysics®. The assumption is made, that the predominant heat transfer mode is heat conduction. Both a stationary and a transient model are developed. The stationary model is employed for determining the ETC, while the transient model is utilized to examine the time-dependent behavior of the composite PCM and its dependency on cell size, as presented in Section 4.1.2. In the stationary model, material properties are assumed to be constant over the investigated range. To reduce the computational effort, a quarter of the cell cross-section is employed, given the symmetry of the cells through the center point, as already presented by Hubert et al. [55]. Multiple cells are stacked atop one another, with a minimum of seven cells yielding stable results, wherein further stacking does not significantly alter the ETC. Figure 4.4 illustrates the model and the boundary conditions. The temperature difference is measured at the central cell to determine the conductivity using Equation 4.17.

$$\lambda_{\text{eff}} = \frac{\dot{q}H}{T_2 - T_1} \tag{4.17}$$

with $\dot{q}$ representing the heat flux flowing through the domain, H is the cell size, T_1 is the temperature at the top interface of the cell and T_2 is the temperature at the bottom interface. A mesh-convergence analysis is conducted for each cell. The maximum element size of 1.82 mm and minimum element sizes of 0.078 mm for the cell dimensions $H = 10$ mm and $\gamma = 45°$ have been determined to yield an error less than 0.1%. The number of elements required is contingent on the cell's complexity. Consequently, the f_2bccz unit cell necessitates the highest number of elements to achieve mesh convergence due to the highest number of struts and the presence of the most complex nodes. In each case, the smallest radius examined (i.e., the highest porosity) is used for the cells, as this scenario requires the smallest elements and thus the highest quantity

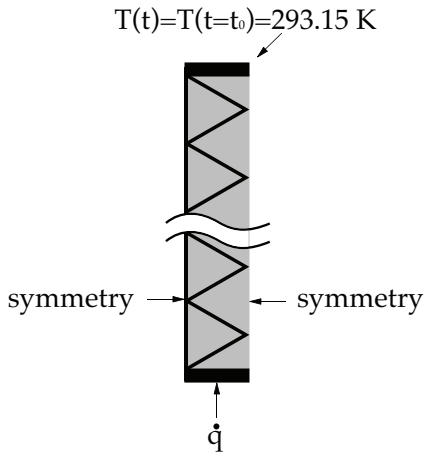

Fig. 4.4: Simulation model for the calculation of the ETC and boundary conditions applied, with a constant value of the heat flux $\dot{q}$. The black lines represent the struts of the unit-cell

of them. Figure 4.5 illustrates the convergence plot for the f_2bccz unit-cell.

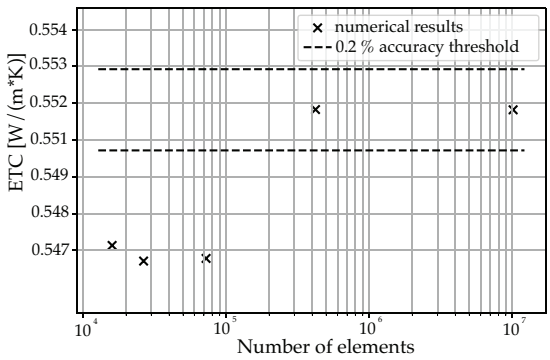

Fig. 4.5: Convergence study of the stationary model for the f_2bccz cell, which requires the most elements.

Numerical results obtained through steady-state thermal simulations are utilised for verification. The empirical parameters for the ETC model are calibrated through numerical outcomes from a parametric study. The model is then verified using geometric parameters distinct from those used in calibration.

The comparison involves the proposed model, numerical outcomes, and literature data, as illustrated in Figure 4.6. However, this comparison is restricted to specific cases due to limitations in the available literature [55], specifically addressing f_2cc, f_2ccz, bcc, and $bccz$ cell topologies, all characterized by an angle of $\gamma = 45°$.

For a more extensive assessment, the equations are verified within a parameter range defined as $20° < \gamma < 65°$ and $0.01 < r/h < 0.13$. The equations demonstrate validity for porosities

surpassing $\varepsilon > 0.65$, suitable for lightweight structural designs aiming at high porosity values.
The comparison between the derived equations and numerical results in the x,y-direction is

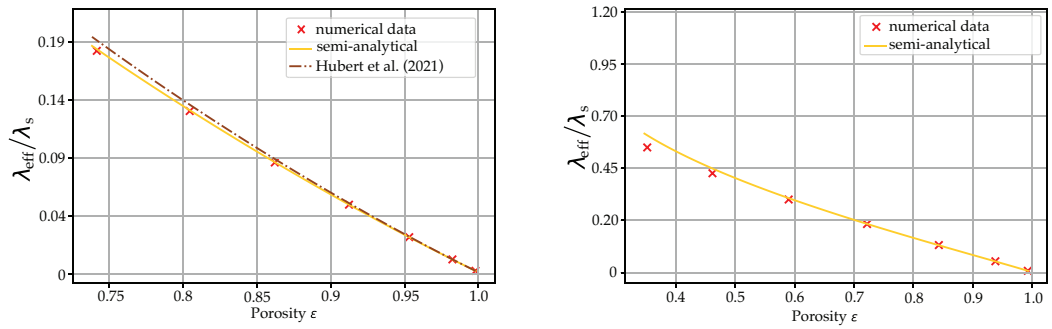

(a) $\gamma = 45°$ (b) $\gamma = 65°$

Fig. 4.6: Comparison of the different models for calculation the ETC in z-direction of the unit-cell f_2ccz. The radius is varied in a range from $r = 0.1$mm to $r = 1.3$mm. The height of all cells is $H = 10$mm, while the angle is specified in the captions.

illustrated in Figure 4.7. Generally, there is good agreement between the analytical results and numerical outcomes. However, the equations encounter challenges in predicting conductivity for high angles ($> 60°$). This limitation arises from struts that are not directly involved in heat conduction in the x- and the y-direction, such as the z struts. At high angles, these struts significantly shorten the conduction path and result in high material accumulations. However, this effect is not considered in the equations. Consequently, the semi-analytical equations can only be reliably applied for angles $\gamma < 60°$. Within this parameter range, the equations demonstrate accuracy with errors below 5% for porosities exceeding $\varepsilon > 0.65$. However, for given unit-cells, this range can be higher, as shown in Figure 4.7b.

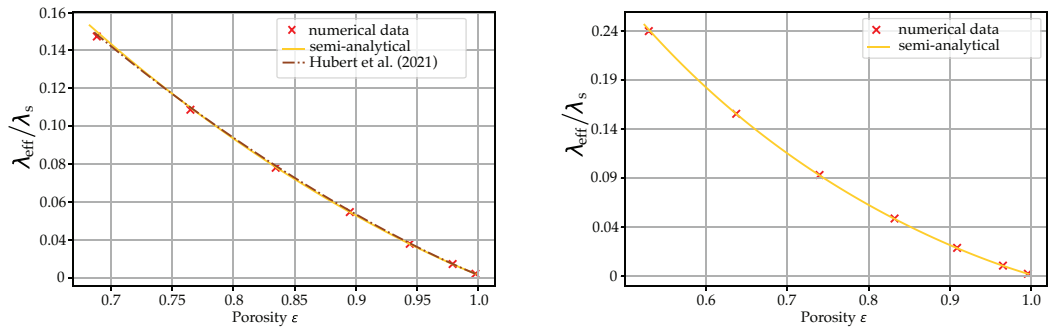

(a) $\gamma = 45°$ (b) $\gamma = 54.74°$

Fig. 4.7: Comparison of the different models for calculation of the ETC in x,y-direction, for the unit-cell $bccz$. The radius is varied for in a range from $r = 0.1$mm to $r = 1.3$mm. The height of all cells is $H = 10$mm, while the angle is specified in the captions.

4.1.2 Results and Discussion

The provided semi-analytical ETC model, in conjunction with mixture laws for density and specific heat capacity, facilitates the homogenization of thermophysical properties within the composite PCM. This homogenisation enables a detailed exploration of the influence of diverse geometric parameters on the thermal characteristics of the composite. The focus of this section is to meticulously examine the impact of each parameter in isolation from the others.

Strut radius In Figure 4.8, both the effective thermal conductivity in z and in x,y- directions for all considered unit cells at varying porosity are shown. The effective thermal conductivity (λ_{eff}) is normalised against the one of the bulk material of which the lattice structure is made (λ_s). For the case shown in Figure 4.8 the unit cell size is fixed at 5 mm and the angle γ is kept at 45°, thus maintaining a cubic unit cell.

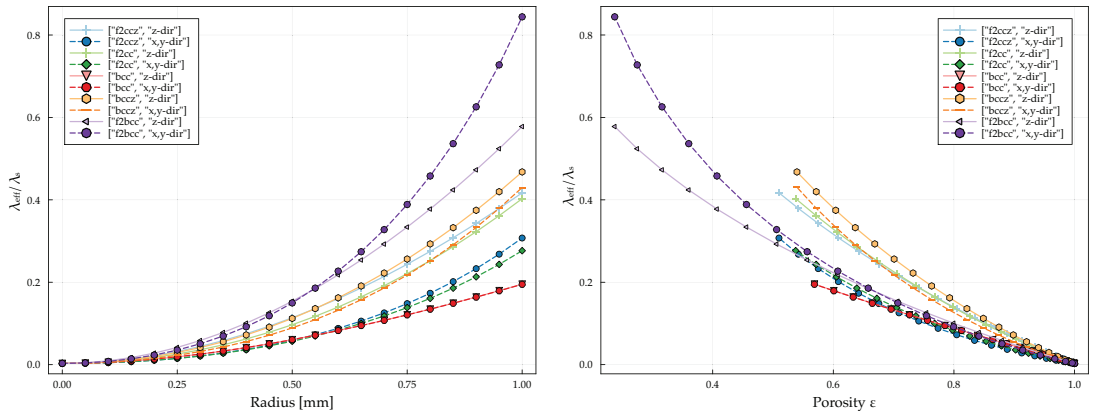

(a) ETC in both directions against a variable radius, within the range $r = [0,1]mm$

(b) As in (a), plotted against the porosity variation resulting from a radius variation.

Fig. 4.8: Effective thermal conductivity of all considered cells for varying porosity obtained by varying only the strut radius.

The data depicted in Figure 4.8 unambiguously illustrates that unit cells incorporating struts aligned in the z-direction (z struts) manifest the highest effective thermal conductivity along that particular axis. Notably, among the various unit cell types, those characterized by a face-centered structure exhibit the most pronounced thermal conductivity in the z-direction. In contrast, unit cells with a body-centered structure demonstrate the lowest thermal conductivity in this regard. This distinction can be ascribed to variations in the angles (γ) of the struts within these unit cells. Specifically, struts in body-centered cells possess a smaller angle compared to their counterparts in face-centered cells with an equivalent aspect ratio. Consequently, unit cells predominantly composed of body-centered struts present a higher thermal resistance due to the elongated heat conduction path, aligned along space-diagonals instead of face-diagonals as observed in face-centered counterparts. Conversely, when evaluating the x and y-directions,

the disparity in effective thermal conductivity among unit cells diminishes. This occurrence stems from the limited impact of z-struts on directions perpendicular to them. In this scenario, unit cells characterized by a face-centered structure with z-struts exhibit the lowest effective thermal conductivity, while those with a body-centered structure display the highest thermal conductivity.
It is worth mentioning, that as explained above, the validity of the proposed equations is limited to unit cells with porosity $\varepsilon > 0.65$. The displayed curves reach lower values only for an illustrative purpose.

Aspect ratio (angle γ) Figure 4.9 shows the effect of varying only the angle γ on the ETC. As previously shown in Figure 4.8, the variation of the geometric parameter is intrinsically associated with a variation of the porosity as well, which thus affects the ETC. In general, an increase of the aspect ratio is associated with an increase of the ETC. It is interesting to notice that, as shown in Figure 4.9b for the *bcc* and the *bccz* samples, the variation of γ for body-centered unit-cells is particularly efficient on a lightweight design perspective. Indeed, a variation of the aspect ratio leads to an asymptotic increase of the ETC, but a minimal reduction of the porosity (i.e. minimal mass increment).
The combined effect of a variation of the strut radius and of the aspect ratio is shown in Figure 4.10, where the y-axis exhibits the same scale in order to emphasize the effect. While the trend remains unvaried, it is quantitatively more relevant for unit cells with a higher strut radius.

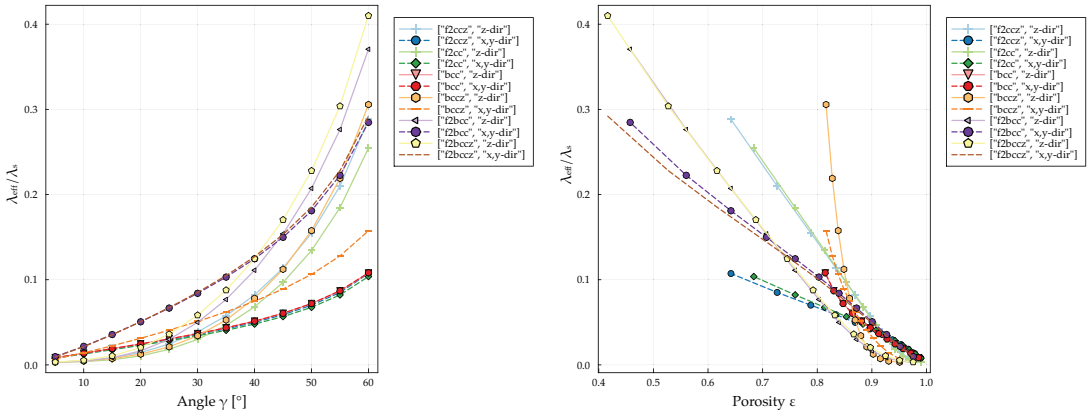

(a) Effect of angle (i.e. aspect ratio) variation, within the range $5° < \gamma < 60°$.

(b) Same as in (a), plotted against the effect of the angle on the porosity.

Fig. 4.9: Effect of the angle γ on the ETC. The strut radius and the cell size are fixed at $r = 0.5$ mm and $H = 5$ mm, respectively.

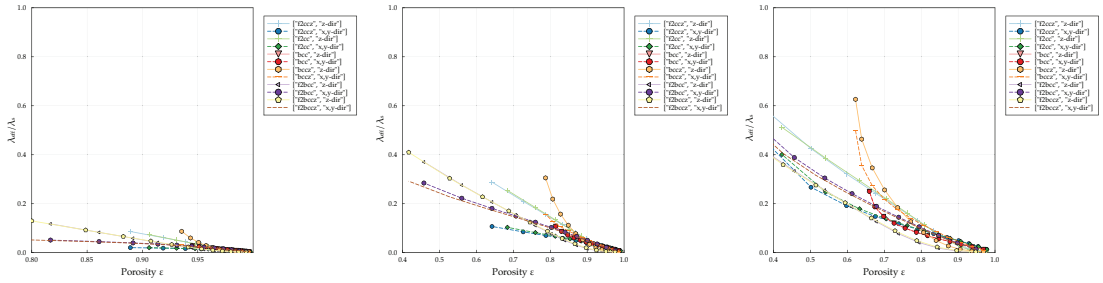

(a) $r = 0.25$mm (b) $r = 0.5$mm (c) $r = 0.75$mm

Fig. 4.10: Combined effect of a variation of the strut radius r, and of the aspect ratio γ for $H = 5$ mm.

Scale variance: effect of cell size and number of cells No direct influence of cell size on the ETC could be evidence. When the cell size is increased while maintaining a constant porosity, achieved by proportionally increasing the strut radius, there is no observable impact on effective thermal conductivity, as depicted in Figure 4.11. In this investigation, the cell size is varied within the range of 5 to 30 mm, while the radius ranged from 0.5 to 3 mm. This observation aligns with previously reported findings in the literature concerning the effect of cell size on thermal properties in metal foams [54, 51]. While the described results do accurately predict

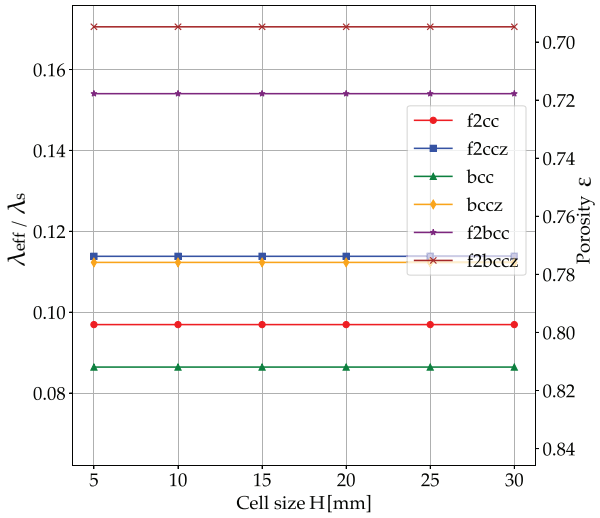

Fig. 4.11: Cell size effect on the effective thermal conductivity λ_{eff} obtained by scaling the strut radius according to the cell size variation.

the effective thermophysical properties, this alone does not offer a comprehensive understanding of the **transient response** of a composite involving a Phase Change Material and a cellular solid. Specifically, lattice structures produced through additive manufacturing or investment casting techniques provide the flexibility to vary cell sizes over a broad spectrum. In practical

applications, adjustments to both cell size and cell count may be made based on diverse boundary conditions, particularly when dealing with confined system volumes. Hence, it becomes crucial to explore the influence of scale variation on the transient thermal behavior of such systems. To address this, a numerical investigation is undertaken, comparing both a discrete model and a homogenised model under identical boundary conditions, as illustrated schematically in Figure 4.12. The homogenised model is built upon the presented formulae for the effective thermophysical properties, and a range of geometric parameters is systematically varied across all considered cells.

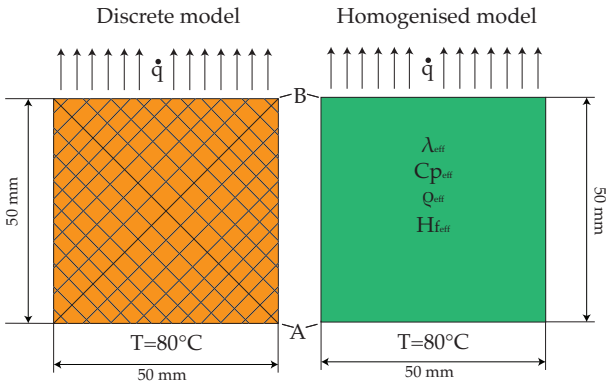

Fig. 4.12: Schematic view of the compared numerical models to investigate the scale variance.

In reference to Figure 4.12, a pertinent boundary condition in the numerical framework is established by $\dot{q}$, where its magnitude is set at 1000 W/m^2, serving as one facet of the computational domain. Conversely, the opposing boundary condition is defined by a fixed temperature of 80°C. The materials under scrutiny encompass n-Octadecane Paraffin wax and aluminum alloy 6061, with their respective properties delineated in Appendix B. Each examined geometry constitutes a cubic volume measuring 50 mm along each axis, characterized by diverse geometric attributes for the lattice structures embedded within this domain.
To ensure the achievement of a steady-state condition across all porosities, the simulation duration is established at $t = 1800s$. The selection of cell sizes is meticulously executed to enable the accommodation of an integer count of cells within the 50 mm domain, as detailed in Table 4.3. The adjustment of the radius is orchestrated to maintain a constant porosity throughout the array of cell sizes. The porosity spectrum considered spans from ε= 0.95 to ε=0.7, with incremental steps of 0.05. Simulations are systematically conducted for both the z-direction and the x,y-direction for each cell type, thereby generating a matrix of 36 simulations for each orientation of each cell type. The temperature variation ΔT between point A and point B of Figure 4.12 is measured. The value for a time $t = 1800s$ is considered so that full melting is reached for all samples. A normalised ΔT, indicated as Γ, is considered. This represents the ratio between the temperature variation for the discrete vs homogenised models is calculated.

$$\Gamma = \frac{\Delta T_{discrete}(t = t^*)}{\Delta T_{homogenised}(t = t^*)} \tag{4.18}$$

Number of cells	Cell size [mm]	Radius [mm]	Aspect ratio angle γ [°]	ε
20	2.5	0.129	45	0.95
10	5	0.259	45	0.95
5	10	0.517	45	0.95
4	12.5	0.647	45	0.95
2	25	1.294	45	0.95
1	50	2.587	45	0.95

Table 4.3: Example of the geometric variables for the study of the scale variance considered for the case of a f_2ccz cell with porosity 0.95.

The results for the unit cells f_2ccz, f_2cc, bcc, $bccz$ are reported in Figure 4.13,4.14. Observa-

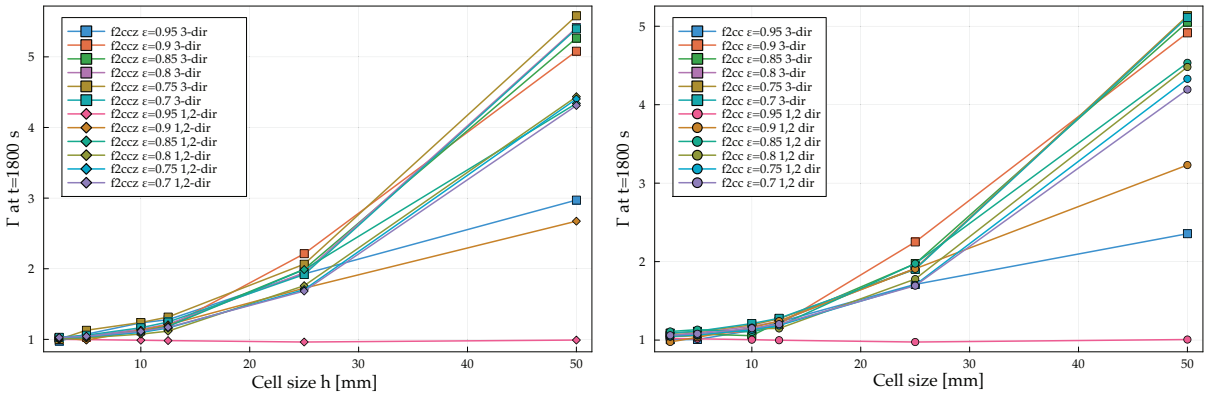

(a) f_2ccz scale variance, (b) f_2cc scale variance.

Fig. 4.13: Scale variance for face-centered cells

tions indicate that modifications to the cell size, leading to a reduction in the number of cells within the domain, introduce deviations from the predictions of the homogenised model. The homogenised model closely approximates the discrete model, particularly when employing a substantial number of cells, corresponding to smaller cell sizes in this context. However, it is noteworthy that this deviation is interconnected with other cell parameters. Specifically, for all unit cells, higher porosities (resulting in lower effective thermal conductivities) lead to a reduced or negligible deviation. This implies that, for such cases, the thermal behaviour closely mirrors that of a pure PCM, with the metallic matrix exerting minimal influence.
As porosity diminishes, the deviation increases, with its precise magnitude heavily influenced by the unit cell topology. Moreover, supplementary analyses are conducted to distinguish the impact of cell size from that of the number of cells. Figure 4.15 illustrates the outcomes of an additional parametric investigation, wherein the domain size adjusts proportionally with both the cell size and the number of cells. To ensure the manifestation of deviation in scenarios involving large cell sizes and a small number of cells, a porosity value of $\varepsilon = 0.85$ is selected

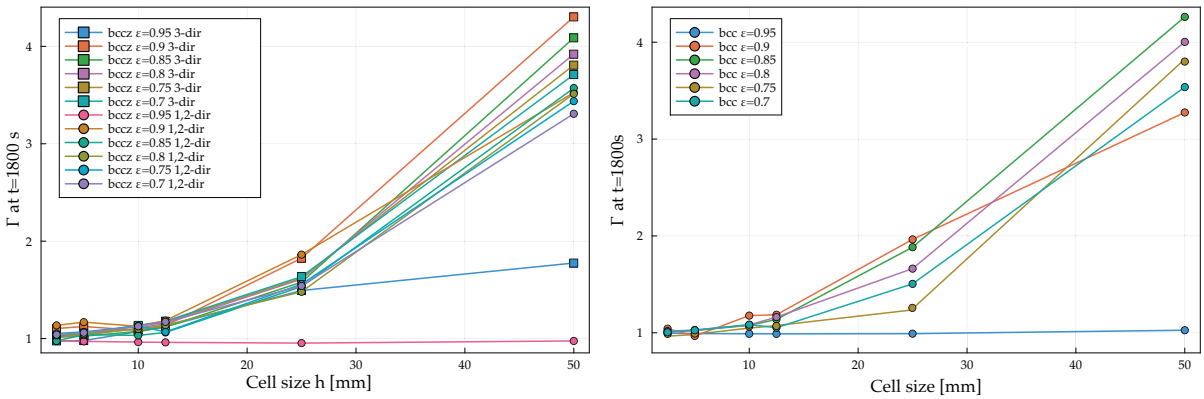

(a) *bccz* scale variance. (b) *bcc* scale variance.

Fig. 4.14: Scale variance for body-centered cells

for unit cell *bccz* (refer to Figure 4.14a). It is evident that a substantial number of cells within

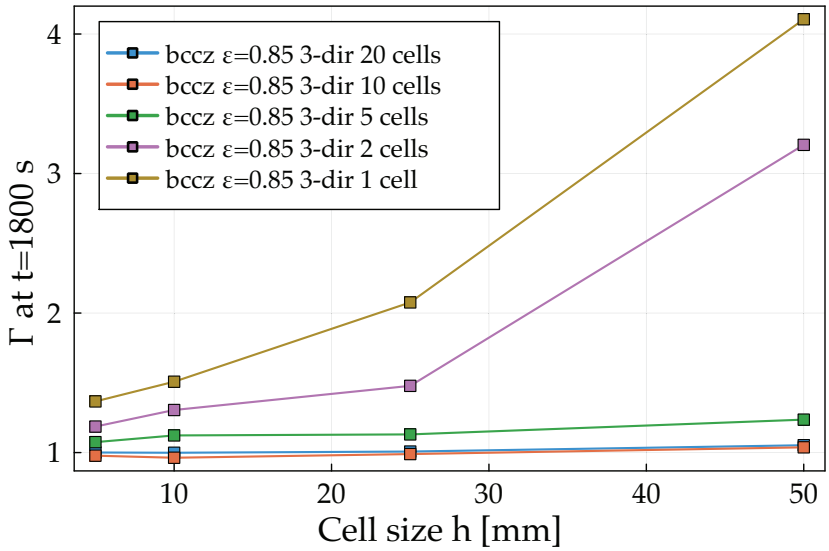

Fig. 4.15: Isolated effect of varying the number of cells.

a given domain consistently yield accurate predictions in accordance with the homogenised model, irrespective of the cell size. However, a distinct trend emerges as the quantity of cells decreases. While significant discrepancies between discrete modeling and the homogenised approach are noticeable even at smaller cell sizes (as depicted in Figure 4.15), the magnitude of deviation tends to grow with increasing cell size. As a result, it can be concluded that this model offers dependable estimations as long as a sufficient number of cells with consistent geometric characteristics populate the domain. This supports the conclusion that an homogenisation is only valid when the number of cells is sufficiently high, so that the material can be defined as a cellular solid, in relation to the percolation theory (Chapter 2).
Thus, although the effective thermal conductivity, and in general the thermophysical properties,

are scale invariant, the transient thermal behaviour of the composite is not. Homogenisation techniques shall be assumed valid only when dealing with a considerable amount of unit cells within a domain, so that the structure can be considered a porous medium and, in particular, a cellular solid. A minimum amount of 10 cells is found to deliver satisfactory results.

4.1.3 Updated conductive model

The simplified conductive model in Section 2.3.1 showed clear limitations, which motivated the work presented thus far. In particular, while the mixing rules of equations 2.10, 2.11, and 2.58 still apply, the effective thermal conductivity model was valid only for high porosities above 90%. The effective thermal conductivity model presented in this work exhibits a wider validity range, and can be thus used to evaluate all the effective thermophysical properties, as well as the simplified transient behaviour. Figures 4.16, 4.17 show the effective thermophysical properties as a function of the lattice volume fraction χ considering the instance of a f_2cc unit cell with cubic shape (i.e. aspect ratio 1). The effective thermal conductivity obtained from the presented model is plotted against the volume fraction and compared in each plot with the other thermophysical properties, obtained via weighted mixture laws. A comparison of the figures 4.16a),b), and 4.17a) shows that, while the density increases with the volume fraction, which would tend to reduce the effective thermal diffusivity, the combined effect of the thermal conductivity and the specific heat is dominant. Indeed, the thermal diffusivity monotonously increases with increasing volume fraction, indicating that the effective thermal conductivity and the reciprocal of the specific heat have a steeper increase with respect to the increase of the density. It's important to note that, as depicted in Figure 4.17b, the effective latent heat exhibits an opposite trend to the effective thermal conductivity. Therefore, when considering a thermal control system, there is no trivial optimum in increasing thermal conductivity. As the effective latent heat decreases with an increase in volume fraction, the amount of thermal energy that can be absorbed through the phase change consequently decreases. This may eventually lead to a temperature increase despite increasing the thermal conductivity of the composite, which is the primary goal of this study and much of the current literature. Thus, it is essential to take this fundamental aspect into account when analyzing or optimizing a similar composite.

The simplified analytical solution to the Stefan Problem is proposed again in Figure 4.18, considering the effective thermophysical properties shown in Figures 4.16, and 4.17. While it is clear that the melting front is continuously accelerated by increasing the volume fraction (reducing the porosity), the increment of the melting front position at a given time between an increment in volume fraction and the next is not constant. This is explicitly described in Figure 4.19. Indeed such increment, described as Δs, is highest close to volume fraction 0.05. After such threshold, diminishing returns can be noticed, i.e. the increase of the volume fraction of the lattice structure does not increase the melting front velocity as effectively. Furthermore, as shown in Figure 4.20 the thermal energy that is stored latently within the time $t = 300s$ peaks at a volume fraction close to 0.45.

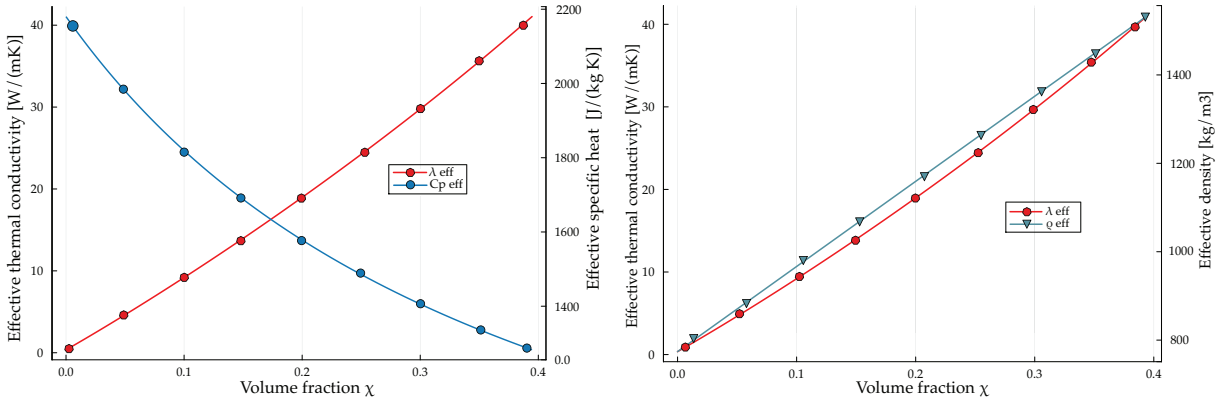

(a) Effective thermal conductivity and Specific heat capacity against volume fraction, for a f_2cc unit cell.

(b) Effective thermal conductivity and density against volume fraction, for a f_2cc unit cell.

Fig. 4.16: Effective thermal conductivity, specific heat and density as a function of the volume fraction.

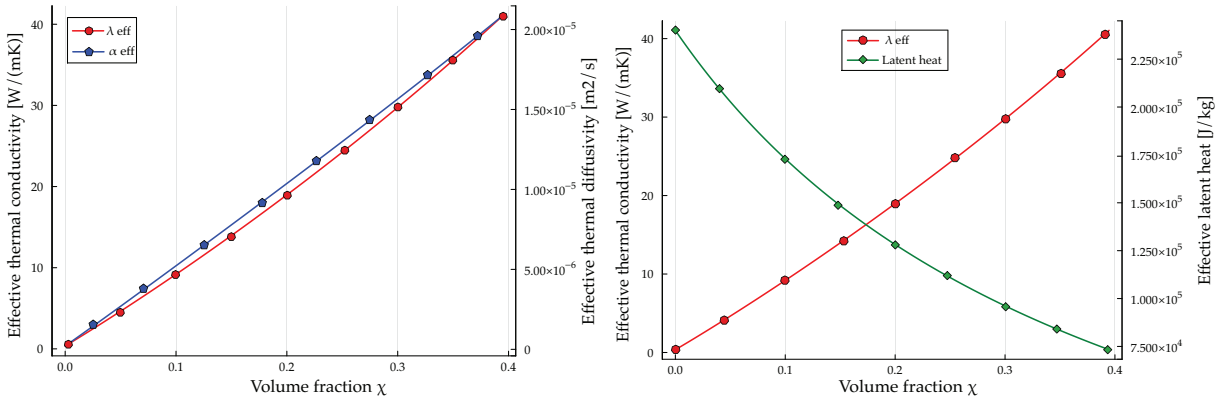

(a) Effective thermal conductivity and thermal diffusivity against volume fraction, for a f_2cc unit cell.

(b) Effective thermal conductivity and latent heat against volume fraction, for a f_2cc unit cell.

Fig. 4.17: Thermophysical properties as a function of the volume fraction for an exemplary f_2cc unit cell.

The results discussed thus far indicate that no trivial optimum exists when considering the ETC as well as the stored energy as goal functions. Indeed, while the ETC monotonously increases, its effect on the melting front is highest for relatively low volume fractions (high porosities). Furthermore, due to the opposite trend of the effective latent heat with respect to the ETC, but the different orders of magnitude, an optimum energy storage is possible far from such peak. The topic of optimisation is discussed in Chapter 6.

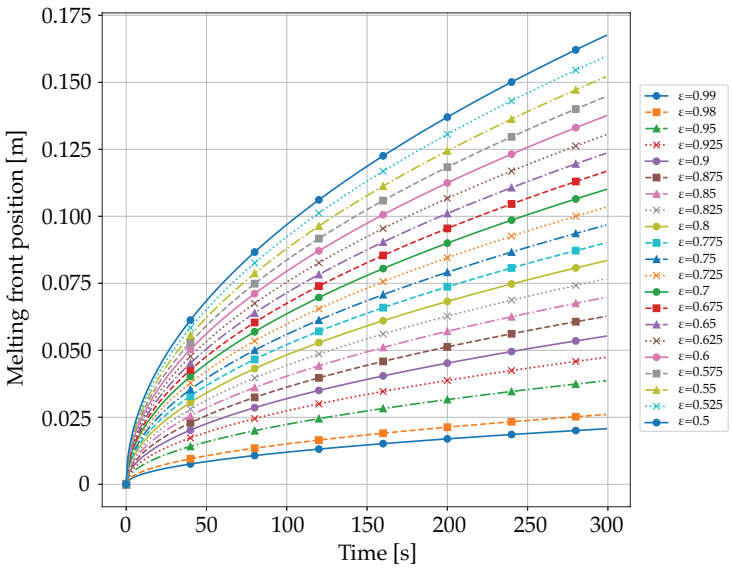

Fig. 4.18: Melting front position evloution against time, for different porosities. The reference unit cell is f_2cc with cell size 10 mm and aspect ratio 1. Compared to Figure 2.12.

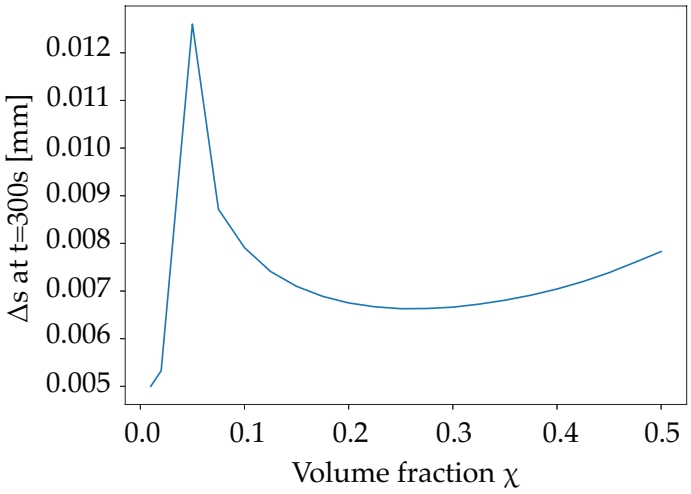

Fig. 4.19: The variation of the melting front position at end of the considered time, for increasing volume fractions χ (i.e. reducing porosity). The behaviour is similar to the one of Figure 2.13.

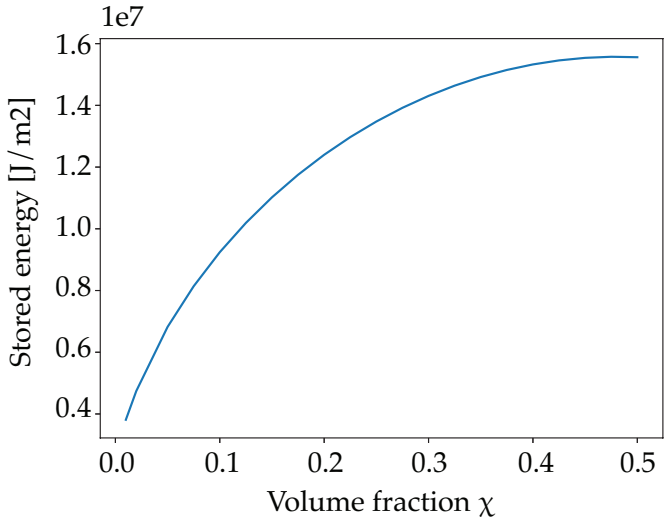

Fig. 4.20: Stored energy at t=300s against volume fraction χ of the lattice.

4.2 Experimental investigation and validation

The previously presented model for the effective thermophysical properties lacks experimental validation. Only the effective thermal conductivity model was validated this far (see Section 4.1.1, Figures 4.6,4.7), based on results presented in the literature [55]. Here, an experimental investigation is proposed to validate the conductive model considering transient conditions. Furthermore, experimental and numerical investigations previously performed on metallic foams [75, 74, 83] already showed that, depending on the inclination of the heat source with respect to the local gravity vector, natural convective movements can affect the thermal behaviour of the composites. The same has to be assumed for lattice structures, thus, the experimental campaign aims also at analysing the behaviour of the composite under different orientations. Finally, a comparison of the thermal performance of different unit cells, with particular focus on lightweight design is proposed.

Experimental setup All specimens utilized in the experiment were additively manufactured by EOS GmbH, utilizing an AlSi10Mg aluminum alloy. They possess a cubic morphology with a 50 mm edge length and feature a periodic internal structure consisting of a single unit cell topology. These samples exhibit unit cells with uniform cell widths of 5 mm, 1 mm strut diameters, and a cubic shape. Owing to variations in the number and geometric arrangement of struts within each cell, the volume fraction differs among the tested specimens, and this information is detailed in Table 4.4.
A schematic view of the experimental setup is given in Figure 4.22. It comprises the composite specimens shown in Figure 4.21, a heating system, a containment box, measurement instruments, and a data acquisition system. The heating is performed via cartridge heater, modulated via Pulse Width Modulation (PWM) to deliver a constant power of 40W. The acquisition of data is performed via PT100 temperature sensors, and via a Germanium window, through Infrared frames. These are useful to detect the shape of the melting front at different orientations.

Cell topology	Vol. fraction χ [vol %]	Porosity ε [vol %]
bcc	17.8	82.2
f_2ccz	16.6	83.4
bccz	20	80
f_2bcc	29.3	70.7

Table 4.4: Unit cell geometry of the tested samples. The cell size is 5 mm for all samples, the strut diameter is 1 mm and the aspect ratio angle γ is 45°.

The chosen PCM material is n-Octadecane paraffin wax (99% purity, produced by abcr GmbH, Germany), characterised by a melting point of 29°C. The thermophysical properties of the PCM are detailed in Table B.2.

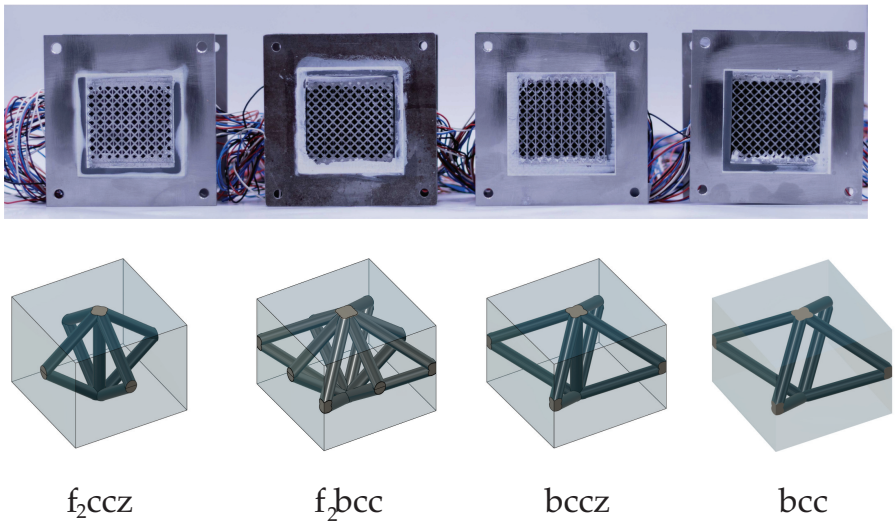

Fig. 4.21: Tested specimen with correspondent unit cell for each sample.

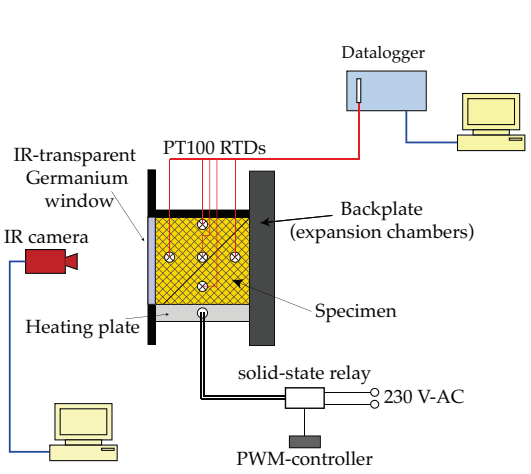

(a) Schematic description of the experimental setup with the infrared (IR) camera.

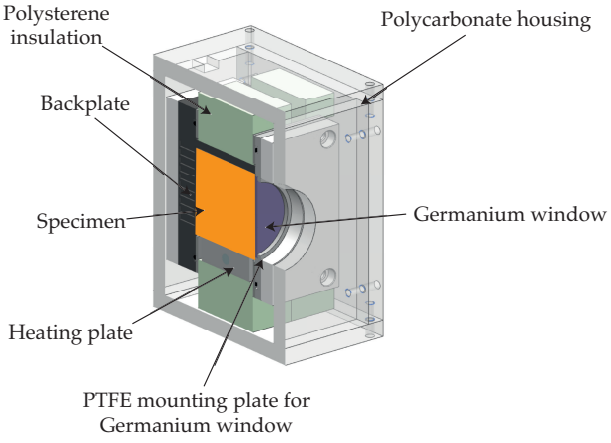

(b) Section view of the Computer-Aided Design (CAD) for the test cell with the Polytetrafluoroethylene (PTFE) moving plate.

Fig. 4.22: Schematic drawings of the experimental setup.

Further details on the experimental setup can be found in the Appendix D, as well as in the dedicated publication [130].

Test campaign methodology

All the experiments were conducted while maintaining a consistent heat flux, delivering a constant power of 40 W. The trials were repeated with varying orientations relative to gravity to investigate the influence of convective heat transfer within the specimens. Three distinct orientations of the heat flux vector in relation to gravity were examined, as depicted in Figure 4.23. The sample's orientation is determined by the relative alignment of the heat flux vector and the gravitational acceleration's one.
In order to assure repeatability, each individual cell undergoes testing in each of the three orientations three times. As illustrated in Figure 4.23, the designations "top" and "bottom" refer to cases where the heat flux aligns parallel or anti-parallel to gravity, respectively. In the "side" orientation, the heat flux vector is perpendicular to the gravitational acceleration vector.
It's crucial to note that the variation in inclination is applied by simultaneously rotating both the heat source and the test sample. This implies that samples featuring z-struts (f_2ccz and $bccz$) are consistently heated in a direction parallel to these struts, regardless of the orientation.
To standardize the initial conditions, each test sample is filled with paraffin wax and cooled down to 18°C inside a climate chamber (Espec® ARS-1100). This ensures a uniform starting temperature for all samples and runs. The tests involve heating the sample and monitoring it throughout the melting process. Infrared images and temperature data are collected continuously at a sampling rate of 5 Hz throughout the entire melting period. The tests are concluded either when the paraffin wax is completely melted or when either sensor 2 or 7 reach a temperature of 60°C. This protocol is implemented to prevent overheating of the Styrodur® insulation, as it begins to decompose above 80°C.

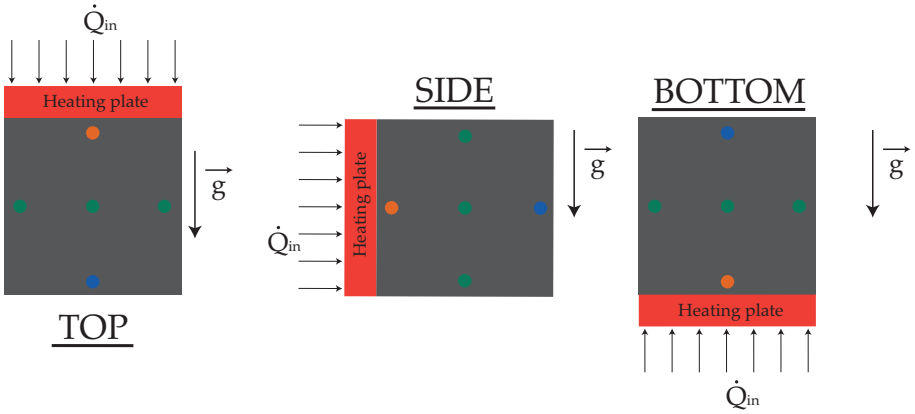

Fig. 4.23: Orientations considered in the experimental campaign and relative position of the PT100 sensors for heat power $\dot{Q}_{in}$.

4.2.1 Results

The thermal performance analysis of each sample is performed by comparing temperature evolutions during the melting process. The detailed temperature curves for each sensor of the whole experimental matrix are shown in Appendix E, Figures E, E, E. As each experiment for each sample was repeated three times, the curves show the average for each sensor. A shaded area of the same colour of the respective curve is used to represent the standard deviation. At the initial moment ($t = 0$), when heat is introduced via the heating plate, temperature gradients emerge among various points on the solid material's surface. These gradients correspond to the proximity of these points to the heat source. As the temperature of each point approaches the melting point, the curves slopes tend to flatten horizontally, exhibiting minimal change. Subsequently, the temperature resumes its upward trajectory, albeit with a distinct slope, indicating the transition from a solid to a liquid state took place.
Once the temperatures reach the melting point, the material exhibits diverse behaviors depending on its orientation. The standard deviation for experiments conducted at top orientation is low with respect to side and bottom orientations. This is evident comparing Figure E with Figures E and E where several sensors exhibit much wider standard deviations. This is due to the insurgence of natural convection when the heating is either orthogonal or parallel (opposite direction) to the local gravity vector. Specifically, when heating from the side orientation (Figure E), the temperature trends observed in the central sensors on one side (sensors 1, 3, 5) and the other (sensors 6, 8, 10) exhibit distinct slopes compared to those shown in the plots for the top and bottom orientations (Figures E, and E). This discrepancy indicates a spatially uneven expansion of the melting front, likely attributed to the emergence of a convection regime.
To provide quantitative context, the average maximum temperature reached during the test with the top heating configuration is 60.8°C after 900 seconds. Conversely, for tests conducted with the side orientation, the average maximum temperature at the same experiment duration is 54.6°C, while it is 54.3°C for tests conducted with the bottom orientation.
The infrared (IR) frames for each sample at different time points can be found in Appendix E.

The thermal behavior of individual samples is effectively described by the temperature at the heating surface. Enhanced thermal performance of a sample as a thermal control device is associated with a reduced degree of wall overheating concerning the melting temperature recorded at the heating surface. An additional noteworthy temperature pattern pertains to the sensors positioned at a "mid" location (i.e. sensors 1, 3, 5, 6, 8, 10 in Figure D.2). The instant at which these sensors attain the melting point is correlated with the time required for the samples to undergo melting. To evaluate the effect of orientation on the thermal behaviour of the samples, the results are reported again in Figures 4.24 to 4.27. For ease of representation, the following figures show only sensors 2, 3, and for side orientation, sensors 7 and 8. In Figures 4.24 to 4.27 the thermal behaviour for each sample under different orientations is compared. It is clear that the orientation has a major effect on the thermal behaviour of the sample. In particular, the occurrence of natural convection in the side and bottom orientations generally causes an

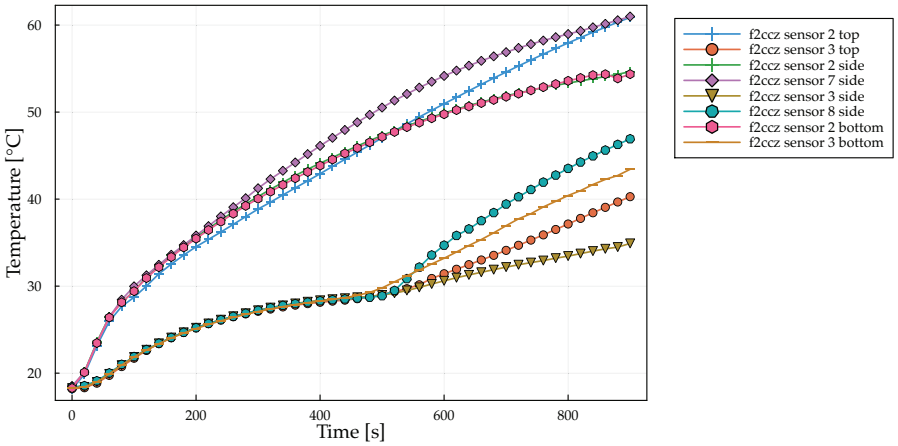

Fig. 4.24: Comparison of the sensors 2, 3, 7, and 8, for the f_2ccz sample.

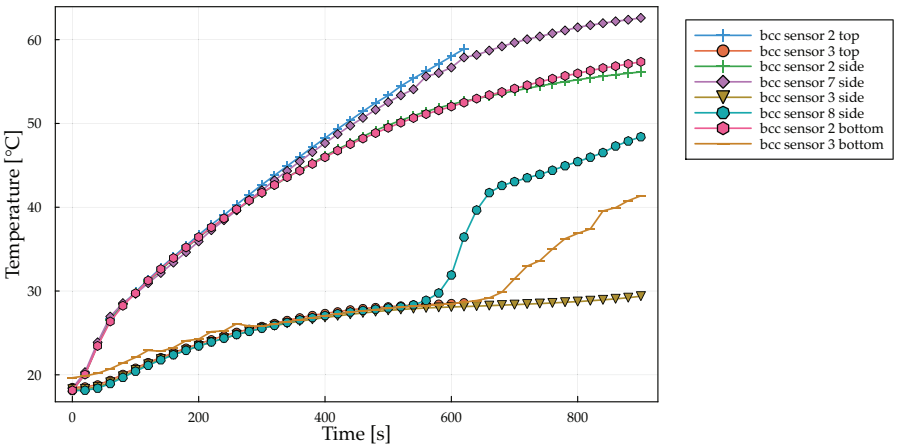

Fig. 4.25: Comparison of the sensors 2,3, 7, and 8, for the *bcc* sample.

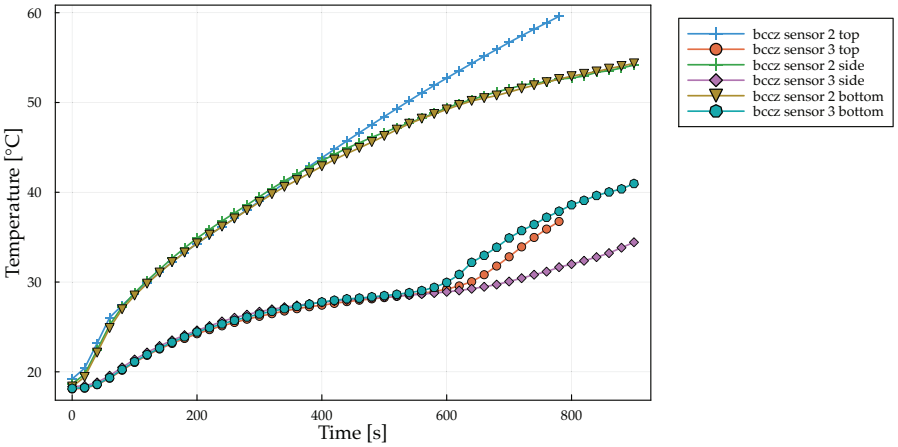

Fig. 4.26: Comparison of the sensors 2 and 3 for the *bccz* sample.

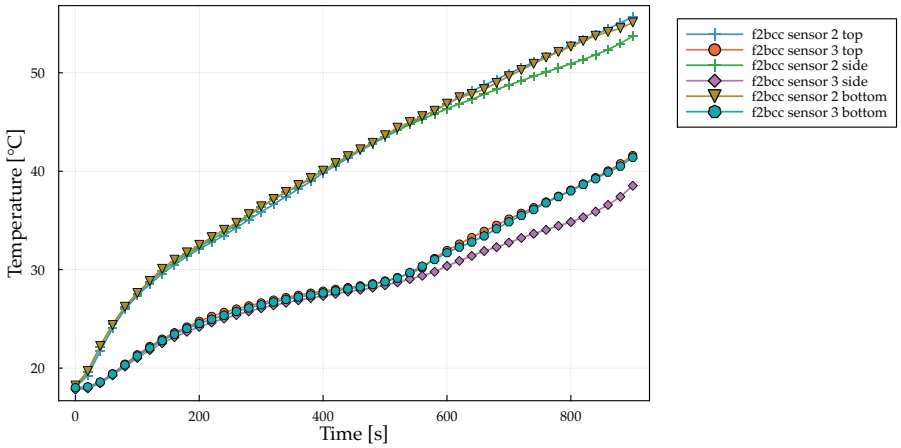

Fig. 4.27: Comparison of the sensors 2 and 3 for the f_2bcc sample.

acceleration of the melting front. This can be visualized noticing that the temperature curves of the sensor 2 for side and bottom orientations are consistently lower than the top orientation case. Similarly, for side and bottom orientation, the sensor 3 exhibits a steeper curve and a faster deviation from the melting point. This is qualitatively valid for all samples, except the f_2bcc, as one can appreciate from Figure 4.27. Due to the high porosity, the permeability of the lattice is probably very low and the effective thermal conductivity too high. Thus, the thermal behaviour for this sample can be considered to be dominated by conduction only. The side orientation is cause for inhomogeneous melting front expansion, which can be appreciated comparing sensors 2 and 7, as well as 3 and 8.

The sample structured according to the f_2ccz cell topology exhibits the second smallest temperature increase on the heating wall, with $bccz$ and bcc cell types following closely behind. Notably, the extent of wall overheating in the f_2bcc case is 65% lower compared to the least favorable scenario (bcc). This discrepancy highlights a 31.2% difference in the maximum recorded temperatures between the f_2ccz and bcc samples, despite a minimal 1.2% variation in their porosities. This observation underscores the predominant role played by the cell topology in influencing heat transfer within the sample.

A significant reduction of 28% in dimensionless temperature is observed for the bcc sample when comparing its top and bottom orientations. A similar trend is noted for various lattice topologies, albeit with slightly smaller reductions: 21% for the $bccz$ sample, 8% for the f_2ccz sample, and 3% for the f_2bcc sample. These findings underscore the non-negligible influence of natural convection when assessing the heat transfer characteristics of PCMs embedded within lattice structures.

To facilitate a meaningful comparison between the results obtained from these lattice cells and data pertaining to foams, it is advantageous to establish a connection between the geometry of the tested lattice structures and that of a metal foam. The key parameter affecting convection onset in foams is the Pores Per Inch (PPI). Regrettably, as previously mentioned, the geometric parameters of lattice structures do not inherently encapsulate the concept of PPI for an unambiguous geometric characterisation. Hence, the geometric properties of these lattice cells are

analysed using the commercial software nTopology®. The software maps and calculates the diameters of pores contained within the tested samples. The pore diameter is defined as the diameter of the largest sphere that can fit inside a pore without overlapping with the solid structure. However, it's important to note that these pores can overlap with one another. This calculation is based on the graph representation of the lattice structures, constructed from the centerlines of individual struts. Consequently, the calculated pore diameters are independent of the strut diameters and rely solely on the cell size and the unit cell topology. In Figure 4.28, the lattice structure is depicted in gray, while the spherical pores are marked in pink. The equivalent pore diameter is derived through a weighted average of the resultant mapped pores, providing what is referred to as an equivalent-PPI for each cell, as detailed in Table 4.5. Remarkably, the data

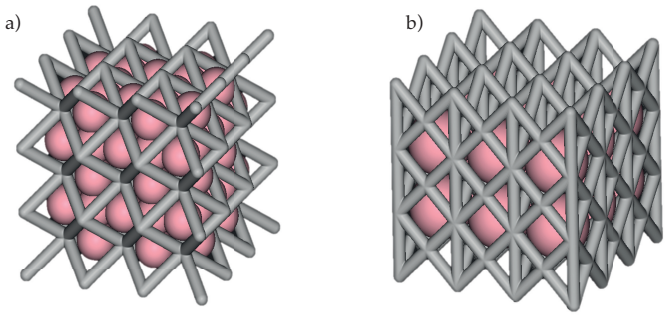

Fig. 4.28: Geometric representation of the pores and the spheres whose diameters are used to calculate the equivalent PPI. Exemplary representation for the *bcc* (a) and f_2ccz (b) samples.

Table 4.5: Equivalent pores per inch for each tested sample, in order of decreasing porosity.

Unit cell topology	PPI_{eq}
f_2ccz	5
bcc	8
bccz	8
f_2bcc	20

obtained for the f_2ccz, *bcc*, and *bccz* cells can be correlated with metal foams characterized by low PPI values. Several researchers have explored the impact of PPI on the thermal performance of metal foam/PCM composites, as found in references [75, 85, 83, 131, 71]. Their findings indicate that lower PPI values, when maintaining the same foam porosity, lead to lower wall temperatures and shorter melting durations. A similar qualitative trend is observed for the tested lattice structures. Nonetheless, it should be emphasized that lattice cells and foams are not entirely equivalent. It is possible to have lattice cells topologies with the same equivalent PPI, but the thermal behaviour can differ. For example, the orthotropic structure of the cell sample based on the *bccz* cell, which exhibits the same equivalent PPI as the *bcc* cell, demonstrates a smaller reduction in wall temperature. A comparable situation is observed for the f_2ccz

sample, even though it features the lowest equivalent PPI. This behavior can be attributed to a combination of factors: the conductive and convective contributions to the thermal behavior of the composite are intertwined, and the permeability of the structure does not exhibit a direct correlation with the number of pores. Furthermore, notably, most cells exhibit orthotropic topologies, which may also introduce direction-dependent permeabilities. Additionally, the impact of thermal conductivity along the orthogonal plane (x,y-direction) cannot be disregarded. This factor also affects the dynamic shape of the melting front and, subsequently, the thermal performance. Particularly in the case of the bottom orientation, where convective effects are expected to be less pronounced than in the side orientation, transversal thermal conductivity can play a pivotal role in heat transfer. All together, when predicting the behavior of lattice cell structures, it is imperative not to overlook the role of convection and the interwinded effect it can have on the melting front expansion.

4.2.2 Validation of the model for the effective thermophysical properties

The selection of cell topologies for the examined samples is guided by the aim of achieving a favorable balance between thermal efficiency, mechanical strength, and low overall mass. In order to assess the thermal performance and the lightweight potential of different samples, an assessment criterion is proposed in the following. With the goal of facilitating a comparison of the experimental outcomes across various samples and heating orientations, a non-dimensional criterion for evaluating thermal performance is established. This criterion draws inspiration from the method proposed by Diani and Campanale [69] for assessing metal foams, which has also been adapted by Righetti et al. [70] for lattice structures. The criterion which will be proposed in the following requires a valid description of the effective thermophysical properties. The model presented above (Section 4.1.3) is validated against the experimental data of the top orientation.

Considering that the tested samples satisfy the condition of a sufficient amount of unit cells in the domain, as described in 4.1.2, the conductive model can be easily validated. To such purpose, the model presented in sections 4.1 and 4.1.3 is used to calculate the effective thermophysical properties of the tested samples. A homogenised material model is then implemented in a Finite Element model based on the apparent heat capacity method, available as a module in COMSOL Multiphysics®. The same boundary and initial conditions which are fixed for the experimental campaign are recreated in the numerical model. The comparison between the homogenised model and the experiments is shown in Figures 4.29 to 4.32. In order to simplify the readability, the thermal behaviour of the numerical model is reported in only three points, namely the ones which correspond to the position of the sensors 2, 3, and 9 in Figure D.2, i.e. representing the heating plate, the central sensor and the sensor furthest from the heating plate, respectively. It is worth noticing that only the results for the top-heating orientation are compared to the present model. This is due to the fact that only under such orientation the effect

of natural convection in the melt is negligible, and a purely conductive regime can be assumed. As previously discussed, additional operations are needed to homogenise the behaviour of such composites when natural convection acts on the component. The validation for such a case is discussed in the following section.

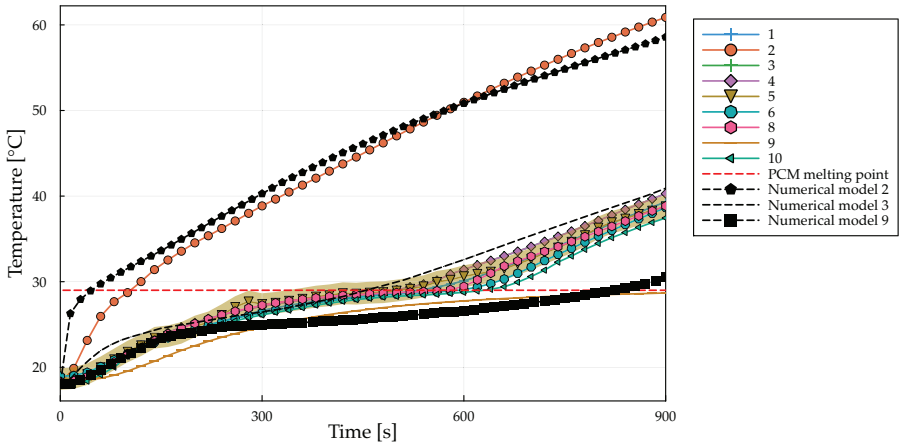

Fig. 4.29: Validation of the model for the thermophysical properties obtained comparing the experimental results for the top-orientation and a finite element homogenised numerical model for the f_2ccz unit cell.

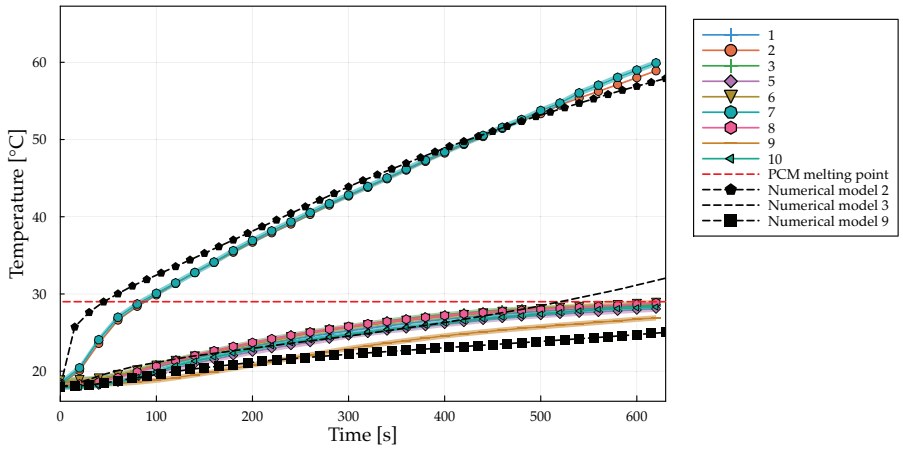

Fig. 4.30: Validation of the model for the thermophysical properties obtained comparing the experimental results for the top-orientation and a finite element homogenised numerical model for the *bcc* unit cell.

The model is in general very accurate in describing the thermal behaviour under a conductive regime. The maximum deviation is 8.58% and takes place at the beginning of the experiment, while the temperature curve develop with a mugh higher level of agreement.

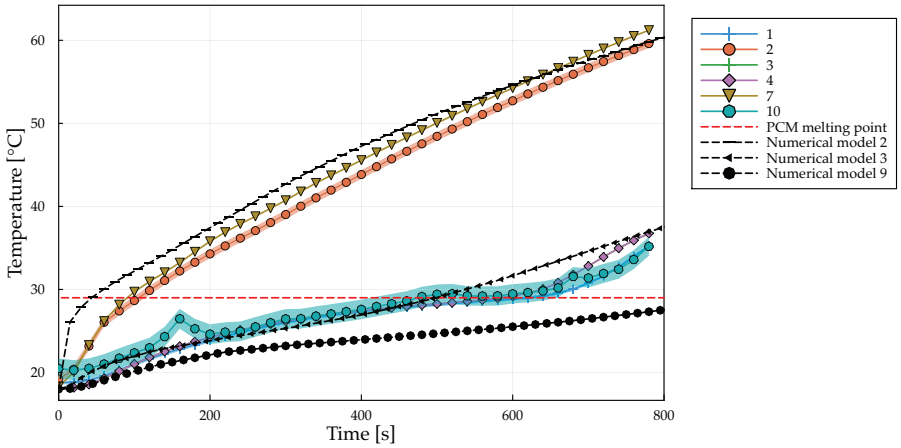

Fig. 4.31: Validation of the model for the thermophysical properties obtained comparing the experimental results for the top-orientation and a finite element homogenised numerical model for the *bccz* unit cell.

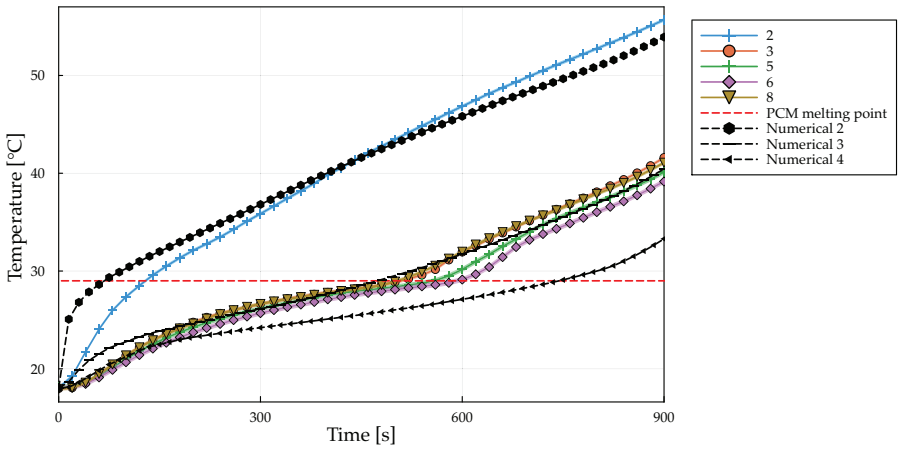

Fig. 4.32: Validation of the model for the thermophysical properties obtained comparing the experimental results for the top-orientation and a finite element homogenised numerical model for the $f2bcc$ unit cell.

4.2.3 Discussion

Having demonstrated that the model for the calculation of the effective thermophysical properties is valid, the assessment of the performance can be performed, for which the effective properties are needed. Initially, the wall overheating temperature, denoted as the temperature recorded by the sensor number 2, is normalized as follows.

$$\Theta = \frac{T_2 - T_{melt}}{T_{melt} - T_i} \tag{4.19}$$

where Θ is the non-dimensional wall overheating temperature, T_i is the experiment initial temperature, which in this campaign was fixed at 18°C, T_{melt} is the paraffin wax melting temperature and lastly, T_2 is the temperature of the sensor 2, corresponding to the heated wall temperature on the A-A side of the sample (as shown in Figure D.2). Subsequently, the Fourier number Fo and Stefan number Ste' are employed to quantify the transient heat conduction and the extent of latent heat absorption throughout the experiment. These parameters are determined based on the effective diffusivity of the composite material, which is obtained by employing the conductive model for effective thermophysical properties proposed above. The Fourier number is defined as

$$Fo = \frac{\lambda_{eff_3} t^*}{\rho_{\text{eff}} Cp_{\text{eff}} L^2} \tag{4.20}$$

where t^* is the characteristic time and L is the edge length of the sample. t^* is considered as $t^* = t = 635s$. This specific value represents the time it takes for the central sensors in the *bcc* sample, heated from the "top" orientation, to reach the melting point of the PCM. Notably, this duration is the longest time required for these sensors to attain the specified temperature. In contrast, for the same sensors in the other samples at various orientations and the *bcc* sample in different orientations, this threshold temperature is reached in a shorter amount of time during the experimental process. The revised Stefan number is formulated by taking into account the subcooling effect resulting from the initial temperature being lower than the melting point, as recommended by Groulx and Lacroix [132].

$$Ste' = \frac{Cp_{\text{eff}} (T_2 - T_{melt})}{h_{\text{eff}} + Cp_{\text{eff}} (T_{melt} - T_i)} \tag{4.21}$$

The non-dimensional temperature Θ is plotted against the ratio of the Stefan and Fourier numbers in Figure 4.33. This number is a ratio of time scales, specifically the Fourier number, which relates to the time it takes for heat to conduct through a material, and the Stefan number, which represents the latent heat absorbed or released during the phase change. This dimensionless number helps in assessing the relative importance of heat conduction and phase change heat storage. Indeed, a low value of the Ste'/Fo number can be attained if a low wall temperature is attained, as well as high thermal diffusitivity is characterising the sample. A low value of both Θ and Ste'/Fo indicate a good thermal control performance, i.e. a low wall temperature is obtained through to a high quantity of latent heat storage as well as a high thermal diffusivity.

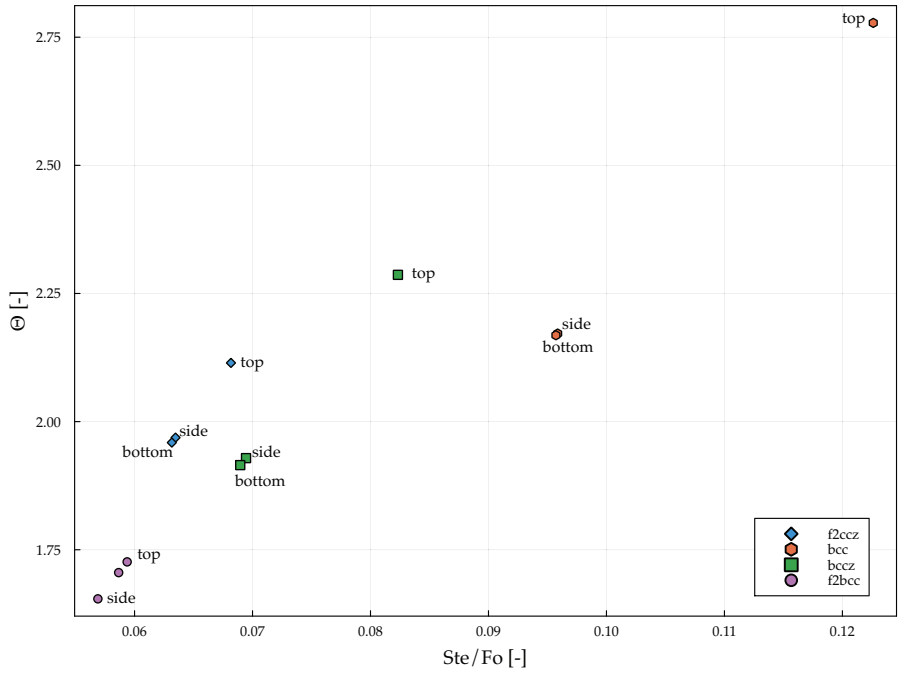

Fig. 4.33: Non-dimensional temperature Θ plotted against the Ste'/Fo' ratio.

One can thus see that, due to the low porosity, the sample f_2bcc performs the best. On the other hand, because the low thermal conductivity, the *bcc* at top heating orientation exhibits the highest values of both Θ and Ste'/Fo. The effect of natural convection on the thermal behaviour of these samples is evident. The same sample exhibits a lower Θ and, due to the presence of the wall temperature term also in the Stefan number, a lower Ste'/Fo. The effect is particularly strong for the *bcc* and the *bccz* samples, while, although still quantitatively relevant, reduced for the f_2ccz sample. The discussion on the effect of natural convection on the thermal behaviour is presented in Section 4.2.1 and is treated further in detail in Section 4.3. Keeping the goal of this work in mind, it is relevant to assess the thermal performance of the different samples also regarding their lightweight potential. Indeed, being the lattice structure made of material which is denser than the PCM, a low porosity affects negatively the mass of the composite sample. Thus, while the wall temperature attained for the f_2bcc sample is the lowest, this does not directly represent the best thermal performance when considering the system mass. To address this, the data shown in Figure 4.33 can be extended to a third dimension considering the volume fraction of the lattice χ, as shown in Figure 4.34. Figure 4.34 clearly shows that, although the f_2bcc sample exhibits the best thermal performance, this is due to the high volume fraction.
To properly address the thermal performance considering the lightweight potential, a novel index is introduced here, which makes the evaluation of the thermal performance more immediate. First, the median of both the volume fraction and of the Ste'/Fo numbers are calculated. Then, both the volume fraction and the Ste'/Fo are normalised dividing by their respective median value. This allows to compare both quantities without incurring in issues related to different

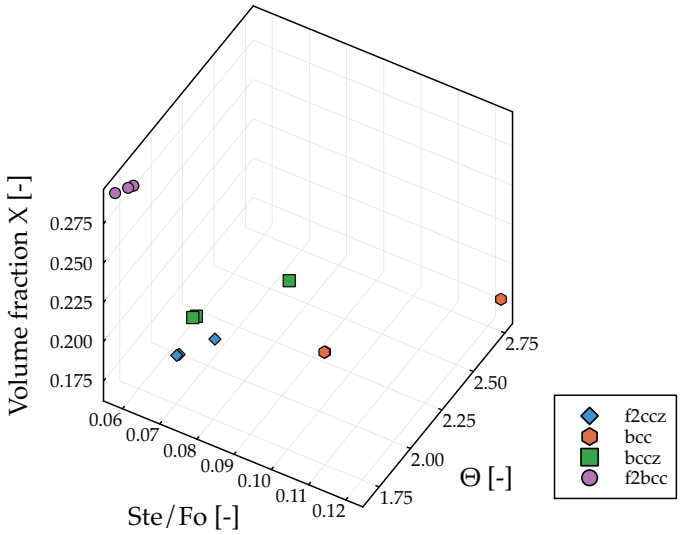

Fig. 4.34: 3D scatter plot showing the data already presented in Figure 4.33 with the addition of the volume fraction dependence.

orders of magnitude. Finally, the (mass) Specific Thermal Performance (STP) is calculated as described in Equation 4.22.

$$STP_i = \sqrt{\left(\frac{\chi_i}{\mathbb{M}\left[\chi\right]}\right)^2 + \left(\frac{Ste/Fo_i}{\mathbb{M}\left[Ste/Fo\right]}\right)^2} \tag{4.22}$$

The terms in Equation 4.22 are, from left to right,: STP_i the Specific Thermal Performance of the i-th sample, χ_i the volume fraction of the i-th sample, $\mathbb{M}\left[\chi\right]$ is the median of the volume fraction dataset, Ste'/Fo_i is the i-th Ste'/Fo number and $\mathbb{M}\left[Ste'/Fo\right]$ is the median of the respective dataset. There is no need to consider the wall temperature any further, as its effect is already considered in the Stefan number. The results can be then easily visualised in Figure 4.35, which shows a scatter plot of the calculated STP for each sample at each tested orientation. The optimal STP is achieved when the data points get close to the origin.

It is evident from the data presented in Figure 4.35 that the optimal STP is achieved when the samples display a combination of characteristics: a minimal increase in wall temperature, a high effective latent heat, and a high thermal diffusivity, thus resulting in a low Ste'/Fo ratio. Additionally, it is essential for the sample to possess a low volume fraction or, in other words, a high porosity. Due to these factors, it can be observed that the f_2bcc sample, while having the lowest Ste/Fo ratio, only offers a marginal advantage over the f_2ccz sample or the $bccz$ one when tested in the bottom/side orientation. Considering the volume fraction in the calculation of the thermal performance allows to identify unit cells that represent a combined optimum of lightweight and thermal behaviour. Thus, the best STP for this study is obtained by f_2ccz samples.

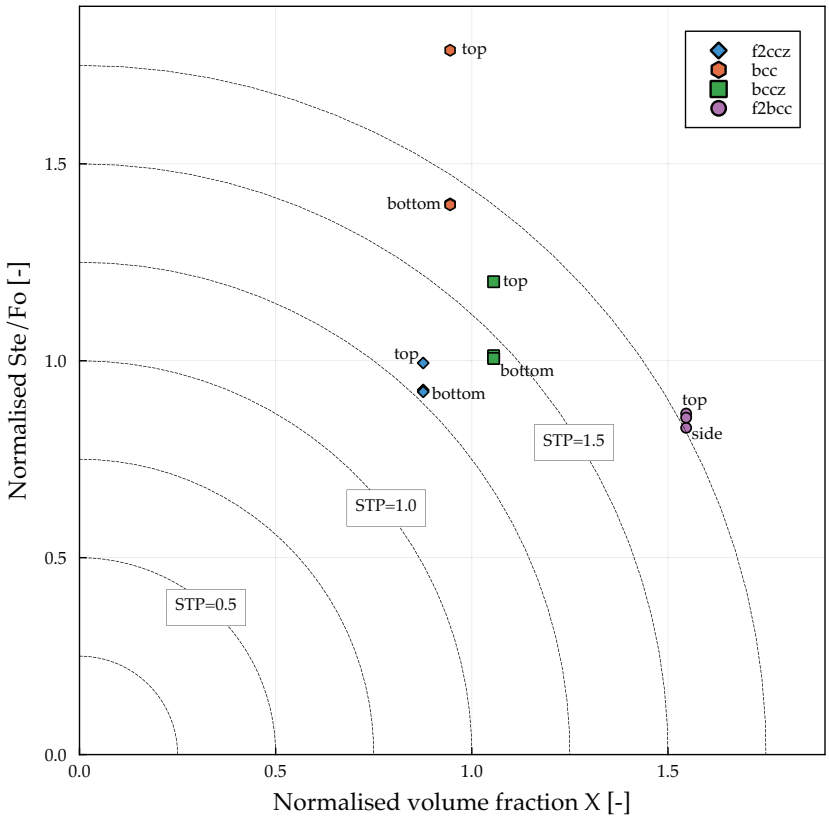

Fig. 4.35: Specific Thermal Performance (STP), obtained by comparing normalised volume fraction χ and Ste'/Fo ratio.

The results presented thus far all indicate that, when the component experiences a potential acceleration field (i.e., for static applications on Earth, the normal gravity acceleration) natural convection in the melt has a strong influence on its thermal behaviour.
However, while the sample f_2ccz exhibits the lowest number of PPI in z-direction and the highest porosity, the quantitative effect of natural convection on the thermal behaviour is not as high as for *bcc* or *bccz* unit cells. This can be related to the fact that the f_2ccz exhibits the specifically highest thermal conductivity. One can thus suppose that the conductive regime remains more dominant for these unit cells, and the transition to a purely convective regime is delayed.
For this reason, further efforts to mathematically describe the thermal behaviour under the occurrence of such phenomenon are presented in the upcoming Section 4.3.

4.3 Analysis of natural convection

This far, the assumption was made that the thermal behaviour of the composite is dominated only by conduction both in the solid and the liquid phases. The assumption is justified for composites based on cellular solids with small enough pores, i.e. metal foams with high number of PPI. However, in the previous section (4.2.1) of this work, it was shown that this assumption is mostly not valid for lattice structures of interest. The scale variance affecting the transient behaviour of the composite in a conductive regime (Section 4.1.2) is not the only scale-dependent effect. As well known in the literature ([83, 62, 65]), and discussed in Chapter 2, the effect of natural convection in the melt is not negligible if the heat flux orientation is either in the opposite direction or orthogonal to the direction of the local acceleration resulting from volume forces (i.e. in the case of static systems the local gravity acceleration). Natural convection is responsible for both a variation of the melting front shape and an acceleration of the melting front with respect to the case of a purely conductive regime. Furthermore, as shown in Section 4.2.1, the effect of natural convection on the wall temperature reduction is particularly strong, quantitatively more than what was presented this far in most literature about stochastic metal foams.
However, the orthotropic nature of the unit cells complicates the mathematical treatment of such composites.
To be able to analyse this phenomenon in detail, a novel framework for numerical investigation of thermal behaviour and fluid flow of the composite is needed. Investigations into additively manufactured lattice structures for use as porous media at high thermal conductivity in combination with PCMs are relatively recent, resulting in a limited available dataset of numerical and experimental analyses. To delve deeper in the analysis of this phenomenon, a solver capable of simulating the melting behavior of PCM-lattice composites is introduced. It is based on the *CoMeTFoam* solver developed by Schüller et al. [133], written in OpenFOAM®. The present solver adds an orthotropic Darcy-Brinkman term to the momentum equation, in order to model the fluid flow within the domain treated as a porous medium. The solver is based on the enthalpy-porosity method. The results achieved with this solver undergo a thorough validation process. First, a comparison with the results proposed by Iasiello et al. [83] is conducted,

before delving into the investigation of the lattice structures. Then, the results obtained for lattice structure samples are compared with the experimental data of Section 4.2.1. Finally, relevant analysis of the obtained numerical data allows to find useful correlations for future design purposes. This is based on the scaling theory proposed by Jany and Bejan [76].

Mathematical model

In Chapter 2, the modified conservation equations are introduced to account for the presence of metallic foams, and these very equations are employed here to model composites involving lattice structures. The main difference lies in the necessity to describe the effective thermal conductivity and the permeability with use of tensors, rather than scalars. To provide a comprehensive overview, these conservation equations are presented once more. The Boussinesq approximation allows to neglegt density changes, leading to:

$$\nabla \boldsymbol{u} = 0 \tag{4.23}$$

$$\frac{\rho_{PCM}}{\varepsilon}\left(\frac{\partial \boldsymbol{u}}{\partial t} + \frac{1}{\varepsilon}\nabla(\boldsymbol{u}\otimes\boldsymbol{u})\right) = -\nabla p + \frac{\mu_{\text{eff}}}{\rho_{PCM}}\nabla^2\boldsymbol{u} - \mathbf{g}\beta(T-T_m) - \frac{\nu_{PCM}}{\boldsymbol{K}}\boldsymbol{u} - C\frac{(1-\Phi^2)}{(\Phi^3+q)}\boldsymbol{u} \tag{4.24}$$

$$\begin{aligned}(\rho C_p)_{\text{eff}}\left(\frac{\partial T}{\partial t} + \boldsymbol{u}\,\nabla T\right) &= \nabla(\boldsymbol{\lambda}_{\text{eff}}\,\nabla T) - h_{\text{eff}}\left[\frac{\partial \Phi}{\partial t} + \boldsymbol{u}\nabla\Phi\right] \\ &\quad + T_m\left[\frac{\partial(\rho C_p)_{\text{eff}}}{\partial t} + \nabla((\rho C_p)_{PCM}\,\boldsymbol{u})\right]\end{aligned} \tag{4.25}$$

where ν_{PCM} is the kinematic viscosity of the fluid. The terms and variables present in the equations are introduced in Chapter 2. The main difference lies in the notations of the therms $\mathbf{K}$ and $\boldsymbol{\lambda}_{\text{eff}}$ which are now represented by tensors rather than scalar quantities, in order to consider the orthotropic nature of these composites. The formulation of the equations was predicated on the assumption of thermal equilibrium. Within the scope of this assumption, solving a singular energy equation proves sufficient, leading to notable computational time and resource savings. Furthermore, it's important to acknowledge the current lack of available data pertaining to heat transfer coefficients from lattice structures to the surrounding fluid within this specific application, as far as the author's knowledge extends.
For sake of brevity, further details on the material model and the algorithm implementation can be found in Appendix F.
To properly describe the motion of the fluid in the porous medium, the calculation of the permeability tensor $\mathbf{K}$ and of the effective Brinkman-viscosity μ_{eff} is of paramount importance.

The first is discussed in detail in Section 4.3.1. The second is discussed in Section 4.3.2.

4.3.1 Permeability

Similar to the effective thermal conductivity, the permeability of lattice structures is, in general, orthotropic, i.e. it can be described by the tensor **K**:

$$\mathbf{K} = \begin{bmatrix} K_{x,y} & 0 & 0 \\ 0 & K_{x,y} & 0 \\ 0 & 0 & K_3 \end{bmatrix} \tag{4.26}$$

The permeability of the lattice structures is determined via numerical modelling. Simulations for assessing permeability are carried out employing the open-source software *OpenFOAM*®v9. The simulations are based on a model representing an incompressible fluid with constant density and viscosity, while assuming fully developed flow conditions. The computational task employs the *simpleFoam* solver, which is utilized to solve the Navier-Stokes equations, using the Semi-Implicit Method for Pressure Linked Equations (SIMPLE) scheme:

$$\nabla \boldsymbol{u} \;=\; 0 \tag{4.27}$$

$$\nabla(\boldsymbol{u} \otimes \boldsymbol{u}) \;-\; \nabla \mathbf{R} \;=\; \nabla p \;+\; S_u \tag{4.28}$$

where, p stands for the kinematic pressure, $\boldsymbol{u}$ for the velocity, $\mathbf{R}$ for the stress tensor, and S_u for the momentum source.
Due to the complex geometry, a wide amount of cells within the mesh is needed to appropriately describe the fluid flow across such structures. To reduce the computational effort, the periodicity of lattice structures is exploited. Thus, a single column of stacked unit cells can be employed, imposing symmetry boundary conditions on the outer faces of the domain. For all unit cells except *bcc*, the simulations are conducted both with inlet flow incoming from the z-direction and from 1 or 2 one. To simplify operations, the domain always has the same inlet and outlet, but the unit cells are turned by 90°. Figure 4.36 shows schematically the domain and the boundary conditions. A velocity boundary condition is imposed on the inlet, at the left side of the domain, and a static pressure boundary condition, conveniently put equal to 0, is imposed on the outlet. Symmetry is imposed on the left, right, top and bottom side walls, while a no-slip condition is imposed for all other walls, i.e. the walls of the lattice structure. Around these walls, boundary layer mesh elements are built, as shown in Figure 4.37.

In a Darcy-flow, the permeability can be easily calculated via Equation 4.29:

$$K_i = \frac{q_i \mu \Delta L}{\Delta p}, with i = x, y, z \tag{4.29}$$

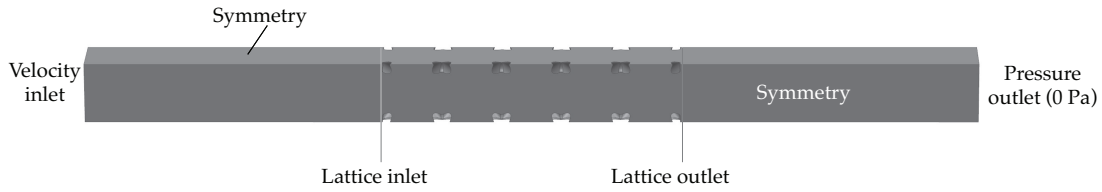

Fig. 4.36: Domain for the CFD model used to calculate the permeability of the lattice structures.

where q_i is the mass flux, μ is the dynamic viscosity, Δp is the pressure loss over the length ΔL. The index i represents the orientation. Consider that the x and y directions are equivalent. The permeability is a property of the geometry only, thus it is independent from the kind of fluid flowing within the domain. Taking advantage of that, the permeability can be efficiently calculated, by considering a highly viscous fluid and a low inlet velocity. This is necessary because the permeability can be determined via application of Darcy's law only as long as the flow lies in a Darcy regime. Such regime can be assumed valid as long as the flow is slow enough for viscous forces to be dominant, i.e. it is valid for Reynolds number $Re << 1$. To maintain the Re well below one, a fictitious fluid is considered, with the properties listed in Table 4.6.

Table 4.6: Properties of the fluid considered to calculate the permeability

Property	Value
Density ρ	$1000\,\mathrm{kg\,m^{-3}}$
Dynamic viscosity μ	$1\,\mathrm{Pa\,s}$
Kinematic viscosity ν	$110^{-3}\mathrm{m^2\,s^{-1}}$

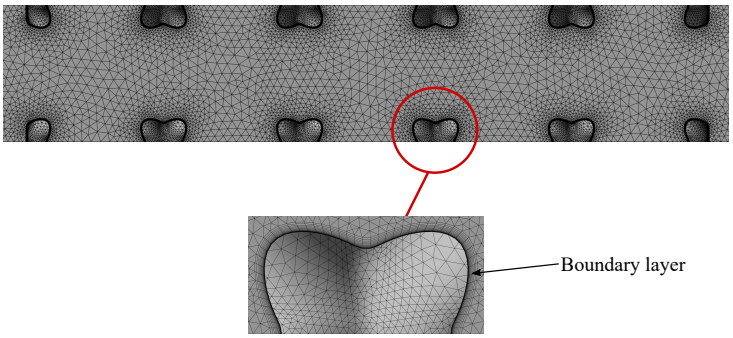

Fig. 4.37: Section of the mesh from the *bcc* unit-cell.

A mesh-convergence study is performed, in order to minimize the computational effort while achieving numerically accurate results. The convergence threshold for both pressure and velocity variables was chosen to be 10^{-8}.
For the first convergence study the number of elements in the mesh is varied. Initially, 0.4 mm is chosen as the maximum element size. This value is then reduced to analyse the impact on the

permeability. A boundary layer with 16 layers and a first layer thickness of 10^{-6} m is chosen. The influence of the number of unit-cells is also investigated, as shown in Figure 4.38. Here, the number of unit-cells is varied from 3 to 20. Since the number of unit-cells has a huge impact on the simulation time, the tolerance to the most accurate result is increased to 1.5 %. Since an increase in the number of unit cells considered to calculate the permeability causes a linear increase of the computational time, the amount of unit cells considered is fixed at 5 for all further permeability investigations.

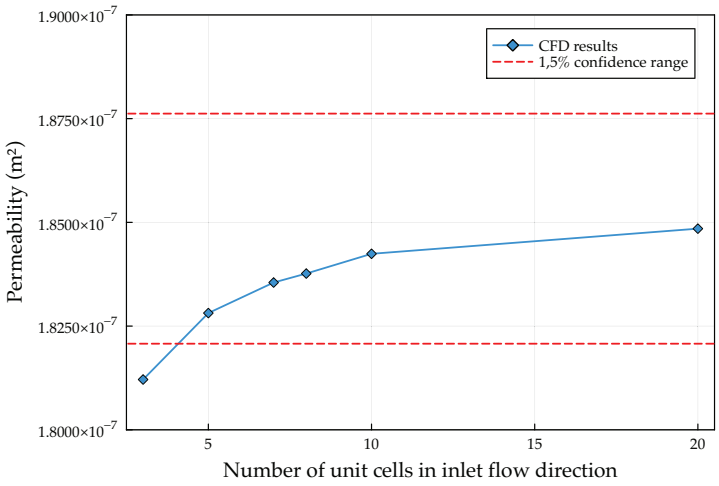

Fig. 4.38: Convergence plot of the calculated permeability for increasing amount of unit cells in the direction of the inlet flow.

A check for physical plausibility is performed as well. As previously explained, as the velocity of the fluid within the porous medium increases, the relationship between the pressure drop across the medium and the Darcy velocity starts to deviate from a linear one. Forchheimer or Brinkman terms must be introduced ([81]) to mathematically describe such relationship. The deviation from a linear relationship when approaching $Re = 1$, as shown in Figure 4.39, indicates that the results are physically plausible and can be considered correct until further experimental validation.

Figure 4.41 shows the results of the permeability, in each direction, of the sample tested within the experimental campaign of Section 4.2. One can notice that the permeability in the z-direction is higher than the one in x,y-direction for all samples, except the *bcc* one, which is isotropic. In particular, the f_2ccz sample exhibits a permeability in z-direction that is more than twice higher than the x,y-direction. This is due to the fact that face-centered struts are placed on the outer faces of the unit-cell's geometry. Thus, channel-like pores are built within the inner volume of the unit cell. On the contrary, body-centered unit cells show a higher flow resistance in any direction. The samples in Figure 4.41 are ordered from, left to right, in order of decreasing porosity, i.e. f_2ccz is the most porous and f_2bcc is the least. A clear correlation

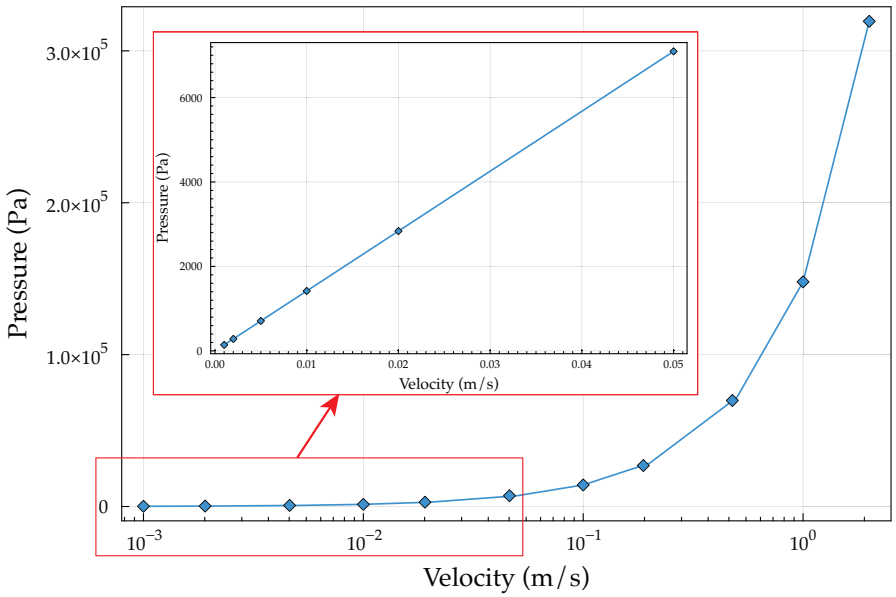

Fig. 4.39: Variation of the pressure loss across the f_2ccz sample, in x,y-direction, plotted against the inlet velocity of the fluid.

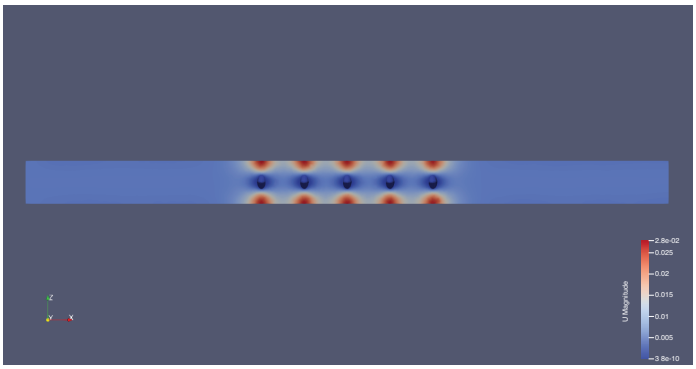

(a) Velocity profile, with inlet velocity equal to 5 mm/s

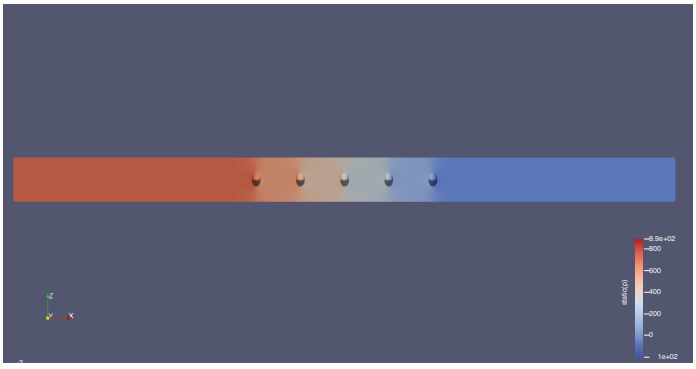

(b) Static pressure profile, with inlet velocity equal to 5 mm/s

Fig. 4.40: Velocity and static pressure profiles for a f_2ccz sample with flow in x,y-direction and inlet velocity 5 mm/s.

between permeability and porosity can be identified. More porous unit-cells exhibit, as obvious, higher permeability. However, for these samples, this effect is coupled with the different topology, which affects a quantitative comparability. Ekade and Krishnan [134] proposed a

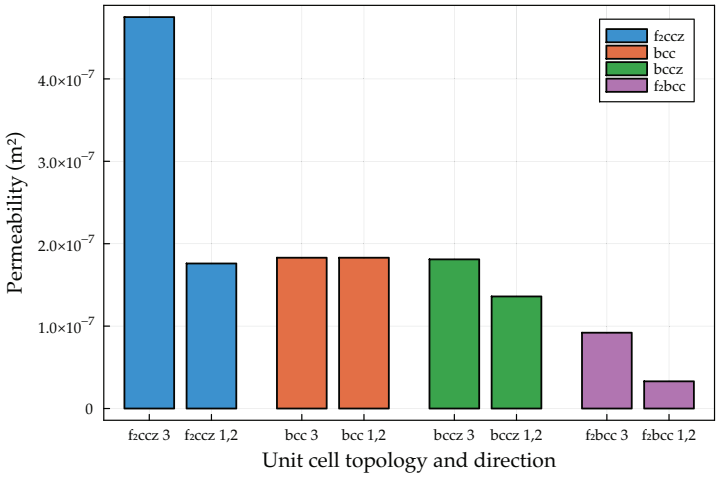

Fig. 4.41: Permeability of each unit cell considered in the experimental campaign of Section 4.2

correlation for octet-truss lattices by normalising the permeability with the square of the strut diameter. One should consider that the geometries that they analysed all showed different cell sizes, thus it is not possible to separately analyse whether a variation of the permeability is given by a variation of the porosity or a variation of the unit cell size. Figure 4.42 proposes the results shown in Figure 4.41, normalised with the same methodology proposed by the two authors, and compared with the very same results proposed by them. One can notice how the results in general lie within the same quantitative range as what suggested by Ekade and Krishnan [134] for octet trusses. However, while the scale variation is somehow accounted for by normalising the value of the permeability with the square of the strut diameter, the unit cell size is not directly considered. One can notice that most of the results presented in this work lie slightly under the ones for octet truss lattices. If one would consider only the porosity and the strut diameter as a geometrical factor, this would result counterintuitive, as octet truss lattices exhibit more struts within the unit cell than the lattices considered in this work. Because of this, a higher tortuosity, and thus a lower permeability would be expected. The reason for this discrepancy can be found considering that the unit cell sizes considered by Ekade and Krishnan are all bigger than the ones considered in this work, thus positively affecting the pores size and consequently the permeability.
To further investigate this aspect, an additional numerical investigation is performed. The goal is to decouple the variation of the porosity from the variation of the unit cell and of the cell size. Thus, using the relationships proposed in Section 3, a new set of probes is considered, whose properties are reported in Table 4.7.

The porosity is fixed for all samples so that it can be excluded as a parameter. The same cell sizes are considered for both topologies. Thus, the only parameter that remains relevant is the

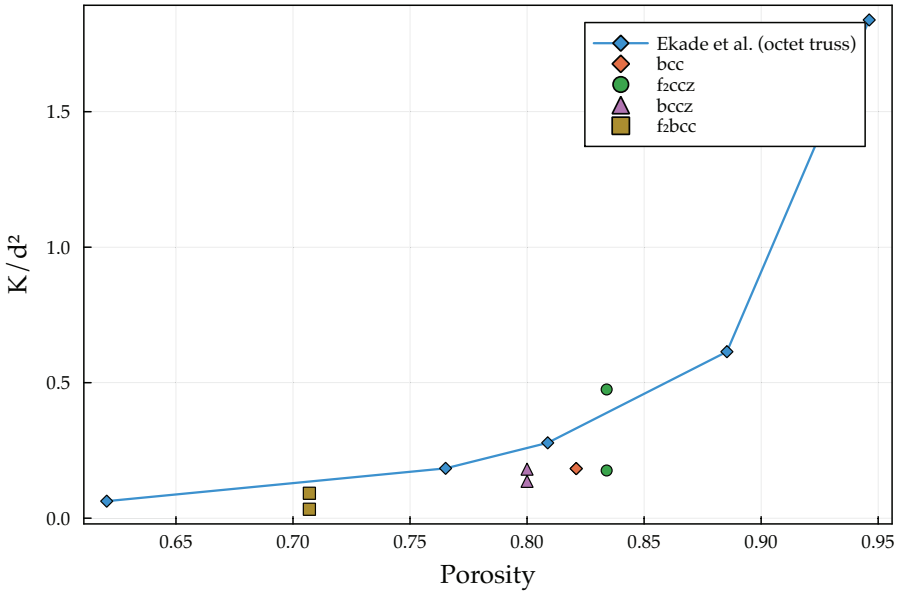

Fig. 4.42: Normalised permeability against porosity of the samples, as proposed by Ekade and Krishnan [134].

Table 4.7: Geometry of the samples considered for the investigation of the permeability, decoupled from the porosity.

Cell topology	Cell size h [mm]	Strut diameter d [mm]	Porosity ε
bcc	5	0.747	0.9
bcc	10	1.494	0.9
bcc	25	3.735	0.9
f_2ccz	5	0.727	0.9
f_2ccz	10	1.454	0.9
f_2ccz	5	3.635	0.9

strut diameter, or its ratio with the cell size.
With the same methodology described above, the permeability is calculated via a numerical investigation. The results are reported in Table 4.8 and in Figure 4.43.

Table 4.8: Permeability values for the samples considered with a fixed porosity of $\varepsilon = 0.9$.

Sample	Permeability in x,y-direction $K_{x,y}$ [m^2]	Permeability in z-direction K_3 [m^2]
bcc, h=5mm	2.8610^{-7}	2.8610^{-7}
bcc, h=10mm	1.1410^{-6}	1.1410^{-6}
bcc, h=25mm	7.1310^{-6}	7.1310^{-6}
f_2ccz, h=5mm	2.7310^{-7}	6.2210^{-7}
f_2ccz, h=10mm	1.0810^{-6}	2.4910^{-6}
f_2ccz, h=25mm	6.7810^{-6}	1.5510^{-5}

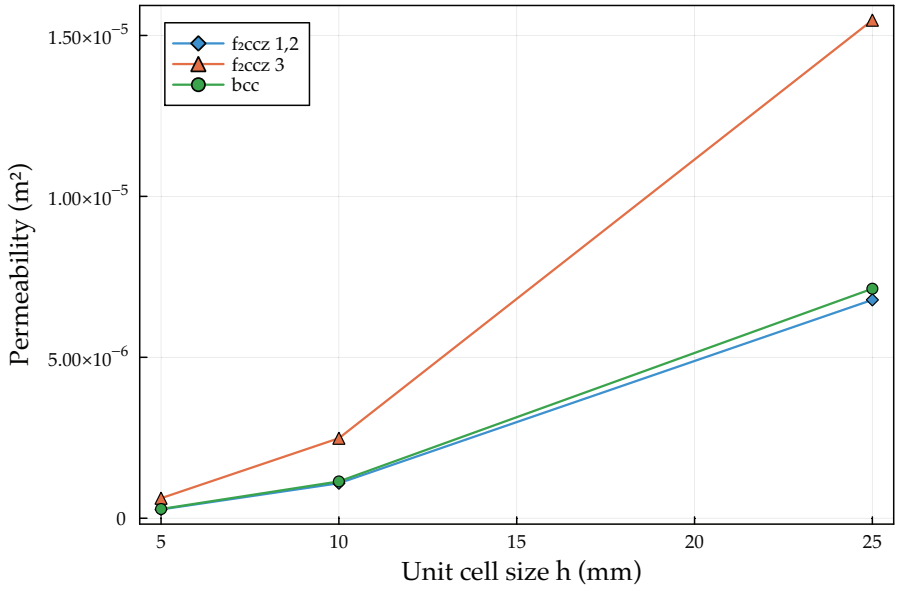

Fig. 4.43: Permeability plotted against the unit cell size of the samples, which exhibit the same porosity $\varepsilon = 0.9$.

It can be noticed that the permeability has a quadratic relationship with the unit cell size, i.e. scale variance is present. Similarly to what proposed by Ekade and Krishnan [134], a normalisation can be proposed. However, it is more meaningful to normalise the value by considering the hydraulic diameter of the unit cell, rather than the of the strut diameter as suggested by the authors. This way, the results indicate a measure of the flow resistance with respect to the cross section of the channel created by treating each single unit cell as a separated entity. Thus, it represents a description of the hydraulic conductivity in relationship to the maximum possible

mass flow. Equation 4.30 describes the calculation of the ratio proposed, where K_i is the generic permeability of a unit cell, in direction i, D_H^2 is the hydraulic diameter, V_{cell} is the volume of the unit cell,i.e. for a cubic cell the third power of the cell size, $Aout_{lattice}$ is the surface area of the lattice structure, which is calculated via CAD measurement.

$$\frac{K_i}{D_H^2} = \frac{K}{\left(\frac{V_{cell}}{Aout_{lattice}}\right)^2} \tag{4.30}$$

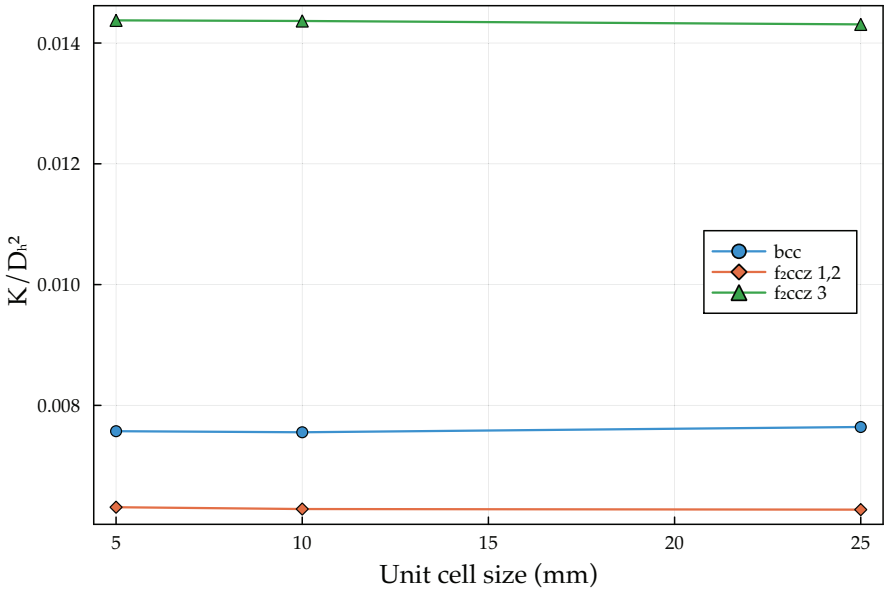

Fig. 4.44: Normalized permeability plotted against the unit cell size.

Figure 4.44 shows the results obtained from Equation 4.30. It is interesting to notice that the ratio K/D_H^2 is constant for varying cell size. This indicates that the permeability is a scale variant property of the cell geometry, but it is directly proportional to the cell size. Thus, if the permeability for a given unit cell is known, scaled values can be obtained through Equation 4.31.

$$K_{i_1}(\varepsilon = \varepsilon^*, h_1, \gamma = \gamma^*, r_1) h_1^2 \sin\gamma^* = K_{i_2}(\varepsilon = \varepsilon^*, h_2, \gamma = \gamma^*, r_2) h_2^2 \sin\gamma^* \tag{4.31}$$

where the geometric variables were introduced in Section 3, and the * symbol is used to indicate that the topology is fixed for both unit cells, thus only the cell size and the strut radius may vary. In Equation 4.30 the lattice surface area is used, while in Equation 4.31 the cell frontal area. One could argue that they are not the same. However, these are unequivocally related to each other through the geometric description of the unit cell given in Section 3. Thus, the ratio of surface areas for scaling unit cells is the same as the ratio of the frontal areas, identified as h_2^2/h_1^2.

To the author's knowledge, the described scale variance relationship was not yet presented in

the literature.
The permeability calculated in this section can be used further as a geometric property of the homogenised lattice-PCM composite.

4.3.2 Solver verification and validation

Convergence

To eliminate the need to manually determine the appropriate time step based on the spatial step, OpenFOAM has the capability to automatically adapt the time step to match specific conditions. Within this process, the Courant number is calculated at each time step, and subsequently, the time step magnitude is modified accordingly.
Additionally, employing a high-resolution mesh is crucial to accurately depict the numerical problem. Previous studies, like the one conducted by Iasiello et al.[83] found that a 100x100 element mesh provided sufficiently accurate results. However, to ensure the precision of the present study, a convergence analysis is undertaken to ascertain if the mesh resolution used adequately represents the problem. Given the rectangular domain, a structured grid comprising square elements is employed. Meshes of varying resolutions—200x200, 300x300, 400x400, and 500x500 elements— are evaluated in this convergence study. The simulations are carried out on a computing cluster, facilitating the execution of simulations involving high-resolution meshes within a reasonable timeframe (less than 24 hours). Figure 4.45 is obtained by performing simulations on the *bcc* sample considered in the experimental campaign (Section 4.2). The simulations are carried out for a convective case with an arbitrary heat flux of 11.000 $\mathrm{W/m^2}$ from the bottom side. A mesh-convergence is achieved for 200x200 elements.

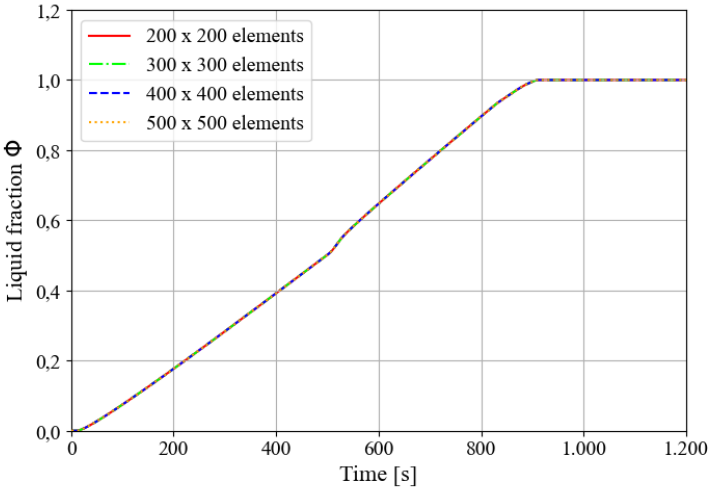

Fig. 4.45: Convergence study for different numbers of mesh elements for the *bcc* unit-cell.

Validation

In the following, a complete validation is presented. The solver is first validated against present literature, in particular against the experimental and numerical results presented by Iasiello et al. [83]. The authors made use of a metal foam as a porous medium in which the PCM was embedded. The solver introduced here is capable to handle foams as well, which represent the special case of lattices with isotropic permeability and thermal conductivity. Furthermore, the solver is also validated against the experimental results presented in Section 4.2.

Comparison with the literature In contrast to the solver developed here, the simulations presented in [83] were carried out under the premise of local thermal non-equilibrium (LTNE). For LTNE, the approach involves solving two distinct energy equations, one for the phase change material (PCM) and the other for the matrix. This method is theoretically expected to provide a more precise representation of real-world conditions. Their investigation involved the examination of various foams with different porosities and pore densities. Specifically, a foam possessing a porosity of 0.88 and 40 pores per inch (PPI) was chosen for validation purposes.

Within their study, a heat flux of 1.152 W/cm^2 was initiated from one side. The impact of convection was evaluated by applying the heat flux separately from the bottom and the side. Material parameters used in their simulations are detailed in Table 4.11. The effective thermal conductivity and permeability values were determined using the formulations outlined in the work from Iasiello et al. [83] and mixing laws. The calculated values are available in Table 4.11. To validate the solver, the advancement of the melting front, i.e. the liquid fraction, is compared. This comparison is conducted for two different heating directions: one from the bottom and another from the side. Beginning with the evaluation of the bottom orientation, the progression of the melting front is compared at two specific time points: $t^* = t - t_m 240s$ and $t^* = t - t_m = 480s$ after the onset of melting. Figure 4.46 displays the outcomes, with the results from Iasiello et al. [83] presented first (a), followed by the findings from this investigation (b).

Table 4.9: Material properties of the used materials in the simulations of [83].

Properties	PCM, liquid	PCM, solid	Foam
Density ρ [kg/m^3]	850	850	2700
Heat capacity c_p [J/kgK]	2490	2490	900
Thermal conductivity λ [W/mK]	0,15	0,20	220
Dynamic viscosity μ [Pa s]	$3,8510^{-3}$		
Thermal expansion coefficient β [1/K]	$7,7810^{-4}$		
Melting temperature T_m [K]	330,15		
Latent heat h [kJ/kgK]	185		

Table 4.11: Calculated effective properties of the used materials in the simulations of [83]

Properties	Value
Effective density ρ_{eff} [kg/m^3]	1072
Effective specific heat capacity $C_{\text{p,eff}}$ [J/kgK]	2009,44
Effective thermal conductivity λ_{eff} [W/mK]	8,47 (liquid) 8,52 (solid)
Effective permeability K [m^2]	3,99 10^{-8}

Upon comparing the melting front's evolution and its structure at both time points in Figure 4.46, a significant resemblance is observed. Evaluating the areas of the molten region, the results from this study show a deviation of 6.24% after 240 seconds and 3.64% after 480 seconds. Although, small, these discrepancies can be caused by the different thermal equilibrium assumptions and by the different Mushy zones assumed, namely a ΔT of 1 K for the reference work [83], whereas this study uses a ΔT of only 0.5 K. Consequently, the mushy zone is smaller in this investigation, resulting in a larger area where the liquid fraction equals one.
A similar conclusion emerges when analyzing the side heating case. The progression and form of the melting front exhibit remarkable similarity. After 240 seconds, the maximum deviation in melted surfaces is 10.74%, reducing to 3.82% after 480 seconds.

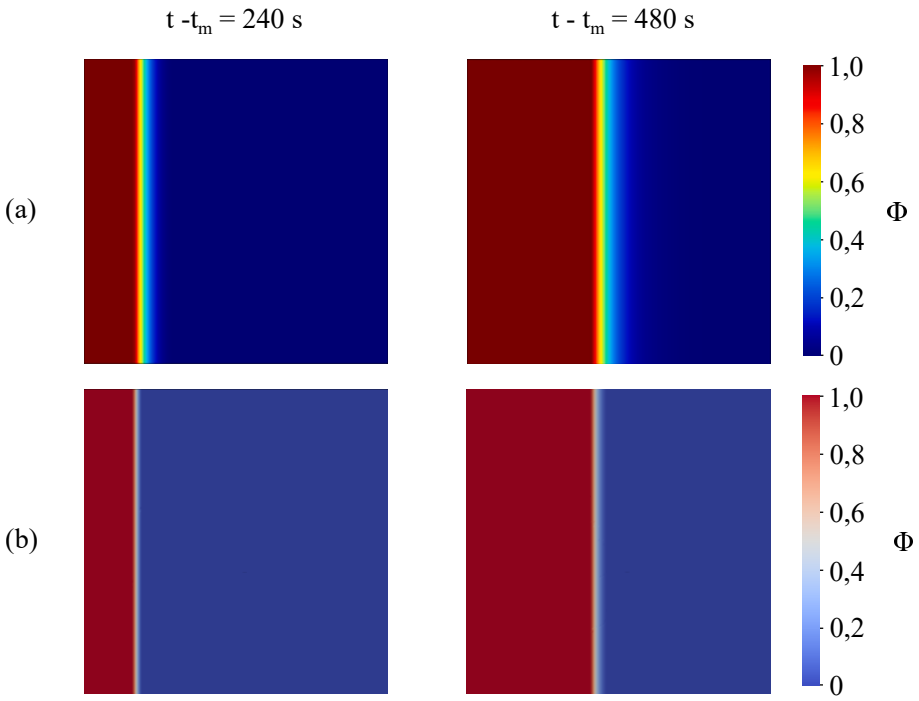

Fig. 4.46: Melting front evolution for a bottom-heated case: (a) the results of Iasiello et al. [83] (reproduced with consent from Elsevier®); (b) the results obtained from the presented solver.

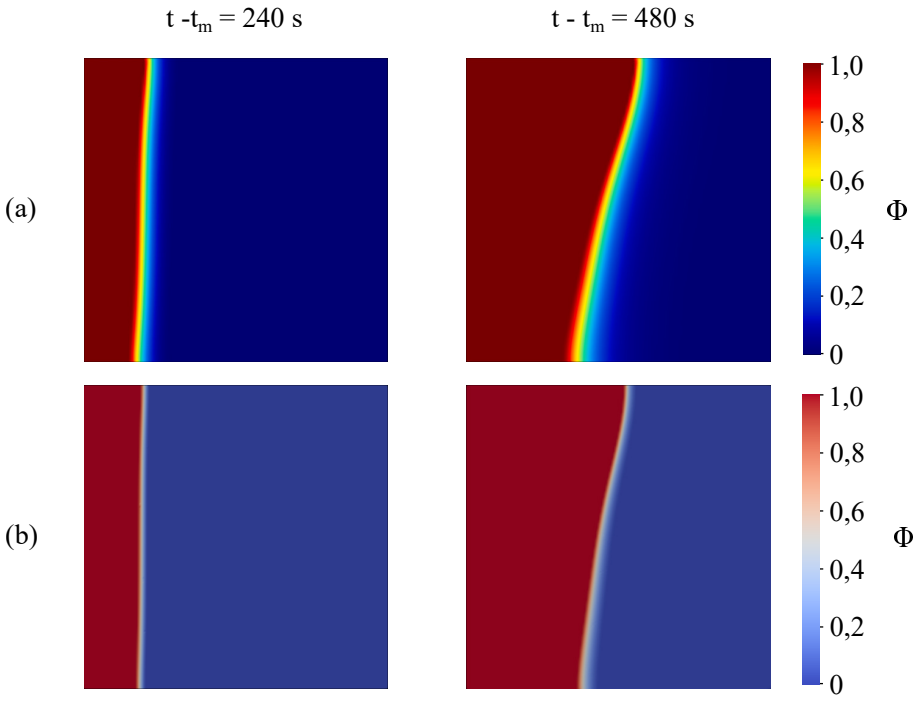

Fig. 4.47: Melting front evolution for a side-heated case: (a) the results of Iasiello et al. [83] (reproduced with consent from Elsevier®); (b) the results obtained from the presented solver.

Validation against the experimental campaign The goal of the solver introduced in this work is to present a tool capable to simulate the behaviour of a PCM composite with, in general, orthotropic topology. To demonstrate this, a comparison of the simulation results with the experimental results presented above is discussed.
The boundary conditions imposed during the experiments are reproduced in the simulation environment. The effective thermophysical properties are described in Section 4.2.1. Moreover, the introduction of heat flux into the setup, facilitated by a heating plate and an intermediate layer between the heat source and lattice structure, causes a delay in the initial heating of these sections, leading to distortions in the temperature curves. Figures 4.48 and 4.49 show the temperature curves and the melting front position of both the experiment and the simulation, for the top orientation of the f_2ccz sample. The melting front for the experiment is acquired via IR imaging as described in Section 4.2. The same data for other samples are reported in Appendix E. In general a good agreement between the solver solution and the experimental results can be found for all samples heated at top orientation. This once again validates the formulae proposed for the effective thermophysical properties (Section 4.1.3). The melting front is straight and it shows that no convective effect is present for top heating orientations.

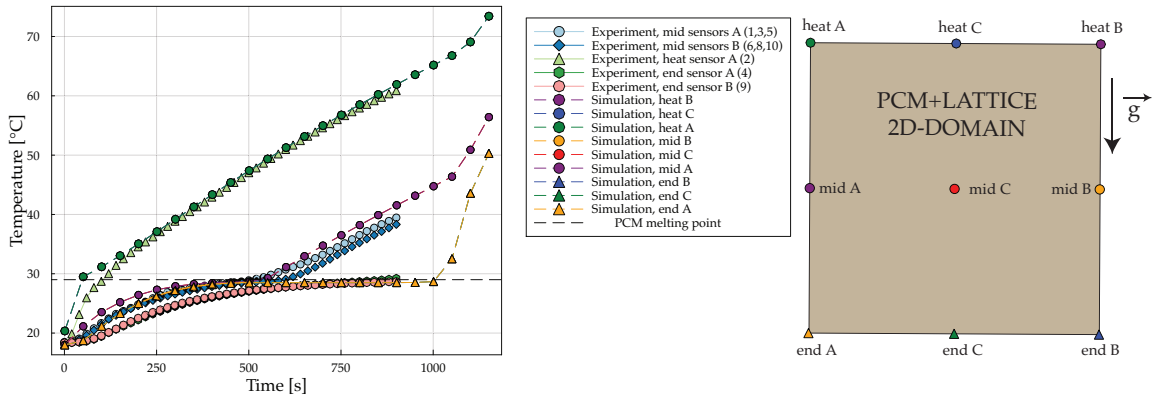

Fig. 4.48: Comparison of the simulation results with the experimental campaign: f_2ccz sample, top orientation. The simulation data have dashed lines. The position of the simulation probes is reported and corresponds to the position of the sensors in the experimental campaign. The central sensors are averaged among each other.

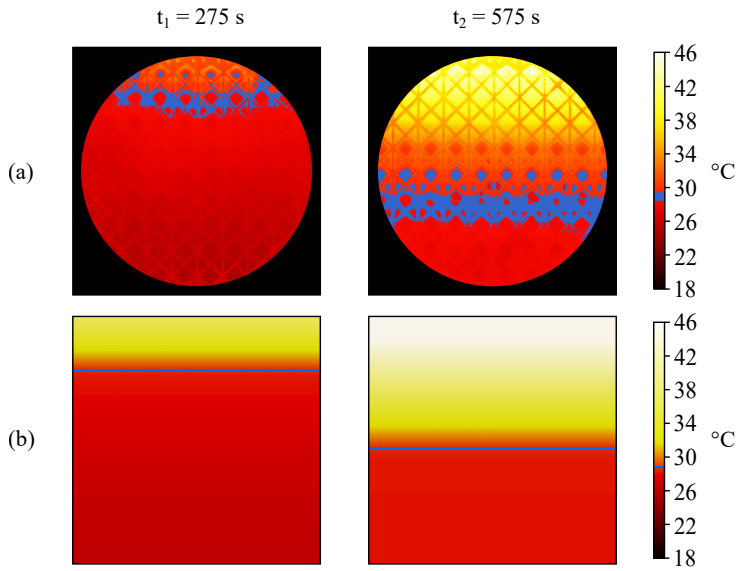

Fig. 4.49: Temperature distribution of experiments (a) and simulations (b) for a f_2ccz unit-cell, top heating orientation.

Effective Brinkman viscosity Before discussing the validation of the results for other orientations it is necessary to discuss the estimation of the effective Brinkman viscosity μ_{eff}, as it affects the accuracy of the results. As mentioned in Section 2.3, the value of μ_{eff} for a given geometry is a matter of debate in the literature. Often, either the Einstein's or Brinkman's model (Equations 2.32 and 2.33) are used. These strongly differ from each other, as shown in Table 4.13.

Due to the lack of established data regarding porous media like a lattice structure, the value of

Table 4.13: Comparison of the effective viscosity models for the considered n-Octadecane PCM, with dynamic viscosity $\mu = 3.210^{-3} Pas$.

Sample	Porosity ε	Einstein $[Pas]$	Brinkman $[Pas]$
bcc	0.821	1.2210^{-2}	0.29
$bccz$	0.8	1.2010^{-2}	0.22
f_2ccz	0.834	1.2310^{-2}	0.35

μ_{eff} is estimated via a parametric study, and by comparing the results of the simulations with the experimental data. The value of μ_{eff} is varied within the range of the values reported in Table 4.13. Using the values from the Brinkman's model inhibits the occurrence of natural convection within the domain. This can be appreciated from the temperature curves obtained, which align with the one obtained from the top heating orientation. The implementation of the Einstein's model, instead, delivers accurate results, which can be validated for the side heating orientation, as one can exemplarily appreciate in Figure 4.50 for the bcc sample. The same results for the

bccz and f_2ccz samples are reported in Appendix E.

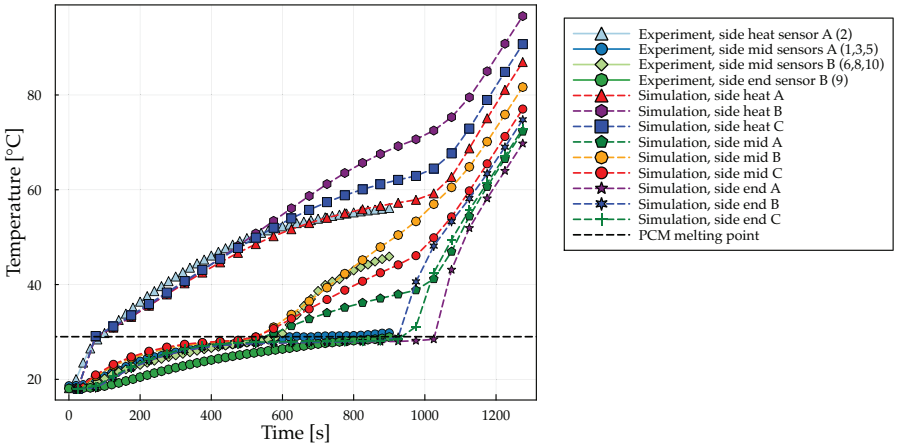

Fig. 4.50: Comparison of the simulation results with the experimental campaign: *bcc* sample, side orientation. The simulation data have dashed lines. The position of the simulation probes is reported and corresponds to the position of the sensors in the experimental campaign. In the experimental campaign the central sensors are averaged among each other.

For the bottom heating orientation, a good agreement is more challenging to obtain, as depicted in Figure 4.51. A similar trend can be appreciated for the *bcc* and *bccz* samples, which are

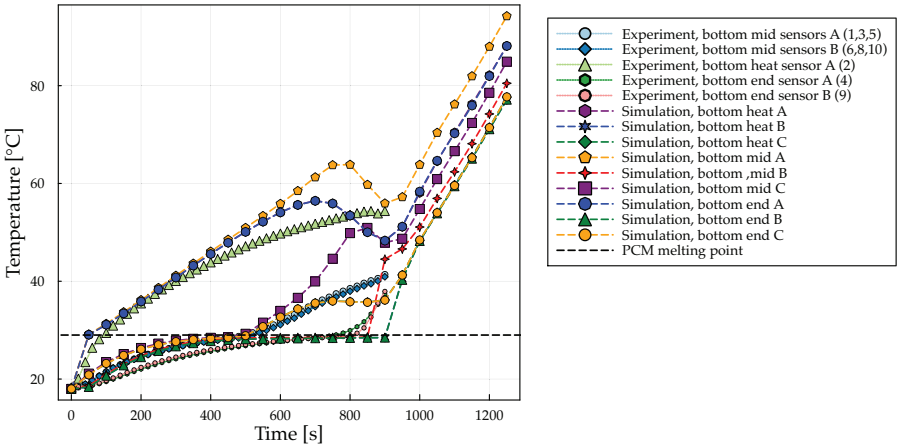

Fig. 4.51: Comparison of the simulation results with the experimental campaign: f_2ccz sample, bottom orientation. The simulation data have dashed lines. The position of the simulation probes is reported and corresponds to the position of the sensors in the experimental campaign. In the experimental campaign the central sensors are averaged among each other.

reported in Appendix E.
As one can notice, soon after the onset of convection the temperature curve relative to the C sensors starts to deviate from the A and B sensors. This cannot be verified by the experimental

data, as sensors are available only at A or B location. Furthermore, the sensors A and B at each location deviate from the experimental data, exhibitng a wavy pattern. It is thus necessary to delve deeper in the analysis of such results.
To do so, it is necessary to consider the fluid flow within the porous medium and the melting front expansion after the onset of convection. The results are compared qualitatively with the IR frames of the experiments in Figure 4.52 for the f_2ccz sample.
One can notice that, after the conduction dominant regime, the fluid starts to move within the porous medium. This is evident in the simulation data, as the melting front starts to deviate from a straight line. Such a pattern, however, cannot be appreciated in experimental data.
The origin of the deviation of the simulation data can be understood by visualizing the fluid velocity and temperature plots of the simulation, shown in Figure 4.53b. In the simulation, the melting front starts to expand following the shape of Rayleigh-Benàrd convective cells. In the considered case, four vortices are first built. As the simulation time advances, with the increasing amount of molten material, the fluid gets faster and the cells coalesce in two vortices, with a chaotic fluid motion, causing the temperature drop shown in Figure 4.51. Once the coalescence period is over, a stable front expansion with two vortices proceeds, as shown in Figure 4.53b for t=800s.

The described effect cannot be evidenced in the experiments. This macroscopic discrepancy can be ascribed to several reasons, the main one being the homogenisation technique chosen. The solver here presented is based on the assumption that the porous medium can be considered as a homogeneous material, with effective properties. The Darcy-Brinkman term with use of Einstein's effective viscosity is not able to appropriately take into account the fluid flow conditions within the porous medium. This might be attributed to the orthotropic geometry of the lattice structure, which is not considered in the calculation of the scalar effective viscosity. Indeed, in directions opposite to the heat flux, the lattice structure of the f_2ccz sample is less permeable than in the direction of the heat flux. While this is considered for the linear Darcy-term via the permeability tensor, it is not considered for the Brinkman term.
However, the method demonstrated to deliver accurate estimations of the fluid flow behaviour for the side heating orientation, as shown in Figure 4.50. This discrepancy requires further investigations.
While the convective movement of the fluid does take place and convective cells are built, their size and stability depends on the unit cell size and topology. Indeed the melting fronts for all bottom heating orientations tend to be rather horizontal, as shown for the $bccz$ unit cell in Figure F.6 and for all samples in AppendixE. One can conclude that the magnitude of the convective movement is affected by the homogenisation technique employed and by the permeability of the sample. This is particularly evident when considering highly orthotropic samples like the f_2ccz one. For other samples, such as the $bccz$ one, the results of the simulation are in good agreement with the experimental data, as shown in Figure F.6. In such case, the liquid fraction $\Phi = 1$ is reached at the same time for both the experiment and the simulation, indicating a good predictability given by the present solver.

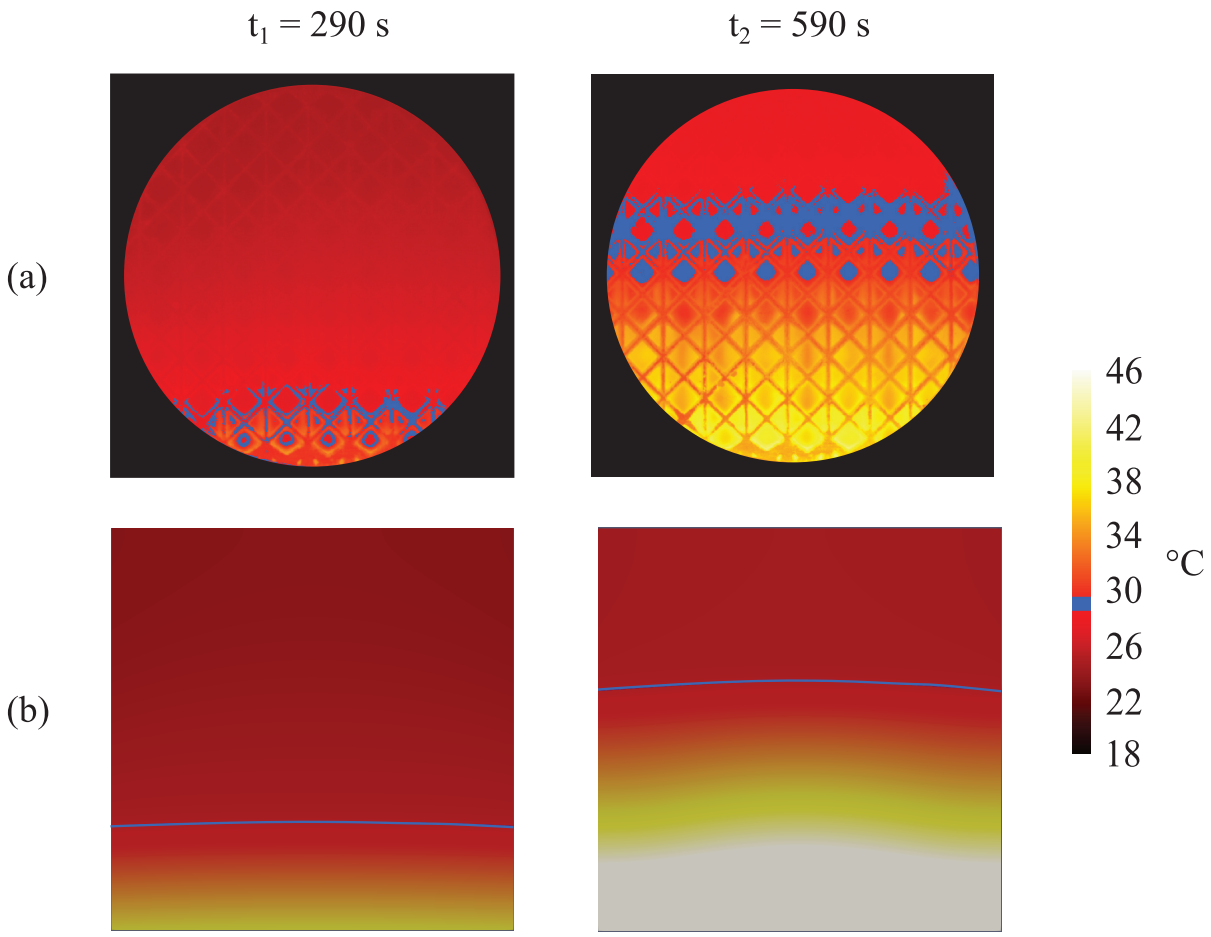

Fig. 4.52: Temperature distribution and melting front expansion: (a) experiments and (b) simulations for the f_2ccz sample, bottom heating orientation.

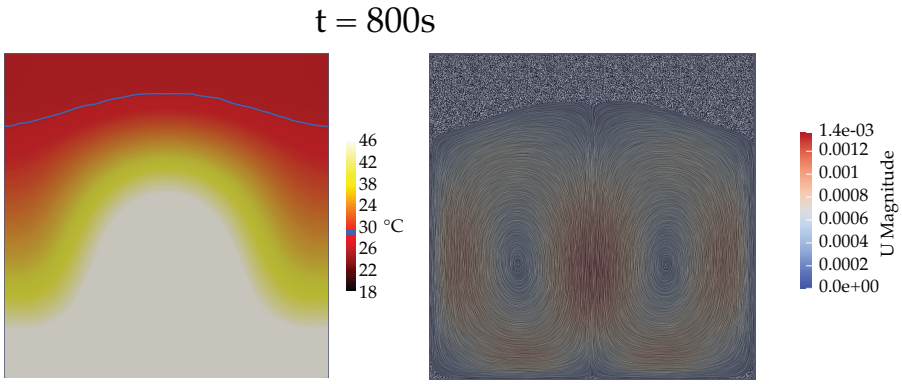

(a) Temperature distribution, melting front expansion, and streamlined velocity profile of the f_2ccz sample at t = 800 s.

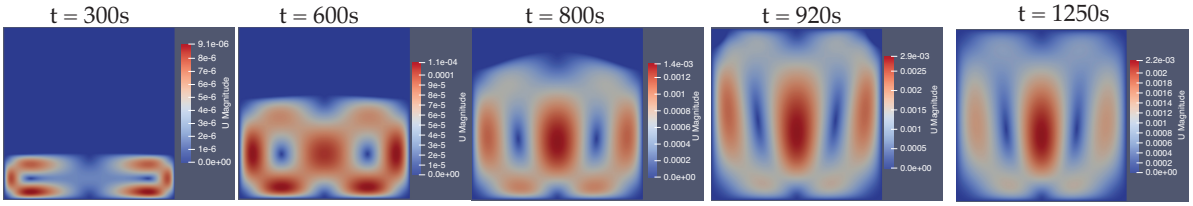

(b) Velocity field for different time steps of the f_2ccz sample, bottom heating orientation. The scale of the velocity field is changed at each time step to better visualize the velocity profile.

Fig. 4.53: Temperature and velocity fields for the f_2ccz sample, bottom heating orientation, evidencing the occurrence of Rayleigh-Benàrd convection cells.

The results presented thus far indicate that the solver here presented in general shows a good agreement with experimental data, as it was validated both with experimental and numerical data from the literature [83], as well as with the experimental data presented above. Criticality appears when considering the f_2ccz sample, which exhibits a particularly high permeability, and a high porosity. This way, relatively high fluid flow velocities can take place, inducing a deviation from a purely Darcy flow regime. It worth mentioning that, altough with different magnitude, the same effect can be evidenced in the literature, e.g. in Iasiello et al. [83]. To the author's knowledge, this phenomenon has not yet been thoroughly investigated in the literature, with many authors erroneously stating that the effective viscosity for the Darcy-Brinkman model is the same of the PCM. This aspect shall be delved into in future works.

4.3.3 Scale analysis of the natural convection

Although already discussed, it is worthwhile reminding that the effect of natural convection on the thermal behaviour evidences a discrepancy between the sample with the highest permeability (f_2ccz), and the one which was influenced the most by convection (bcc). This is also appreciable from Figure 4.35 in Section 4.2.1 compared to the values of permeability obtained in Section 4.3.1.

To better identify the effect of natural convection, and allow a scale analysis on the effect and onset of natural convection, the data relative to the samples tested, both experimentally and numerically, are reported in Figure 4.54 and correlated to non-dimensional numbers of relevance. The sample f_2bcc is neglected, as the effect of convection is found to be negligible. Figure 4.54 reports the wall temperature and liquid fraction evolution for each relevant sample and each orientation. The wall temperature is reported as an area averaged value, with the reference area being the the heat wall surface, i.e. L^2. Figure 4.54a shows that the insurgence of natural convection in the melt for the side and bottom heating orientations is cause for a deviation of the average wall temperature from the one related to the top heating orientation. It can be noticed that the time point at which convection becomes relevant is different for different samples and different orientations. In general, the samples heated at side heating orientation are affected sooner by natural convection. The bottom heating orientation undergoes a purely conductive regime for a longer time, but its effect on the average temperature is more evident.
As also shown in the experiments (see Section 4.2.1), the overall effect of natural convection on the average temperature is identical for both the side and bottom heating orientations. Indeed, at the last time step in Figure4.54a, the temperature values of both heating orientations for a given sample almost coincide.
The liquid fraction is affected by the phenomenon as well, as one can appreciate in Figure 4.54b, where a ca. 20% difference between the fastest and the slowest full melting can be evidenced.

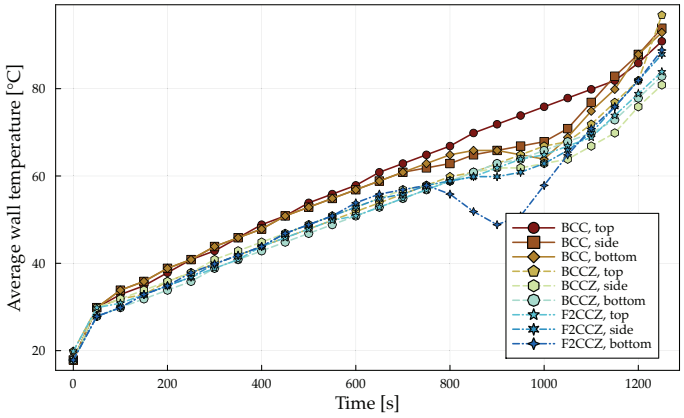

(a) Area-averaged wall temperature curves against time

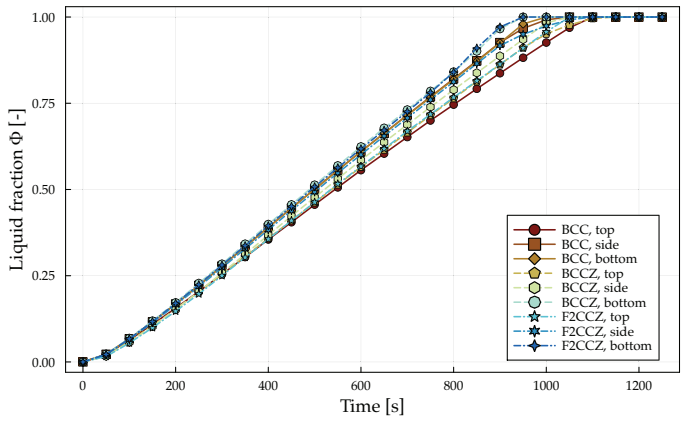

(b) Liquid fraction evolution against time

Fig. 4.54: Temperature and liquid fraction evolution for the selected samples and heating orientations.

It is useful to describe the reported data in terms of relevant non-dimensional numbers, namely the Stefan, the Fourier, and the Rayleigh number. They indicate that strongest effect of natural convection on the wall temperature are achieved for the *bcc* sample, which exhibits the lowest effective thermal conductivity. This seems counterintuitive as it also is the sample which exhibits the lowest permeability. The opposite is true for the f_2ccz sample, which exhibits the highest effective thermal conductivity and highest permeability (in z-direction), but a comparably lower influence of natural convection on the thermal behaviour. Thus, one can assert that the onset of convection and its effect on the thermal behaviour is strongly related to the effective thermal diffusivity of the medium. Indeed, a low thermal diffusivity of the domain is a cause for enhanced overheating of its wall. This causes a higher temperature gradient between the wall itself and the melting front, allowing to surpass sooner critical values for convection onset.
This can be better visualized when comparing the Rayleigh and the Fourier numbers of the samples, as shown in Figure 4.55. The Fourier number is calculated as in Equation 4.20. The Rayleigh number is reported coherently to the expression proposed by Nield [135] for a porous medium, and adapted for a PCM, similarly to what proposed by Azad et al. [78] for a pure

PCM material. This means defining the length scale in the equation as the area-averaged liquid fraction times the length of the probe in the heat flux direction.

$$Ra(t) = \frac{g\rho_{\text{eff}}\beta\Delta T_m(t)K_i\Phi_{avg}(t)L}{\nu\alpha_{\text{eff}}} \tag{4.32}$$

where Ra is the Rayleigh number, g is the local gravity acceleration, β is the thermal expansion coefficient of the molten PCM, $\Delta T_m(t)$ is the temperature difference between the average wall temperature and the temperature at the boundary of the liquid domain, i.e. the melting point, K_i is the permeability $K_{x,y}$ if the side orientation is considered and K_z if the bottom or top orientations are considered. $\Phi_{avg}(t)$ is the area-averaged liquid fraction, L is the edge length of the samples, ν is the kinematic viscosity of the PCM, and α_{eff} is the effective thermal diffusivity.

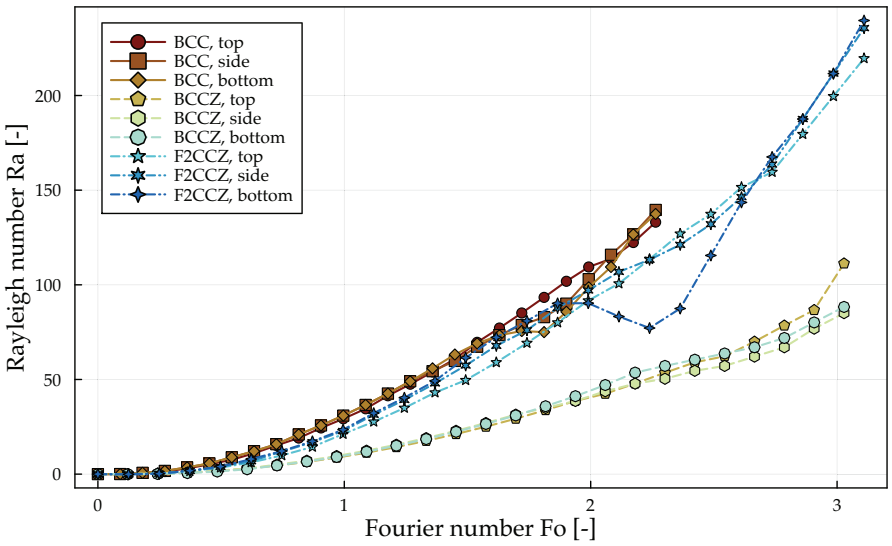

Fig. 4.55: Rayleigh number plotted against the Fourier number.

The data reported indicate different critical values for the onset of convection, which are listed in Table 4.14. The results indicate that the critical Fourier number is directly correlated with the sample's diffusivity, i.e. the lower the diffusivity, the lower the critical Fourier number. The opposite is true for the critical Rayleigh number. One can notice that, while the permeability is inversely correlated to the critical Rayleigh number, this relationship is not linear, indicating that the coupled effect of thermal diffusion is affecting the results. To highlight this appropriately, it is useful to evaluate the diagram shown in Figure 4.56, as it provides an evident indication of the effect of the thermal diffusivity on the onset of convection.

Table 4.14: Critical values of Rayleigh, Fourier, and Stefan numbers, and, for comparison, the permeability in the respective orientations.

Sample	Ra_{crit}	Fo_{crit}	Ste'_{crit}	Molten Volume $[mm^3]$	$K_i[10^{-7}m^2]$
bcc side	8.78	0.54	0.15	34.37	1.82
bccz side	8.59	0.94	0.16	44.12	1.36
f_2ccz side	9.74	0.68	0.10	30.87	1.76
bcc bottom	13.38	0.75	0.04	51.12	1.82
bccz bottom	25.54	1.52	0.25	81.62	1.81
f_2ccz bottom	21.46	0.92	0.15	45.12	4.74

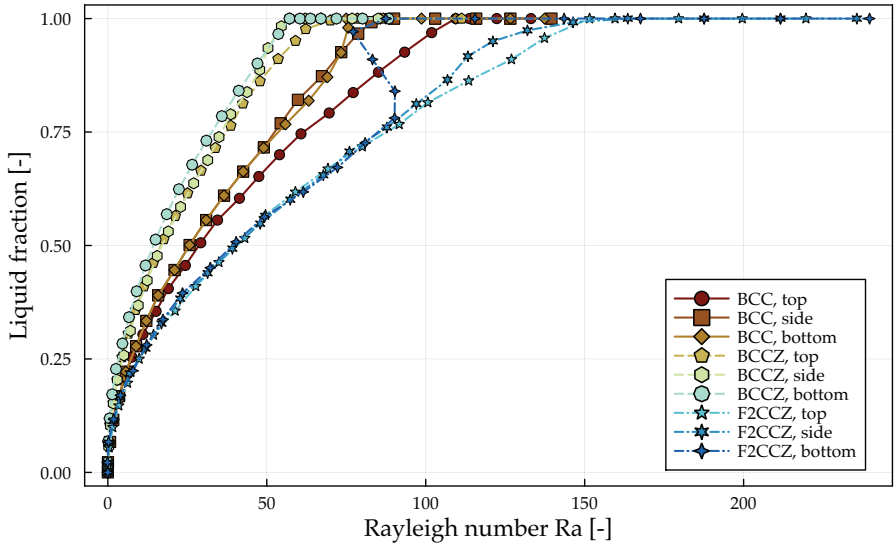

Fig. 4.56: Liquid fraction against Rayleigh number.

Looking at Figure 4.56, one can appreciate that a strong deviation takes place after the onset of convection. The higher the permeability in the heat flux direction, the stronger this effect. However, the onset of convection takes place more gradually, as a transition regime is present, in which the fluid flow acquires velocity, but the melting front expansion is not yet strongly affected by the convective movements. For this reason, the critical onset-numbers are calculated searching for a deviation of 10% from the purely conductive regime, which occurs at top heating orientation.

To further analyse the data, the liquid fraction is reported in Figure 4.57 against the Fourier number, the corrected Stefan number (see Equation 4.21) and their product, which represents a commonly used non-dimensional time. Figure 4.57c shows that the curves of different samples for the top heating orientation overlap. This indicates that, in a purely conductive regime, the liquid fraction can be expressed as an analytical function of the Stefan-Fourier number. Via

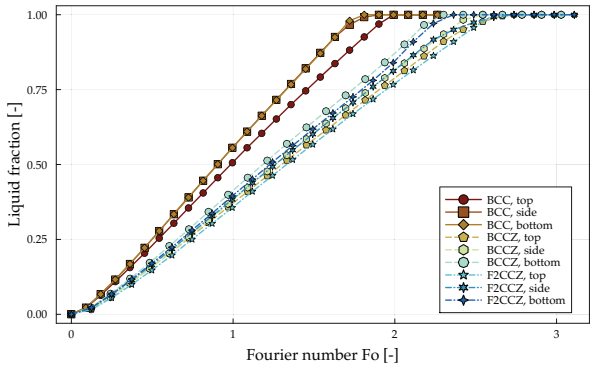

(a) Liquid fraction against Fourier number.

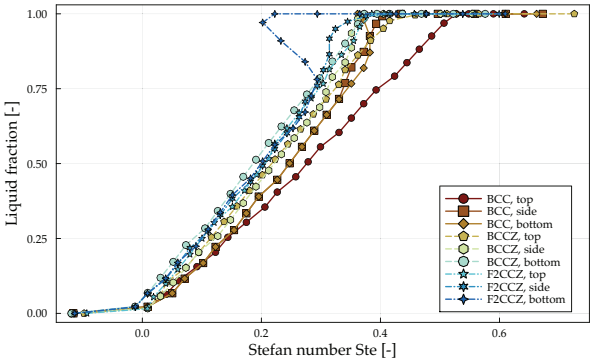

(b) Liquid fraction against corrected Stefan number.

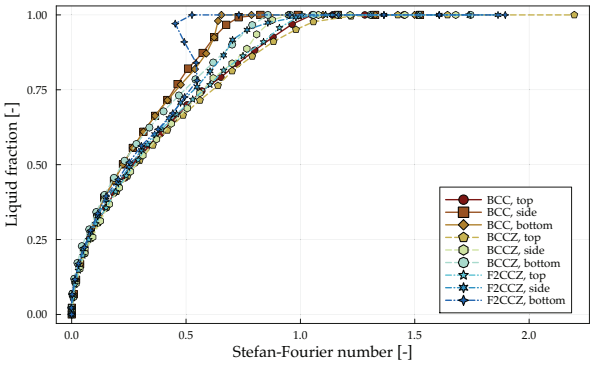

(c) Liquid fraction against Stefan-Fourier number.

Fig. 4.57: Liquid fraction relationship with the Fourier, the Stefan and the Stefan-Fourier numbers.

curve fitting with means of an exponential function, the liquid fraction Φ for the top orientation can be related to the Stefan-Fourier number by Equation 4.33.

$$\Phi(\varpi)_{top} = -1.121e^{(-1.347\varpi)} + 1.253 \tag{4.33}$$

where ϖ is used to indicate the Stefan-Fourier number.

4.4 Conclusion

In this chapter, an extensive characterisation of the thermal behaviour of composites based on lattice structures embedded with PCMs was presented. Analytical correlations, as well as numerical and experimental investigations were conducted to achieve a comprehensive description of thermal phenomena governing such composites. The analytical correlations obtained were used to pursue an homogenisation approach, which shall simplify the future analysis and design of such composites. The main findings of this chapter are listed below:

- A semi-analytical description of the geometry of lattice structures with cuboid unit cells was developed. The analytical calculation of Steinmetz's solids volume was partially used to describe the intersection of the lattice struts. Empirical coefficients were deemed necessary to accurately describe the geometry of the lattices. This is due to a difficult generalisation of the integrals for the calculation of the Steinmetz's solids for struts which cross at different angles. Additionally at struts crossings, a variable material accumulation can take place during the additive manufacturing process, which depends on the machine parameters. Thus, to be able to flexibly adapt the presented geometric description, empirical parameters which can be changed at need are considered useful and necessary. The introduced formula univocally correlate the lattice porosity with the other geometric parameters.
- A semi-analytical description of the effective thermal conductivity of the composites was presented. A thermal resistance network was modelled, in which the struts and the nodes at which they cross are treated as connected resistances. Empirical parameters were obtained performing several parametric sweeps based on numerical investigations, performed with the commercial software COMSOL Multiphysics®, based on a finite element implementation of the apparent heat capacity method. Additionally to the effective thermal conductivity, also the other effective thermophysical properties were obtained.
- A numerical analysis of the transient behaviour of the composites under a purely conductive regime indicated that the homogenisation approach is scale invariant as long as minimum number of equal unit cells can be found in the domain. This value is correlated to the porosity of the unit cell and descreases with increasing unit cell porosity. Thus, the thermal behaviour can be assumed scale invariant, if the domain contains a sufficient number of periodic unit cells, or highly porous one, i.e. $\varepsilon > 0.95$.

- A simplified conductive model based on the effective thermophysical properties indicated diminishing returns in increasing the volume fraction of the lattice unit cells in order to improve the thermal diffusivity of the composite. In particular if the design goal is the one of realising a latent heat-thermal energy storage device, the increase of the volume fraction reduces the amount of heat stored latently. Thus an optimal trade-off between a high diffusivity and high latent heat exists. The quantitative value of the correlated volume fraction depends on the lattice topology.

- An experimental campaign was conducted for a variety of purposes. A validation of the semi-analytical model for the effective thermophysical properties was achieved this way. Thus, the homogenisation approach can be deemed valid if the conditions on the scale variance are respected and natural convection can be neglected. The experimental campaign was conducted under several orientations with respect to the local gravity vector, and shed light on the effect of natural convection on the thermal behaviour of the samples. A significant effect of natural convection was found even for lattice samples with relatively low porosity. To quantify the effect, the permeability of the samples was investigated. However, the sample exhibiting the highest porosity and the highest permeability (f_2ccz) showed a reduced effect of convection on its wall temperature and on the liquid fraction, with respect to the *bcc* and *bccz* samples. This is attributed to a coupled effect of conduction and convection. The high thermal diffusivity of the sample caused a delayed onset of convection with respect to other samples.

- The effect of natural convection was delved into deeper with means of a purposedly developed numerical solver. The solver is based on OpenFOAM®. Due to the orthotropic nature of the effective thermal conductivity and of the permeability, a new solver was needed to address the numerical solution of the conservation equations. The solver makes use of the enthalpy-porosity method. The results are coherent with the results present in the literature [83], which is based on composites made of metal foams and PCMs. Thus, the code can considered to be verified. The results are compared with the experimental campaign performed in this work. Discrepancies affecting the temperature curves and the melting front shape can be noticed especially for bottom heating orientation. These are caused by the treating of the composite as a homogeneous material, which only gives a global, rather than local, description of the flow resistance given by the lattice structure, by means of the Darcy term in the momentum equation. The effective viscosity calculated as a scalar via the Einstein's model delivered good results for the side-heating orientation, but lacked to allow an accurate description of the thermal behaviour for a bottom heating orientation. However, the quantitative values of the liquid fraction and the full melting time are in good agreement with the experimental data.

- Finally, with the goal of quantifying both the effect of natural convection on the thermal behaviour, and in order to find onset criteria for the occurrence of natural convection in the melt, a scale analysis was proposed. The data which are analysed are the ones obtained from the numerical simulations, made via use of the developed solver, which replicate

the experimental campaign. This because rather than having only a few data points in the domain, area averaged values could be obtained for both temperatures and liquid fraction. The results of the scale analysis indicate that the onset of convection is strongly affected by the effective thermal diffusivity, with a low diffusivity aiding the occurrence of natural convective movements in the melt. This is evident when comparing the obtained critical values for the Rayleigh and the Fourier numbers.
Furthermore, when analysing the liquid fraction evolution in relation to the Stefan-Fourier number, one can notice that for top-heating orientations, the behaviour of all samples can be described by the same function. Via curve fitting, an analytical correlation is obtained, as indicated in Equation 4.33.

5 Stability of lattice structures embedded with PCM

Problem statement The Phase Change Material embedded within the metallic lattice structure can exhibit a wide range of mechanical properties. Thus, in addition to the discussed thermal behaviour, it is relevant to investigate the mechanical behaviour of these novel composites.

In general, PCMs considered for room temperature application, e.g. paraffin waxes, exhibit relatively low stiffness and strength [136, 137] with respect to materials employed for structural purposes, i.e. metallic alloys of fiber reinforced plastics. Thus, their contribution to the effective stiffness of the composite can be considered to be negligible. Other PCMs, i.e. salts and salt eutectic mixtures exhibit higher stiffness, however their application can be considered only for high-temperature applications. The treatment of such materials would impose additional considerations connected to the thermomechanical behaviour of the composite, which is not scope of this work.

The most relevant aspect to be considered for the PCM-lattice structure composites is the effect that the PCM can have on the stability of the lattice struts. Indeed, in order to achieve lightweight components, the volume fraction of the lattice shall be minimised, while remaining withing strength constraints. This can lead to rather slender struts, which can be affected by stability issues. Thus, the buckling behaviour of the composite is treated within this chapter.

The PCM is treated as an elastic medium, in which the beams are embedded. A similar approach was already proposed in the case of lattice structures embedded with plastic foams by Wu et al. [138].

First, the problem is simplified by embedding a single horizontal beam with hinged supports in an elastic foundation. Then, an extension to lattice cells is presented. The treatment of full lattice components is secondary as it does not add novel findings with respect to the single strut and cell studies. The interested reader is referenced to such investigation in Appendix**??**. Finally, an experimental investigation is presented.

5.1 Numerical investigation of the stability behaviour of PCM-lattice composites

In the following sections a comprehensive study is presented, regarding the buckling behavior of lattice structures. Both analytical and numerical methods, comparing scenarios with and without an elastic bed, are used. The anticipated buckling phenomena are localized within the individual struts of the lattice.

The systems under investigation, namely the strut, cell, and lattice, are denoted as *isolated* when devoid of an elastic medium and *embedded* when surrounded by one. To streamline discussions, analytical results are denoted as "ANA" while numerical results are designated as "NUM".
The elastic medium's properties are modeled after a specific PCM, namely an n-Octadecane Paraffin wax, in its solid state. For the lattice structure itself, the aluminium AlSi10Mg alloy is employed, given its prominence as the typical lightweight material for lattice structures produced via Laser Powder Bed Fusion (LPBF) printing. This alloy is of relevance also as it is employed for the thermal studies presented above. The properties of AlSi10Mg are obtained from averaged values reported in [139]. For paraffin, which constitutes the elastic medium, the elastic modulus, as well as tensile and compressive yield stresses, are determined from sources [136] and [137]. It is worth noting, based on Andrianov [140], that solid paraffin can be treated as de-facto incompressible, with a Poisson ratio of 0.499. The material data are reported in Appendix B.

5.1.1 Analytical solution for an individual strut

The structural element representing a single lattice strut is idealized as a beam with hinged ends, reflecting the basic end condition typical of lattice struts. In the case of an isolated strut, the basic equation for Euler critical buckling (Equation G.15) is employed with the end constraint factor fixed at $n = 1$. Considering that the lattice struts in this study uniformly feature circular cross-sections, the second moment of area is defined as $I = \pi/4(D/2)^4$. Consequently, the non-dimensional parameter L/D, representing the slenderness of the strut, is varied. The default presentation in this work is in terms of this parameter, and with the strut length fixed at $L = 10mm$, i.e. only the strut diameter is varied in order to vary the slenderness.
The determination of the value of m yielding the smallest critical load is performed using Equation 2.79. The foundation modulus k is approximated using the Vesic (Equation H.5) and Herrmann (Equation H.4) formulae. The Vesic expression is multiplied by 2 to account for an all-sided foundation, rather than a monodirected one, as recommended by Attewell [141].
Figure 5.1 depicts the results for both isolated and embedded struts, with logarithmic scales applied to the axes for enhanced visualization. As illustrated, the critical buckling load of the strut P_{cr} decreases with increasing slenderness, consistent with expectations. Notably, the embedded struts exhibit higher P_{cr} values. The improvement is quantified by $P_{cr,embedded}/P_{cr,isolated}$, which increases with higher slenderness ratios. Consequently, the impact of the elastic medium on the critical buckling load becomes more pronounced for struts with elevated slenderness. Regarding the foundation modulus, the Herrmann approximation appears to yield higher P_{cr} values. This aligns with expectations due to the added rigidity introduced by accounting for shear effects.

While the application of the beam theory typically assumes a slenderness of $L/D \geq 10$, slenderness values are initiated at $L/D = 5$ in this analysis to showcase results for low slenderness struts. It is crucial to note that the precision of solutions in the lower range of slenderness (i.e.

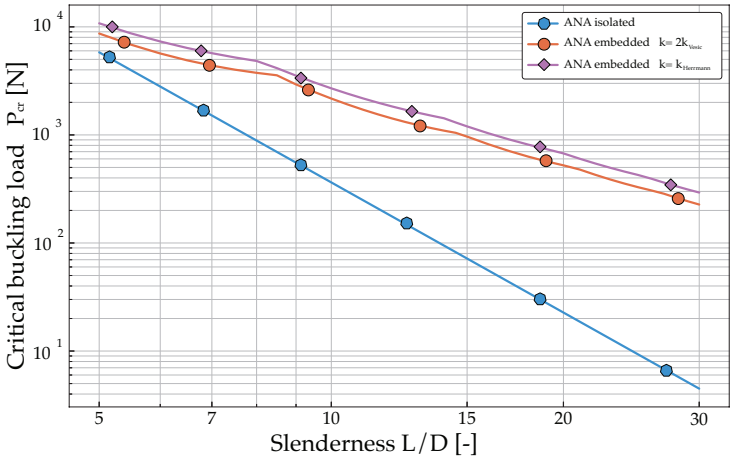

Fig. 5.1: Analytical solution for critical buckling load of isolated and embedded struts.

$L/D < 10$) may be limited, considering the neglect of shear deformation effects. The variation in slenderness extends up to $L/D = 30$.
To obtain the critical buckling stress (σ_{cr}), the critical buckling load is divided by the strut's cross section. Figure 5.2 presents the plot of σ_{cr}, revealing a distinct pattern in the curves of the embedded struts. Notably, the y-axis employs a linear scale to emphasize this pattern. This repeating pattern, observed in works such as [102], arises from a discontinuity during an increase in the value of m. Each parabola-like section corresponds to a specific value of half-sine waves m in the deflection curve, starting with $m = 1$ for the first parabola, $m = 2$ for the second, and so on. Additionally, the critical buckling stresses of the embedded struts consistently remain above the value $2\sqrt{kEI}/A$. This value corresponds to the solution of an infinitely long beam on an elastic foundation with $P_{cr} = 2\sqrt{kEI}$ ([102]). For the Herrmann solution of the infinite beam, k_{Herrmann} is averaged across all slenderness ratios, as it is not constant.
As depicted in Figure 5.2, σ_{cr} consistently remains above the yield strength for the embedded struts, whereas as expected, above a certain slenderness, it falls below such threshold for the isolated strut. Consequently, for this specific model, it can be inferred that the embedded struts are prone to failure through yield and rupture only, rather than buckling.

5.1.2 Numerical models for an individual strut

The numerical models are obtained using the Lanczos eigensolver available in the ANSYS® APDL solver. Two modeling approaches are employed for the strut: one with beam elements (referred to as "BEAM") and another with volumetric elements (referred to as "VOL"). The BEAM model is designed to streamline computational efficiency by utilizing fewer nodes, whereas the VOL model, despite longer computational time, incorporates shear effects of the foundation. To enhance accuracy, higher-order elements with quadratic displacement behavior

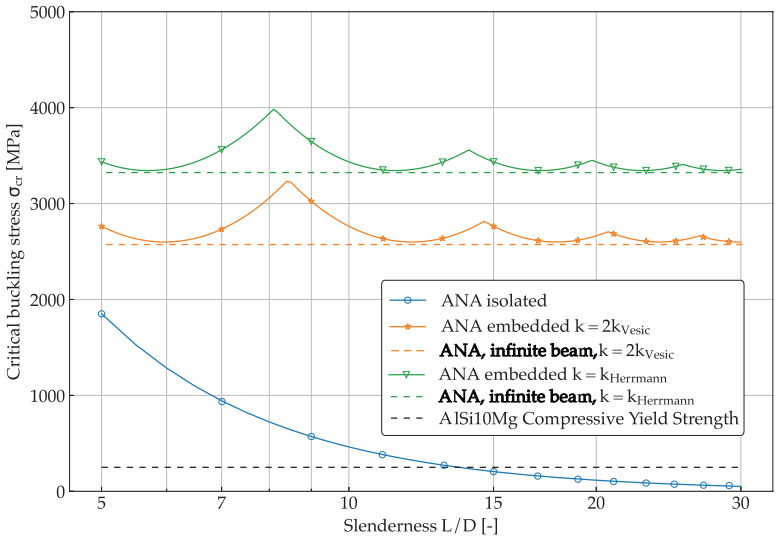

Fig. 5.2: Analytical solution for critical buckling stress of isolated and embedded struts. Lower bounds for embedded struts given by $2\sqrt{kEI}/A$.

are employed: BEAM189 (3 nodes) for the beam elements and SOLID186 (20 nodes) for volumetric elements.

Beam elements The simulation of hinged supports is achieved by defining rigid regions at the ends of the strut. At each end, a massless node, referred to as the "master node", is created, and the corresponding end nodes of the strut, denoted as "slave nodes", are rigidly connected to it. Boundary conditions are then imposed on the master nodes, restricting only translational displacements to ensure free rotation. An axial load P is applied at one of the two master nodes, with that particular master node permitted to move freely in the axial direction. Additionally, rotation around the x-axis is restricted at one of the master nodes, as illustrated in Figure 5.3. This configuration of boundary conditions is consistently applied to all strut and lattice unit cell models in this study.

Fig. 5.3: Model of the isolated strut: cyan triangles indicate translational restrictions, orange triangles signify rotational restrictions, and pink triangles denote constraint equations between nodes due to rigid regions.

In the case of the beam-type strut, the elastic medium can be simulated through a Winkler foundation model, by connecting each node of the beam with a perpendicular spring element. The utilized spring elements belong to the COMBIN14 type, characterised as a longitudinal tension-compression element with three translational degrees of freedom at each node. The spring constant α is derived from Equation H.1 and is equal to $\alpha = ka$, where a represents half the element length, given the presence of a middle node in each beam element. For the foundation modulus, only $2 \cdot k_{\text{Vesic}}$ is employed, as k_{Herrmann} relies on m, which is not known ab-initio. The model effectively provides numerical solutions for the individual strut, as the plane of buckling is deemed irrelevant. However, for more intricate structures like cells or lattices, the plane of buckling for individual struts might be influenced by end conditions and the surrounding environment. It is imperative not to prescribe the plane of buckling by restraining nodes in a specific direction, i.e. there should be no preferred plane of buckling. This challenge can be addressed by introducing multiple rows of springs symmetrically aligned with the strut axis. The simplest configuration involves three rows of springs at 120° from each other, as shown in Figure 5.4.
Increasing to three the number of springs which act on each node mandates that the spring stiffness be updated. For the same infinitesimal spring deflection ds, the forces produced on a node by the single row spring model must be equal to the forces produced by the triple row spring model. This derivation is visualized in Figure 5.5.

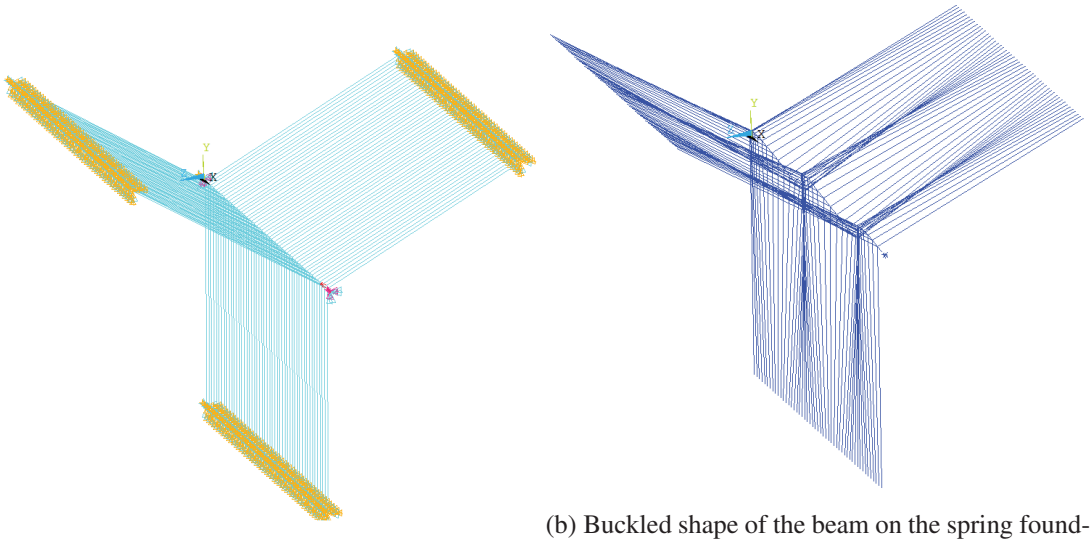

(a) Model: notice the three rows of springs.

(b) Buckled shape of the beam on the spring foundation.

Fig. 5.4: Example of the model and results of a beam embedded via three rows of springs. A slenderness ratio $L/D = 30$ is used for this example.

Equating the total forces acting in the y-direction for both models ($\sum F_{single} = \sum F_{triple}$) yields

$$F_{1,single} = F_{1,triple} + 2F_{2,triple}\sin(30°) \tag{5.1}$$

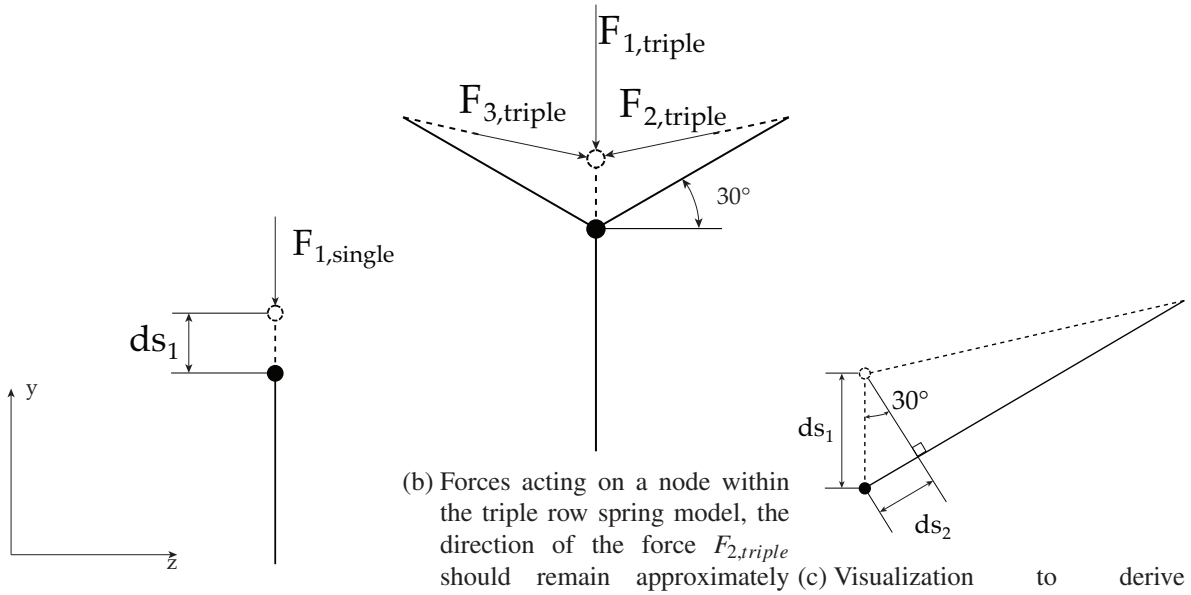

(a) Forces on a node in the single row spring model.

(b) Forces acting on a node within the triple row spring model, the direction of the force $F_{2,triple}$ should remain approximately consistent as the infinitesimal displacement $\mathrm{d}s_1$ occurs.

(c) Visualization to derive the geometrical relation $\mathrm{d}s_2 = \mathrm{d}s_1 \sin(30°)$.

Fig. 5.5: Schematic representation of the forces F acting on a generic node for different spring models.

Inserting $F = \alpha\,\mathrm{d}s$ and $\sin(30°) = 1/2$ results in the following relation for the spring constants.

$$\alpha_{single}\,\mathrm{d}s_1 = \alpha_{triple}(\mathrm{d}s_1 + \mathrm{d}s_2) \tag{5.2}$$

Utilizing the relation $\mathrm{d}s_2 = \mathrm{d}s_1 \sin(30°) = \mathrm{d}s_1/2$, which can be deduced from Figure 5.5c, it follows that the α of each spring in the three-rows model is related to the α of each spring in the one-row model, by

$$\alpha_{triple} = \frac{2}{3}\alpha_{single}, \tag{5.3}$$

i.e., the spring constants in the triple row spring model must be multiplied by a factor $2/3$.
Once the model is set up, a mesh-convergence analysis is conducted. A threshold of 0.1% is defined. As illustrated in Table 5.1, an element size of $L/10$ is sufficient for the isolated strut. However, for the embedded strut, particularly at high strut slenderness ratios, the differences in mesh size do not seem to fall below the threshold until an element size of $L/25$ is reached (refer to Table 5.2). One possible explanation is that embedded struts with high slenderness ratios entail a significantly higher number of half sine waves, requiring more elements to accurately represent the deflection curve. Thus, an element size of $L/30$ is applied for all future analyses with beam elements in this work.

Table 5.1: Mesh convergence analysis for isolated strut (beam elements).

	$L/D = 5$		$L/D = 10$		$L/D = 30$	
Element length	P_{cr} [N]	Difference	P_{cr} [N]	Difference	P_{cr} [N]	Difference
$L/5$	5400.2	-	356.10	-	4.469	-
$L/10$	5398.2	(-0.037%)	355.96	(-0.039%)	4.467	(-0.039%)
$L/15$	5398.1	(-0.002%)	355.95	(-0.002%)	4.467	(-0.002%)

Table 5.2: Mesh convergence analysis for embedded strut (beam elements).

	$L/D = 5$		$L/D = 10$		$L/D = 30$	
Element length	P_{cr} [N]	Difference	P_{cr} [N]	Difference	P_{cr} [N]	Difference
$L/5$	8070.3	-	2023.6	-	224.65	-
$L/10$	8069.1	(-0.015%)	2015.2	(-0.419%)	213.14	(-5.127%)
$L/15$	8069.2	$(+0.002\%)$	2014.9	(-0.014%)	211.43	(-0.799%)
$L/20$	8069.3	$(+0.001\%)$	2015.0	$(+0.001\%)$	211.15	(-0.135%)
$L/25$	8069.4	$(+0.001\%)$	2015.0	$(+0.001\%)$	211.08	(-0.032%)

The numerical solution using beam elements, and a comparison to the analytical solution are depicted in Figure 5.6. Both the single row spring model and the triple row spring model solutions are plotted, and it can be observed that they coincide perfectly. Therefore, the expression found in Equation 5.3 can be considered to be exact.
When visualizing the buckled beam, it becomes apparent that the number of half-sine waves in the deformed curve increases at the same slenderness ratios where there are local maxima in the curve, as expected. For instance, the deformed curve has one half-sine wave in the interval $5 \leq L/D \leq 7.5$, two in the interval $8 \leq L/D \leq 13.5$, and so on. Deformation curves representing each of these intervals are added to Figure 5.6 to illustrate this pattern. At low slenderness ratios, a small deviation between analytical and numerical solutions becomes apparent. This discrepancy arises from the fact that the numerical solution employs Timoshenko-type beam elements, while the analytical solution is based on Euler-Bernoulli beam theory.

Model based on volumetric elements

Numerical analyses employing beam elements yield results that closely align with the analytical solution. This is a rather obvious result, since the analytical equations were derived using beam

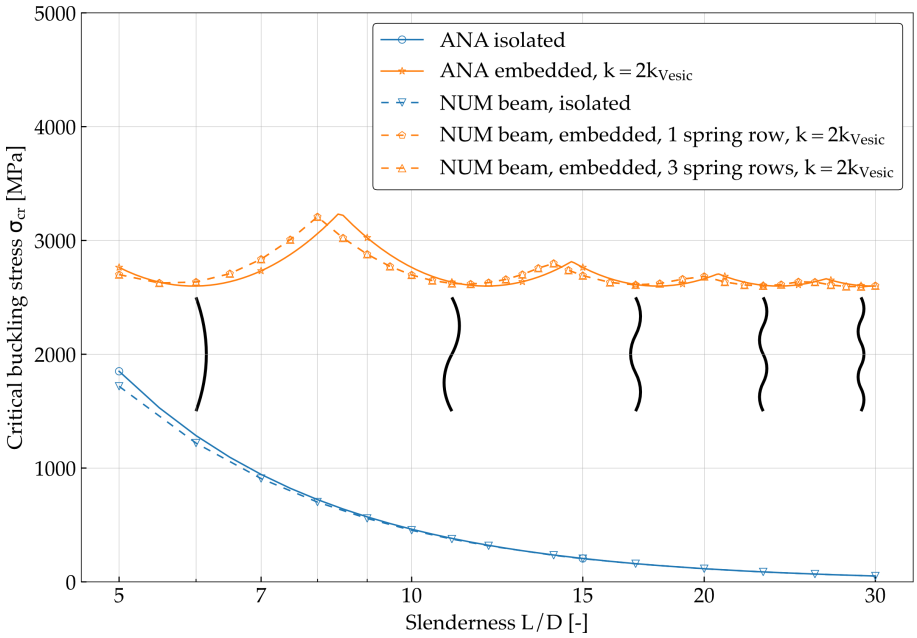

Fig. 5.6: Numerical and analytical solutions for critical buckling stress of individual strut (beam elements).

theory. However, it's important to remind that in such model the elastic medium is modeled as a one-parameter foundation model without accounting for shear effects.
The use of volumetric elements is expected to deliver more realistic results, incorporating directly the relevant material properties of the medium, and, through the continuum formulation, including shear effects. This comes with higher computational effort.
The strut's cross section can be meshed and extruded, resulting in a uniform mesh with hexahedral elements. The elastic medium is modeled by creating a concentric volume around the strut (see Figure 5.7), where the inner elements share the same nodes as the outer elements of the strut. The depth of the elastic medium is defined by the parameter $\mu = D_{\text{Foundation}}/D_{\text{Strut}}$, representing the ratio between the diameter of the foundation and the one of the strut. The influence of this parameter on the results is discussed in the following.
The same boundary conditions as those employed in the beam model are applied, including the use of rigid regions to couple all nodes at the strut ends. Additionally, nodes at the outer faces of the elastic medium are fixed in the radial direction.

A mesh convergence analysis is conducted. A foundation depth of $\mu = 10$ is utilized, and the results are presented in Table 5.3. The mesh size is defined in terms of fractions of the strut radius R. A mesh size of $R/3$ is employed, as the computational effort for finer meshes become prohibitively high for cases involving an elastic medium. For reference, Figure 5.8 illustrates the resulting mesh of the strut section for the analysed mesh sizes from Table 5.3. It is essential to note that higher-order elements are used, thus incorporating a middle node on each element edge. An additional convergence analysis is conducted to identify a ratio μ where the changes

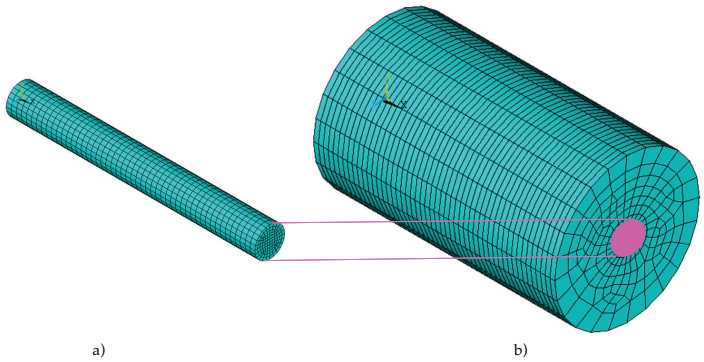

Fig. 5.7: Meshed volumetric model of isolated a) and embedded b) strut for $L/D = 10$, $\mu = 5$. Notice that the violet ellipse is used merely to differenciate the mesh of the elastic medium from the one of the embedded strut, which is actually shown in (a).

in buckling load become negligible with the increase in foundation depth. To this purpose, Figure 5.9 illustrates the critical buckling stress of the embedded strut for various diameter ratios μ. It is evident that the critical buckling stress decreases with an increasing diameter ratio μ. This is expected, as μ determines the distance from the strut to the outer faces of the elastic medium, which are radially fixed. For low distances, the rigidity provided to the strut by fixing the outer faces is higher, thereby increasing the critical buckling load. The magnitude of this effect diminishes with an increasing distance of the outer faces to the strut, as the elastic medium has more volume to deform freely. Although not obvious at low slenderness ratios, the curves from Figure 5.9 seem to converge with increasing μ. A value $\mu = 30$ is chosen as a limit due to the increased computational effort.

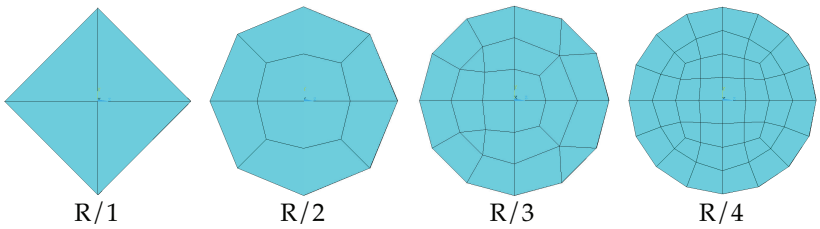

Fig. 5.8: Mesh of the strut section for different radial element sizes.

Table 5.3: Mesh convergence analysis for embedded strut (volumetric elements).

	$L/D = 5$		$L/D = 1$		$L/D = 30$	
Element length	P_{cr} [N]	Difference	P_{cr} [N]	Difference	P_{cr} [N]	Difference
$R/1$	10146	-	2729.8	-	359.10	-
$R/2$	10077	(-0.674%)	2686.9	(-1.572%)	351.31	(-2.171%)
$R/3$	10044	(-0.335%)	2678.3	(-0.322%)	349.84	(-0.419%)
$R/4$	10055	$(+0.118\%)$	2679.9	$(+0.061\%)$	350.55	$(+0.205\%)$

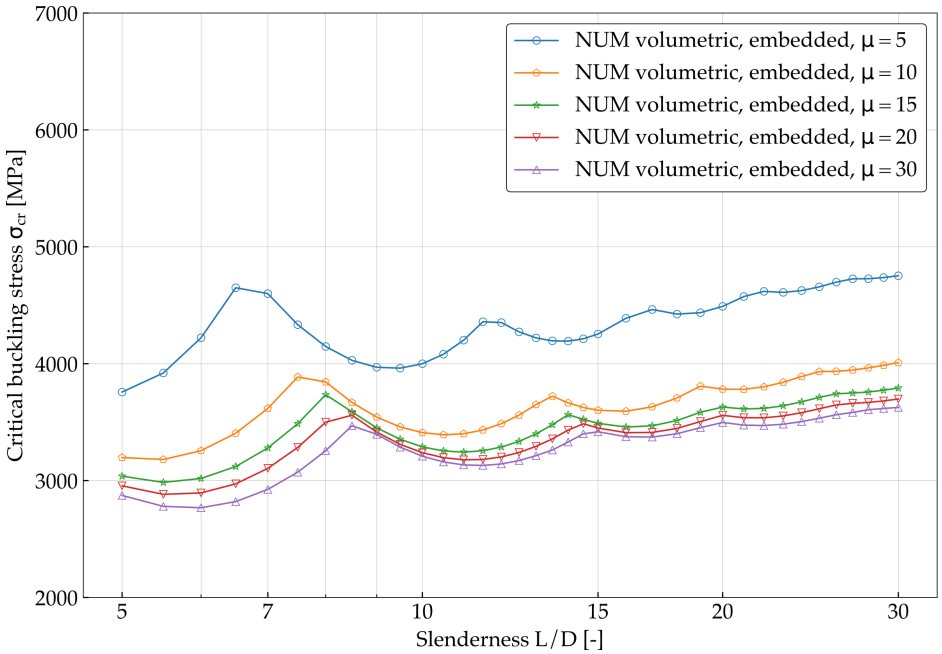

Fig. 5.9: Critical buckling stress of embedded strut for different diameter ratios μ (volumetric elements).

Figure 5.10 presents the numerical results for beam and volumetric models, along with the analytical results. For the isolated strut, the volumetric and beam models essentially yield the same buckling loads. However, significant differences between the models are observed in the embedded case. This discrepancy arises because the spring model, used for the beam elements-case, effectively corresponds to a one-parameter foundation model (with parameter $2k_{\text{Vesic}}$), while the volumetric model corresponds to a two-parameter foundation model (with parameters E_f, ν_f), which includes shear effects.

Analysing Figure 5.10, it is evident that the values produced by the volumetric model are closer to the solutions of the beam model and the analytical solution for k_{Vesic} at low slenderness and

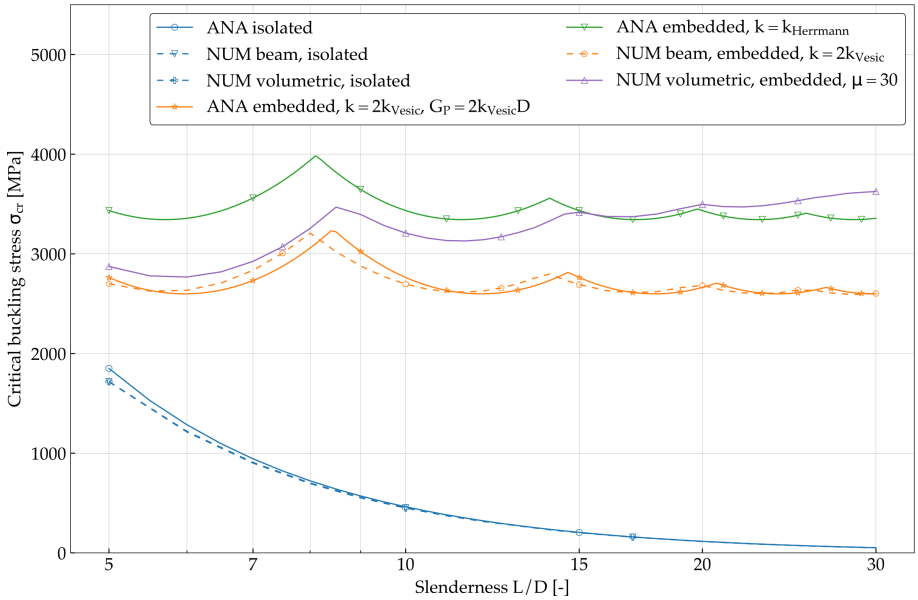

Fig. 5.10: Numerical and analytical solutions for critical buckling stress of individual strut (beam and volumetric elements).

closer to the solution for k_{Herrmann} at high slenderness. Overall, the curve for the volumetric elements deviates from the solution for beam elements with rising slenderness. This deviation can be attributed to the added shear effect in the volumetric model. Assuming that the difference between the analytical solution and the volumetric model is solely due to the shear effect from the foundation, the stiffness of the shear layer, G_P, can be approximated. This allows for the computation of the analytical solution for the critical buckling load for a Pasternak foundation (Equation 2.81). Given that G_P has the unit of a load and the foundation modulus k has the unit of a load per square unit length, it seems reasonable to assume that the stiffness of the shear layer G_P should depend on the foundation modulus k multiplied by two dimensions of length. A simple expression that yields good results is

$$G_P = 2k_{\text{Vesic}}D\frac{L}{10}, \tag{5.4}$$

using the diameter D and length L of the beam. Assuming such a dependence, the analytical solution comes relatively close to the volumetric model, as shown in Figure 5.11.

5.1.3 Analysis of a lattice structure unit cell

This section aims to analyse the buckling behavior of four different unit cells, namely the *bcc*, *bccz*, f_2cc, and f_2ccz ones, in both isolated and embedded cases.
To streamline the computationally intensive calculations, an aspect ratio angle $\gamma = 45°$ is assumed. It is essential to note that, due to this assumption, the angles between the diagonal struts

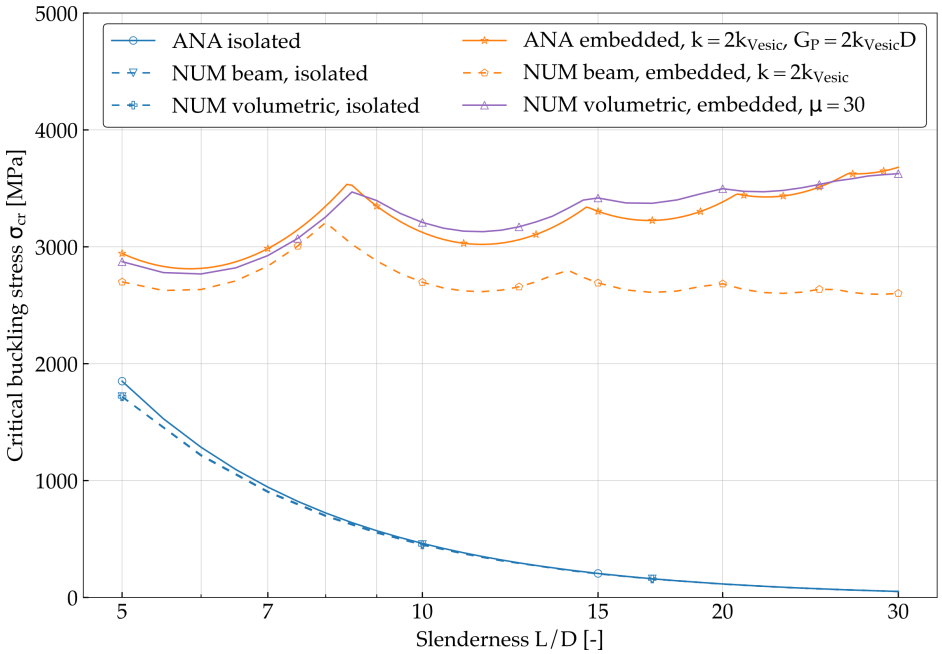

Fig. 5.11: Solutions for critical buckling stress of individual strut. The analytical solution uses a Pasternak foundation model with $k = 2k_{\text{Vesic}}$ and $G_P = 2k_{\text{Vesic}}D$.

and the xy-plane are as follows: $\phi_{d,f_2cc} = \arctan(1/1) = 45°$ and $\phi_{d,bcc} = \arctan\left(1/\sqrt{2}\right) \approx 35.26°$. Similarly, the length of the diagonal struts is $L_{d,f_2cc} = (\sqrt{2}/2)h$ and $L_{d,bcc} = (\sqrt{3}/2)h$, where h is the size of the cell. For cells with a vertical strut, there are two different strut lengths (the vertical $L_v = h$ and diagonal L_d strut lengths).
The question arises as to how to define the slenderness in this case. As the critical buckling load is lower for higher strut lengths, it stands to reason that the critical strut (the strut which buckles first) will generally be the longest. Thus, the slenderness will be defined as L_{cr}/D, where L_{cr} is the length of the critical strut, assumed to be the longest strut. Therefore, for cells without the vertical strut (bcc, f_2cc, etc), the slenderness is trivially defined. For cell types with a vertical (z) strut, it is defined in relation to the length of the vertical strut. In this second case, this leads to different slenderness ratios for diagonal and vertical struts, as the strut radius is assumed to be the same.

Numerical solution for unit cells

All four types of unit cells have six vertices: the lower, upper, and the four lateral vertices. Setting the boundary conditions at each vertex is not a trivial operation. If the cell were part of a lattice structure, the six vertices might experience displacement or rotation due to the influence of adjacent cells. However, when considering a single cell, the influence of surrounding cells is not considered. This leads to different buckling behavior compared to the one observed when an entire lattice component is simulated, resulting in different critical buckling loads. Never-

theless, the findings presented in the following provide good approximations and contribute to understanding the buckling phenomenon of these composites.
When analyzing lattice components, it can be observed that local buckling occurs in the form of rotations of the vertices and bending of the struts (see, for an example, Figure 5.12). Displacements of the vertices appear to be very small, with the exception of vertices at the free ends of the component. It must be noted that, for the two cell types without a vertical strut (f_2cc and bcc), local buckling will only occur if transverse strain of the lattice is inhibited. This means that the nodes at the lower and upper faces of the lattice must be fixed. Otherwise, under a vertical load, the f_2cc and bcc cells will compress vertically and expand laterally without buckling. Lattices exhibiting unit cells with a vertical strut (f_2ccz and $bccz$) will buckle locally without the need for transverse fixing.
Due to this, it seems logical to use hinged supports at the vertices when simulating a single unit cell, thus inhibiting translations but allowing rotations. For the cell types with a vertical strut, a support on the lateral vertices is not needed for the vertical strut to buckle, although both versions (with hinged supports at the lateral vertices and without) are studied in this case.

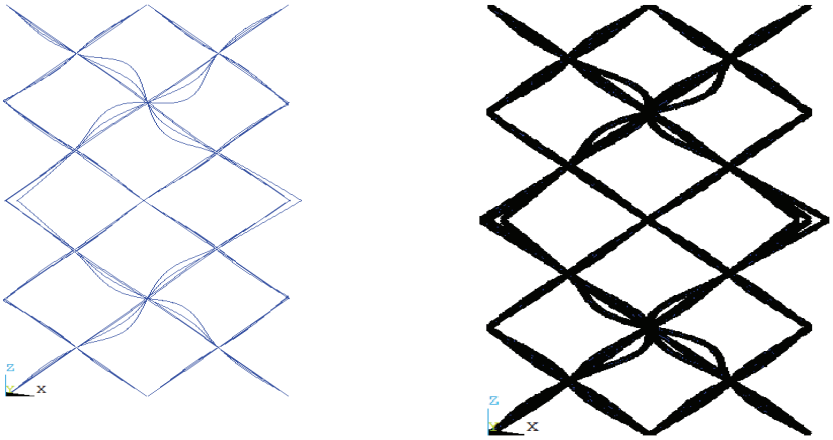

(a) Buckled shape, beam elements (b) Volume elements

Fig. 5.12: Local buckling in a simulated bcc lattice component with $2 \times 2 \times 4$ cells, for an isolated case. The load acts in vertical direction, and is applied on the strut nodes. A strut slenderness of $L/D = 20$ is used in this example.

Numerical model The unit cell struts are represented using beam elements with an element size of $L_{cr}/30$. To simulate hinged supports, rigid regions are established at each vertex of the unit cells by connecting a massless master node to the corresponding node of the vertex. The master nodes are then fixed laterally in x-y directions, and the lower vertex is additionally fixed vertically in the z-direction, including rotation. The compressive load is applied to the upper master node, as schematically shown in Figure 5.13.The modelling of the springs for a lattice unit cell is no trivial task, and requires the implementation of a dedicated procedure. For sake of brevity, such procedure is reported in Appendix I. The resulting configuration with spring

elements attached is depicted in Figure 5.14.

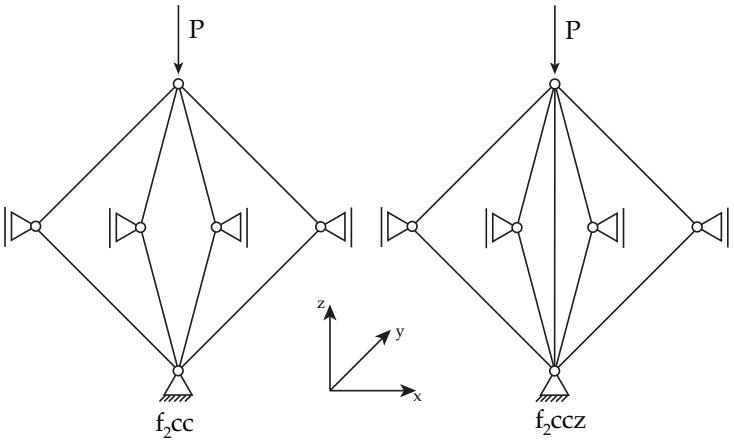

Fig. 5.13: Boundary conditions on the cells. Here, f_2cc and f_2ccz cells are shown. The same boundary conditions are applied for body-centered unit cells. The supports represent a fixation in x- and y-direction.

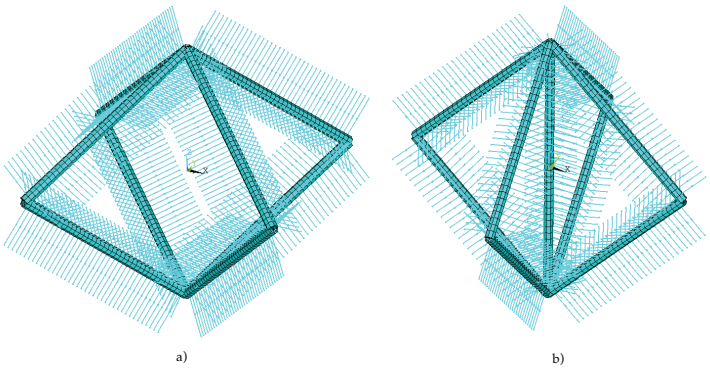

Fig. 5.14: Beam models for a f_2cc unit cell (a), and a f_2ccz unit cell (a). The beam elements are visually represented with volumetric shapes to enhance clarity. It is important to note that, for improved visualization, relatively short springs have been employed in this representation.

Figure 5.15 exemplarily shows the results of the presented model for both embedded and isolated unit cells. The buckling shapes are reported for unit cells in which the struts' slenderness ratio is $L/D = 20$. In general, it can be observed that in the embedded case, the critical struts exhibit an increasing number of half-sine waves, and certain sections of the cells appear to remain unbent. This is associated to an increased critical buckling load. In order to allow a proper comparability between the different models, the results for all the slenderness spectrum are reported in Figures 5.17-5.21, where the results of the analytical solution and of the volumetric model are also reported.

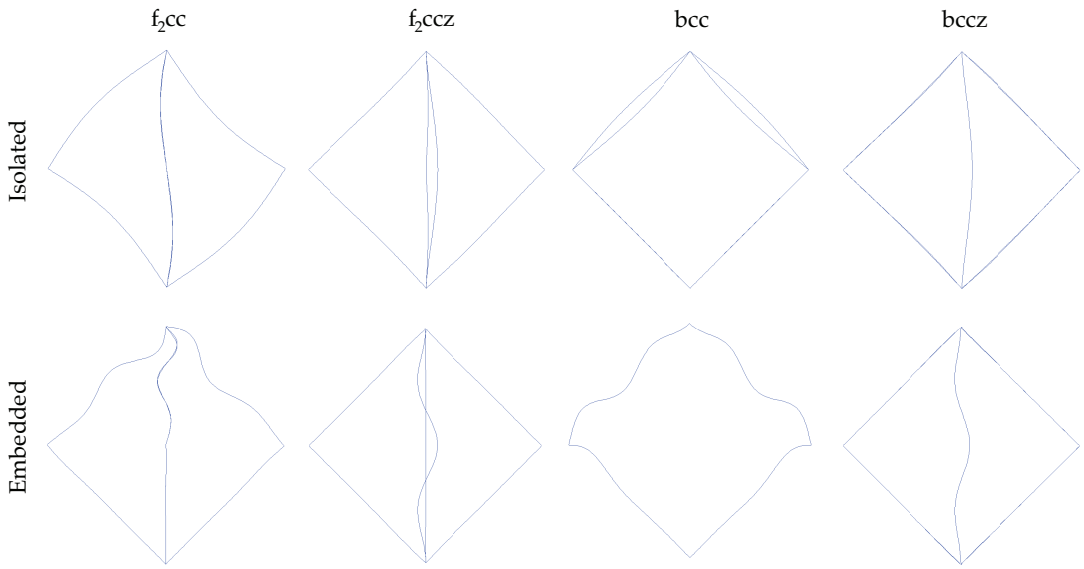

Fig. 5.15: Buckling shapes for the considered example. It is important to note that the f_2cc case might be visually confusing, as the diagonal struts in the plane perpendicular to the image appear as a single vertical strut.

An analytical solution is sought in order to describe the phenomenon. The approach proposed by Bühring [142] to use the equivalent member method is considered and adapted for the case of embedded lattice struts. In the embedded case, the critical buckling load is determined using Equation H.11. As it is not feasible to solve this equation directly for P_{cr}, the following approach is employed:

- The determinant's value from Equation H.11 is computed for a range of loads, initiating with the smallest viable solution $P_{min} = \sqrt{4kEI}$, as it has been established that the beam will not buckle at smaller values. Increments of $\Delta P = 1N$ are applied, with a maximum load of $P_{max} = 4P_{min}$ seeming sufficient.
- A curve is fitted to the data points employing a piecewise polynomial.
- The zeroes of the fitted curve are calculated using an iterative method. The critical load corresponds to the first zero greater than P_{min}. Higher-valued zeroes indicate higher modes of buckling for the beam.

The procedure to obtain the stiffness matrices and then calculate the critical load is described in detail in Appendix I.1.
The modelling approach followed to model the system with use of volumetric elements is similar to that employed for beam elements, incorporating identical boundary conditions and rigid regions. As previously done for single struts, the volumetric model is compared to the beam numerical solution and the analytical one.

Figures 5.18 to 5.20 present both numerical and analytical results for various unit cells. The discrepancies between the results are quantified using the relative deviation Υ, defined as

$$\Upsilon = \frac{P_{cr} - P_{cr,ref}}{P_{cr,ref}} \tag{5.5}$$

Υ is the relative deviation between the numerical and analytical solutions, P_{cr} is the critical buckling load obtained from the numerical solution, and $P_{cr,ref}$ is the critical buckling load obtained from the analytical solution.
Deviations between the results are expressed as percentages, with the lower value serving as the reference for consistency. The following additional points should be noted:

- A cell size of $h = 10mm$ is employed for all solutions.
- For both analytical and numerical solutions with beam and spring elements, $2k_{\text{Vesic}}$ is used for the foundation modulus.
- For cells without a vertical strut, i.e. f_2cc, bcc, analytical solutions are conducted with the Pasternak model using $k = 2k_{\text{Vesic}}$ and $G_P = 2k_{\text{Vesic}}D$ to account for shear deformations in the foundation at high slenderness ratios.
- Analytical solutions for embedded f_2ccz and $bccz$ cells assume a Winkler model, disregarding shear effects in the foundation due to the unavailability of a solution for the Pasternak model with rotational springs at the ends.
- For cells with a vertical strut (f_2ccz, $bccz$), numerical analyses are performed without (refer to Figure 5.19) and with pinned supports at the lateral vertices (refer to Figure 5.20). Analytical solutions are conducted without pinned supports for both cases, since a solution with pinned supports at the lateral vertices is not available.

Considering these points, the results can now be interpreted, starting with a comparison between the two numerical approaches (i.e. beam/spring elements and volumetric elements). Figure 5.18 displays the critical buckling loads for the f_2cc and bcc cell types.
For the isolated case, the beam and volumetric solutions coincide at high L/D. At low slenderness ratios, the critical buckling load is higher with volumetric elements. This discrepancy can be explained by the stiffness increase caused by the vertices. When using volumetric elements the growth of the strut diameter and its effect of the volume of the struts' intersections is considere (see Figure 5.16). This delivers a non-negligible contribution to the overall stiffness. This effect is more pronounced in cells with a vertical strut (Figures 5.19 and 5.20), as the presence of the vertical strut increases the volume of the Steinmetz solid which represents the node. For instance, this leads to a deviation between the solutions of beam and volumetric elements of 163% in the case of the f_2ccz cell with hinged lateral supports for $L/D = 5$.
The same kind of deviation can be observed in the embedded cases, again, being considerably more pronounced for the f_2ccz and $bccz$ cells.

For the f_2cc and bcc cells, the beam element solution exhibits slightly higher critical buckling loads than the volumetric solution at high slenderness ratios, but in general a good agreement.

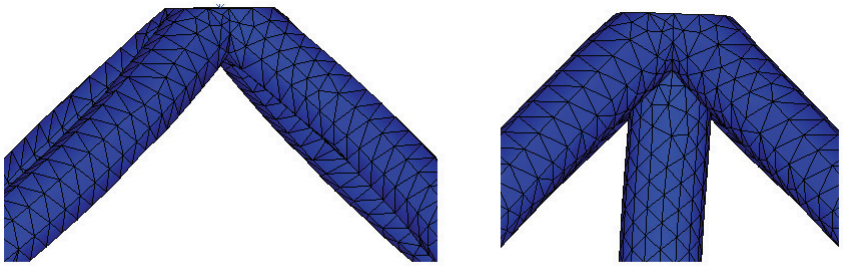

Fig. 5.16: Vertex of deformed *bcc* cell (a) and *bccz* cell (b) for $L/D = 7$. Due to material accumulation at the nodes, the rigidity of the structure is increased. The effect is increased with lower strut slenderness ratios and with the presence of a vertical strut.

This seems to contradict results from the single-strut model, where volumetric elements showed higher stability due to the inclusion of shear stresses in the foundation. A potential explanation lies in the differing boundary conditions and foundation depth between the two models. The spring model assumes completely fixed ends for the springs, resulting in independent foundations for individual struts. In contrast, the volumetric model allows stress transmission between struts, especially near the vertices where the foundation volume is thin. This could induce stresses counteracting the embedding effect, reducing stability.
Interestingly enough, the f_2ccz cell does not exhibit this effect, suggesting that the presence of a vertical strut maintains the additional stiffness from material accumulation at the vertices, offsetting the stability loss from the volumetric foundation model at high slenderness ratios.
The results for the *bccz* cell in the embedded case without hinged lateral supports show an unusual curve for the volumetric solution, deviating to lower critical buckling loads than the beam element solution around $L/D = 9$. Examination of the buckling modes (Figure 5.17) reveals an additional mode involving the rotation of the outer cell, distinct from the expected vertical strut buckling mode. This extra mode reduces the critical buckling load. It does not appear for the f_2ccz cell, possibly due to shorter diagonal struts being less prone to induce this mode. The disappearance of this mode with hinged supports at the lateral vertices inhibits the rotation of the outer cell in this case.
The comparative analysis of analytical and numerical results for the f_2cc and *bcc* cells in isolated conditions reveals a consistent discrepancy at medium to high slenderness ratios. This disparity, expected due to the analytical focus on the critical strut and neglect of additional stiffness from interconnected struts at the vertices, stands at 16% for the f_2cc and 19% for the *bcc* cell at $L/D = 30$.
In the embedded case, particularly at medium to high slenderness ratios, the analytical curve converges more closely with the beam model for the f_2cc cell and with the volumetric model for the *bcc* cell. However, at low slenderness ratios, the analytical solution consistently underestimates the numerical results, a phenomenon likely influenced by a combination of previously discussed factors and the analytical oversight of vertex stiffening.
Analyzing the f_2ccz and *bccz* cells in isolated conditions, the analytical solution closely matches

numerical results obtained with beam elements. However, a slight deviation is noted for the *bccz* cell at low slenderness ratios. This suggests that the equivalent member method offers satisfactory accuracy in approximating results obtained with beam elements in isolated scenarios. Deviations from the volumetric element solution are attributed to the impact of volume overlap at the vertices. When hinged supports are introduced at lateral vertices, numerical solution curves shift to higher values. As no analytical solution is available for this specific case, conventional analytical solutions are presented for comparison.

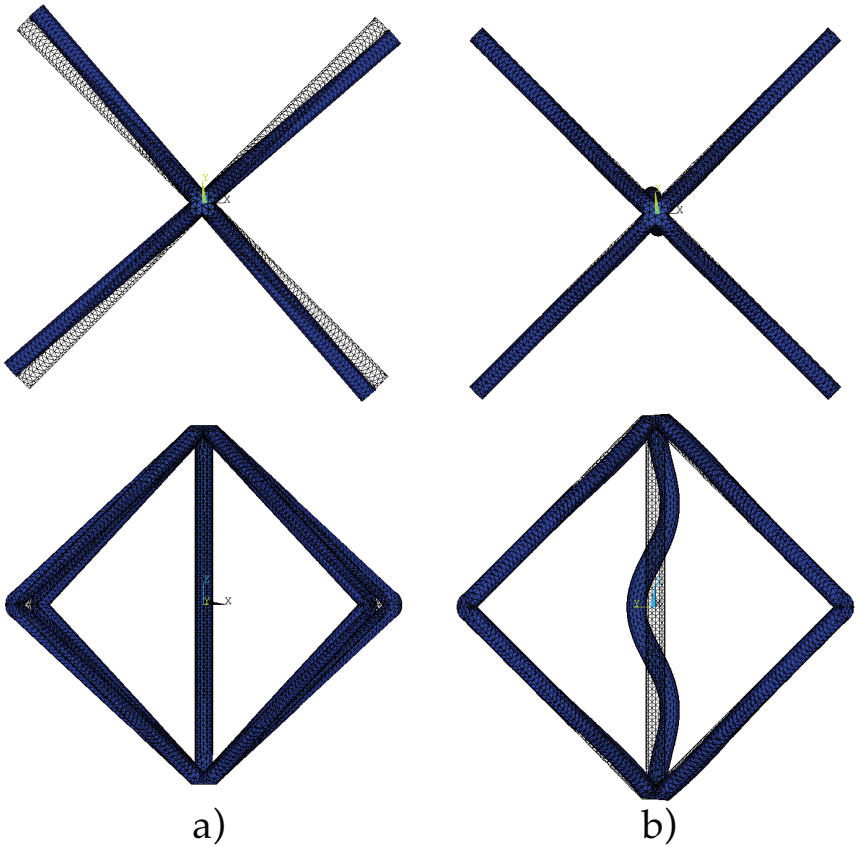

Fig. 5.17: First (a) and second (b) buckling modes for the *bccz* cell. No hinged supports at the lateral vertices are considered, and $L/D = 20$.

In the embedded configuration, the analytical solutions consistently exhibit an underestimation compared to the numerical curves, except for the *bccz* cell without hinged supports at the lateral vertices. The latter case features an additional buckling mode, explaining the deviation. Nevertheless, the analytical underestimation is relatively minor at low slenderness ratios. To elucidate the widening discrepancy with increasing slenderness ratios, several hypotheses are postulated and explored.

One initial hypothesis posits that the disparity arises from the analytical model utilizing a Winkler foundation without a shear layer. However, this can be dismissed, as the numerical model

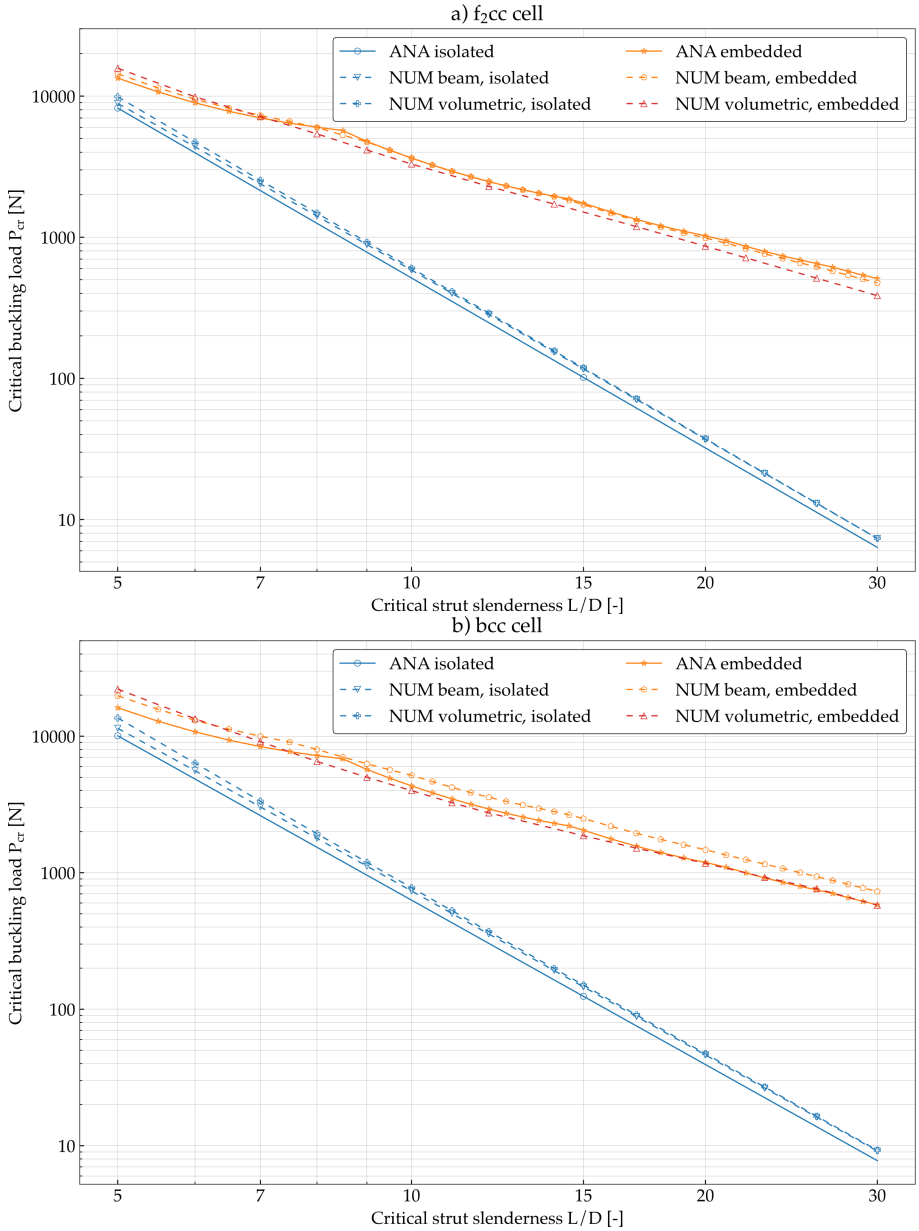

Fig. 5.18: Critical buckling loads for the f_2cc (a) and *bcc* (b) cell types.

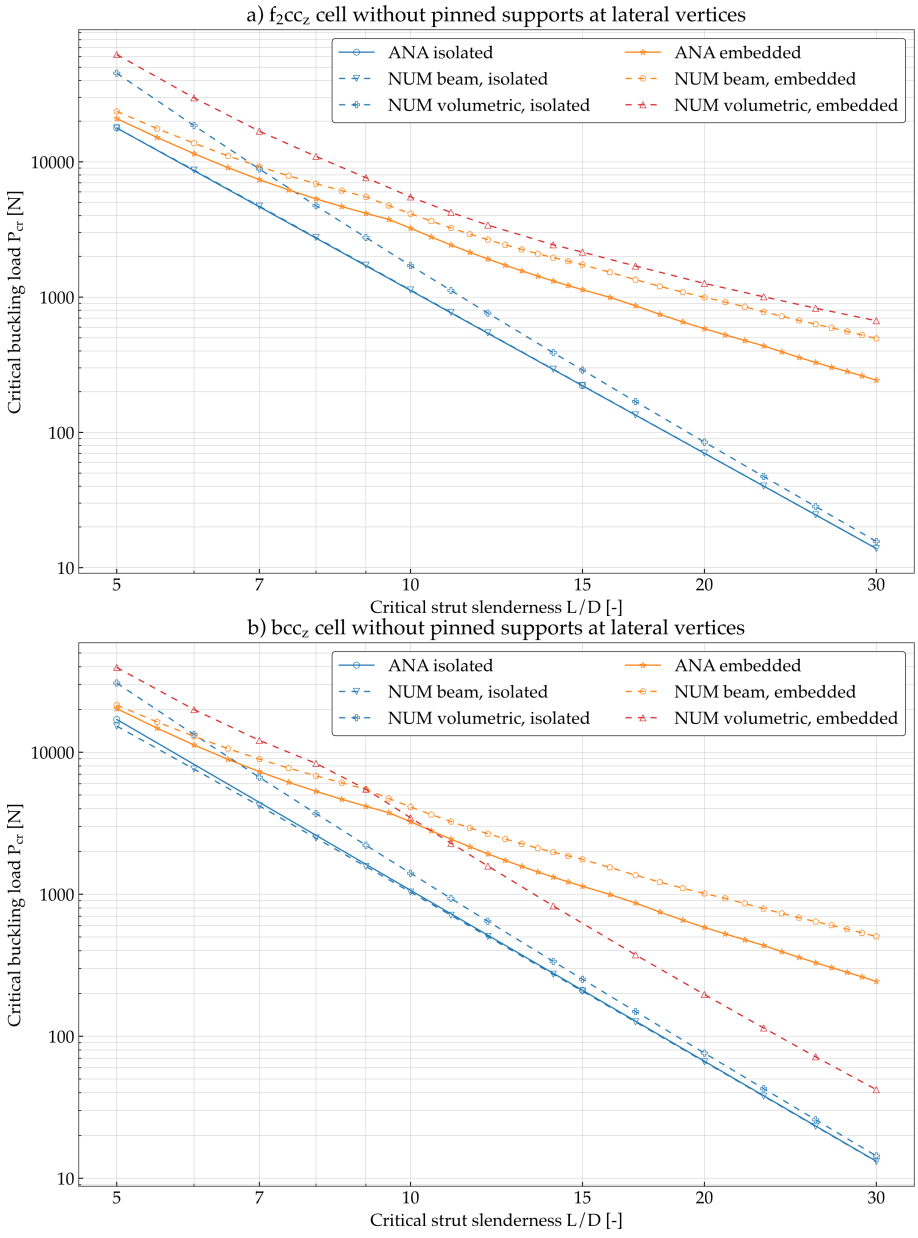

Fig. 5.19: Critical buckling loads for the f_2ccz (a) and $bccz$ (b) cell types without pinned supports at the lateral vertices in the numerical models.

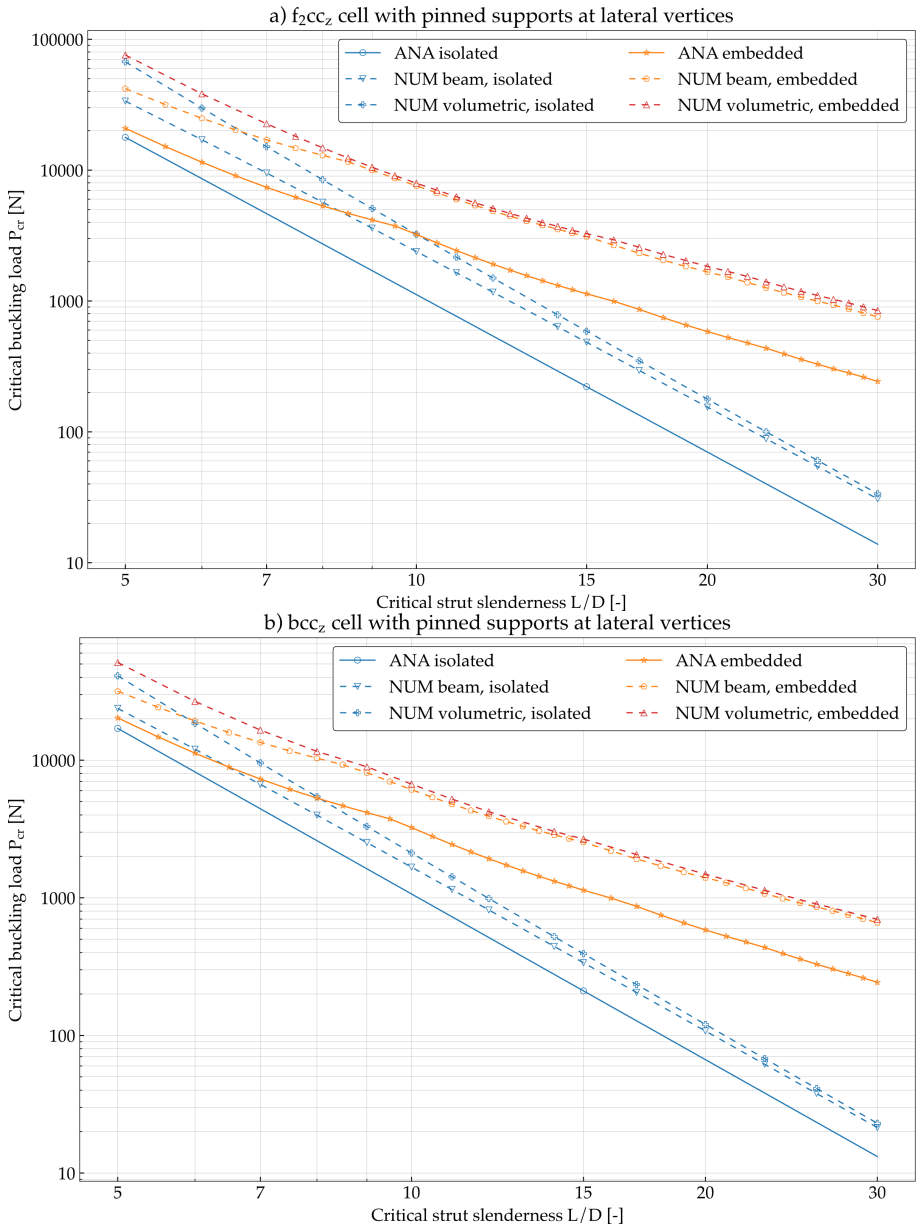

Fig. 5.20: Critical buckling loads for the f_2ccz (a) and $bccz$ (b) cell types with pinned supports at the lateral vertices in the numerical models.

with beam elements similarly neglects shear effects in the foundation. A second hypothesis suggests that the stiffness matrices of the diagonal beams lack an additional unknown stiffness from the foundation, leading to an underestimation of the rotational spring stiffness used in the analytical solution. To test this, an extreme case is considered, wherein the stiffness of the rotational springs is infinite by setting the fixity factor to 1. Alternatively, the solution for an embedded beam with fixed ends, as provided by Hetényi [102], is directly employed (Equation 5.6). The critical buckling load derived from this equation is depicted in Figure 5.21 in red. Notably, at high slenderness ratios, the solution still significantly underestimates the numerical calculations. Therefore, the deviation cannot be attributed to the stiffness matrices of the diagonal beams.

$$P_{cr} = 4\frac{\pi^2 EI}{L^2} + \sqrt{4kEI} \tag{5.6}$$

To delve deeper into this matter, a new Finite Element (FE) model is formulated with beam/spring elements, where only the vertical strut is embedded with spring elements. The result for this model is presented in Figure 5.21 in green. Strikingly, the solution aligns with the original analytical curve. Consequently, the analytical results correspond to a scenario where only the vertical strut is embedded within the cell. The outcomes for the f_2ccz cell, excluding pinned supports at the lateral vertices, are illustrated in the plot.

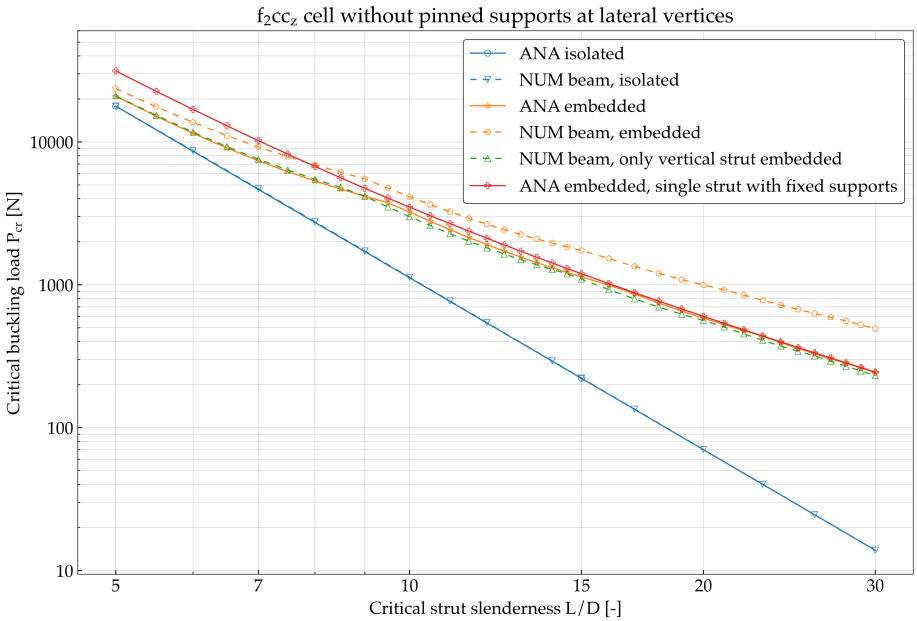

Fig. 5.21: The graph encompasses, alongside the previously described results, a beam model in which solely the vertical strut is embedded (depicted in green) and the analytical solution for a single strut with fixed supports (depicted in red).

A third hypothesis posits that the critical buckling load is augmented because a portion of the compressive load is absorbed by the embedding of the diagonal struts, consequently diminish-

ing the load on the vertical strut. To investigate this, an analysis is conducted to determine the stresses in the cell just before buckling. Table 5.4 presents the average beam stresses in the vertical strut and the diagonal struts for an isolated cell, a cell with only the vertical strut embedded, and a fully embedded cell. In the first two cases, the stresses in the diagonal struts are relatively low compared to those in the vertical strut. In the third case, the ratio between the stresses is significantly lower, suggesting that a substantial portion of the load is channeled through the diagonal struts, thereby increasing the critical buckling load. In comparison to the cell with only an embedded vertical strut, the stress in the vertical strut remains nearly unchanged, while the critical buckling load is almost doubled. The assumption that the entire load is borne by the vertical strut appears valid for the first two cases, given the low stresses in the diagonal struts. However, this assumption does not hold for the fully embedded cell, resulting in a notable discrepancy between the analytically and numerically determined buckling loads.

Table 5.4: Average stresses in the beam, at buckling load, for the vertical and diagonal struts of a f_2ccz cell (modelling based on beam elements, $L/D = 30$).

Element length	$P_{cr}[N]$	$\sigma_{average,vertical}$ [MPa]	$\sigma_{average,diagonal}$ [MPa]	Ratio
Isolated	14	156	2.2	70.9
Embedded (only vert. strut)	240	2620	7.3	358.9
Embedded (fully)	470	2600	330	7.88

5.1.4 Discontinuous contact model

The analyses conducted thus far assume an idealized condition concerning the transfer of stresses between the lattice structure and the elastic medium. This assumes continuous contact between the two materials, with the elastic medium consistently reacting in opposition to the deflection of the beams, irrespective of their deflection direction. However, in real-world scenarios, detachment may occur when the yield stresses of the elastic medium are surpassed.
For instance, in the case of soil serving as the elastic medium, Papachristou [143] observes that soil can only react under pressure from the beam. Similarly, for paraffin, a similar behavior is anticipated, given its very low tensile yield strength (around $1-2$ MPa). Consequently, it is likely that a crack forms between the Paraffin and the aluminum when the tensile yield strength is exceeded, resulting in a discontinuous contact between the lattice and the PCM. As noted by Cook [144], considering separation renders the problem non-linear, as both the contact pressure and the contact region are unknown at the initiation of the analysis. Therefore, this section employs a non-linear analysis to investigate the problem by progressively increasing the applied load on the structure until buckling occurs.
Due to the computational demands associated with non-linear analyses, the single strut model is utilized. The volumetric model is employed to simulate the discontinuous contact. The level of

adhesion between the two materials and the precise stresses at which detachment occurs remain unknown. A lower bound for the critical buckling load is established using a model without any adhesion between the materials, signifying exclusive contact between the strut and the foundation under pressure. For comparison, a non-linear analysis is also conducted on a model with full adhesion, analogous to the model employed in previous analyses.
To induce buckling, a perturbation in the form of a lateral displacement of $10^{-3}L$ is introduced at the node where the load is applied. A small gap of 1% of the strut diameter is defined between the strut and the elastic medium, and a contact pair model is implemented to simulate the contact between the two bodies. Apart from this, the same model is utilized as in Section 5.1.2. A diameter ratio of $\mu = 10$ is maintained for all analyses. The non-linear problem is addressed using the arc-length method, recommended for instability problems, as detailed by Vasios [145]. The buckling load is identified as the maximum load at which the maximum deflection of the strut is below a critical arbitrary value (here 0.1 mm is used), acknowledging the approximation introduced by discrete load increments.
Figure 5.22 illustrates a buckled strut with a slenderness of $L/D = 20$ using the discontinuous contact model. Notably, the deflection curve of the strut exhibits more than one half-sine wave, characteristic of the embedded case at high slenderness ratios. The figure illustrates that the elastic medium deforms solely under pressure through the bending of the strut.

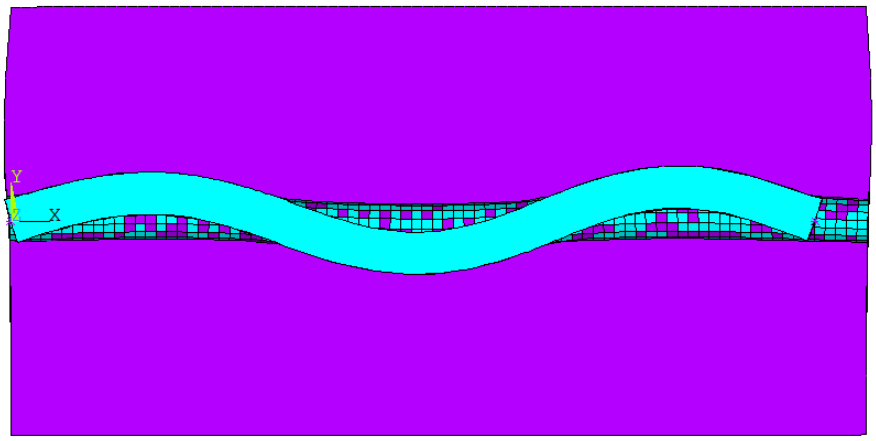

Fig. 5.22: Buckled strut ($L/D = 20$) in an elastic foundation with no adhesion between the two materials.

For the case described, several slenderness values are considered. Figure 5.23 exhibits the critical buckling stress resulting from the non-linear analysis for both the full-adhesion and the no-adhesion models. The solutions of linear eigenvalue analyses are shown for comparative purpose, for both the isolated and embedded struts. The number of half-sine waves of the deflection curve of the strut is annotated below the data points of the non-linear analyses. Interestingly, the number of half-sine waves coincides for both models with the exception of the data points at $L/D = 20$, where there is a difference of one half-sine waves between the models.

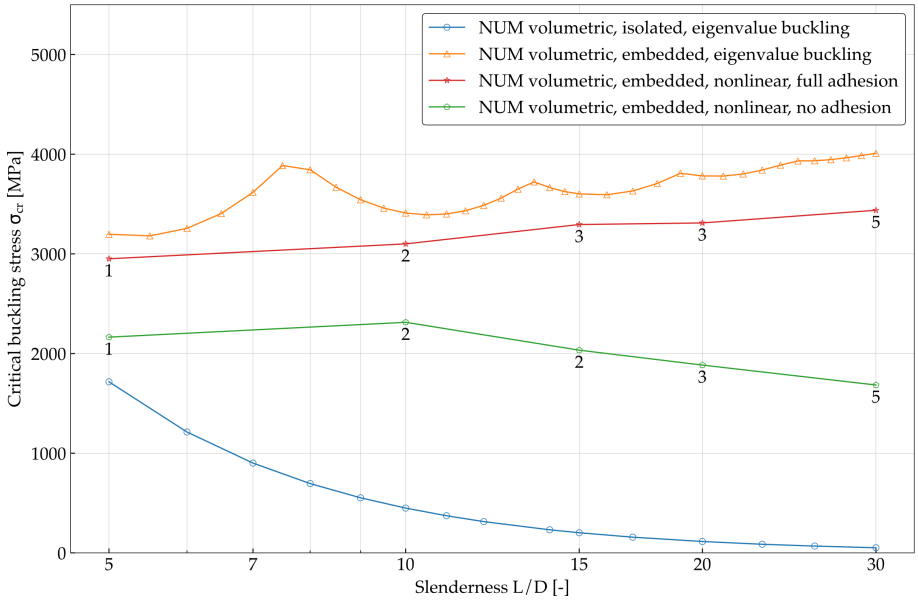

Fig. 5.23: Critical buckling stress of individual struts. The results derived through eigenvalue buckling analysis are compared to results derived by non-linear analysis. A diameter ratio of $\mu = 10$ is used for all analyses.

The model with full-adhesion shows a similar, but conservative, trend compared to the curve of the embedded strut using eigenvalue analysis. The model where adhesion is hindered indicates an opposite trend, with the critical buckling stress for $L/D = 30$ being approximately half the value of the full-adhesion model. A realistic scenario shall be found between the two extremes. The observed halving of the critical buckling stress is anticipated. In essence, for every half-sine wave in the deflection curve of the strut, the foundation exerts forces solely on one side of the strut—the side in contact. This asymmetry in force application contributes to the reduction in the critical buckling stress, aligning with expectations. Nevertheless, one should notice that even the model with hindered adhesion indicates an much higher critical buckling stress than the isolated model. Even in the worst case scenario, of a complete lack of adhesion, the critical buckling stress never falls under the yield strength of the strut material.
This indicates that, if a lattice is embedded in a PCM, buckling shall never be a failure mode of concern.
To delve deeper on these last statements, the Von Mises stresses within the elastic medium just before buckling of the strut are reported in Figure 5.24. In the absence of adhesion in the model, stress concentrations occur exclusively on the side of the strut that is in contact. Conversely, in the full-adhesion model, stress levels are significantly elevated, primarily due to the transfer of shear stresses between the strut and the elastic foundation. The analysis demonstrates that these stresses surpass the tensile yield strength of paraffin, suggesting a likelihood of detachment.

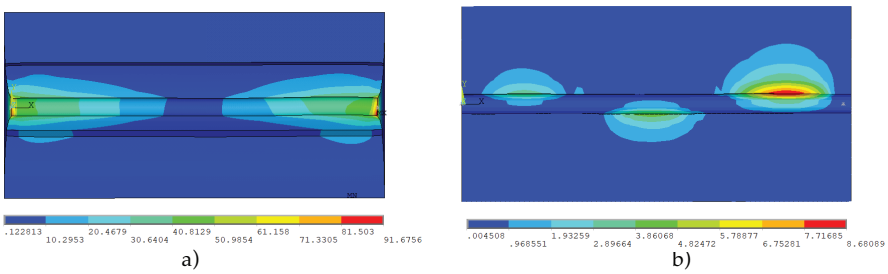

Fig. 5.24: Von Mises stresses [MPa] in the elastic foundation before buckling obtained through the non-linear analysis for the full-adhesion (a) and no adhesion (b) models ($L/D = 20$).

5.2 Experimental verification of the stability behaviour

The previous section introduced a numerical and analytical investigation on the effect of the PCM on the stability of lattice struts and cells. With successive approximations, increasingly complex models were discussed. The main, and general, takeaway is that buckling shall not be of concern for struts or lattices embedded in a PCM.
An experimental verification of the presented model is necessary. However questions about the feasibility of such verification are raised. The numerical results indicate that, in all cases, rupture failure occurs before buckling. This would be the case even at very high slenderness. Therefore, the quantitative experimental validation of the present model is not guaranteed.
One could attempt an experimental test using struts with extremely high slenderness. However, manufacturing and experimental setup limitations impede doing that with metallic alloys, while not assuring that rupture failure will take place before the buckling one. To achieve buckling failure before rupture, employing more ductile materials than the metallic alloy analysed thus far can be considered. Indeed, in this work a general purpose resin for additively manufactured plastic components is used. The resin is a proprietary compound developed by Formlabs®. A characterisation performed by Bühring et al.[40] indicates an elastic material behaviour of components based on this resin. The properties of the resin are compared to the ones of the thus far considered aluminium alloy are reported in Table 5.5.

Table 5.5: Comparison of mechanical properties of the aluminium alloy and the general purpose resin from Formlabs®.

	$E[MPa]$	$\sigma_{max}[MPa]$	E/σ_{max} [-]
AlSi10Mg	$7.5 \cdot 10^4$	396.5	189.155
General Purpose Resin	$1.6 \cdot 10^3$	38	42.1

One can see that the ratio between the Young modulus E and the ultimate tensile strength σ_{max} is 4.5 times lower than the one of aluminium, indicating that this elastic material can represent a good candidate for triggering buckling before rupture. In the following the experimental setup

and the test campaign are described. The results indicate a qualitative agreement with the model presented above, although quantitative comparisons could not be obtained.

In this chapter, a look into the design and fabrication process of the different components of the experimental set-up is given. The goal of the experiment is to analyse the influence of embedding a strut with phase change material on its buckling behaviour, or failure behaviour, when submitted to a compressive load. Different slenderness ratios are studied. Paraffin wax is selected as the phase change material for the elastic embedding, despite being classified as a viscoelastic material. Viscoelastic materials possess both viscous (time-dependent deformation) and elastic properties. In the case of paraffin wax, although it is mainly considered viscoelastic, it also shows elastic characteristics when subjected to minor deformations. The results are to be compared and validated later with those of the analytical and numerical models developed, with the same purpose. It is therefore essential to create a set-up which resembles these models as closely as possible. For this reason, a meticulous approach has been followed to design the custom-made parts tailored to fulfill the requirements as accurately as possible.

In the following pages, a step-by-step methodology employed for the design and fabrication of the pieces of the experimental set-up is laid out.

5.2.1 Experimental setup

The testing machine used to carry out the experiments is an Instron® 5567 tensile/compression testing machine. A custom test-setup is needed for this experiments. This is shown in Figure 5.25. Struts with variable length are considered, while the strut diameter is fixed to 3 mm. The Paraffin elastic bed has surrounds the strut and its enclosed within a 5 mm thick cylinder. The inner diameter of the cylinder is 90 mm, thus showing an embedding ratio $\mu = 30$.
The setup is fixed to the testing machine via a 6 mm thick base-plate, which has both the purpose of containing the paraffin when its liquid, and providing a stiff encastre as a boundary condition for the strut.

The investigated strut lengths and slenderness are displayed in Table 5.6.

Table 5.6: Strut lengths corresponding to each slenderness ratio.

Slenderness (L/D)	Length L [mm]
50	150
60	180

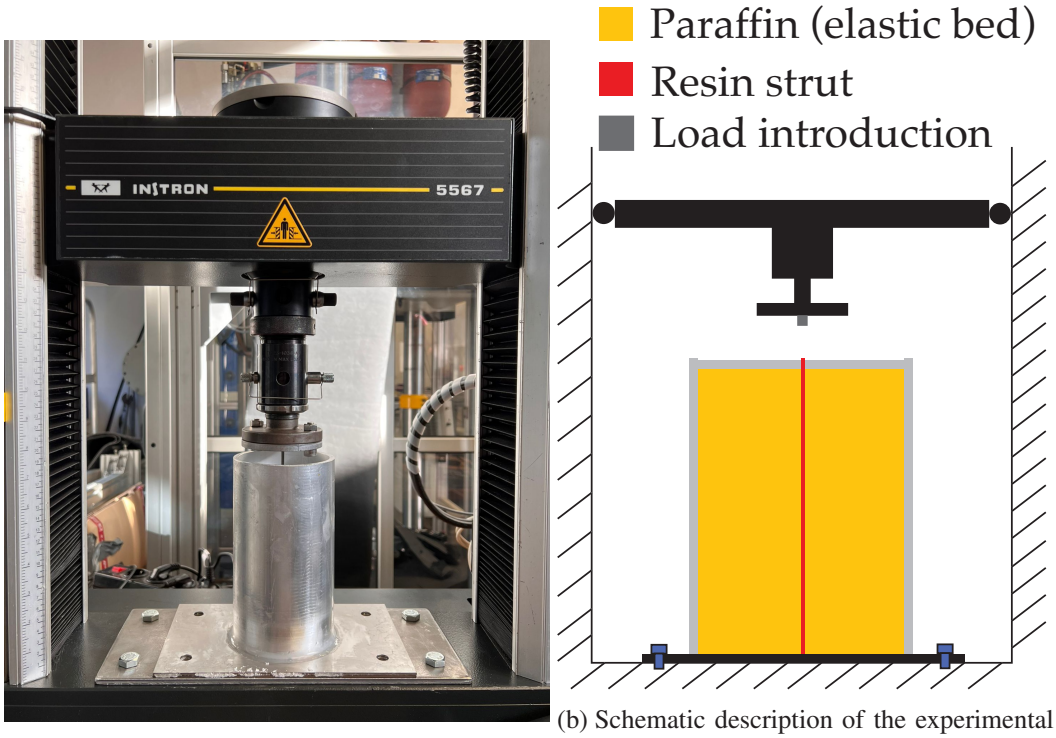

(a) Setup as built.

(b) Schematic description of the experimental set-up and its components.

Fig. 5.25: Experimental setup.

The shell carries out two main functions. On the one hand, it serves as a container of the paraffin wax, shaping the foundation. On the other hand, it is needed to simulate the boundary conditions of the spring-model explained in the theory, as it inhibits the springs from moving outwards. The shell's diameter therefore depends on the parameter μ, which defines the ratio of the diameter of the foundation to the diameter of the strut. As concluded above, a higher μ allows for a lower critical buckling load, so the aim is to have a wide enough cylinder. However, melting time of the Paraffin affects the speed at which each test can be repeated. For every test, the paraffin has to be melted first, and then solidified. These processes are carried out in a climate chamber (Espec® ARS-1100). Due to the low thermal conductivity of pure paraffin and due to the high volume of the component, approximately 4 hours are needed to melt and other 4 hours are needed to freeze the Paraffin within the setup. Thus, each test repetition requires approximately 10 hours to be executed. Due to availability reasons, such limitation imposes choosing a ratio of $\mu = 30$.

The load introduction is based on a circular steel plate with 80 mm diameter. Additionally to it, a small steel cube is bonded to the center. This serves to directly apply the load into the beam cross section, and avoiding that the load introduction device touches the paraffin elastic bed, thus affecting the boundary conditions of the experiment. The machine is set-up to interrupt the experiment once the force applied drops by more than 20% of its maximum.

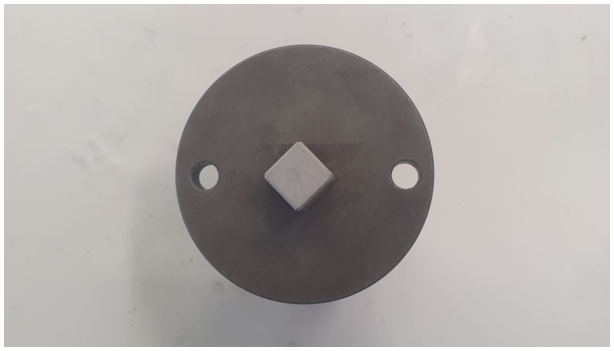

Fig. 5.26: Load introduction device.

5.2.2 Results and Discussion

In order to establish a comparability, first the test is conducted with an isolated strut of length $L = 160$ mm and no PCM surrounding it. The load-displacement curve is shown in Figure 5.27. The analytical value of the critical load, calculated via Euler Buckling formula, is 4.4 N. One can see that the applied load approaches this value, before failure due to buckling and consequent rupture. The noise which can be appreciated in the plot is due to the, sensitivity of the machine in this low scale of maximum applied load, with respect to the range of forces applicable by the machine.

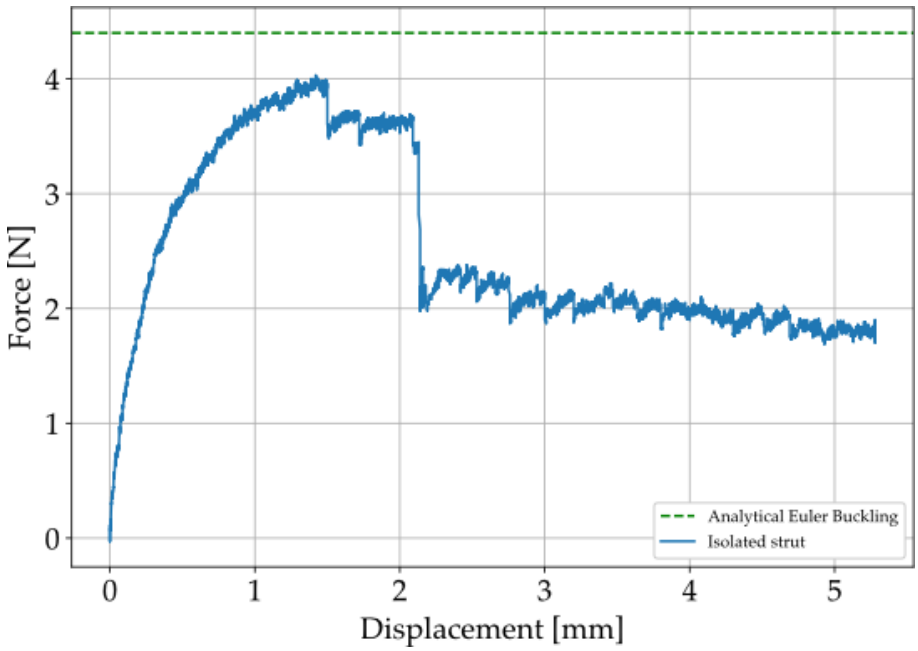

Fig. 5.27: Load-displacement curve for isolated strut, $L = 160$ mm.

The results for embedded struts are described in the following.
Figure 5.28 shows the results for all tested samples. One can notice that, in general, all tested

samples exhibit failure for loads much higher than the buckling load value for an isolated strut. This represents a qualitative validation that the buckling load is increased by embedding the strut within paraffin wax.
However, the erratic behaviour of the Force-Displacement curves and the wide deviation of the results is of concern.

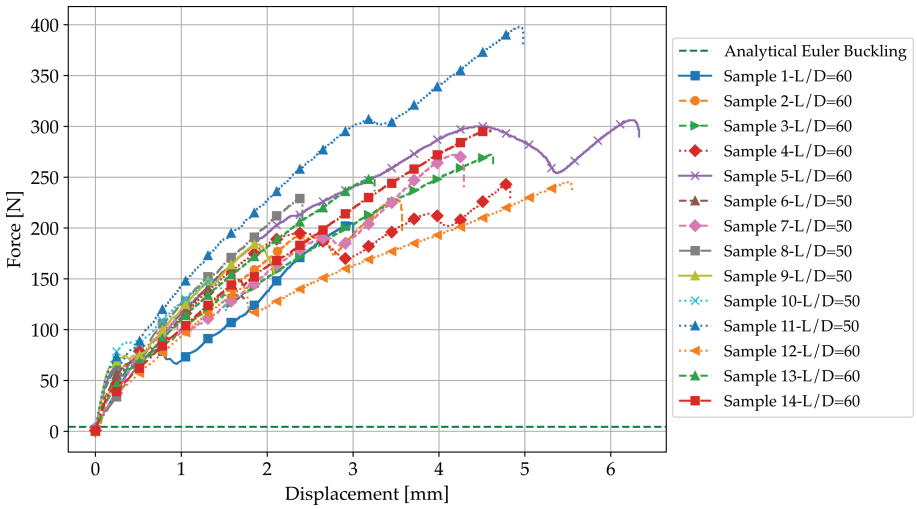

Fig. 5.28: Load-displacement curve for all samples,i.e. L=180mm and L=150mm.

As depicted in Figure 5.28, various irregularities manifest. These can be attributed to several factors, which are succinctly discussed below.
Firstly, the irregularities stem from the pre-testing cutting and filing of the struts, necessitated by the separation of the strut from the support structures. This process creates an edge, resulting in an uneven surface. Achieving a perfectly parallel surface to the applicator during cutting is unattainable, even with subsequent filing. This leads to a minor slipping motion, identified as the stick-slip phenomenon [146].
During the initial contact between the applicator and the strut, the surface asperities interlock, generating high contact pressure and static friction—a phase known as sticking. As pressure accumulates, the edge deforms until it "flattens," triggering rapid sliding, marking the stick-slip transition. Once the contact between the strut and the applicator becomes flat and complete, it reverts to a sticking phase. In this phase, a slip transition is not reached, as the load is now entirely perpendicular to the cross-section. This phenomenon recurs in subsequent tests and typically occurs around 75 N, though the specific threshold varies for each probe due to inherent differences in the cutting and filing processes.

Sample 1 in Figure 5.28 displays premature buckling leading to subsequent failure compared to other samples. This phenomenon is attributed to the local buckling of a reduced section of the beam. Analysis revealed the presence of a sizable air bubble in the upper layers of the

foundation, as illustrated in Fig. 5.29. The propensity of paraffin to trap air and form cavities during its solidification process resulted in a section where paraffin did not encapsulate the strut, consequently diminishing its contribution to stiffness. This reduction in stiffness allowed the strut to buckle under specific pressure conditions. The point of buckling is easily discernible as the initiation of instability, followed by apparent entry into the plastic region. The distinctive jerky wave formation observed can be attributed to the Portevin-Le Chatelier (PLC) effect, an unstable plastic flow characterised by serrated yielding in the temporal domain and strain localization in the spatial domain [147]. The PLC effect arises from the interaction between solute atoms and mobile dislocations during plastic deformation [148]. While more commonly associated with alloys, this instability, albeit rare, can also manifest in polymeric materials, as demonstrated in a study by Bedi et al. [149], where it hindered polymer chain movement and increased maximum tensile strength [150].

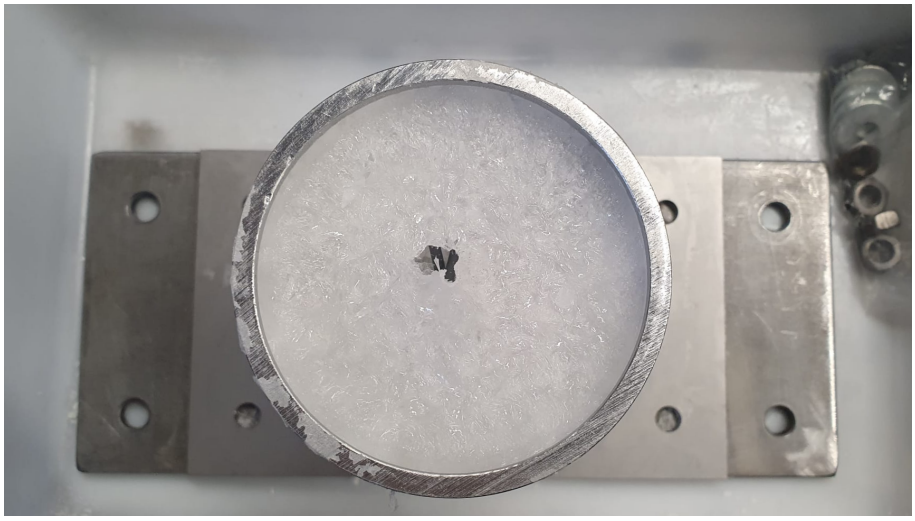

Fig. 5.29: Air bubble formed in solid paraffin foundation.

The development of air cavities within paraffin assumes a critical role in the interaction between the strut and the foundation. As elucidated earlier, this constitutes a pivotal parameter significantly impacting stability. Therefore, it is imperative to execute the solidification process with utmost control and uniformity to prevent the formation of air bubbles. To achieve this objective, all tests involve a degassing phase, accomplished by subjecting the liquid paraffin to a 40-minute vacuuming process. This step aims to eliminate as much trapped air as possible before the solidification phase.
The influence of this degassing process becomes evident when comparing Sample 3 (subjected to vacuuming) and Sample 2 (non-vacuumed), as illustrated in Fig. 5.30. The improvement of the stability is obvious, while also retarding the breaking point by almost 25% in this case, as illustrated in Table 5.7.

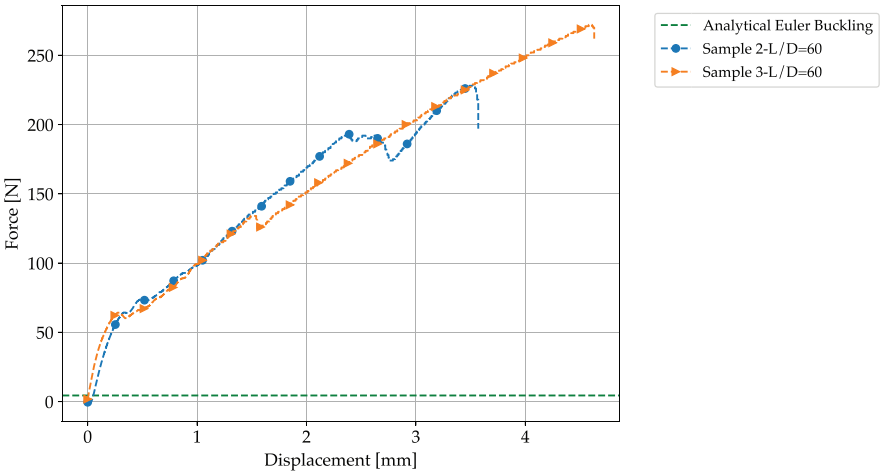

Fig. 5.30: Load-displacement curve for Samples 2 and 3, L=180mm.

Table 5.7: Test results for rupture for Samples 2 and 3.

Sample	F_{rupt} [N]	σ_{rupt} [MPa]
2	197	27.87
3	262	37.06

As the struts, constructed through additive manufacturing with resin, exhibited deformation over time, adopting a curved configuration, the validity of the experiments is jeopardized. In order to restore their original shape, certain struts underwent a heating process. While this method proved effective in rectifying the curvature, it was anticipated that there would be consequential alterations in the mechanical properties of the struts. Additionally, all struts are kept at an elevated temperature for a duration of 4 hours, due to the freezing process of the paraffin. This implied a potential unintentional curing process of the resin. To substantiate this hypothesis, a comparative analysis between heated and non-heated probes is conducted in this study.
In the case of post-cured general-purpose resin, a theoretical increase in ultimate tensile strength from 38 to 65 MPa is anticipated after 60 minutes of curing at 60°C. Although an enhancement in strength is also expected for the chosen duration of 4 hours at 45°C, as elucidated further on, characterizing the behavior of a strut cured under these conditions proves to be challenging.
The cured probe exhibits a noticeable augmentation in the stiffness of the strut, as evidenced by the slope of the curve within the linear region. Additionally, there is a discernible increase in the rupture load (Figure 5.31). Notably, the rupture load surpasses the value corresponding to the theoretical ultimate tensile strength of the resin, which is 38 MPa. This observation lends support to the notion that the heating process employed to straighten the strut induces a curing process, thereby altering the mechanical properties of the resin.

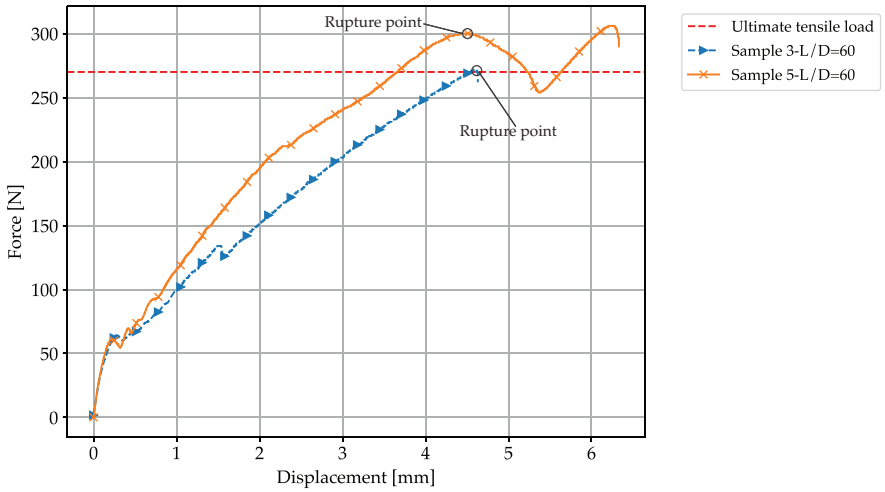

Fig. 5.31: Load-displacement curve for Sample 3 and 5, L=180mm. The two curves compare a non-cured strut (sample 3) with a cured one (sample 4).

Table 5.8: Test results for rupture Samples 3 and 5.

Sample	F_{rupt} [N]	σ_{rupt} [MPa]
3	262	37.065
5	290	41.027

As previously mentioned, the curing process results in material hardening and increased stiffness but also leads to heightened brittleness. This reduced ductility is evident in the rupture patterns of each strut. More brittle struts, particularly the cured ones, exhibit more rupture points compared to their non-cured counterparts, as depicted in Figure 5.32.

The tests show that not all cured struts display neither the same stability nor the same rupture load, which isn't the case for the real scenario. One should notice that the presence of a wide variety of rupture points can be correlated to the jittery curves shown in the previous Figures. Indeed, being the strut embedded within solid wax, even after rupture, the component retains a certain load-bearing capability as the broken pieces are stacked upon each other. The testing machine only interrupts the test when a threshold of 20% force reduction is sensed. However, due to the stacking most ruptures indicate just a reduction of the force which is below this threshold. This causes the wavy behaviour of the load-displacement curve.

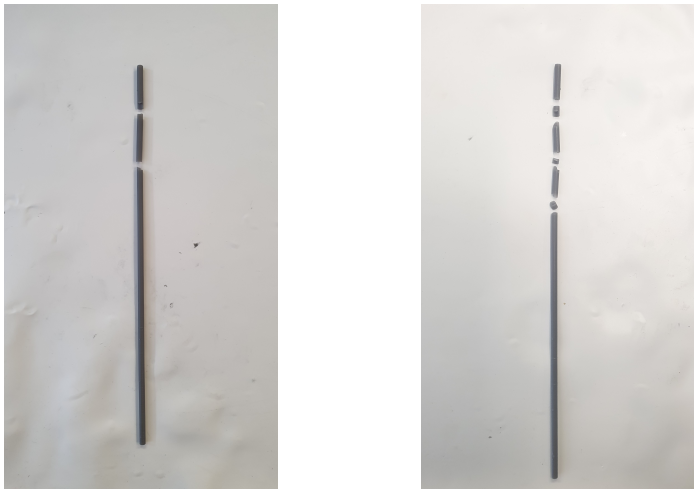

(a) Sample 2 after rupture (not cured). (b) Sample 5 after rupture (cured).

Fig. 5.32: Comparison of rupture pattern between cured and non-cured probes.

Regardless of all taken measures, the struts fail by rupture before buckling, which allows a shift in the focus of this analysis. Even though it is difficult to specifically study the buckling behaviour of the set-up, the available data and resources do render the chance of carrying out a general characterisation of the failure behaviour of the struts embedded in paraffin.
Some of the fluctuations evidenced above remain unexplained.
An irregularity which repeats itself throughout most of the force-displacement curves is the fluctuation marked in some examples in Figure 5.33. The form of the fluctuation is very similar for all tests.

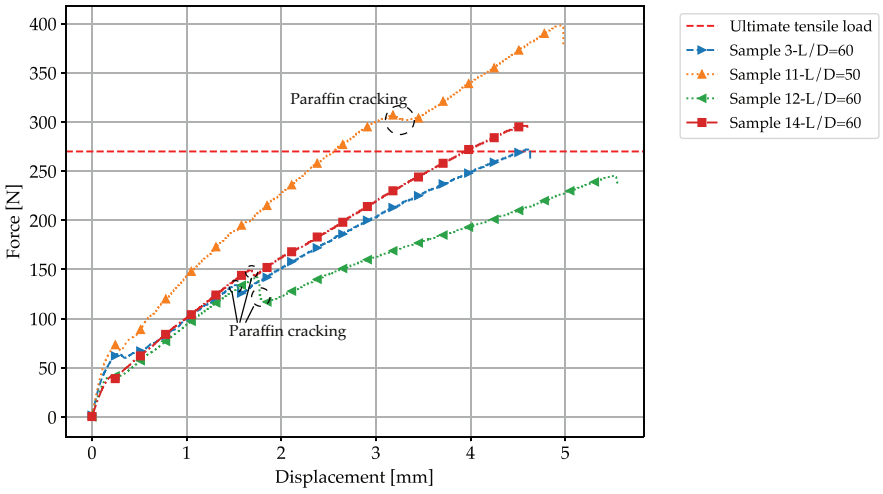

Fig. 5.33: Fluctuation caused by cracking of paraffin wax.

While providing a comprehensive definition of the solidification pattern of paraffin is challenging, it is evident that it undergoes radial freezing. The process initiates by freezing radially inward from the cylinder wall and outward from the strut. Both the strut and the cylinder possess higher thermal conductivity than paraffin, serving as nucleation points for the solidification front. This, coupled with the substantial contraction experienced by paraffin during solidification, results in the upper layer solidifying around the strut, as illustrated in Figure 5.34 (1). This leads to a less robust embedding around a short outer section of the strut. As previously mentioned, paraffin behaves as an elastic material up to small deflections; therefore, under specific loads and shear stresses from the deforming strut, it is prone to cracking. Consequently, it ceases to contribute to the stiffness of that particular section. It was observed that the layer cracking coincided with fluctuations in the machine's drawing mentioned earlier. The consistent correlation between these events suggests a causal relationship, offering an explanation for yet another irregularity observed in the curves.

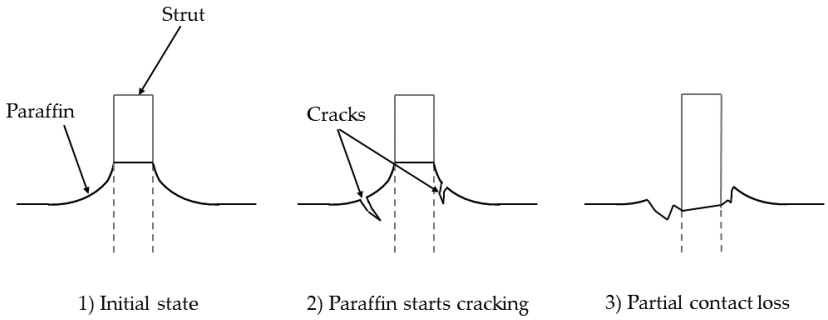

Fig. 5.34: Cracking process in the upper layer of paraffin wax.

5.3 Conclusion

The focus of the research detailed in this chapter centers on the phenomenon of local buckling within the discrete lattice struts. Both analytical and numerical examinations, employing the finite element method, reveal a discernible enhancement in the critical buckling load when PCM is introduced as an elastic medium. In the absence of PCM, slender struts are susceptible to local buckling. The incorporation of the elastic medium significantly elevates the critical buckling stresses, surpassing values well beyond the yield strength of the strut material. Consequently, this practically eradicates local buckling as a conceivable failure mode.

The numerical investigations in this study employ various models, specifically utilizing volumetric elements and beam/spring elements. In the former, the foundation is directly modeled through the material properties of paraffin, while in the latter, the rigidity of the springs is determined using the Vesic formula, approximating the modulus of the foundation from the material properties of the elastic medium. The beam/spring model, lacking simulation of shear stress transfer between lattice and foundation, tends to yield lower critical buckling loads compared to the volumetric model, providing a conservative estimation.

Analytical solutions for the critical buckling load are also presented, including a formula for the Pasternak parameter for a strut on an elastic foundation, offering a close approximation to the critical buckling load obtained through numerical analyses with volumetric elements. Analytical solutions for the critical buckling loads of unit cells are provided, though the employed equivalent member method underestimates results for embedded cells, with the identified reason elucidated in this work.

Stresses in the foundation surpass the yield strength of the foundation material during buckling, potentially causing cracks between the lattice and the elastic medium. Discontinuous contact is investigated through nonlinear analysis using a discontinuous contact model on an individual strut. The analysis reveals a reduction in critical buckling stress (approximately halved at high slenderness ratios) in the absence of adhesion between materials. This situation serves as a lower bound, as some degree of adhesion is expected. However, even with no adhesion, the model yields critical buckling stresses in the strut exceeding the yield strength of aluminum. Conclusively, local buckling is not a dimensioning concern for these composites in all considered scenarios.

Experimental validation proves challenging due to an expected lack of buckling at the strut level. Attempts to induce buckling, using softer resin struts within a paraffin-wax bed, encounter challenges such as air bubbles affecting results and unintentional curing during paraffin freezing. Despite variations in results, consistently exceeding the critical buckling load for an isolated strut without failure suggests qualitative validation of the presented model. Quantitative evaluations are hindered by premature failure, occurring before reaching the predicted critical load, and a high dispersion of results due to the aforementioned factors, necessitating caution in interpreting actual failure load values.

5.3.1 Prospects

This study was conducted under the assumption of a solid paraffin, recognizing that the state of the PCM will evolve during its operational lifespan. Particularly intriguing is the exploration of the impact of a molten PCM on the buckling behavior of the lattice structure. It is hypothesized

that if the molten PCM imparts pressure on the upper and lower plates of the lattice-core sandwich structure, and the pressure differential to the external environment is positive, an axial load should ensue, countering the compressive load. Consequently, even in such a scenario, buckling is anticipated to be a negligible concern.

Global buckling has not been addressed in this work, as the practical application of slender lattice-PCM structures remains unclear. However, future investigations may delve into the realm of global buckling. Another promising avenue for research is the dynamic behavior of lattice structures filled with PCM. Subsequent studies can build upon prior research on vibrational analyses of lattice structures filled with foams, such as the one presented by Yang et al. [151].

-

6 Multivariate Topology Optimisation

Having introduced the thermal and mechanical characterisation of the treated composites, the subsequent focus pertains to the potential design considerations. Specifically, the optimal design under mass constraints becomes imperative. Thermal control requisites may result in configurations diverging from those dictated solely by structural considerations.
The introduction of mass constraints in a multi-functional structural component is coupled with diverse objective functions. Thus the design necessitates engagement with optimisation procedures. Given the potential conflict between functional and design requirements, optimal compromises must be identified during the design of such components that fulfill integrated functionalities. In essence, a lattice structure tailored for load-bearing purposes may not inherently serve as an effective medium for enhancing thermal conductivity in a PCM, and vice versa. The assessment of geometric configurations that meet both structural and thermal criteria while minimizing mass entails employing multivariate optimisation. This linkage is inherently tied to a topology optimisation algorithm, which constitutes the focal point of this chapter.
In summary, designing lattice-PCM composites for either thermal or structural functionality in parallel is futile. The imperative is to integrate constraints, compelling the utilization of topology optimisation algorithms as a standard design strategy for achieving a holistic, coupled design approach.
Thus, here a multivariate topology optimisation is presented, which is capable of generating a component that is optimal for both structural and thermal purposes. The tool is developed in the *Julia* language and makes use of Automatic Differentiation (AD) to accelerate the evaluation of gradients necessary to perform the optimisation procedures. While this represents a fundamental novelty of this work with respect to the literature, the same results could be achieved with normal iterative procedures. Therefore, the basic notions on dual numbers and AD are reported in Appendix K.

In general, the structural design tends to minimize a compliance function of the domain considered, in order to achieve a maximum stiffness and strength with the minimum mass possible. Thermal control requires a high thermal diffusivity of the component, but also, for the case of a PCM embedded in porous metallic media, an energy-storage potential, which limits the range of feasible porosity which the lattice structures can be designed with.
It is rather clear that the optimal topology for a purely structural design deviates from the one of a purely thermal one. Figure 6.1 shows the different results of the same domain, optimised for structural and thermal problems separately. Structural topology optimisation of a continuum domain tends to generate truss-like structures (Figure 6.1a). Thermal optimisation, on the other hand tends to generate tree branch-like structures (Figure 6.1b). The question is thus raised, on

how the combined optimal design of such a component shall be approach.

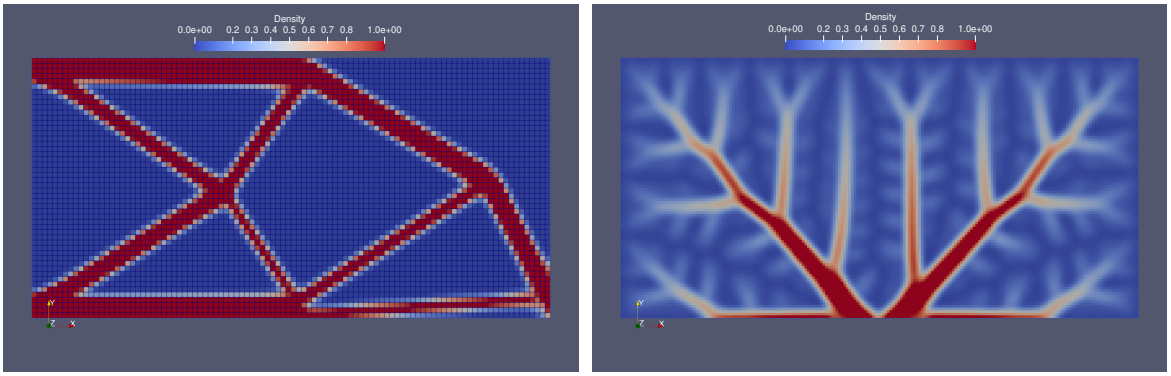

(a) Example of the result of an optimal topology with stiffness as a goal function.

(b) Example of the results of an optimal topology with thermal conductivity as a goal function.

Fig. 6.1: Examples of different optima for continuum mechanic and thermal problems, in which the material within the domain can range between 0 (no material) and 1, where 1 represents the considered solid material.

To address this, a multivariate topology optimisation is described in this chapter. The goal is to present the framework of a tool capable to merge the different optima in a single component, accepting a deviation from so-called Utopia Points, which represent the optima for each single variable considered. With use of a Pareto front, the optimal design is then found.
The following sections describe first the approach utilized for the topology optimisation of the single functions, in order to then describe the methods employed to achieve a global optimum.

6.1 Single functional optimisations

The homogenised lattice properties are needed in order to ascribe the effective properties to the single finite elements of the domain. To this goal, the porosity is calculated with the formulae presented in Chapter 3. The effective thermophysical properties are the ones presented throughout this work as well. The effective stiffness is calculated with means of the formulae proposed by Bühring et al. [40].
The assumption is made, that the unit cells have a fixed cell size, as well as a fixed aspect ratio angle of 45°, i.e. cubic unit cells. The definition of a porosity equal to 0 or 1 makes no physical sense, as in such case an homogeneous material would be defined. However, the relative density function for the topology optimisation must range between 0 and 1. Thus, the relationship between the relative density ρ^* of the topology optimisation program, and the porosity ε is given by Equation 6.1.

$$\varepsilon = \rho^* \left(\varepsilon_{min} - \varepsilon_{max}\right) + \varepsilon_{min} \tag{6.1}$$

In general ε_{min} and ε_{max} can be chosen as small, and as big as desired, respectively. However, it is reasonable to chose these values within feasible manufacturing and design constraints. In this work, a minimum of 2.5% and a maximum of 25% are considered.
The topology optimisation results in a distribution of relative densities, which univocally correlates to a distribution of porosity. The geometry is defined inverting the relationships between porosity and cell size, strut radius, unit cell morphology and aspect ratio angle (Section 3). Being the cell size and the aspect ratio fixed, with help of a root finding algorithm based on the Newton's method, the radius is found. The Newton's method is a gradient-based method. To reduce the computational time, the gradients required are calculated via automatic differentiation, with help of the *Julia* library *ForwardDiff* [152].

A classical SIMP method is implemented to perform the topology optimisation. A schematic flow chart of the fundamental steps is shown in Figure 6.2.

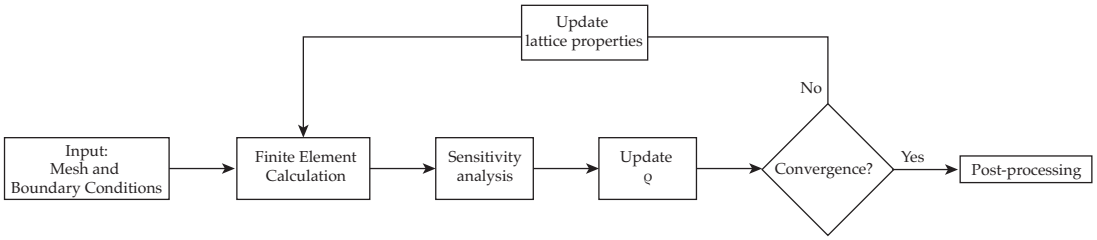

Fig. 6.2: Flow chart of a single functional optimisation.

The Finite Element problem is assembled using the dedicated toolbox *Ferrite.jl*. The elements are linear and Gauss quadrature rules are implemented. The sensitivity is computed as in Equation 2.94 for the structural problem, or as in Equation 2.96 for the thermal one. The update of the relative density follows the procedure described by Kim et al. [108], which is described in section 2.5.1.
The minimisation of the compliance for both the structural and the standard thermal problem represents a well-known problem. The implementation for the purpose of this work does not deviate from common works in the literature, except that the element properties are orthotropic, due to the generally orthotropic nature of both the stiffness matrix and effective thermal conductivity of the lattice structures.
The phase-change problem, instead requires additional effort. Some authors already proposed topology optimisation schemes for PCMs [153, 154, 155, 156]. The phase-change problem intrinsically represents a transient non-linear one. One challenge arises from the complexity of computing the derivative of the compliance. As described in Equation 2.95, the compliance is defined in a manner that does not readily lend itself to straightforward differentiation. In the context of transient phase change problems, utilising the conventional approach for deriving

element sensitivities becomes impractical.
To overcome this hurdle, a fresh derivation is pproposed by initiating with the compliance gradient, as illustrated in Equation 6.2, with **T** - temperature tensor and the forcing vector **f**. The intricacies of this derivation, crucial for addressing the transient phase change problem, are described in detail in Appendix L.

$$\frac{\partial c}{\partial \rho^*} = \frac{\partial \mathbf{T}^T}{\partial \rho^*}\mathbf{f} + \mathbf{T}^T \frac{\partial \mathbf{f}}{\partial \rho^*} \tag{6.2}$$

The primary challenge with the given equation lies in the term $\frac{\partial \mathbf{T}}{\partial \rho^*}$, which poses difficulties in computation. While automatic differentiation, particularly with the *ForwardDiff* library, could be a potential solution, its efficiency is compromised. This is primarily attributed to the fact that, during the forward pass, each dual variable is traced through the entire program, despite most of them exerting no influence on the final result. This inefficiency becomes pronounced because the forcing vector **f** is predominantly composed of zeros. An alternative approach involving reverse mode automatic differentiation is considered, but it demands substantial memory resources, especially when multiple Newton iterations are necessary to resolve non-linearity. To circumvent these challenges, a manual derivation of the gradient was undertaken. The $\frac{\partial \mathbf{T}}{\partial \rho^*}$ term was computed manually, as automatic differentiation methods proved to be impractical. It's noteworthy that the latent heat vector and latent heat matrix also evade automatic differentiation due to their dependency on the gradient of the temperature vector with respect to the relative density. Utilizing automatic differentiation for their computation would entail performing the entire simulation with this method, which contradicts the intended avoidance of such an approach.
For these reasons, the results presented in this work are limited to the multi-functional optimisation of the structural and thermal conductivity problems.
While an accurate treatment requires the consideration of the phase-change problem, the results of the thermal conductivity optimisation are still valid for the phase-change one within a certain range of lattice volume fractions.
Indeed, as shown in Section 4.1.3, the energy stored via latent heat monotonically increases with the thermal conductivity, till a peak is reached at a volume fraction of approximately 0.5. In this work, such values are not approached, thus it is reasonable to assume that the results of the thermal conductivity optimisation are still valid for the phase-change one.

6.1.1 Results of single functional optimisations

The structural, the thermal, and the phase-change optimisation problems are solved first as a single functional optimisation. The same domain is chosen, which is then used for a multi-functional optimisation.

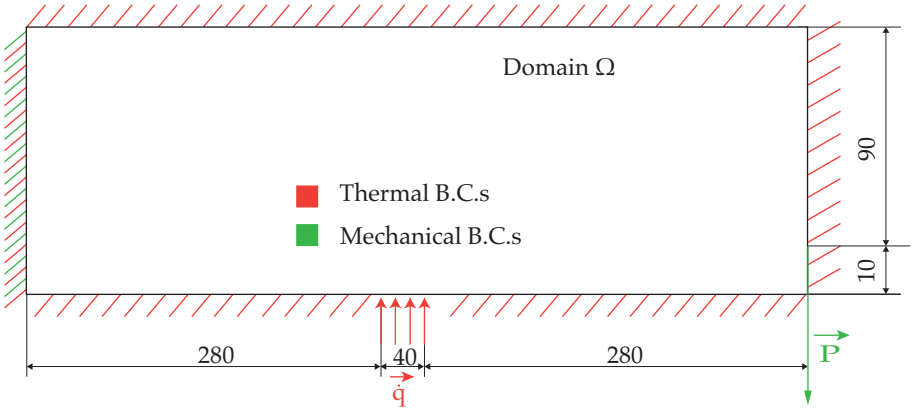

Fig. 6.3: Schematic description and measurs of the domain considered for topology optimisation. In green the boundary conditions for the structural problem, which resembles a cantilever beam. In red, the thermal boundary conditions, which resemble a heat source of, e.g., a power dissipation of electronics unit, with otherwise adiabatic boundaries.

For the discretatisation of the domain, the opensource program *Gmsh* is used. 2D elements, based on the algorithm "Frontal-Delaunay for Quads" are used. The post-processing is done with help of *Paraview*.
For each problem, both the **mesh convergence** and the **filter radius refinement** studies are presented. These are intertwined problems, which cannot be treated in a disjunct fashion. As delineated in section 2.5.1, employing a filter is imperative in topology optimisation to mitigate the checkerboard issue. However, a notable drawback of incorporating a filter is the transformation of the optimisation problem, leading to a deviation from the original one [19]. Consequently, the obtained topology is contingent upon both the chosen filter radius and the mesh fineness. A finer mesh permits the use of a smaller filter radius, consequently generating higher-resolution structures.
The results are reported for both a generic topology optimisation, and a lattice structure topology optimisation, and a comparison is made. The volume fraction is constrained for all problems at 0.2.

6.1.2 Structural solution

Figure 6.4 shows the results of the mesh convergence and filter radius analysis for a purely structural problem, i.e. where the material properties are based on a pure, isotropic aluminium alloy, and the relative density ρ^* represents the amount of material present in the domain. Table 6.1 reports the calculated values of compliance for the considered combinations of mesh size and filter radius. As one can appreciate from Figures 6.4a - 6.4e, the checkerboard pattern affects the solutions with a coarse mesh, as well as the ones with a finer mesh, but a filter radius which is smaller than element size. However, as shown in Figure 6.4g, the filter radius shall be

as small as possible. Indeed Figures 6.4h and 6.4f produce results where the material within the domain is particularly non-binary, which is a non-physical solution. As shown in Table 6.1, a sweet spot is identified when the filter radius is slightly higher than the element size, and the mesh convergence is reached.

Table 6.1: Compliance values for different combinations of mesh size and filter radius. The percentual deviation from the lowest compliance is reported in parenthesis.

	Mesh size 5mm	Mesh size 2.5mm	Mesh size 1.25mm
Filter radius 5mm	$1.754 \cdot 10^{-5}$ (23.9%)	$1.918 \cdot 10^{-5}$ (35.5%)	$1.964 \cdot 10^{-5}$(38.7%)
Filter radius 2.5mm	$1.749 \cdot 10^{-5}$ (23.5%)	$1.618 \cdot 10^{-5}$(14.3%)	$1.531 \cdot 10^{-5}$(8.1%)
Filter radius 1.5mm	$1.749 \cdot 10^{-5}$ (23.5%)	$1.618 \cdot 10^{-5}$ (14.3%)	$1.416 \cdot 10^{-5}$ (-)

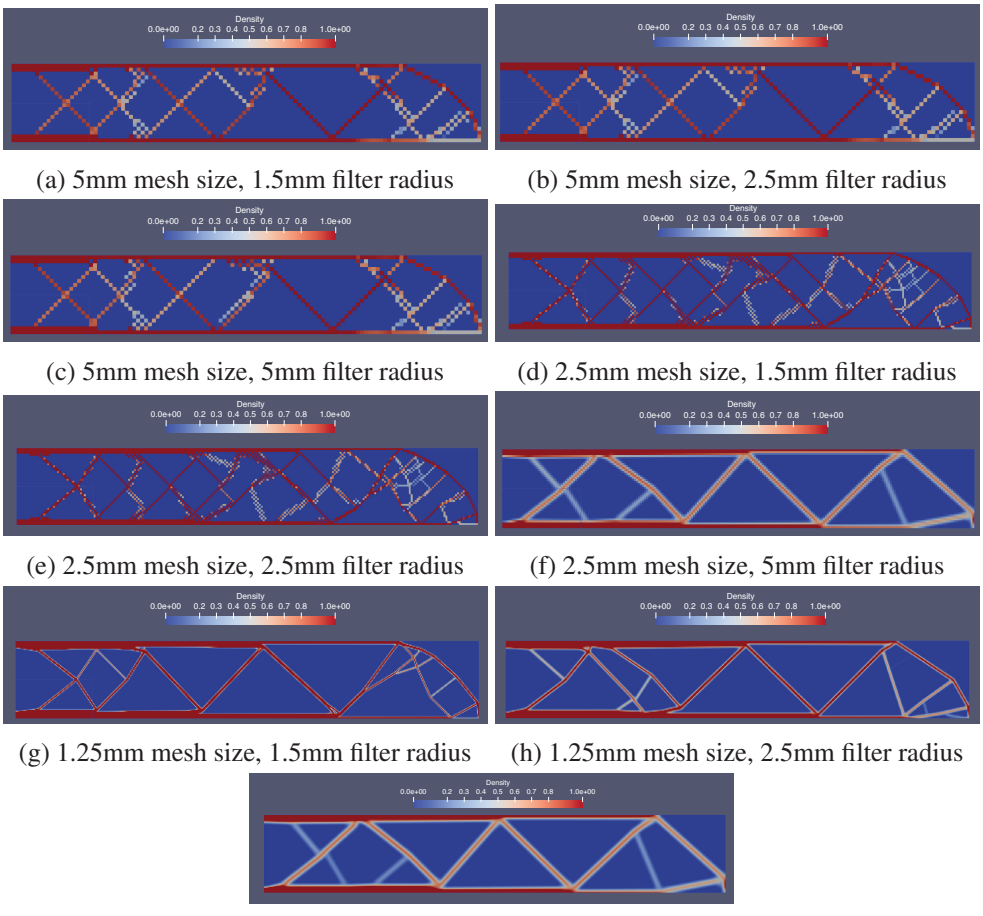

(a) 5mm mesh size, 1.5mm filter radius (b) 5mm mesh size, 2.5mm filter radius

(c) 5mm mesh size, 5mm filter radius (d) 2.5mm mesh size, 1.5mm filter radius

(e) 2.5mm mesh size, 2.5mm filter radius (f) 2.5mm mesh size, 5mm filter radius

(g) 1.25mm mesh size, 1.5mm filter radius (h) 1.25mm mesh size, 2.5mm filter radius

(i) 1.25mm mesh size, 5mm filter radius

Fig. 6.4: Combined results of the mesh convergence and filter radius refinement analysis for the purely structural problem. Generic, isotropic material properties are assumed. The full material is represented by an aluminium alloy with Young's modulus equal to 70GPa.

Lattice structures

The use of lattice structures imposes the use of an orthotropic material tensor. The values are obtained from Bühring et al. [40].The resulting structure diverges from the typical outcome of topology optimisation, which typically yields a structure resembling a truss. Instead, the obtained result exhibits apparently disconnected regions. It is crucial to acknowledge that these seemingly empty regions actually consist of cells with 2% volume fraction. In practice, each of these regions is interconnected by cells with relatively high stiffness. Increasingly higher stiffness is needed only in the regions where the bending stress is highest, i.e. top and bottom areas, and close to the fixed boundary.
Only a slight difference can be appreciated between the results for the *bcc* unit-cell (Figure 6.5a) and the f_f2ccz one (Figure 6.5b). This is because the stiffness for cubic unit cells (aspect ratio angle $\gamma = 1$) is similar in the 1,2-directions, while it differs only in the 3-direction, which is not particularly relevant for the considered case.

$$D = \begin{pmatrix} \frac{E_x}{1-\nu_{xy}\nu_{yx}} & \frac{\nu_{xy}E_y}{1-\nu_{xy}\nu_{yx}} & 0 \\ \frac{\nu_{xy}E_y}{1-\nu_{xy}\nu_{yx}} & \frac{E_y}{1-\nu_{xy}\nu_{yx}} & 0 \\ 0 & 0 & G_{xy} \end{pmatrix} \tag{6.3}$$

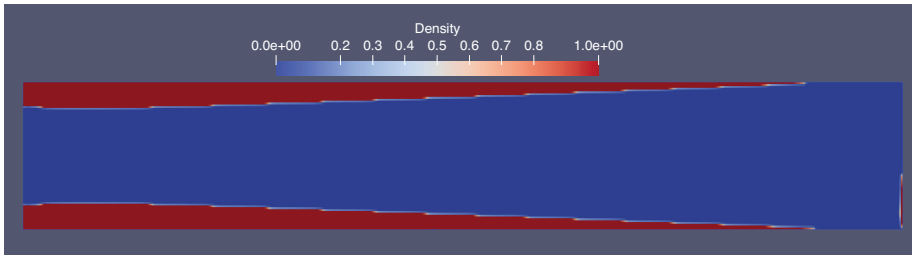

(a) Result for a domain filled with *bcc* unit-cells, with volume fraction χ varying from 2% to 20%.

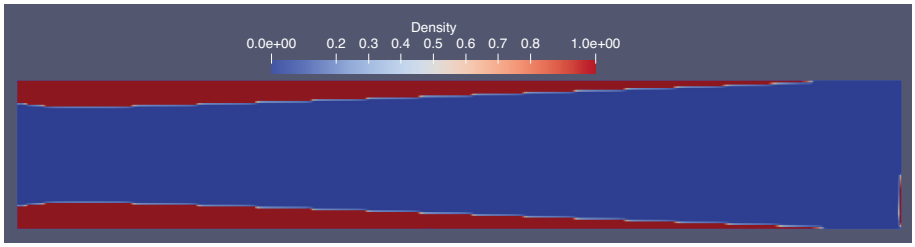

(b) Result for a domain filled with f_2ccz unit-cells, with volume fraction χ varying from 2% to 20%.

Fig. 6.5: Results of the stiffness maximisation for lattice structures with volume fraction χ varying from 2% to 20%.

6.1.3 Thermal conductivity solution

The thermal solution differs not only in shape, but only in the behaviour of the compliance. The mesh convergence is reached relatively fast. However, the filter radius analysis shows that a finer radius would be needed. For sake of brevity, Figure 6.6 shows only the result for the combination of 1.25 mm element size and 1.5 mm filter radius. One can appreciate that, even with such a fine mesh, whitin the domain a big number of elements exhibits a relative density ρ^* which is intermediate between 0 and 1. This indicates that a further reduction of the filter radius would be appropriate. However, in order to avoid incurring in the checkerboard problem, a further mesh size reduction is needed, which comes with increased computational cost and reduced benefits. Figure 6.6b shows the results for a 1mm mesh size and filter radius of 1.1mm, which requires a 15% longer computational time. The results almost overlap, while intermediate densities are still present.

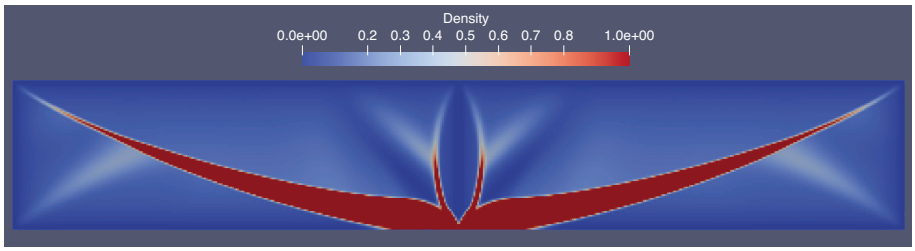

(a) Topology for the thermal optimisation with 1.25 mm mesh size and 1.5mm filter radius.

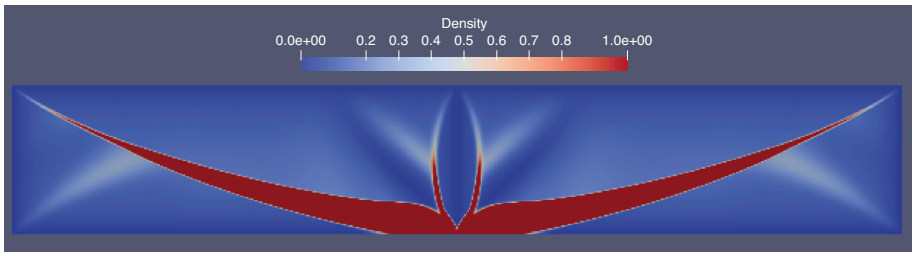

(b) Topology for the thermal optimisation with 1mm mesh size and 1.1mm filter radius

Fig. 6.6: Results for finer mesh and filter radii, but an already achieved convergence on the compliance. The intermediate densities indicate that a further refinement would be needed.

As already mentioned, the intermediate densities have no physical meaning in this conventional topology optimisation. In a lattice structure topology optimisation, they do. Indeed, recalling Equation 6.1, an intermediate value of ρ^* indicates a specific value of the lattice volume fraction. This can be exploited to ones advantage, as long as mesh converge is achieved.

Lattice structures Figure 6.7 shows the optima for both the *bcc* celltype and the f_2ccz one. The volume fraction χ varies between 2% to 20%, i.e. a relative density $\rho^* = 0$ correspondes to $\chi = 0.02$, while $\rho^* = 1$ corresponds to $\chi = 0.2$. The results differ strongly. This is due to the orthotropic nature of the f_2ccz unit-cell. The effective thermal conductivity in 1,2-direction is much smaller than the one in 3-direction. This imposes that, in order achieve an optimal heat dissipation from the central heat source, more material is placed in the lateral direction, rather than what shown for the *bcc* case, which resembles more the results shown in Figure 6.6.

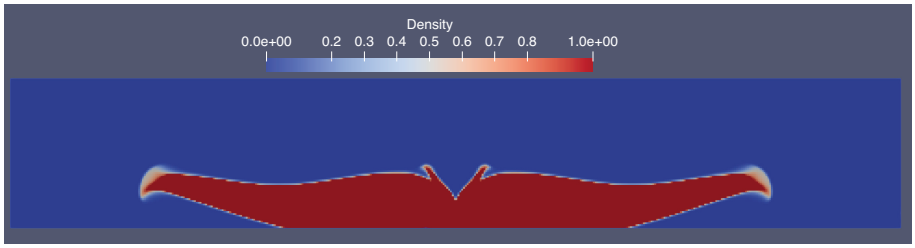

(a) Result for a domain filled with *bcc* unit-cells.

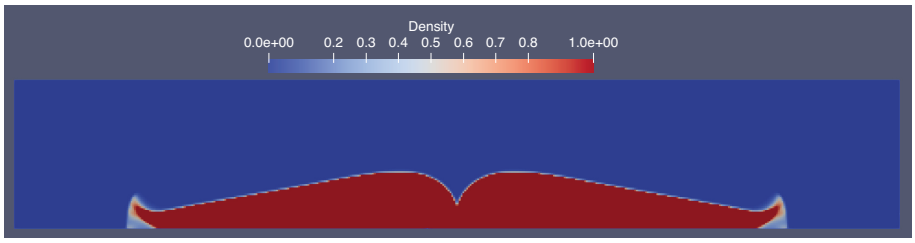

(b) Result for a domain filled with f_2ccz unit-cells.

Fig. 6.7: Results of the thermal conductivity maximisation for lattice structures with volume fraction χ varying from 2% to 20%.

6.2 Multi-functional optimisation

Having established the effectiveness of single-functional optimisation methods, the next step involves integrating them into a multi-functional optimisation framework. This entails combining the two distinct functions into a unified objective function, enabling the determination of an optimal solution. In this work, the weight method has been employed for this purpose.
Another viable approach is the constraint method, wherein one function acts as a constraint on the other. However, a limitation of this method is that the resulting optimal structure may satisfy one constraint but not the other. The trade-off between the two constraints might impose undue strictness on the unconstrained function. While it is possible to iterate towards the true minimum with this method, the weight method was selected for its elegant and practical qualities.
The weight method imposes a constraint that the sum of the weights must equal one [20]. This technique transforms multiple objective functions into a unified equation. Equation 6.4 illustrates the single objective function applied to normalised thermal (c_t^*) and structural (c_s^*)

compliance, w being the weight.

$$J(w,\rho^*) = wc_t^*(\rho^*) + (1-w)c_s^*(\rho^*) \tag{6.4}$$

To ensure reasonable results, both functions are normalised, aligning their compliance values to a comparable scale. This normalisation also ensures that the gradients of each individual objective function are of a similar order. For sensitivity analysis, Equation 6.4 is differentiated with respect to the relative density, ρ^*, as demonstrated in Equation 6.5.

$$\frac{\partial J}{\partial \rho^*} = w\frac{\partial c_t^*}{\partial \rho^*} + (1-w)\frac{\partial c_s^*}{\partial \rho^*} \tag{6.5}$$

This approach allows for the generation of a Pareto front by varying the weight between 0 and 1, where the extremes correspond to the single-function objective.
Figure 6.8 presents three optimal configurations achieved with varying lattice configurations: without lattices (Figure 6.8a), with a domain filled with *bcc* unit-cells (Figure 6.8c), and with a domain filled with f_2ccz unit-cells (Figure 6.8b), all corresponding to a weight value of $w = 0.66$.
The result depicted in Figure 6.8a suggests the achievement of an optimum by blending the two solutions. The structure is characterised by full material at the top and bottom of the domain, serving structural purposes, with recognizable truss-like strands. Additionally, originating from these trusses, tree branch-like strands emerge within the domain, aiming to maximise thermal conductivity. Notably, the thickest trusses, emanating from the bottom-central area of the domain, serve a dual purpose of structural support and thermal optimisation.
As observed in preceding sections, the growth of elements within the domain is influenced by lattice structures properties. Nevertheless, a comparable trend is discernible between Figures 6.8c- 6.8b, and 6.8a. Denser unit-cells accumulate near structural boundaries and the heat source. Two strands can be identified, diverging in a direction approximately similar to the primary strands in Figure 6.8a, primarily serving a thermal purpose. It is also interesting to notice that the growth within the domain for the f_2ccz case (Figure 6.8b) is reduced with respect to the *bcc* one (Figure 6.8c. This is due to the higher thermal conducitivy in 3-direction of the first. The opposite can be said about the lateral direction, which involves the 1,2 components of the effective thermal conductivity tensor.

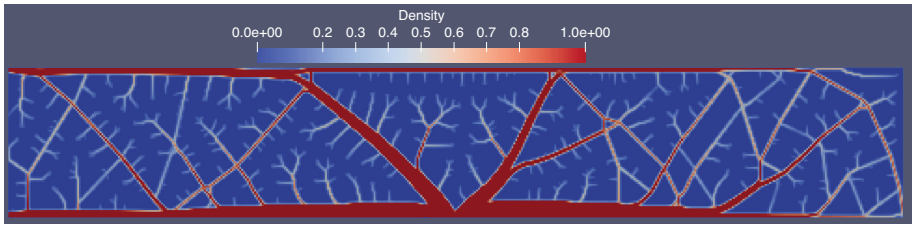

(a) Result for a domain based on standard material properties.

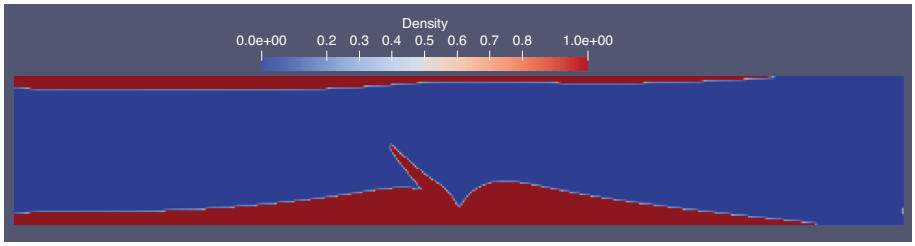

(b) Result for a domain filled with f_2ccz unit-cells.

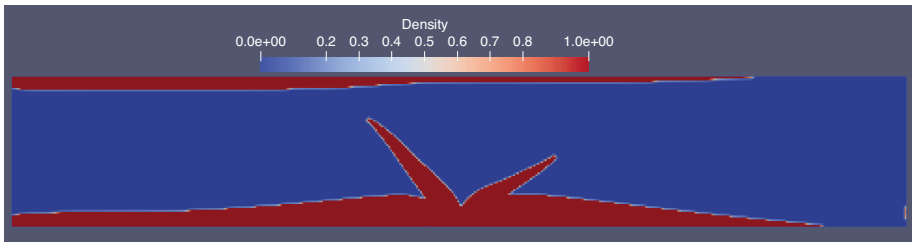

(c) Result for a domain filled with *bcc* unit-cells.

Fig. 6.8: Comparison of the multi-functional optimum for a weight $w = 0.66$.

6.2.1 Pareto optimality

The result shown in Figure 6.8 represents the optimal structures for a generically chosen value of the weight w.
An appropriate search for a global optimum is obtained by finding a value of w which is the closest to an unfeasibily optimal point. Such point is named utopia point, and its coordinates are the compliances of the purely thermal and the purely structural optima, coupled.
While the generation of a Pareto front for a given set of weights is feasible, it constitutes a computationally intensive process, devoid of a guarantee of identifying a true optimum. Thus, employing an iterative approach becomes imperative to approximate the minimum effectively. It is essential to emphasise that the compliance for each problem remains indeterminate until a topology optimisation is executed. Additionally, the construction of the Pareto front shape necessitates a priori knowledge, prompting the proposed iterative optimisation strategy illustrated in this work.

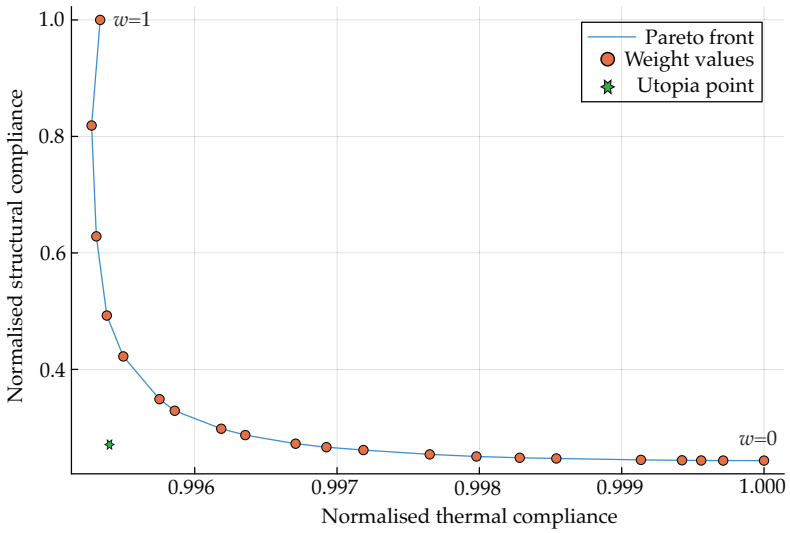

Fig. 6.9: Pareto front of the normalised compliances, for the weight w ranging from 0 to 1 with a spacing of 0.05. A weight $w = 1$ correspond to a purely thermal optimisation, and a weight $w = 0$ is a purely structural optimisation.

Under the assumption of convexity in the Pareto front, a singular point of minimal error is anticipated. The convergence rate is intricately tied to the precision of the initial estimate. Formulating an accurate initial guess hinges on an understanding of the bounds of the Pareto front. However, a generalised empirical determination of these bounds proves improbable due to the specific variability nature of forces, heat fluxes, and domain shapes and sizes. Instead, the bounds are derived through the optimisation of single-functional problems. This optimisation yields the compliance range for each problem and facilitates the normalisation of the single-functional compliances, which is used to plot the Pareto front in Figure 6.9.
A first guess has to be made, regarding the optimal point in the feasible range. As only the utopia point is known, the first guess is estimated by projecting the utopia point onto the segment joining the extremes, i.e. $w = 0$, $w = 1$. Then, the true optimum is iterated to. This is done via *quadratic fit search*, as described by Kochenderfer and Wheeler [20]. This method iteratively fits a parabula to three bracketing points. Then it solves for the minimum, and repeats till a given tolerance is reached. The method is gradient-free and is appropriate for convex problems. The assumption of a convex Pareto front is fundamental for the success of this method. A concave function would mean that several local minima can be found. However, for the specific case considered, it is found that the two functions tend to contribute to each other, thus the Pareto Front is always convex.

6.3 Results and Discussion

The results displayed so far are functional to describe the methodology implemented and the differences with respect to a standard-topology optimisation.
In the following, the results of this novel method are introduced. In particular, the results for both the *bcc* and the f_2ccz lattice structure unit-cells are considered. First the optimal weight is sought through the procedure described above, then the topology is optimised for the found value of w.
It is useful to remind that the topology optimisation is a mass-constrained procedure. The mass of the resulting domain is fixed via a volume fraction value, which is not the volume fraction of the lattice structure. The two are related via the relative density function, as described in Equation 6.1. Here, a minimum porosity of the lattice structure of $\varepsilon_{min} = 98\% = \varepsilon(\rho^* = 0)$ is considered, while the maximum lies at a value of $\varepsilon_{max} = 80\% = \varepsilon(\rho^* = 1)$. Thus, the domain volume fraction which is fixed as a constraint indicates the average porosity of the lattice structure, i.e. a domain volume fraction of 0.1 corresponds to an average ε throughout the domain equal to 98%. Similarly, a volume fraction of 0.3 corresponds to an average ε of 94%.
In the following, the results for different values of volume fraction, ranging from 0.1 to 0.5 are presented to exemplarily show how the variation of the volume fraction affects the growth of the material within the domain.

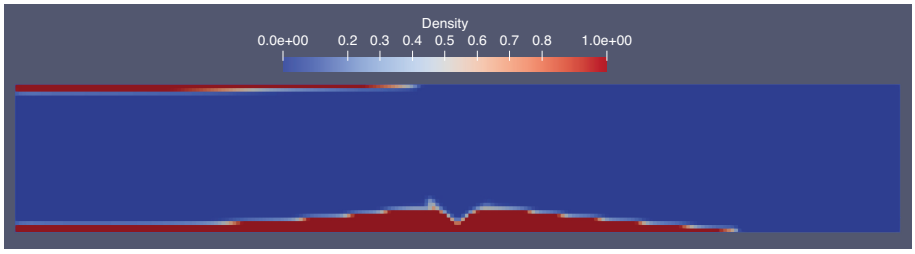

(a) *bcc* unit cells, weight $w_{opt} = 0.63$.

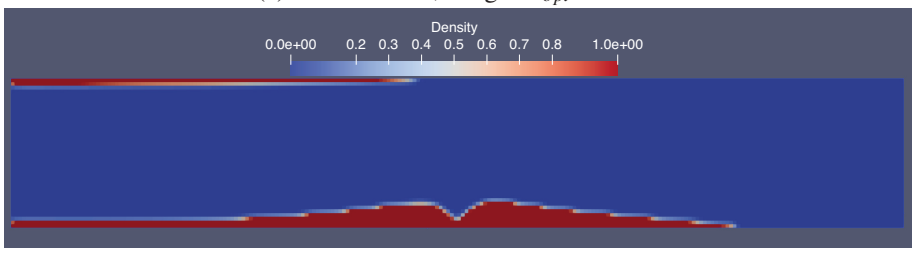

(b) Pareto optimal structure for a domain filled with f_2ccz unit cells, weight $w_{opt} = 0.65$.

Fig. 6.10: Pareto optimal structures for *bcc* and f_2ccz unit-cells, volume fraction 0.1.

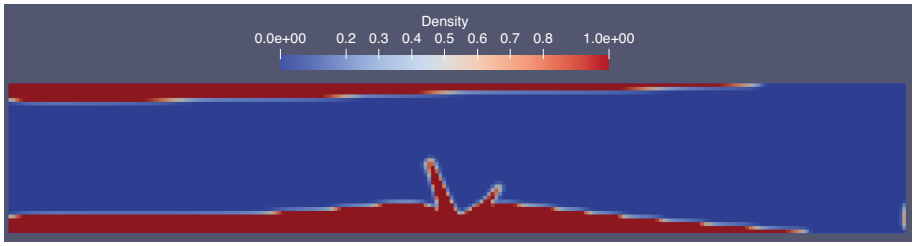

(a) Pareto optimal structure for a domain filled with *bcc* unit cells, weight $w_{opt} = 0.5$.

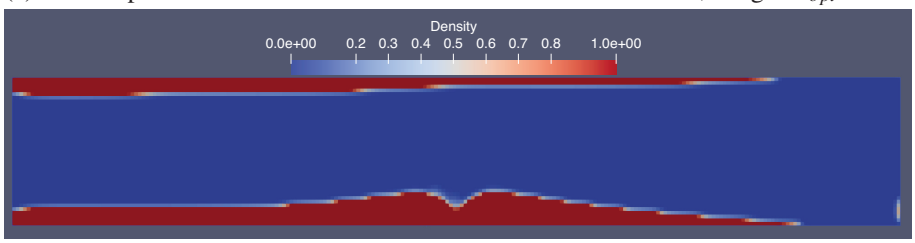

(b) Pareto optimal structure for a domain filled with f_2ccz unit cells, weight $w_{opt} = 0.5$.

Fig. 6.11: Pareto optimal structures for *bcc* and f_2ccz unit-cells, volume fraction 0.2.

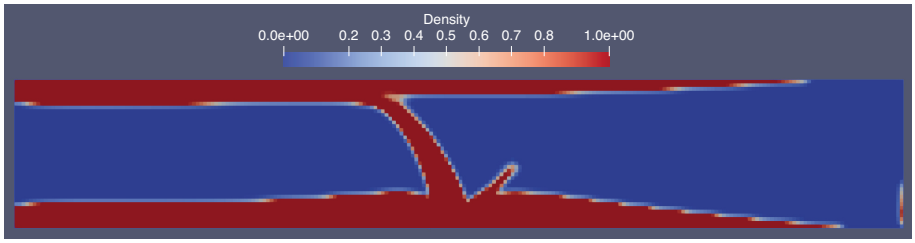

(a) Pareto optimal structure for a domain filled with *bcc* unit cells, weight $w_{opt} = 0.5$.

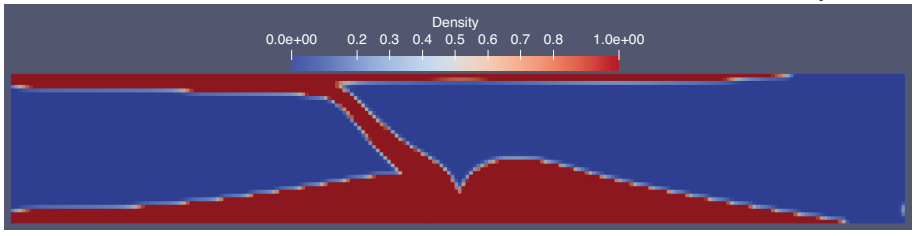

(b) Pareto optimal structure for a domain filled with f_2ccz unit cells, weight $w_{opt} = 0.76$.

Fig. 6.12: Pareto optimal structures for *bcc* and f_2ccz unit-cells, volume fraction 0.3.

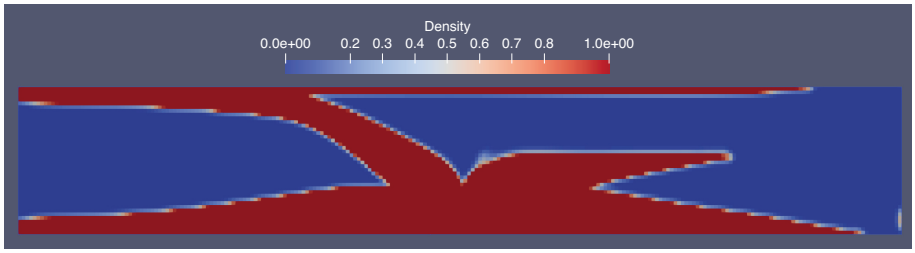

(a) Pareto optimal structure for a domain filled with *bcc* unit cells, weight $w_{opt} = 0.85$.

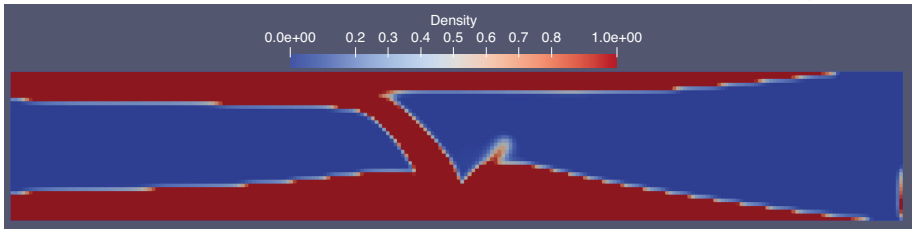

(b) Pareto optimal structure for a domain filled with f_2ccz unit cells, weight $w_{opt} = 0.5$.

Fig. 6.13: Pareto optimal structures for *bcc* and f_2ccz unit-cells, volume fraction 0.4.

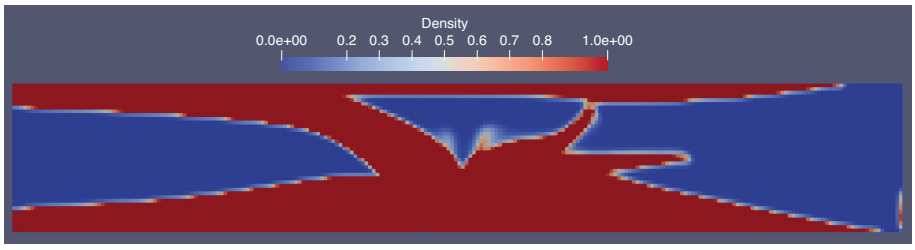

(a) Pareto optimal structure for a domain filled with *bcc* unit cells, weight $w_{opt} = 0.82$.

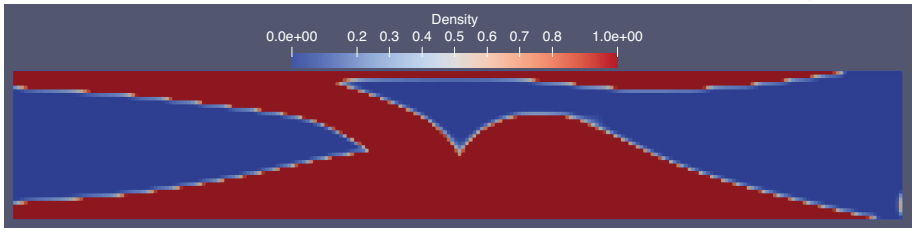

(b) Pareto optimal structure for a domain filled with f_2ccz unit cells, weight $w_{opt} = 0.85$.

Fig. 6.14: Pareto optimal structures for *bcc* and f_2ccz unit-cells, volume fraction 0.5.

6.3.1 De-homogenisation and future works

One of the main challenges posed to the field of topology optimisation is being capable to obtain a real, manufacturable structure from the obtained relative density distribution. The results presented thus far are available only in such form, which, as already mentioned, is correlated with a local variation of the lattice porosity ε.

The porosity describes a homogenised lattice structure, which, only given three of the other four geometrical parameters, (i.e. cell size, strut radius, aspect ratio angle, and unit-cell topology), can univocally identify a lattice structure. One can understand how a generalised mapping of the results to a realistic structure proves challenging. In this work, the assumption was made, that the aspect ratio was 1 (cubic unit-cells) and the cell size was fixed to 5 mm, while the unit-cell topology is fixed a priori. Thus, a variation of the porosity is only related to a variation of the strut radius. This way, a univocal mapping of the relative density to the geometry of the lattice structure can be obtained. However, an additional challenge makes the task not straightforward. Indeed, in order to obtain accurate results, a mesh refinement is necessary. As shown in the results illustrated in Figure 6.6, for the domain and boundary conditions considered in this problem, a mesh size of 1.25 mm is chosen. This means that the element size is a fraction of the unit-cell one. Thus, challenges emerge, especially regarding the elements lying in a region where a transition from $\rho^* = 1$ to $\rho^* = 0$ takes place. Therefore, the de-homogenisation, i.e. the univocal mapping of the elements relative density to the unit-cell porosity represents a non-trivial issue. Here, a simplified approach is used. First, the finding of the optimal weigth w, is performed with a refined mesh and an appropriate filter radius. Then, once the results are obtained, a second topology optimisation with the appropriate weight is performed, by using a mesh size as big as the cell size of the lattice structure. This allows a one-to-one mapping of the relative density to the lattice structure geometry. This procedure is possible as the mesh size in general has little influence on the resulting geometry, only the filter radius does (compare for example Figure 6.4a and Figure 6.4g).
The results of this mapping deliver a distribution of unit cells with variable strut radius, as shown Figure 6.15, where a *bcc* unit-cell is used.

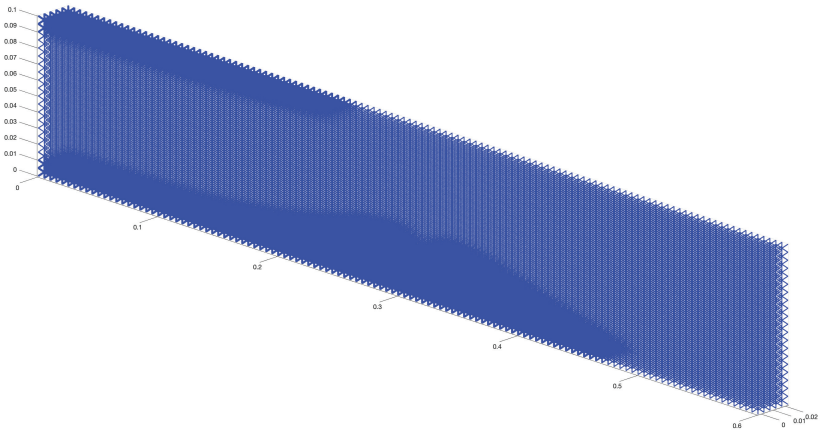

(a) Isometric view

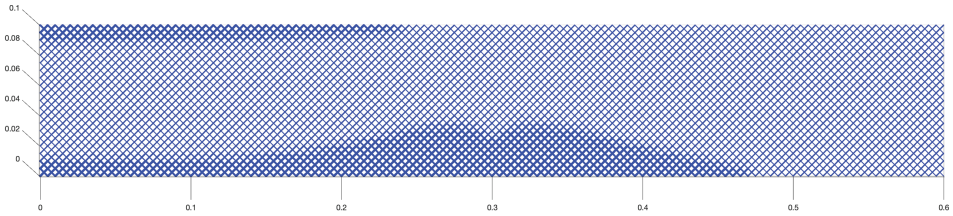

(b) Side view

Fig. 6.15: Domain after de-homogenisation. The darker areas represent areas where the strut radius is higher, i.e. the relative density increases.

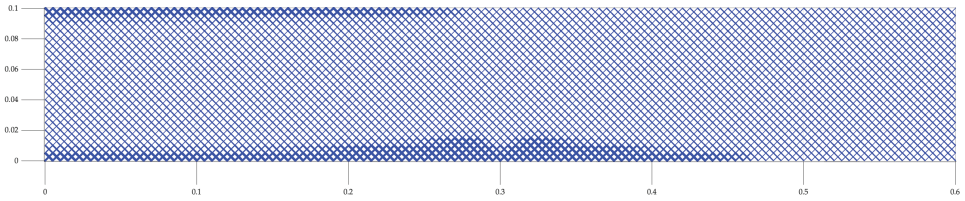

(a) Volume Fraction 0.1, $w = 0.5$

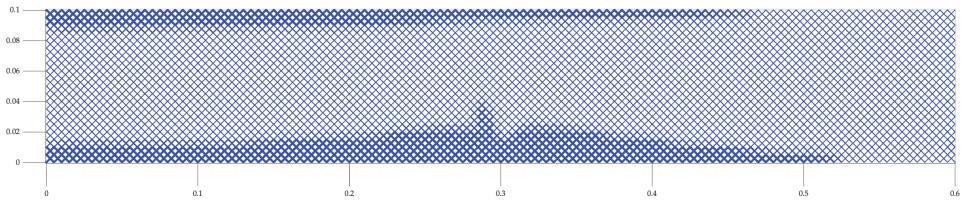

(b) Volume Fraction 0.,$w = 0.5$

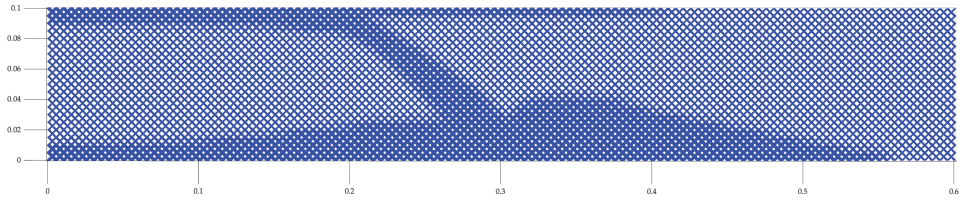

(c) Volume Fraction 0.3,$w = 0.77$

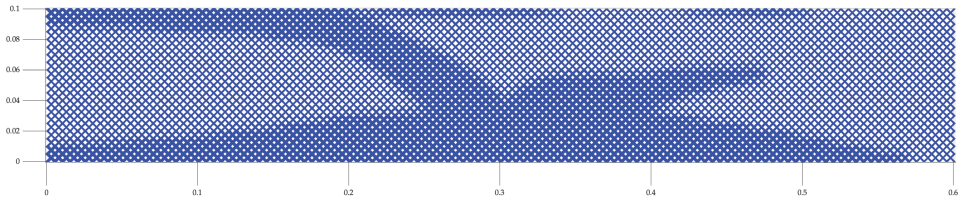

(d) Volume Fraction 0.4, $w = 0.84$

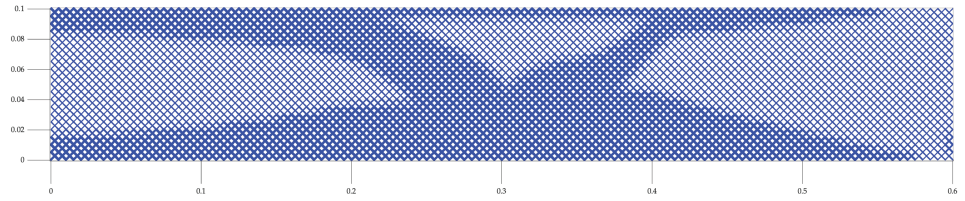

(e) Volume Fraction 0.5, $w = 0.87$

Fig. 6.16: Domain after de-homogenisation for the geometries found in Figure 6.10a, 6.11a, 6.12a,6.13a, 6.14a.

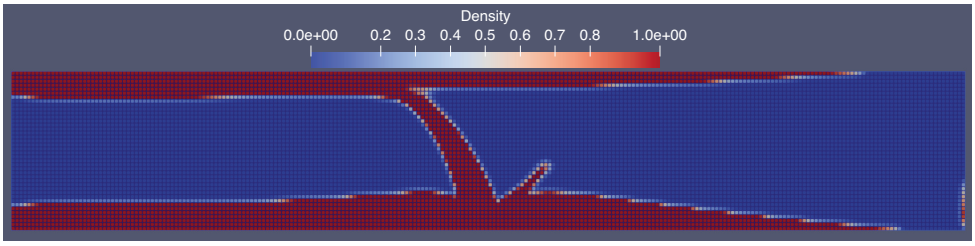

(a) Result of the optimisation for a volume fraction of 0.3, with a mesh size of 2.5mm.

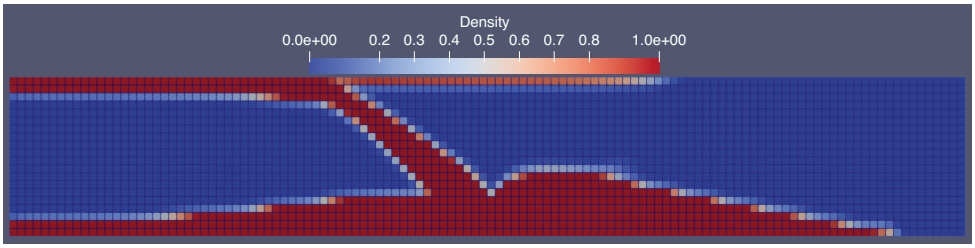

(b) Result of the optimisation for a volume fraction of 0.3, with a mesh size of 5mm.

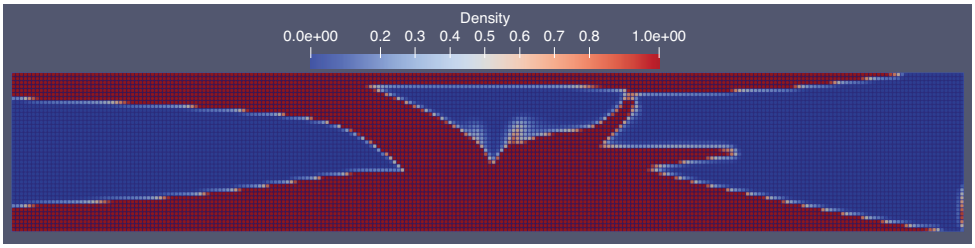

(c) Result of the optimisation for a volume fraction of 0.5, with a mesh size of 2.5mm.

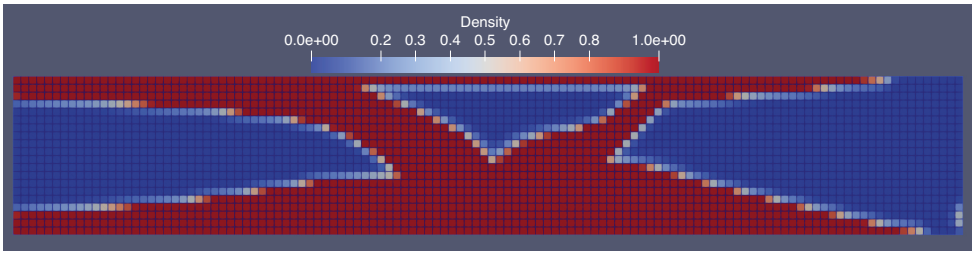

(d) Result of the optimisation for a volume fraction of 0.5, with a mesh size of 5mm.

Fig. 6.17: Results with a different mesh size, 5 mm and 2.5 mm, with filter radii 6 mm and 3 mm respectively.

It is important to remark that the results obtained thus far assume a value of the penalization coefficient p equal to 3. This is needed in order to achieve a binary value of the relative densities throughout the domain, in order to avoid not-physical results. The value is suggested often in the literature, as explained above. However, it worth noting that with the modification introduced in this work, an intermediate relative density does have a physically meaningful result. Thus, the value of p can be reduced, in order to obtain a smoother transition between the two extremes. This is shown in Figure 6.18a, where the results for a *bcc* unit-cell are shown for a volume fraction of 0.5, and a penalisation coefficient $p = 1$. The mesh size is 5 mm, in order to aid a fast convergence of the results, and the filter radius is 6 mm. One can appreciate how the

distribution of relative densities varies strongly with respect to the case of $p = 3$.
This represents a peculiar advantage with respect to conventional topology optimisation, as the results are more flexibly tailorable, and less restrictions apply to the setup of the optimisation problem.

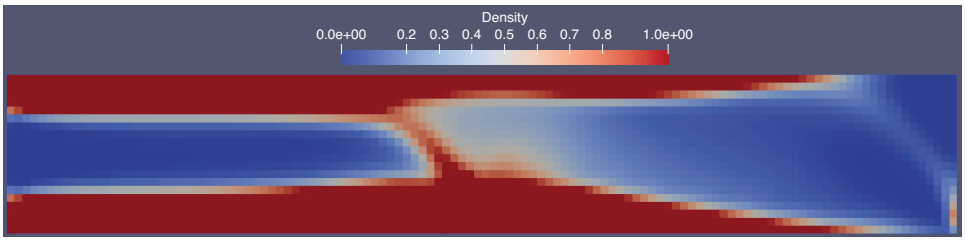

(a) Pareto optimal structure for a domain filled with f_2ccz unit cells, volume fraction 0.5, penalization coefficient $p = 1$. Notice the smoother transition between the two extremes, especially in the upper part of the domain.

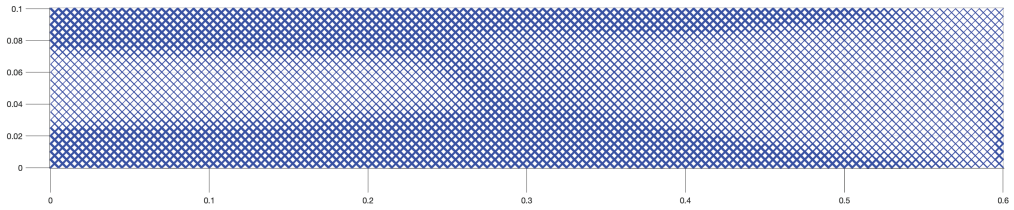

(b) Dehomogenised structure.

Fig. 6.18: Results for a penalization coefficient $p = 1$.

Future works In this thesis, several assumptions were employed to streamline the development of the introduced framework. Specifically, the assumption was made that the effective thermophysical properties introduced above and the effective stiffness presented by Bühring [40] could adequately define the properties of each unit-cell of the lattice structure-PCM composite within the domain. This assumption holds true as long as scale-variance does not impact the properties of the cells, requiring a sufficient number of unit-cells within the domain. While this condition is generally met, it remains uncertain how this assumption holds when there are enough unit-cells in the domain, but their geometry is locally tailored. A discrete numerical study and experimental investigations would be beneficial to verify this.
The current framework serves as a suitable foundation for various multifunctional topology optimisation tools. Additional goal functions can be introduced and linked to those presented in this study. Furthermore, diverse geometries, such as surface-based lattices like the Triply Periodic Minimal Surfaces, can be incorporated. Expanding to the third dimension would enhance the tool's applicability. Realistic boundary conditions, concentrated in specific three-dimensional points (e.g., a power electronics unit as a punctual heat source), suggest that the optimal topology may resemble a branch-like structure extending in three directions, akin to a tree found in the nature. Similar considerations apply to the structural problem, significantly

influencing the final optimal result.
It is noteworthy that the study exclusively considered heat transfer via conduction. To broaden the solutions to convective heat transfer, the inclusion of the Navier-Stokes equation and appropriate approximations, such as the Boussinesq approximation, becomes necessary.

7 Conclusions and Outlook

This work introduced novel multifunctional components, based on metallic lattice structures embedded with Phase Change Materials. While these could be applied within the fields of thermal management and thermal energy storage, particularly interesting application fields lie with lightweight multifunctional structures. These are evermore object of research and development actions in various engineering fields. Even in cost-driven industries, like the automotive one, multifunctional load-bearing elements are becoming relevant, as vehicles masses reach legal limits, due to electrification. The increasing need for holistic solutions allows to consider complex components, such the ones analysed in this work. These novel composites present advantages due to sinergies. Indeed, the lattice structure, offers both a core with a high specific stiffness, and a thermal conductivity enhancement method for the PCM. With the advantages, also come challenges regarding their characterisation. Furthermore, the concept itself of a multifunctional structure directly raises the matter of optimisation. Indeed, the different functionalities impose different requirements, which can be in countertendence.
All these aspects were treated in detail throughout this work. The main results are listed in the following.

1. A homogenisation technique was presented, which aimed at describing the thermophysical properties of the composite via effective values. These can be used to substitute the complex discrete structure via representative volumes.

2. The transient thermal behaviour is however affected by the amount of cells within the domain. This indicates that scale-variance is present. Thus, the homogenisation approach proposed in this work is only valid when a minimum amount of cells is present within the domain. This is a reasonable result, as the structure can only be treated as a porous medium only based on the percolation theory.

3. The homogenisation was validated by an experimental campaign, which however evidenced that the proposed approach is only valid when natural convection in the PCM melt can be neglected.

4. Following the experimental results, an attempt to further characterize the thermal behaviour of the PCM-lattice composite was made, by extending a dedicated solver based on the enthalpy porosity method. The fluid flow within the melt was accounted for by means of a Darcy term, which again represents an homogenisation approach. The results indicate that, while a qualitative agreement exists with experimental data, this approach cannot take into account the effect of the discrete morphology of the lattices on the fluid flow. Indeed, Rayleigh-Benàrd vortices are built during the simulation of the homogenised PCM, which instead during the experiment could not be evidenced. However, critical values for the estimation of the onset of convection within such composites were found through the models developed. It was found that these are indepent of the unit-cell topology, which indicates a general validity of the results.
   Furthermore, it is found that, for a purely conductive regime, no matter the unit-cell topology, the liquid fraction evolution with respect to a non-dimensional time represented by the Stefan-Fourier number is represented by the same function. This resembles an errof function and is thus express as a power law of this.

5. After the thermal characterization, the consideration of the effect of PCMs on the mechanical behaviour of the composites is treated. The effect of the considered PCMs on the effective stiffness of the component is mostly negligible, due to the low Young Modulus of such materials. However, the material in its solid state still constitutes an elastic bed for the lattice struts. A numerical investigation was performed, which showed that the elastic bed constituted by the PCM impedes de-facto a failure due to buckling of the lattice struts. An experimental verification was attempted. This qualitatively demonstrated that this is the case, and that failure through rupture of the struts occures always before buckling.

6. With the findings obtained in the previous chapters, in particular making use of the effective thermophysical properties obtained in Chapter 4, and of the effective stiffness presented by Bühring et al. [40], a framework for the multi-functional optimisation of these components was successfully developed. Particular focus is set at the finding of Pareto-optimal geometries, capable to satisfy the mass constraints fixed by the designer, as well as requirements of maximum stiffness and maximum thermal conductivity. The framework was extended to a topology optimisation in which rather than maximising the thermal conductivity, the thermal goal function is the minimisation of the wall temperature with consideration of phase transition. This is done via the proposed effective thermophysical properties and implementation of an apparent heat capacity method. The results indicate that the two goal functions are essentially monotonic in the same direction, thus the maximisation of the thermal conductivity can mostly be used to find an optimal geometry. This holds true up to a critical volume fraction, after which the amount of PCM within the domain is so reduced that the two functions are in counter-tendence.

With these results, the hypotheses made in Chapter 1 can be reviewed. The first hypothesis is validated, although the analytical form of the effective thermal conductivity tensor could be only obtained via fitting with numerical data. The second hypothesis is confirmed, as long as minimum 10 unit-cells can be found within the domain, for each relevant heat transfer direction. The third hypothesis is confirmed. The fourth hypothesis is confirmed without restriction, except the missing consideration of a liquid PCM. However, further experimental verification is needed, and an extension to three-dimensional domains and boundary conditions is necessary to represent realistic scenarios.

Outlook Detailed outlooks for each considered section are given in the respective chapters. However, some general remarks can be made.

This work focused on the thermal and mechanical behaviour of the considered composites. However, the effect of the phase change on the mechanical behaviour was not considered. This is a relevant aspect, as the phase change is associated with a volume change, which can induced significant load cases on the structural component. Furthermore, the assumption was made that the PCM has no influence on the effective stiffness of the composite. While this can be considered to be true, as the Young Modulus of the considered PCMs is significantly lower than the one of the lattice struts, PCMs employed for high temperature applications, i.e. salt mixtures, exhibit Young moduli which are in the same order of magnitude of aluminium. Thus, the effect of the PCM on the effective stiffness of the composite should be considered.

Finally, the coupled thermomechanical behaviour of the composite was not considered in this work. For room temperature applications, the thermal expansion is limited, and of poor relevance. However, for high temperature applications, or there where thermal loads constitute a design driver, e.g. in satellite structures, the thermomechanical behaviour should be modelled as well, including the derivation of the effective coefficient of thermal expansion of the composite material.

The results could be implemented in the framework presented in Chapter 6, to extend the multi-functional optimisation of the composites.

To do so, it is necessary to improve the optimisation of the domain by consideration of the phase-change problem, and addition of natural convection within the optimisation scheme. This is particularly relevant if the acceleration field caused by volume forces acting on the domain are higher than 1g, i.e. in multi-functional structures for reusable launch vehicles.

Bibliography

[1] G.J. DOMINGUEZ CALABUIG et al. Eco-design of future reusable launchers: insight into their life-cycle and atmospheric impact. In: (2022). Artwork Size: 21 pages Medium: PDF Publisher: Proceedings of the 9th European Conference for Aerospace Sciences. Lille, France, 27 June - 1 July, 2022, 21 pages. DOI: 10.13009/EUCASS2022-7353. URL: https://www.eucass.eu/doi/EUCASS2022-7353.pdf (visited on 18/12/2023).

[2] Ray GALVIN. Are electric vehicles getting too big and heavy? Modelling future vehicle journeying demand on a decarbonized US electricity grid. In: Energy Policy 161 (Feb. 2022), p. 112746. ISSN: 03014215. DOI: 10.1016/j.enpol.2021.112746. URL: https://linkinghub.elsevier.com/retrieve/pii/S0301421521006121 (visited on 18/12/2023).

[3] K.K. SAIRAJAN, G.S. AGLIETTI and K.M. MANI. A review of multifunctional structure technology for aerospace applications. In: Acta Astronautica 120 (Mar. 2016), pp. 30–42. ISSN: 00945765. DOI: 10.1016/j.actaastro.2015.11.024. URL: https://linkinghub.elsevier.com/retrieve/pii/S0094576515300217 (visited on 13/10/2021).

[4] Karen N. SON et al. Design of multifunctional lattice-frame materials for compact heat exchangers. In: International Journal of Heat and Mass Transfer 115 (Dec. 2017), pp. 619–629. ISSN: 00179310. DOI: 10.1016/j.ijheatmasstransfer.2017.07.073. URL: https://linkinghub.elsevier.com/retrieve/pii/S0017931016342429 (visited on 13/10/2021).

[5] Ioan SARBU and Calin SEBARCHIEVICI. A Comprehensive Review of Thermal Energy Storage. In: Sustainability 10.1 (14th Jan. 2018), p. 191. ISSN: 2071-1050. DOI: 10.3390/su10010191. URL: https://www.mdpi.com/2071-1050/10/1/191 (visited on 20/05/2023).

[6] Liange HE et al. Review of thermal management system for battery electric vehicle. In: Journal of Energy Storage 59 (Mar. 2023), p. 106443. ISSN: 2352152X. DOI: 10.1016/j.est.2022.106443. URL: https://linkinghub.elsevier.com/retrieve/pii/S2352152X2202432X (visited on 20/05/2023).

[7] Pablo RALON et al. IRENA (2017), Electricity Storage and Renewables: Costs and Markets to 2030. Abu Dhabi: International Renewable Energy Agency, 2017. URL: https://www.irena.org/publications.

[8] Luisa F. Cabeza. Advances in Thermal Energy Storage Systems. Elsevier, 2021. ISBN: 978-0-12-819885-8. DOI: 10.1016/C2019-0-00061-1. URL: https://linkinghub.elsevier.com/retrieve/pii/C20190000611 (visited on 27/11/2022).

[9] D. Cabaleiro et al. Review on phase change material emulsions for advanced thermal management: Design, characterization and thermal performance. In: Renewable and Sustainable Energy Reviews 159 (May 2022), p. 112238. ISSN: 13640321. DOI: 10.1016/j.rser.2022.112238. URL: https://linkinghub.elsevier.com/retrieve/pii/S1364032122001617 (visited on 27/11/2022).

[10] Cristina Prieto and Luisa F. Cabeza. Thermal energy storage with phase change materials in solar power plants. Economic analysis. In: Journal of Energy Storage 43 (Nov. 2021), p. 103184. ISSN: 2352152X. DOI: 10.1016/j.est.2021.103184. URL: https://linkinghub.elsevier.com/retrieve/pii/S2352152X21008847 (visited on 27/11/2022).

[11] R. Aridi and A. Yehya. Review on the sustainability of phase-change materials used in buildings. In: Energy Conversion and Management: X 15 (Aug. 2022), p. 100237. ISSN: 25901745. DOI: 10.1016/j.ecmx.2022.100237. URL: https://linkinghub.elsevier.com/retrieve/pii/S2590174522000605 (visited on 20/05/2023).

[12] Hong Shi et al. Thermal Management Techniques for Lithium-Ion Batteries Based on Phase Change Materials: A Systematic Review and Prospective Recommendations. In: Energies 16.2 (12th Jan. 2023), p. 876. ISSN: 1996-1073. DOI: 10.3390/en16020876. URL: https://www.mdpi.com/1996-1073/16/2/876 (visited on 20/05/2023).

[13] Hassan Nazir et al. Recent developments in phase change materials for energy storage applications: A review. In: International Journal of Heat and Mass Transfer 129 (2019). ISSN: 00179310. DOI: 10.1016/j.ijheatmasstransfer.2018.09.126.

[14] Theodore L. Bergman et al. Incropera's principles of heat and mass transfer. 8th edition, global edition. Hoboken, NJ: Wiley, 2017. 978 pp. ISBN: 978-1-119-38291-1.

[15] T. H. G. Megson. Aircraft structures for engineering students. Sixth edition. Elsevier aerospace engineering series. OCLC: ocn954224012. Amsterdam ; Boston: Butterworth-Heinemann is an imprint of Elsevier, 2017. 891 pp. ISBN: 978-0-08-100914-7.

[16] Leichtbau. Klassiker der Technik. Berlin, Heidelberg: Springer Berlin Heidelberg, 2007. ISBN: 978-3-540-33656-3 978-3-540-33657-0. DOI: 10.1007/978-3-540-33657-0. URL: http://link.springer.com/10.1007/978-3-540-33657-0 (visited on 19/12/2023).

[17] G. Prathap. The Finite Element Method in Structural Mechanics. Red. by G. M. L. Gladwell. Vol. 24. Solid Mechanics and Its Applications. Dordrecht: Springer Netherlands, 1993. ISBN: 978-90-481-4326-9 978-94-017-3319-9. DOI: 10.1007/978-94-017-3319-9. URL: http://link.springer.com/10.1007/978-94-017-3319-9 (visited on 23/12/2023).

[18] Junuthula Narasimha REDDY, N. K. ANAND and P. ROY. Finite element and finite volume methods for heat transfer and fluid dynamics. Cambridge New York, NY Port Melbourne, VIC New Delhi Singapore: Cambridge University Press, 2023. 385 pp. ISBN: 978-1-00-927548-4. DOI: 10.1017/9781009275453.

[19] Martin P. BENDSØE. Topology optimization: Theory, methods, and applications. Berlin, Heidelberg: Springer Berlin Heidelberg, 2004.

[20] Mykel J. KOCHENDERFER and Tim A. WHEELER. Algorithms for optimization. Cambridge, MA: The Mit Press, 2019.

[21] T. DEBROY et al. Additive manufacturing of metallic components – Process, structure and properties. In: Progress in Materials Science 92 (Mar. 2018), pp. 112–224. ISSN: 00796425. DOI: 10.1016/j.pmatsci.2017.10.001. URL: https://linkinghub.elsevier.com/retrieve/pii/S0079642517301172 (visited on 22/12/2023).

[22] Robert MINES. Metallic Microlattice Structures: Manufacture, Materials and Application. SpringerBriefs in Applied Sciences and Technology. Cham: Springer International Publishing, 2019. ISBN: 978-3-030-15231-4 978-3-030-15232-1. DOI: 10.1007/978-3-030-15232-1. URL: http://link.springer.com/10.1007/978-3-030-15232-1 (visited on 16/09/2021).

[23] Christopher T. RICHARD and Tsz-Ho KWOK. Analysis and Design of Lattice Structures for Rapid-Investment Casting. In: Materials 14.17 (27th Aug. 2021), p. 4867. ISSN: 1996-1944. DOI: 10.3390/ma14174867. URL: https://www.mdpi.com/1996-1944/14/17/4867 (visited on 22/12/2023).

[24] Wei SHYY et al. Computational Techniques for Complex Transport Phenomena. 1st ed. Cambridge University Press, 13th Oct. 1997. ISBN: 978-0-521-59268-0 978-0-521-02360-3 978-0-511-66546-2. DOI: 10.1017/CBO9780511665462. URL: https://www.cambridge.org/core/product/identifier/9780511665462/type/book (visited on 19/12/2023).

[25] Lorna J. GIBSON and Michael F. ASHBY. Cellular Solids: Structure and Properties. 2nd ed. Cambridge University Press, 1st May 1997. ISBN: 978-0-521-49911-8 978-0-521-49560-8 978-1-139-87832-6. DOI: 10.1017/CBO9781139878326. URL: https://www.cambridge.org/core/product/identifier/9781139878326/type/book (visited on 16/09/2021).

[26] Wahyudin P. SYAM et al. Design and analysis of strut-based lattice structures for vibration isolation. In: Precision Engineering 52 (Apr. 2018), pp. 494–506. ISSN: 01416359. DOI: 10.1016/j.precisioneng.2017.09.010. URL: https://linkinghub.elsevier.com/retrieve/pii/S0141635917302726 (visited on 05/02/2023).

[27] F. SCALZO et al. Experimental study on the high-damping properties of metallic lattice structures obtained from SLM. In: Precision Engineering 71 (Sept. 2021), pp. 63–77. ISSN: 01416359. DOI: 10.1016/j.precisioneng.2021.02.010. URL: https://linkinghub.elsevier.com/retrieve/pii/S0141635921000684 (visited on 05/02/2023).

[28] Zuhal OZDEMIR et al. Energy absorption in lattice structures in dynamics: Experiments. In: International Journal of Impact Engineering 89 (Mar. 2016), pp. 49–61. ISSN: 0734743X. DOI: 10.1016/j.ijimpeng.2015.10.007. URL: https://linkinghub.elsevier.com/retrieve/pii/S0734743X15002134 (visited on 05/02/2023).

[29] Thomas TANCOGNE-DEJEAN, Adriaan B. SPIERINGS and Dirk MOHR. Additively-manufactured metallic micro-lattice materials for high specific energy absorption under static and dynamic loading. In: Acta Materialia 116 (Sept. 2016), pp. 14–28. ISSN: 13596454. DOI: 10.1016/j.actamat.2016.05.054. URL: https://linkinghub.elsevier.com/retrieve/pii/S1359645416304153 (visited on 05/02/2023).

[30] Aamer NAZIR et al. A state-of-the-art review on types, design, optimization, and additive manufacturing of cellular structures. In: The International Journal of Advanced Manufacturing Technology 104.9 (Oct. 2019), pp. 3489–3510. ISSN: 0268-3768, 1433-3015. DOI: 10.1007/s00170-019-04085-3. URL: http://link.springer.com/10.1007/s00170-019-04085-3 (visited on 05/02/2023).

[31] Deepak SHARMA and Somashekhar S. HIREMATH. Additively manufactured mechanical metamaterials based on triply periodic minimal surfaces: Performance, challenges, and application. In: Mechanics of Advanced Materials and Structures 29.26 (26th Oct. 2022), pp. 5077–5107. ISSN: 1537-6494, 1537-6532. DOI: 10.1080/15376494.2021.1948151. URL: https://www.tandfonline.com/doi/full/10.1080/15376494.2021.1948151 (visited on 05/02/2023).

[32] Dietrich STAUFFER and Amnon AHARONY. Introduction to Percolation Theory. 2nd ed. OCLC: 1035517641. Boca Raton: Taylor & Francis Group, 2014. ISBN: 978-1-4822-7237-6.

[33] M.F ASHBY. The properties of foams and lattices. In: Philosophical Transactions of the Royal Society A: Mathematical, Physical and Engineering Sciences 364.1838 (15th Jan. 2006), pp. 15–30. ISSN: 1364-503X, 1471-2962. DOI: 10.1098/rsta.2005.1678. URL: https://royalsocietypublishing.org/doi/10.1098/rsta.2005.1678 (visited on 16/09/2021).

[34] Andrew N. NORRIS. Mechanics of elastic networks. In: Proceedings of the Royal Society A: Mathematical, Physical and Engineering Sciences 470.2172 (8th Dec. 2014), p. 20140522. ISSN: 1364-5021, 1471-2946. DOI: 10.1098/rspa.2014.0522. URL: https://royalsocietypublishing.org/doi/10.1098/rspa.2014.0522 (visited on 09/03/2022).

[35] Tobias MACONACHIE et al. SLM lattice structures: Properties, performance, applications and challenges. In: Materials & Design 183 (Dec. 2019), p. 108137. ISSN: 02641275. DOI: 10.1016/j.matdes.2019.108137. URL: https://linkinghub.elsevier.com/retrieve/pii/S0264127519305751 (visited on 02/04/2023).

[36] V.S. DESHPANDE, M.F. ASHBY and N.A. FLECK. Foam topology: bending versus stretching dominated architectures. In: Acta Materialia 49.6 (Apr. 2001), pp. 1035–1040. ISSN: 13596454. DOI: 10.1016/S1359-6454(00)00379-7. URL: https://linkinghub.elsevier.com/retrieve/pii/S1359645400003797 (visited on 02/04/2023).

[37] J. Clerk MAXWELL. L. *On the calculation of the equilibrium and stiffness of frames*. In: The London, Edinburgh, and Dublin Philosophical Magazine and Journal of Science 27.182 (Apr. 1864), pp. 294–299. ISSN: 1941-5982, 1941-5990. DOI: 10.1080/14786446408643668. URL: https://www.tandfonline.com/doi/full/10.1080/14786446408643668 (visited on 02/04/2023).

[38] Martin LEARY et al. Inconel 625 lattice structures manufactured by selective laser melting (SLM): Mechanical properties, deformation and failure modes. In: Materials & Design 157 (Nov. 2018), pp. 179–199. ISSN: 02641275. DOI: 10.1016/j.matdes.2018.06.010. URL: https://linkinghub.elsevier.com/retrieve/pii/S0264127518304763 (visited on 02/04/2023).

[39] Amir A. ZADPOOR. Mechanical performance of additively manufactured meta-biomaterials. In: Acta Biomaterialia 85 (Feb. 2019), pp. 41–59. ISSN: 17427061. DOI: 10.1016/j.actbio.2018.12.038. URL: https://linkinghub.elsevier.com/retrieve/pii/S1742706118307633 (visited on 02/04/2023).

[40] J. BÜHRING et al. Elastic axial stiffness properties of lattice structures: Analytical approach and experimental validation for bcc and f $_2$ cc,z unit cells. In: Mechanics of Advanced Materials and Structures (13th Nov. 2022), pp. 1–17. ISSN: 1537-6494, 1537-6532. DOI: 10.1080/15376494.2022.2139027. URL: https://www.tandfonline.com/doi/full/10.1080/15376494.2022.2139027 (visited on 02/04/2023).

[41] JÖRG ETTRICH. Fluid Flow and Heat Transfer in Cellular Solids. PhD thesis. Karlsruhe Institute of Technology, 2014. URL: https://publikationen.bibliothek.kit.edu/1000041877.

[42] M. KAVIANY. Principles of Heat Transfer in Porous Media. Red. by Frederick F. LING. Mechanical Engineering Series. New York, NY: Springer New York, 1995. ISBN: 978-1-4612-8710-0 978-1-4612-4254-3. DOI: 10.1007/978-1-4612-4254-3. URL: http://link.springer.com/10.1007/978-1-4612-4254-3 (visited on 15/04/2023).

[43] Z. HASHIN and S. SHTRIKMAN. A variational approach to the theory of the elastic behaviour of multiphase materials. In: Journal of the Mechanics and Physics of Solids 11.2 (Mar. 1963), pp. 127–140. ISSN: 00225096. DOI: 10.1016/0022-5096(63)90060-7. URL: https://linkinghub.elsevier.com/retrieve/pii/0022509663900607 (visited on 28/06/2023).

[44] G. N. Dul'nev and V. V. Novikov. Effective conductivity of systems with interpenetrating components. In: Journal of Engineering Physics 33.2 (Aug. 1977), pp. 923–925. ISSN: 0022-0841, 1573-871X. DOI: 10.1007/BF00860880. URL: http://link.springer.com/10.1007/BF00860880 (visited on 15/04/2023).

[45] J. W. Paek et al. Effective Thermal Conductivity and Permeability of Aluminum Foam Materials. In: International Journal of Thermophysics 21.2 (2000), pp. 453–464. ISSN: 0195928X. DOI: 10.1023/A:1006643815323. URL: http://link.springer.com/10.1023/A:1006643815323 (visited on 15/04/2023).

[46] X. Fu, R. Viskanta and J.P. Gore. Prediction of effective thermal conductivity of cellular ceramics. In: International Communications in Heat and Mass Transfer 25.2 (Feb. 1998), pp. 151–160. ISSN: 07351933. DOI: 10.1016/S0735-1933(98)00002-5. URL: https://linkinghub.elsevier.com/retrieve/pii/S0735193398000025 (visited on 15/04/2023).

[47] Paola Ranut. On the effective thermal conductivity of aluminum metal foams: Review and improvement of the available empirical and analytical models. In: Applied Thermal Engineering 101 (May 2016), pp. 496–524. ISSN: 13594311. DOI: 10.1016/j.applthermaleng.2015.09.094. URL: https://linkinghub.elsevier.com/retrieve/pii/S1359431115010194 (visited on 09/04/2023).

[48] V. V. Calmidi and R. L. Mahajan. The Effective Thermal Conductivity of High Porosity Fibrous Metal Foams. In: Journal of Heat Transfer 121.2 (1st May 1999), pp. 466–471. ISSN: 0022-1481, 1528-8943. DOI: 10.1115/1.2826001. URL: https://asmedigitalcollection.asme.org/heattransfer/article/121/2/466/415714/The-Effective-Thermal-Conductivity-of-High (visited on 15/04/2023).

[49] A. Bhattacharya, V.V. Calmidi and R.L. Mahajan. Thermophysical properties of high porosity metal foams. In: International Journal of Heat and Mass Transfer 45.5 (Feb. 2002), pp. 1017–1031. ISSN: 00179310. DOI: 10.1016/S0017-9310(01)00220-4. URL: https://linkinghub.elsevier.com/retrieve/pii/S0017931001002204 (visited on 28/06/2023).

[50] K. Boomsma and D. Poulikakos. On the effective thermal conductivity of a three-dimensionally structured fluid-saturated metal foam. In: International Journal of Heat and Mass Transfer 44.4 (Feb. 2001), pp. 827–836. ISSN: 00179310. DOI: 10.1016/S0017-9310(00)00123-X. URL: https://linkinghub.elsevier.com/retrieve/pii/S001793100000123X (visited on 28/06/2023).

[51] Miguel A.A. Mendes, Subhashis Ray and Dimosthenis Trimis. A simple and efficient method for the evaluation of effective thermal conductivity of open-cell foam-like structures. In: International Journal of Heat and Mass Transfer 66 (Nov. 2013), pp. 412–422. ISSN: 00179310. DOI: 10.1016/j.ijheatmasstransfer.2013.07.032. URL: https://linkinghub.elsevier.com/retrieve/pii/S0017931013005863 (visited on 28/06/2023).

[52] Z. DAI et al. Correcting and extending the Boomsma–Poulikakos effective thermal conductivity model for three-dimensional, fluid-saturated metal foams. In: International Communications in Heat and Mass Transfer 37.6 (July 2010), pp. 575–580. ISSN: 07351933. DOI: 10.1016/j.icheatmasstransfer.2010.01.015. URL: https://linkinghub.elsevier.com/retrieve/pii/S0735193310000503 (visited on 28/06/2023).

[53] H. YANG et al. A further discussion on the effective thermal conductivity of metal foam: An improved model. In: International Journal of Heat and Mass Transfer 86 (July 2015), pp. 207–211. ISSN: 00179310. DOI: 10.1016/j.ijheatmasstransfer.2015.03.001. URL: https://linkinghub.elsevier.com/retrieve/pii/S0017931015002550 (visited on 28/06/2023).

[54] Xiao Hu YANG et al. An Analytical Unit Cell Model for the Effective Thermal Conductivity of High Porosity Open-Cell Metal Foams. In: Transport in Porous Media 102.3 (Apr. 2014), pp. 403–426. ISSN: 0169-3913, 1573-1634. DOI: 10.1007/s11242-014-0281-z. URL: http://link.springer.com/10.1007/s11242-014-0281-z (visited on 28/06/2023).

[55] Romain HUBERT et al. An effective thermal conductivity model for architected phase change material enhancer: Theoretical and experimental investigations. In: International Journal of Heat and Mass Transfer 176 (Sept. 2021), p. 121364. ISSN: 00179310. DOI: 10.1016/j.ijheatmasstransfer.2021.121364. URL: https://linkinghub.elsevier.com/retrieve/pii/S0017931021004671 (visited on 15/10/2021).

[56] Xiuwu WANG et al. Effective thermal conductivity and heat transfer characteristics for a series of lightweight lattice core sandwich panels. In: Applied Thermal Engineering 173 (June 2020), p. 115205. ISSN: 13594311. DOI: 10.1016/j.applthermaleng.2020.115205. URL: https://linkinghub.elsevier.com/retrieve/pii/S1359431119387587 (visited on 27/06/2023).

[57] Lucia IANNICIELLO, Pascal Henry BIWOLÉ and Patrick ACHARD. Electric vehicles batteries thermal management systems employing phase change materials. In: Journal of Power Sources 378 (Feb. 2018), pp. 383–403. ISSN: 03787753. DOI: 10.1016/j.jpowsour.2017.12.071. URL: https://linkinghub.elsevier.com/retrieve/pii/S0378775317316816 (visited on 29/10/2021).

[58] David G. GILMORE, ed. Spacecraft thermal control handbook. 2nd ed. El Segundo, Calif: Aerospace Press, 2002. 2 pp. ISBN: 978-1-884989-11-7 978-1-884989-14-8.

[59] Zhi LI et al. Applications and technological challenges for heat recovery, storage and utilisation with latent thermal energy storage. In: Applied Energy 283 (Feb. 2021), p. 116277. ISSN: 03062619. DOI: 10.1016/j.apenergy.2020.116277. URL: https://linkinghub.elsevier.com/retrieve/pii/S0306261920316676 (visited on 15/04/2023).

[60] Yongcai HUANG, Alex STONEHOUSE and Chamil ABEYKOON. Encapsulation methods for phase change materials – A critical review. In: International Journal of Heat and Mass Transfer 200 (Jan. 2023), p. 123458. ISSN: 00179310. DOI: 10.1016/j.ijheatmasstransfer.2022.123458. URL: https://linkinghub.elsevier.com/retrieve/pii/S0017931022009279 (visited on 22/12/2023).

[61] Su Ho KIM et al. Enhanced thermal performance of phase change material-integrated fin-type heat sinks for high power electronics cooling. In: International Journal of Heat and Mass Transfer 184 (Mar. 2022), p. 122257. ISSN: 00179310. DOI: 10.1016/j.ijheatmasstransfer.2021.122257. URL: https://linkinghub.elsevier.com/retrieve/pii/S0017931021013569 (visited on 22/12/2023).

[62] TAUSEEF-UR-REHMAN et al. A critical review on heat transfer augmentation of phase change materials embedded with porous materials/foams. In: International Journal of Heat and Mass Transfer 135 (June 2019), pp. 649–673. ISSN: 00179310. DOI: 10.1016/j.ijheatmasstransfer.2019.02.001. URL: https://linkinghub.elsevier.com/retrieve/pii/S0017931018349767 (visited on 14/10/2021).

[63] Ahmad HAJJAR et al. Transient phase change heat transfer in a metal foam-phase change material heatsink subject to a pulse heat flux. In: Journal of Energy Storage 31 (Oct. 2020), p. 101701. ISSN: 2352152X. DOI: 10.1016/j.est.2020.101701. URL: https://linkinghub.elsevier.com/retrieve/pii/S2352152X20315383 (visited on 30/09/2023).

[64] Mahmoud MOEINI SEDEH and J.M. KHODADADI. Thermal conductivity improvement of phase change materials/graphite foam composites. In: Carbon 60 (Aug. 2013), pp. 117–128. ISSN: 00086223. DOI: 10.1016/j.carbon.2013.04.004. URL: https://linkinghub.elsevier.com/retrieve/pii/S0008622313002960 (visited on 11/09/2023).

[65] M. ARAMESH and B. SHABANI. Metal foam-phase change material composites for thermal energy storage: A review of performance parameters. In: Renewable and Sustainable Energy Reviews (Nov. 2021), p. 111919. ISSN: 13640321. DOI: 10.1016/j.rser.2021.111919. URL: https://linkinghub.elsevier.com/retrieve/pii/S1364032121011849 (visited on 29/11/2021).

[66] C Y ZHAO. Heat transfer enhancement for thermal energy storage using metal foams embedded within phase change materials (PCMs). In: Solar Energy (2010), p. 11.

[67] Xusheng HU, Feng ZHU and Xiaolu GONG. Experimental and numerical study on the thermal behavior of phase change material infiltrated in low porosity metal foam. In: Journal of Energy Storage 26 (1st Dec. 2019), p. 101005. ISSN: 2352-152X. DOI: 10.1016/j.est.2019.101005. URL: http://www.sciencedirect.com/science/article/pii/S2352152X19306656 (visited on 27/11/2020).

[68] Simone MANCIN et al. Experimental analysis of phase change phenomenon of paraffin waxes embedded in copper foams. In: International Journal of Thermal Sciences 90 (Apr. 2015), pp. 79–89. ISSN: 12900729. DOI: 10.1016/j.ijthermalsci.2014.11.023. URL: https://linkinghub.elsevier.com/retrieve/pii/S1290072914003354 (visited on 30/11/2020).

[69] Andrea DIANI and Manuela CAMPANALE. Transient melting of paraffin waxes embedded in aluminum foams: Experimental results and modeling. In: International Journal of Thermal Sciences 144 (Oct. 2019), pp. 119–128. ISSN: 12900729. DOI: 10.1016/j.ijthermalsci.2019.06.004. URL: https://linkinghub.elsevier.com/retrieve/pii/S129007291831473X (visited on 25/03/2022).

[70] Giulia RIGHETTI et al. Experimental study of phase change material (PCM) embedded in 3D periodic structures realized via additive manufacturing. In: International Journal of Thermal Sciences 153 (July 2020), p. 106376. ISSN: 12900729. DOI: 10.1016/j.ijthermalsci.2020.106376. URL: https://linkinghub.elsevier.com/retrieve/pii/S1290072919316539 (visited on 20/08/2021).

[71] Arjun PARIDA, Anirban BHATTACHARYA and Prasenjit RATH. Effect of convection on melting characteristics of phase change material-metal foam composite thermal energy storage system. In: Journal of Energy Storage 32 (Dec. 2020), p. 101804. ISSN: 2352152X. DOI: 10.1016/j.est.2020.101804. URL: https://linkinghub.elsevier.com/retrieve/pii/S2352152X20316418 (visited on 19/03/2022).

[72] Xiaohu YANG. Effect of inclination on the thermal response of composite phase change materials for thermal energy storage. In: Applied Energy (2019), p. 12.

[73] Hongyang LI et al. Pore-scale study on Rayleigh-Bénard convection formed in the melting process of metal foam composite phase change material. In: International Journal of Thermal Sciences 177 (July 2022), p. 107572. ISSN: 12900729. DOI: 10.1016/j.ijthermalsci.2022.107572. URL: https://linkinghub.elsevier.com/retrieve/pii/S1290072922001119 (visited on 21/12/2023).

[74] M IASIELLO et al. Simulations of paraffine melting inside metal foams at different gravity levels with preliminary experimental validation. In: Journal of Physics: Conference Series 1599.1 (1st Aug. 2020), p. 012008. ISSN: 1742-6588, 1742-6596. DOI: 10.1088/1742-6596/1599/1/012008. URL: https://iopscience.iop.org/article/10.1088/1742-6596/1599/1/012008 (visited on 29/11/2021).

[75] Sauro FILIPPESCHI, Mauro MAMELI and Paolo Di MARCO. EXPERIMENTAL ANALYSIS OF THE MELTING PROCESS IN A PCM/ALUMINUM FOAM COMPOSITE MATERIAL IN HYPERGRAVITY CONDITIONS. In: Interfacial Phenomena and Heat Transfer 6.4 (2018). ISSN: 2169-2785. DOI: 10.1615/InterfacPhenomHeatTransfer.2019030703.

[76] Peter JANY and Adrian BEJAN. Scaling theory of melting with natural convection in an enclosure. In: International Journal of Heat and Mass Transfer 31.6 (June 1988), pp. 1221–1235. ISSN: 00179310. DOI: 10.1016/0017-9310(88)90065-8. URL: https://linkinghub.elsevier.com/retrieve/pii/0017931088900658 (visited on 30/03/2022).

[77] Mohammad AZAD, Dominic GROULX and Adam DONALDSON. Natural convection onset during melting of phase change materials: Part I – Effects of the geometry, Stefan number, and degree of subcooling. In: International Journal of Thermal Sciences 170 (Dec. 2021), p. 107180. ISSN: 12900729. DOI: 10.1016/j.ijthermalsci.2021.107180. URL: https://linkinghub.elsevier.com/retrieve/pii/S1290072921003410 (visited on 22/12/2023).

[78] Mohammad AZAD, Dominic GROULX and Adam DONALDSON. Natural convection onset during melting of phase change materials: Part II – Effects of Fourier, Grashof, and Rayleigh numbers. In: International Journal of Thermal Sciences 170 (Dec. 2021), p. 107062. ISSN: 12900729. DOI: 10.1016/j.ijthermalsci.2021.107062. URL: https://linkinghub.elsevier.com/retrieve/pii/S129007292100226X (visited on 22/12/2023).

[79] Donald A. NIELD and Adrian BEJAN. Convection in Porous Media. New York, NY: Springer New York, 2013. ISBN: 978-1-4614-5540-0 978-1-4614-5541-7. DOI: 10.1007/978-1-4614-5541-7. URL: https://link.springer.com/10.1007/978-1-4614-5541-7 (visited on 22/12/2023).

[80] H.P. DARCY. Les fontaines publiques de la ville de Dijon. In: Dalmont, Paris (1856).

[81] Wolfgang EHLERS. Darcy, Forchheimer, Brinkman and Richards: classical hydromechanical equations and their significance in the light of the TPM. In: Archive of Applied Mechanics 92.2 (Feb. 2022), pp. 619–639. ISSN: 0939-1533, 1432-0681. DOI: 10.1007/s00419-020-01802-3. URL: https://link.springer.com/10.1007/s00419-020-01802-3 (visited on 21/10/2023).

[82] Bernd MARKERT. A Biphasic Continuum Approach for Viscoelastic High-Porosity Foams: Comprehensive Theory, Numerics, and Application. In: Archives of Computational Methods in Engineering 15.4 (Dec. 2008), pp. 371–446. ISSN: 1134-3060, 1886-1784. DOI: 10.1007/s11831-008-9023-0. URL: http://link.springer.com/10.1007/s11831-008-9023-0 (visited on 20/12/2023).

[83] Marcello IASIELLO et al. Metal foam/PCM melting evolution analysis: Orientation and morphology effects. In: Applied Thermal Engineering 187 (Mar. 2021), p. 116572. ISSN: 13594311. DOI: 10.1016/j.applthermaleng.2021.116572. URL: https://linkinghub.elsevier.com/retrieve/pii/S1359431121000296 (visited on 29/11/2021).

[84] Farida IACHACHENE et al. Natural convection melting of phase change material in corrugated porous cavities. In: Sustainable Energy Technologies and Assessments 53 (Oct. 2022), p. 102734. ISSN: 22131388. DOI: 10.1016/j.seta.2022.102734. URL: https://linkinghub.elsevier.com/retrieve/pii/S2213138822007822 (visited on 21/12/2023).

[85] Chen DING et al. Numerical investigation on melting behaviour of phase change materials/metal foam composites under hypergravity conditions. In: Applied Thermal Engineering 207 (May 2022), p. 118153. ISSN: 13594311. DOI: 10.1016/j.applthermaleng.2022.118153. URL: https://linkinghub.elsevier.com/retrieve/pii/S135943112200117X (visited on 08/04/2022).

[86] J. A. KOLODZIEJ. Influence of the porosity of a porous medium on the effective viscosity in Brinkman's filtration equation. In: Acta Mechanica 75.1 (Dec. 1988), pp. 241–254. ISSN: 0001-5970, 1619-6937. DOI: 10.1007/BF01174638. URL: http://link.springer.com/10.1007/BF01174638 (visited on 21/12/2023).

[87] Francisco J. VALDES-PARADA, J. ALBERTO OCHOA-TAPIA and Jose ALVAREZ-RAMIREZ. On the effective viscosity for the Darcy–Brinkman equation. In: Physica A: Statistical Mechanics and its Applications 385.1 (Nov. 2007), pp. 69–79. ISSN: 03784371. DOI: 10.1016/j.physa.2007.06.012. URL: https://linkinghub.elsevier.com/retrieve/pii/S0378437107006371 (visited on 21/12/2023).

[88] S. I. VASIN and A. N. FILIPPOV. Permeability of complex porous media. In: Colloid Journal 71.1 (Feb. 2009), pp. 31–45. ISSN: 1061-933X, 1608-3067. DOI: 10.1134/S1061933X09010049. URL: http://link.springer.com/10.1134/S1061933X09010049 (visited on 21/12/2023).

[89] M. HABIBISHANDIZ and M.Z. SAGHIR. A critical review of heat transfer enhancement methods in the presence of porous media, nanofluids, and microorganisms. In: Thermal Science and Engineering Progress 30 (May 2022), p. 101267. ISSN: 24519049. DOI: 10.1016/j.tsep.2022.101267. URL: https://linkinghub.elsevier.com/retrieve/pii/S2451904922000749 (visited on 21/12/2023).

[90] Sukumar PATI et al. Critical review on local thermal equilibrium and local thermal non-equilibrium approaches for the analysis of forced convective flow through porous media. In: International Communications in Heat and Mass Transfer 132 (Mar. 2022), p. 105889. ISSN: 07351933. DOI: 10.1016/j.icheatmasstransfer.2022.105889. URL: https://linkinghub.elsevier.com/retrieve/pii/S0735193322000112 (visited on 21/12/2023).

[91] Joseph STEFAN. Über die Theorie der Eisbildung, insbesondere über die Eisbildung im Polarmeere. In: Annalen der Physik 278.2 (1891). Publisher: WILEY-VCH Verlag Leipzig, pp. 269–286.

[92] Myrto ZENELI et al. Numerical methods for solid-liquid phase-change problems. In: Ultra-High Temperature Thermal Energy Storage, Transfer and Conversion (2021), pp. 165–199. DOI: 10.1016/b978-0-12-819955-8.00007-7.

[93] Mehdi DEHGHAN and Mahboubeh NAJAFI. Numerical solution of a non-classical two-phase Stefan problem via radial basis function (RBF) collocation methods. In: Engineering Analysis with Boundary Elements 72 (2016), pp. 111–127. DOI: 10.1016/j.enganabound.2016.07.015.

[94] V. R. VOLLER, M. CROSS and N. C. MARKATOS. An enthalpy method for convection/diffusion phase change. In: International Journal for Numerical Methods in Engineering 24.1 (1987), pp. 271–284. DOI: 10.1002/nme.1620240119.

[95] Y. FROSTIG. Buckling of sandwich panels with a flexible core—high-order theory. In: International Journal of Solids and Structures 35.3 (Jan. 1998), pp. 183–204. ISSN: 00207683. DOI: 10.1016/S0020-7683(97)00078-4. URL: https://linkinghub.elsevier.com/retrieve/pii/S0020768397000784 (visited on 23/12/2023).

[96] Emil WINKLER. Der Eisenbahn-Oberbau. 1871.

[97] P.L. PASTERNAK. „On a new method of analysis of an elastic foundation by means of two foundation constants“. In: 1954. URL: https://api.semanticscholar.org/CorpusID:124773833.

[98] V.Z. VLASOV and U.N. LEONTEV. Beams, plates and shells on elastic foundations. 1966. URL: https://archive.org/details/nasa_techdoc_19670004909.

[99] Leonard R. HERRMANN and William E. MASON. Response of reinforcing wires to compressive states of stress. In: Journal of Composite Materials 1 (1967).

[100] Davood YOUNESIAN et al. Elastic and viscoelastic foundations: a review on linear and nonlinear vibration modeling and applications. In: Nonlinear Dynamics 97.1 (July 2019), pp. 853–895. ISSN: 0924-090X, 1573-269X. DOI: 10.1007/s11071-019-04977-9. URL: http://link.springer.com/10.1007/s11071-019-04977-9 (visited on 08/11/2023).

[101] Stephan Prokof'evitch TIMOSHENKO and James M. GERE. Theory of elastic stability. 2nd ed. Mineola: Dover publ, 2009. ISBN: 978-0-486-47207-2.

[102] Miklós HETÉNYI. Beams on elastic foundation: Theory with applications in the fields of civil and mechanical engineering. 1946.

[103] M. S. EL NASCHIE. Exact asymptotic solution for the initial post-buckling of a strut on linear elastic foundation. In: Journal of Applied Mathematics and Mechanics (1974).

[104] Ole SIGMUND. Morphology-based black and white filters for topology optimization. In: Structural and Multidisciplinary Optimization 33.4 (2007), pp. 401–424. DOI: 10.1007/s00158-006-0087-x.

[105] Ole SIGMUND. On the design of compliant mechanisms using topology optimization*. In: Mechanics of Structures and Machines 25.4 (1997), pp. 493–524. DOI: 10.1080/08905459708945415.

[106] Tyler E. BRUNS and Daniel A. TORTORELLI. Topology optimization of non-linear elastic structures and compliant mechanisms. In: Computer Methods in Applied Mechanics and Engineering 190.26 (2001), pp. 3443–3459. DOI: 10.1016/s0045-7825(00)00278-4.

[107] Krister SVANBERG. The method of moving asymptotes—a new method for structural optimization. In: International Journal for Numerical Methods in Engineering 24.2 (1987), pp. 359–373. DOI: 10.1002/nme.1620240207.

[108] Nam H. KIM et al. Generalized optimality criteria method for topology optimization. In: Applied Sciences 11.7 (2021), p. 3175. DOI: 10.3390/app11073175.

[109] Surya N. PATNAIK, James D. GUPTILL and Laszlo BERKE. Merits and limitations of optimality criteria method for structural optimization. In: International Journal for Numerical Methods in Engineering 38.18 (1995), pp. 3087–3120. DOI: 10.1002/nme.1620381806.

[110] Joe ALEXANDERSEN, Ole SIGMUND and Niels AAGE. Large scale three-dimensional topology optimisation of heat sinks cooled by natural convection. In: International Journal of Heat and Mass Transfer 100 (2016), pp. 876–891. DOI: 10.1016/j.ijheatmasstransfer.2016.05.013.

[111] Younghwan JOO, Ikjin LEE and Sung Jin KIM. Topology optimization of heat sinks in natural convection considering the effect of shape-dependent heat transfer coefficient. In: International Journal of Heat and Mass Transfer 109 (2017), pp. 123–133. DOI: 10.1016/j.ijheatmasstransfer.2017.01.099.

[112] Jeroen P. GROEN and Ole SIGMUND. Homogenization-based topology optimization for high-resolution manufacturable microstructures. In: International Journal for Numerical Methods in Engineering 113.8 (2017), pp. 1148–1163. DOI: 10.1002/nme.5575.

[113] S. D. LARSEN, O. SIGMUND and J. P. GROEN. Optimal truss and frame design from projected homogenization-based topology optimization. In: Structural and Multidisciplinary Optimization 57.4 (2018), pp. 1461–1474. DOI: 10.1007/s00158-018-1948-9.

[114] Rossana R. FERNANDES and Ali Y. TAMIJANI. Design optimization of lattice structures with stress constraints. In: Materials & Design 210 (2021), p. 110026. DOI: 10.1016/j.matdes.2021.110026.

[115] Hesaneh KAZEMI, Ashkan VAZIRI and Julián A. NORATO. Multi-material topology optimization of lattice structures using geometry projection. In: Computer Methods in Applied Mechanics and Engineering 363 (May 2020), p. 112895. ISSN: 00457825. DOI: 10.1016/j.cma.2020.112895. URL: https://linkinghub.elsevier.com/retrieve/pii/S0045782520300773 (visited on 08/11/2023).

[116] Lin CHENG et al. Efficient design optimization of variable-density cellular structures for additive manufacturing: theory and experimental validation. In: Rapid Prototyping Journal 23.4 (20th June 2017), pp. 660–677. ISSN: 1355-2546. DOI: 10.1108/RPJ-04-2016-0069. URL: https://www.emerald.com/insight/content/doi/10.1108/RPJ-04-2016-0069/full/html (visited on 08/11/2023).

[117] S. TORQUATO, S. HYUN and A. DONEV. Multifunctional Composites: Optimizing Microstructures for Simultaneous Transport of Heat and Electricity. In: Physical Review Letters 89.26 (9th Dec. 2002), p. 266601. ISSN: 0031-9007, 1079-7114. DOI: 10.1103/PhysRevLett.89.266601. URL: https://link.aps.org/doi/10.1103/PhysRevLett.89.266601 (visited on 09/11/2023).

[118] S. TORQUATO, S. HYUN and A. DONEV. Optimal design of manufacturable three-dimensional composites with multifunctional characteristics. In: Journal of Applied Physics 94.9 (1st Nov. 2003), pp. 5748–5755. ISSN: 0021-8979, 1089-7550. DOI: 10.1063/1.1611631. URL: https://pubs.aip.org/jap/article/94/9/5748/484111/Optimal-design-of-manufacturable-three-dimensional (visited on 09/11/2023).

[119] S. TORQUATO and A. DONEV. Minimal surfaces and multifunctionality. In: Proceedings of the Royal Society of London. Series A: Mathematical, Physical and Engineering Sciences 460.2047 (8th July 2004), pp. 1849–1856. ISSN: 1364-5021, 1471-2946. DOI: 10.1098/rspa.2003.1269. URL: https://royalsocietypublishing.org/doi/10.1098/rspa.2003.1269 (visited on 09/11/2023).

[120] Niek DE KRUIJF et al. Topological design of structures and composite materials with multiobjectives. In: International Journal of Solids and Structures 44.22 (Nov. 2007), pp. 7092–7109. ISSN: 00207683. DOI: 10.1016/j.ijsolstr.2007.03.028. URL: https://linkinghub.elsevier.com/retrieve/pii/S0020768307001825 (visited on 09/11/2023).

[121] V.J. CHALLIS, A.P. ROBERTS and A.H. WILKINS. Design of three dimensional isotropic microstructures for maximized stiffness and conductivity. In: International Journal of Solids and Structures 45.14 (2008), pp. 4130–4146. DOI: 10.1016/j.ijsolstr.2008.02.025.

[122] Xing ZHANG et al. Design optimization of multifunctional metamaterials with tunable thermal expansion and phononic bandgap. In: Materials & Design 209 (2021), p. 109990. DOI: 10.1016/j.matdes.2021.109990.

[123] Chikwesiri IMEDIEGWU et al. Multiscale thermal and Thermo-structural optimization of three-dimensional lattice structures. In: Structural and Multidisciplinary Optimization 65.1 (2021). DOI: 10.1007/s00158-021-03087-8.

[124] Jun WU, Weiming WANG and Xifeng GAO. Design and Optimization of Conforming Lattice Structures. In: IEEE Transactions on Visualization and Computer Graphics 27.1 (1st Jan. 2021), pp. 43–56. ISSN: 1077-2626, 1941-0506, 2160-9306. DOI: 10.1109/TVCG.2019.2938946. arXiv: 1905.02902[cs]. URL: http://arxiv.org/abs/1905.02902 (visited on 09/11/2023).

[125] Vysakh VENUGOPAL, Nathan HERTLEIN and Sam ANAND. Multi-Material Topology Optimization Using Variable Density Lattice Structures for Additive Manufacturing. In: Procedia Manufacturing 53 (2021), pp. 327–337. ISSN: 23519789. DOI: 10.1016/j.promfg.2021.06.089. URL: https://linkinghub.elsevier.com/retrieve/pii/S235197892100113X (visited on 09/11/2023).

[126] Reza PEJMAN and Ahmad Raeisi NAJAFI. Multiphysics topology optimization of a multifunctional structural battery composite. In: Structural and Multidisciplinary Optimization 66.3 (2023). DOI: 10.1007/s00158-023-03490-3.

[127] Akihiro TAKEZAWA et al. Structural topology optimization with strength and heat conduction constraints. In: Computer Methods in Applied Mechanics and Engineering 276 (2014), pp. 341–361. DOI: 10.1016/j.cma.2014.04.003.

[128] I. O. ANGELL and M. MOORE. Symmetrical intersections of cylinders. In: Acta Crystallographica Section A Foundations of Crystallography 43.2 (1st Mar. 1987), pp. 244–250. ISSN: 0108-7673. DOI: 10.1107/S0108767387099501. URL: https://scripts.iucr.org/cgi-bin/paper?S0108767387099501 (visited on 28/06/2023).

[129] J.H. HUBBELL. Common volume of two intersecting cylinders. In: Journal of Research of the National Bureau of Standards, Section C: Engineering and Instrumentation 69C.2 (Apr. 1965), p. 139. ISSN: 0022-4316. DOI: 10.6028/jres.069C.017. URL: https://nvlpubs.nist.gov/nistpubs/jres/69C/jresv69Cn2p139_A1b.pdf (visited on 01/08/2023).

[130] Stefano PIACQUADIO et al. Experimental Analysis of the Thermal Energy Storage Potential of a Phase Change Material embedded in Additively Manufactured Lattice Structures. In: Applied Thermal Engineering (Aug. 2022), p. 119091. ISSN: 13594311. DOI: 10.1016/j.applthermaleng.2022.119091. URL: https://linkinghub.elsevier.com/retrieve/pii/S1359431122010237 (visited on 04/08/2022).

[131] Girish Kumar MARRI and C. BALAJI. Experimental and numerical investigations on the effect of porosity and PPI gradients of metal foams on the thermal performance of a composite phase change material heat sink. In: International Journal of Heat and Mass Transfer 164 (Jan. 2021), p. 120454. ISSN: 00179310. DOI: 10.1016/j.ijheatmasstransfer.2020.120454. URL: https://linkinghub.elsevier.com/retrieve/pii/S0017931020333901 (visited on 19/03/2022).

[132] Dominic GROULX and Marcel LACROIX. Study of close contact melting of ice from a sliding heated flat plate. In: International Journal of Heat and Mass Transfer 49.23 (Nov. 2006), pp. 4407–4416. ISSN: 00179310. DOI: 10.1016/j.ijheatmasstransfer.2006.05.007. URL: https://linkinghub.elsevier.com/retrieve/pii/S0017931006003097 (visited on 25/03/2022).

[133] Kai SCHÜLLER, Benjamin BERKELS and Julia KOWALSKI. Integrated Modeling and Validation for Phase Change with Natural Convection. In: Recent Advances in Computational Engineering. Ed. by Michael SCHÄFER et al. Vol. 124. Series Title: Lecture Notes in Computational Science and Engineering. Cham: Springer International Publishing, 2018, pp. 127–144. ISBN: 978-3-319-93890-5 978-3-319-93891-2. DOI: 10.1007/978-3-319-93891-2_8. URL: http://link.springer.com/10.1007/978-3-319-93891-2_8 (visited on 04/12/2023).

[134] Pawankumar EKADE and Shankar KRISHNAN. Fluid flow and heat transfer characteristics of octet truss lattice geometry. In: International Journal of Thermal Sciences 137 (Mar. 2019), pp. 253–261. ISSN: 12900729. DOI: 10.1016/j.ijthermalsci.2018.11.031. URL: https://linkinghub.elsevier.com/retrieve/pii/S1290072918307348 (visited on 24/10/2023).

[135] D.A. NIELD. Estimation of an effective Rayleigh number for convection in a vertically inhomogeneous porous medium or clear fluid. In: International Journal of Heat and Fluid Flow 15.4 (Aug. 1994), pp. 337–340. ISSN: 0142727X. DOI: 10.1016/0142-727X(94)90019-1. URL: https://linkinghub.elsevier.com/retrieve/pii/0142727X94900191 (visited on 05/11/2023).

[136] John D. DESAIN et al. Tensile tests of paraffin wax for hybrid rocket fuel grains. 2008.

[137] Ryu SUNGHOON et al. Tensile and compressive strength characteristics of aluminized paraffin wax fuel for various particle size and contents. In: Journal of the Korean Society of Propulsion Engineers 20 (2016).

[138] Zhimin WU et al. Theoretical and experimental study of foam-filled lattice composite panels under quasi-static compression loading. In: Composites Part B: Engineering 60 (Apr. 2014), pp. 329–340. ISSN: 13598368. DOI: 10.1016/j.compositesb.2013.12.078. URL: https://linkinghub.elsevier.com/retrieve/pii/S135983681400002X (visited on 08/11/2023).

[139] Enes SERT et al. Tensile and compressive behaviour of additively manufactured AlSi10Mg samples. In: Progress in Additive Manufacturing 5 (2020).

[140] Artem ANDRIANOV et al. Experimental study of severity level of structural discontinuities in paraffin grains of hybrid propellant rocket. In: Acta Astronautica 162 (2019).

[141] P. B. ATTEWELL, J. YEATES and A. R. SELBY. Soil movements induced by tunnelling and their effects on pipelines and structures. 1986.

[142] J. BÜHRING. Ph.D. thesis. PhD thesis. RWTH Aachen University.

[143] Konstantinos S. PAPACHRISTOU and Dimitrios S. SOPHIANOPOULOS. Buckling of beams on elastic foundation considering discontinuous (unbonded) contact. In: International Journal of Mechanics and Applications (2013).

[144] Robert D. COOK et al. Concepts and applications of finite element analysis. 4th Edition. 2002.

[145] Nick VASIOS. Nonlinear analysis of structures: The arc length method: Formulation, implementation and applications. 2015. URL: https://scholar.harvard.edu/vasios/links/nonlinear-analysis-structures-arc-length-method (visited on 04/08/2022).

[146] Amir R. KHOEI. BOUNDARY FRICTON MODEL. In: Computational Plasticity in Powder Forming Processes. Elsevier, 2005, pp. 101–127. ISBN: 978-0-08-044636-3. DOI: 10.1016/B978-008044636-3/50004-3. URL: https://linkinghub.elsevier.com/retrieve/pii/B9780080446363500043 (visited on 26/11/2023).

[147] Chuanyong CUI et al. Portevin-Le Châtelier effect in wrought Ni-based superalloys: Experiments and mechanisms. In: Journal of Materials Science & Technology 51 (Aug. 2020), pp. 16–31. ISSN: 10050302. DOI: 10.1016/j.jmst.2020.03.023. URL: https://linkinghub.elsevier.com/retrieve/pii/S100503022030284X (visited on 26/11/2023).

[148] S. TAMIMI, A. ANDRADE-CAMPOS and J. PINHO-DA-CRUZ. Modelling the Portevin-Le Chatelier effects in aluminium alloys: a review. In: Journal of the Mechanical Behavior of Materials 24.3 (1st Aug. 2015), pp. 67–78. ISSN: 2191-0243, 0334-8938. DOI: 10.1515/jmbm-2015-0008. URL: https://www.degruyter.com/document/doi/10.1515/jmbm-2015-0008/html (visited on 26/11/2023).

[149] Harpreet S. BEDI, Beant K. BILLING and Prabhat K. AGNIHOTRI. Interphase engineering in carbon fiber/epoxy composites: Rate sensitivity of interfacial shear strength and interfacial fracture toughness. In: Polymer Composites 41.7 (July 2020), pp. 2803–2815. ISSN: 0272-8397, 1548-0569. DOI: 10.1002/pc.25577. URL: https://4spepublications.onlinelibrary.wiley.com/doi/10.1002/pc.25577 (visited on 26/11/2023).

[150] Zhi-Hao WANG. A Novel Soft Sensor Approach of Polymer Process for Resin Monitoring Based on Melt Pressure Spectrum. In: IEEE Sensors Journal 23.15 (1st Aug. 2023), pp. 17551–17558. ISSN: 1530-437X, 1558-1748, 2379-9153. DOI: 10.1109/JSEN.2023.3285106. URL: https://ieeexplore.ieee.org/document/10171159/ (visited on 26/11/2023).

[151] Jin-Shui YANG et al. Hybrid lightweight composite pyramidal truss sandwich panels with high damping and stiffness efficiency. In: Composite Structures 148 (2016).

[152] Jarrett REVELS, Miles LUBIN and Theodore PAPAMARKOU. Forward-Mode Automatic Differentiation in Julia. 26th July 2016. arXiv: 1607.07892[cs]. URL: http://arxiv.org/abs/1607.07892 (visited on 09/11/2023).

[153] Ange-Christian IRADUKUNDA. Transient thermal performance using phase change material integrated topology optimized heat sinks. In: Applied Thermal Engineering (2020), p. 8.

[154] Alberto PIZZOLATO et al. Topology optimization for heat transfer enhancement in Latent Heat Thermal Energy Storage. In: International Journal of Heat and Mass Transfer 113 (Oct. 2017), pp. 875–888. ISSN: 00179310. DOI: 10.1016/j.ijheatmasstransfer.2017.05.098. URL: https://linkinghub.elsevier.com/retrieve/pii/S0017931017303034 (visited on 11/11/2023).

[155] Alberto PIZZOLATO et al. Multi-scale topology optimization of multi-material structures with controllable geometric complexity — Applications to heat transfer problems. In: Computer Methods in Applied Mechanics and Engineering 357 (Dec. 2019), p. 112552. ISSN: 00457825. DOI: 10.1016/j.cma.2019.07.021. URL: https://linkinghub.elsevier.com/retrieve/pii/S0045782519304177 (visited on 11/11/2023).

[156] Y.S. SEE et al. Experimental investigation of a topology-optimized phase change heat sink optimized for natural convection. In: Applied Energy 314 (May 2022), p. 118984. ISSN: 03062619. DOI: 10.1016/j.apenergy.2022.118984. URL: https://linkinghub.elsevier.com/retrieve/pii/S0306261922003932 (visited on 11/11/2023).

[157] N. M. NEWMARK. A Simple Approximate Formula for Effective End-Fixity of Columns. In: Journal of the Aeronautical Sciences 16.2 (Feb. 1949), pp. 116–116. ISSN: 1936-9956. DOI: 10.2514/8.11738. URL: https://arc.aiaa.org/doi/10.2514/8.11738 (visited on 08/11/2023).

[158] Kai SCHÜLLER. CoMeTFoam. URL: https://github.com/geo-fluid-dynamics/CoMeTFoam.

[159] A. D. BRENT, V. R. VOLLER and K. J. REID. ENTHALPY-POROSITY TECHNIQUE FOR MODELING CONVECTION-DIFFUSION PHASE CHANGE: APPLICATION TO THE MELTING OF A PURE METAL. In: Numerical Heat Transfer 13.3 (Apr. 1988), pp. 297–318. ISSN: 0149-5720. DOI: 10.1080/10407788808913615. URL: http://www.tandfonline.com/doi/abs/10.1080/10407788808913615 (visited on 30/10/2023).

[160] Vesselin Krassimirov KRASTEV and Giacomo FALCUCCI. Comparison of enthalpy-porosity and lattice Boltzmann-phase field techniques for the simulation of the heat transfer and melting processes in LHTES devices. In: E3S Web of Conferences 312 (2021). Ed. by ATI ITALIAN TERMOTECNICS ASSOCIATION and ATI ITALIAN TERMOTECNICS ASSOCIATION, p. 01002. ISSN: 2267-1242. DOI: 10.1051/e3sconf/202131201002. URL: https://www.e3s-conferences.org/10.1051/e3sconf/202131201002 (visited on 30/10/2023).

[161] Raghavendra Rohith KASIBHATLA et al. Numerical modelling of melting and settling of an encapsulated PCM using variable viscosity. In: Heat and Mass Transfer 53.5 (May 2017), pp. 1735–1744. ISSN: 0947-7411, 1432-1181. DOI: 10.1007/s00231-016-1932-0. URL: http://link.springer.com/10.1007/s00231-016-1932-0 (visited on 30/10/2023).

[162] M. A. BIOT. Bending of an infinite beam on an elastic foundation. In: Journal of Applied Mechanics (1937).

[163] Aleksandar B. VESIC, ed. Beams on elastic subgrade and winkler's hypothesis. 1961.

[164] J. D. ARISTIZABAL-OCHOA. Stability of slender columns on an elastic foundation with generalised end conditions. In: Ingeniería e Investigación 33 (2013).

[165] Feng ZHAOHUA and Robert D. COOK. Beam elements on two-parameter elastic foundations. In: Journal of Engineering Mechanics 109 (1983).

[166] T. YOKOYAMA. Parametric instability of Timoshenko beams resting on an elastic foundation. In: Computers & Structures 28 (1988).

[167] Ian Richard COLE. Modelling CPV. PhD thesis. Loughborough University, 2015. URL: https://repository.lboro.ac.uk/articles/thesis/Modelling_CPV/9523520 (visited on 23/03/2022).

[168] Ashok Kumar NALLATHAMBI, Eckehard SPECHT and Albrecht BERTRAM. Finite element technique for phase-change heat conduction problem. In: Volume 2: Theory and Fundamental Research; Aerospace Heat Transfer; Gas Turbine Heat Transfer; Computational Heat Transfer (2009). DOI: 10.1115/ht2009-88106.

Parts of this work are related to the results obtained within the scope of the following student theses, which I was the supervisor of:

- Behnke Llanos, David. *Investigation of the mechanical stability of phase change material-lattice structure composites*, submitted April 2022.
- Soika, Johannes Franz. *Semi-Analytical Model for Phase Change Material-Lattice Structure Composites with Generic Topology Parameters*, submitted January 2023.
- Wagner, Dominik. *Numerical Investigation of the Influence of different Lattice Geometries on the Convective Flow in Latent Heat Storage Systems*, submitted June 2023.
- Hernandez Saurbier, Laura. *Experimental Investigation of the Stability Behaviour of slender Beams embedded in Phase Change Materials*, submitted July 2023.
- Hayden, Samuel. *Multi-Functional Topology Optimization of Lattice Structures with embedded Phase Change Materials for use in Spacecraft Structures*, submitted October 2023.

A Non-dimensional numbers for heat transfer

In the following, useful definitions for non-dimensional numbers are introduced, which are used to describe the heat transfer phenomena. These are the Nusselt, Reynolds, Prandtl, Grashof, Rayleigh, Fourier, and Stefan numbers.

$$\bar{Nu} = \frac{1}{\lambda}\left[\int_0^L h dx L\right] \tag{A.1}$$

Empirical correlations relate the Nusselt number to other relevant non-dimensional numbers. Typically, for a natural convection case, the Nusselt number can be expressed as a function of the Rayleigh (*Ra*) and Prandtl (*Pr*) numbers, while for forced convection, the Nusselt number is a function of the Reynolds (*Re*) number and of the Prandtl number. These non-dimensional numbers are defined in the following.

- Prandtl number: is the ratio between the momentum diffusivity and the thermal diffusivity. It is defined as

  $$Pr = \frac{\nu}{\alpha} = \frac{C_p \mu}{\lambda} \tag{A.2}$$

  where ν is the kinematic viscosity, α is the thermal diffusivity, and μ the dynamic viscosity.

- Reynolds number: is the ratio between inertial forces and viscous ones and is associated with the characteristics of a flow, i.e. laminar or turbulent.

  $$Re = \frac{uL}{\nu} \tag{A.3}$$

  where u is the fluid velocity and L is a characteristic length.

- Grashof number: represents the ratio between buoyancy and viscous forces. It is often used for the description of a flow in which natural convection plays a dominant role.

  $$Gr = \frac{g\beta(T_w - T_f)}{\nu^2} \tag{A.4}$$

  where g is the gravitational acceleration, β is the coefficient of thermal expansion, T_w is the surface temperature and T_f is the fluid bulk temperature.

- Rayleigh number: is defined as the product of the Grashof and the Prandtl numbers. For a porous medium it is defined as

$$Ra = \frac{\rho g \beta (T_w - T_f) LK}{\nu \alpha} \tag{A.5}$$

  where K is the permeability of the porous medium, β is the coefficient of thermal expansion, T_w is the surface temperature and T_f is the fluid bulk temperature.

- Fourier number: is the ratio between the thermal diffusivity and the time scale of the process. It is expressed as

$$Fo = \frac{\alpha t}{L^2} \tag{A.6}$$

  where t is the characteristic time and L is a characteristic length.

- Stefan number: is the ratio between the latent heat and the thermal energy. It is defined as

$$Ste = \frac{C_p \Delta T}{H_f} \tag{A.7}$$

  where ΔT is the temperature difference between the considered temperature T and the melting temperature T_m. H_f is the latent heat of fusion.

These non-dimensional numbers are used to describe the heat transfer phenomena in porous media.

B Material properties considered

Table B.1: Mechanical material properties of the lattice structure (AlSi10Mg) and PCM (paraffin).

	AlSi10Mg	Paraffin
Young's modulus E [MPa]	75,000	210
Poisson ratio ν [-]	0.3	0.49
Yield strength (compression) R_{dp} [MPa]	250	~ 3
Yield strength (tension) $R_{p0.2}$ [MPa]	210	$1-2$

Table B.2: Thermophysical properties of the employed n-Octadecane paraffin wax.

Property	Solid	Liquid
Density $[kg/m^3]$	814	774
Specific heat capacity $[J/(kgK)]$	2150	2180
Thermal conductivity $[W/(mK)]$	0.358	0.152
Melting point [°C]	29	-
Latent heat of fusion $[kJ/kg]$	244	-

Table B.3: Thermophysical properties of the considered materials

Material	Density [$\mathrm{kg\,m^{-3}}$]	Specific Heat Capacity [$\mathrm{J\,kg^{-1}\,K}$]	Thermal Conductivity [$\mathrm{W\,m^{-1}\,K}$]	Melting point [°C]	Latent heat of fusion [$\mathrm{kJ\,kg^{-1}}$]
n-Octadecane (liquid)	814	2180	0.358	-	-
n-Octadecane (solid)	774	2150	0.152	29	240
AlSi10Mg (solid)	2700	888	120	-	-

C Effective Thermal Conductivity Formulae

f_2cc

$$\varepsilon = 1 - \frac{\tan\gamma}{W^3}\left[\pi r^2 H\frac{4}{\sin\gamma} - 0.728\cdot\left(\frac{16}{3}r^3\frac{2}{\sin(\pi-2\gamma)} + \frac{96}{3}r^3\sin(\pi-2\gamma)(\mathrm{cosec}(\pi-2\gamma)-\cot(\pi-2\gamma))\right)\right.$$

z-direction:

$$\begin{aligned}
t_2 &= \left(V_2\sin^2\gamma\cos\gamma\right)^{1/3}\\
t_4 &= \left(V_4\sin^2\gamma\cos\gamma\right)^{1/3}\\
R_1 &= \frac{2\sin^2\gamma}{2.024\cos\gamma\, t_4\lambda_s}\\
L_{\mathrm{str}} &= \frac{h}{2\sin\gamma} - \frac{t_2+t_4}{2}\sqrt{\frac{1}{\cos^2\gamma}+\frac{2}{\sin^2\gamma}}\\
R_2 &= \frac{L_{\mathrm{str}}}{\pi r^2\lambda_s}\\
R_3 &= \frac{\sin^2\gamma}{1.793\cos\gamma\, t_2\lambda_s}\\
R_{\mathrm{str}} &= 2\left(R_1+R_2+R_3\right)\\
R_s &= \frac{R_{\mathrm{str}}}{4}\\
\lambda_{\mathrm{f_2cc,z}} &= \varepsilon\lambda_f + \frac{\tan\gamma}{hR_s}
\end{aligned}$$

x,y-direction:

$$
\begin{aligned}
V_4 &= 2\frac{16}{3\sin(\pi-2\gamma)}r^3 - 12\left(\sqrt{8}-\sqrt{6}\right)r^3 \\
t_2 &= \left(V_2 \sin\gamma\cos^2\gamma\right)^{1/3} \\
t_4 &= \left(V_4 \sin\gamma\cos^2\gamma\right)^{1/3} \\
R_1 &= \frac{2\cos^2\gamma}{1.309\sin\gamma\, t_4\lambda_s} \\
L_{\text{str}} &= \frac{h}{2\sin\gamma} - \frac{t_2+t_4}{2}\sqrt{\frac{2}{\cos^2\gamma}+\frac{1}{\sin^2\gamma}} \\
R_2 &= \frac{L_{\text{str}}}{\pi r^2\lambda_s} \\
R_3 &= \frac{\cos^2\gamma}{3.316\sin\gamma\, t_2\lambda_s} \\
R_{\text{str}} &= 2\left(R_1+R_2+R_3\right) \\
R_s &= \frac{R_{\text{str}}}{2} \\
\lambda_{\text{f}_2\text{cc,xy}} &= \varepsilon\lambda_f + \frac{1}{hR_s}
\end{aligned}
$$

$f_2$ccz

$$
\varepsilon = 1-\tan^2\gamma\frac{r^2}{h^2}\left(\pi\left(1+\frac{4}{\sin\gamma}\right)-\frac{16r}{3h}\left(\frac{2.993}{\sin(\pi-2\gamma)}+\frac{3.667}{\sin(\pi/2-\gamma)}\right)\right)
$$

z-direction:

$$
\begin{aligned}
V_2 &= \frac{16}{3\sin(\pi-2\gamma)}r^3 \\
V_4 &= 2\frac{16}{3\sin(\pi-2\gamma)}r^3 - 12\left(\sqrt{8}-\sqrt{6}\right)r^3 \\
t_2 &= \left(V_2 \sin^2\gamma\cos\gamma\right)^{1/3} \\
t_4 &= \left(V_4 \sin^2\gamma\cos\gamma\right)^{1/3} \\
R_1 &= \frac{2\sin^2\gamma}{1.448\cos\gamma\, t_4\lambda_s}
\end{aligned}
$$

$$L_{\mathrm{str}} = \frac{h}{2\sin\gamma} - \frac{t_2 + t_4}{2}\sqrt{\frac{1}{\cos^2\gamma} + \frac{2}{\sin^2\gamma}}$$
$$R_2 = \frac{L_{\mathrm{str}}}{\pi r^2 \lambda_s}$$
$$R_3 = \frac{\sin^2\gamma}{1.168\cos\gamma\, t_2 \lambda_s}$$
$$R_{\mathrm{str}} = 2\left(R_1 + R_2 + R_3\right)$$
$$R_z = \frac{h}{\pi r^2 \lambda_s}$$
$$R_s = \left(\frac{1}{R_z} + \frac{4}{R_{\mathrm{str}}}\right)$$
$$\lambda_{\mathrm{f_2ccz,z}} = \varepsilon\lambda_f + \frac{\tan\gamma}{hR_s}$$

x,y-direction:

$$\varepsilon = 1 - \tan^2\gamma \frac{r^2}{h^2}\left(\pi\left(1 + \frac{4}{\sin\gamma}\right) - \frac{16r}{3h}\left(\frac{2.993}{\sin(\pi - 2\gamma)} + \frac{3.667}{\sin(\pi/2 - \gamma)}\right)\right)$$
$$V_2 = \frac{16}{3\sin(\pi - 2\gamma)} r^3$$
$$V_4 = 2\frac{16}{3\sin(\pi - 2\gamma)} r^3 - 12\left(\sqrt{8} - \sqrt{6}\right) r^3$$
$$t_2 = \left(V_2 \sin\gamma\cos^2\gamma\right)^{1/3}$$
$$t_4 = \left(V_4 \sin\gamma\cos^2\gamma\right)^{1/3}$$
$$R_1 = \frac{2\cos^2\gamma}{1.732\sin\gamma\, t_4 \lambda_s}$$
$$L_{\mathrm{str}} = \frac{h}{2\sin\gamma} - \frac{t_2 + t_4}{2}\sqrt{\frac{2}{\cos^2\gamma} + \frac{1}{\sin^2\gamma}}$$
$$R_2 = \frac{L_{\mathrm{str}}}{\pi r^2 \lambda_s}$$
$$R_3 = \frac{\cos^2\gamma}{2.836\sin\gamma\, t_2 \lambda_s}$$
$$R_{\mathrm{str}} = 2\left(R_1 + R_2 + R_3\right)$$
$$R_s = \frac{R_{\mathrm{str}}}{2}$$
$$\lambda_{\mathrm{f_2ccz,xy}} = \varepsilon\lambda_f + \frac{1}{hR_s}$$

bcc

$$
\begin{aligned}
\beta &= \arctan\left(\tan(\gamma)/\sqrt{2}\right) \\
\varepsilon &= 1 - 2\tan^2\beta\frac{r^2}{h^2}\left(\pi\frac{4}{\sin\beta} - \frac{16r}{3h}\left(\frac{2.993}{\sin(\pi-2\beta)} + \frac{3.340}{\sin(\pi/2-\beta)}\right)\right) \\
V_4 &= 2\frac{16}{3\sin(\pi-2\beta)}r^3 - 12\left(\sqrt{8}-\sqrt{6}\right)r^3 \\
t_4 &= \left(V_4\sin^2\beta\cos\beta\right)^{1/3} \\
R_1 = R_3 &= \frac{2\sin^2\beta}{1.903\cos\beta\ t_4\lambda_s} \\
L_{\mathrm{str}} &= \frac{h}{2\sin\beta} - t_4\sqrt{\frac{1}{\cos^2\beta} + \frac{2}{\sin^2\beta}} \\
R_2 &= \frac{L_{\mathrm{str}}}{\pi r^2\lambda_s} \\
R_{\mathrm{str}} &= 2\left(R_1 + R_2 + R_3\right) \\
R_s &= \frac{R_{\mathrm{str}}}{4} \\
\lambda_{\mathrm{bcc}} &= \varepsilon\lambda_f + \frac{2\tan^2\beta}{hR_s}
\end{aligned}
$$

bccz (z-direction)

$$\beta = \arctan\left(\tan(\gamma)/\sqrt{2}\right)$$

$$\varepsilon = 1 - 2\tan^2\beta\frac{r^2}{h^2}\left(\pi\left(1+\frac{4}{\sin\beta}\right) - \frac{16r}{3h}\left(\frac{3.137}{\sin(\pi-2\beta)} + \frac{4.923}{\sin(\pi/2-\beta)}\right)\right)$$

$$V_4 = 2\frac{16}{3\sin(\pi-2\beta)}r^3 - 12\left(\sqrt{8}-\sqrt{6}\right)r^3$$

$$t_4 = \left(V_4\sin^2\beta\cos\beta\right)^{1/3}$$

$$R_1 = R_3 = \frac{2\sin^2\beta}{1.537\cos\beta\ t_4\lambda_s}$$

$$L_{\text{str}} = \frac{h}{2\sin\beta} - t_4\sqrt{\frac{1}{\cos^2\beta}+\frac{2}{\sin^2\beta}}$$

$$R_2 = \frac{L_{\text{str}}}{\pi r^2\lambda_s}$$

$$R_{\text{str}} = 2\left(R_1+R_2+R_3\right)$$

$$R_z = \frac{h}{\pi r^2\lambda_s}$$

$$R_s = \left(\frac{1}{R_z}+\frac{4}{R_{\text{str}}}\right)$$

$$\lambda_{\text{bccz,z}} = \varepsilon\lambda_f + \frac{2\tan^2\beta}{hR_s}$$

bccz (x,y-direction)

$$
\begin{aligned}
\beta &= \arctan\left(\tan(\gamma)/\sqrt{2}\right) \\
\varepsilon &= 1 - 2\tan^2\beta\frac{r^2}{h^2}\left(\pi\left(1+\frac{4}{\sin\beta}\right) - \frac{16r}{3h}\left(\frac{3.137}{\sin(\pi-2\beta)} + \frac{4.923}{\sin(\pi/2-\beta)}\right)\right) \\
V_4 &= 2\frac{16}{3\sin(\pi-2\beta)}r^3 - 12\left(\sqrt{8}-\sqrt{6}\right)r^3 \\
t_4 &= \left(V_4\sin\beta\cos^2\beta\right)^{1/3} \\
R_1 &= \frac{2\cos^2\beta}{10.95\tan\beta\sin\beta\ t_4\lambda_s} \\
L_{\text{str}} &= \frac{h}{2\sin\beta} - t_4\sqrt{\frac{2}{\cos^2\beta}+\frac{1}{\sin^2\beta}} \\
R_2 &= \frac{L_{\text{str}}}{\pi r^2\lambda_s} \\
R_3 &= \frac{2\cos^2\beta}{4.073\sin\beta\ t_4\lambda_s} \\
R_{\text{str}} &= 2\left(R_1+R_2+R_3\right) \\
R_s &= \frac{R_{\text{str}}}{4} \\
\lambda_{\text{bccz,xy}} &= \varepsilon\lambda_f + \frac{1}{hR_s}
\end{aligned}
$$

$f_2$bcc (z-direction)

$$\beta = \arctan\left(\tan(\gamma)/\sqrt{2}\right)$$

$$\varepsilon = 1 - 2\tan^2\beta\frac{r^2}{h^2}\left(\pi\left(\frac{4}{\sin\gamma}+\frac{4}{\sin\beta}\right)...\right.$$

$$\left. -\frac{16r}{3h}\left(\frac{3.940}{\sin(\pi-2\gamma)}+\frac{4.380}{\sin(\pi/2-\gamma)}+\frac{3.706}{\sin(\pi-2\beta)}+\frac{4.190}{\sin(\pi/2-\beta)}\right)\right)$$

$$V_{2,fc} = \frac{16}{3\sin(\pi-2\gamma)}r^3$$

$$V_{4,fc} = 2\frac{16}{3\sin(\pi-2\gamma)}r^3 - 12\left(\sqrt{8}-\sqrt{6}\right)r^3$$

$$V_{4,bc} = 2\frac{16}{3\sin(\pi-2\beta)}r^3 - 12\left(\sqrt{8}-\sqrt{6}\right)r^3$$

$$V_8 = V_{4,fc} + V_{4,bc} - \frac{16}{3}\left(3+\sqrt{12}-\sqrt{32}\right)r^3$$

$$t_{2,fc} = \left(V_{2,fc}\sin^2\gamma\cos\gamma\right)^{1/3};\ \ t_{8,fc} = \left(V_8\sin^2\gamma\cos\gamma\right)^{1/3}$$

$$t_{4,bc} = \left(V_{4,bc}\sin^2\beta\cos\beta\right)^{1/3};\ \ t_{8,bc} = \left(V_8\sin^2\beta\cos\beta\right)^{1/3}$$

$$R_{1,fc} = \frac{4\sin^2\gamma}{2.145\cos\gamma\, t_4\lambda_s}$$

$$L_{\text{str,fc}} = \frac{h}{2\sin\gamma} - \frac{t_{8,fc}+t_{4,fc}}{2}\sqrt{\frac{1}{\cos^2\gamma}+\frac{2}{\sin^2\gamma}};\ \ R_{2,fc} = \frac{L_{\text{str,fc}}}{\pi r^2\lambda_s}$$

$$R_{3,fc} = \frac{\sin^2\gamma}{1.311\cos\gamma\, t_4\lambda_s}$$

$$R_{1,bc} = \frac{4\sin^2\beta}{2.145\cos\beta\ t_4\lambda_s}$$

$$L_{\text{str,bc}} = \frac{h}{2\sin\beta} - \frac{t_{8,bc}+t_{4,bc}}{2}\sqrt{\frac{1}{\cos^2\beta}+\frac{2}{\sin^2\beta}};\ \ R_{2,bc} = \frac{L_{\text{str,bc}}}{\pi r^2\lambda_s}$$

$$R_{3,bc} = \frac{2\sin^2\beta}{1.311\cos\beta\ t_4\lambda_s}$$

$$R_{\text{str,i}} = 2\left(R_1+R_2+R_3\right)$$

$$R_s = \left(\frac{4}{R_{\text{str,fc}}}+\frac{4}{R_{\text{str,bc}}}\right)$$

$$\lambda_{\text{f}_2\text{bcc,z}} = \varepsilon\lambda_f + \frac{2\tan^2\beta}{hR_s}$$

$f_2$bcc (x,y-direction)

$$\beta = \arctan\left(\tan(\gamma)/\sqrt{2}\right)$$

$$\varepsilon = 1 - 2\tan^2\beta\frac{r^2}{h^2}\left(\pi\left(\frac{4}{\sin\gamma}+\frac{4}{\sin\beta}\right)...\right.$$

$$\left. -\frac{16r}{3h}\left(\frac{3.940}{\sin(\pi-2\gamma)}+\frac{4.380}{\sin(\pi/2-\gamma)}+\frac{3.706}{\sin(\pi-2\beta)}+\frac{4.190}{\sin(\pi/2-\beta)}\right)\right)$$

$$V_{2,fc} = \frac{16}{3\sin(\pi-2\gamma)}r^3$$

$$V_{4,fc} = 2\frac{16}{3\sin(\pi-2\gamma)}r^3 - 12\left(\sqrt{8}-\sqrt{6}\right)r^3$$

$$V_{4,bc} = 2\frac{16}{3\sin(\pi-2\beta)}r^3 - 12\left(\sqrt{8}-\sqrt{6}\right)r^3$$

$$V_8 = V_{4,fc} + V_{4,bc} - \frac{16}{3}\left(3+\sqrt{12}-\sqrt{32}\right)r^3$$

$$t_{2,fc} = \left(V_{2,fc}\sin\gamma\cos^2\gamma\right)^{1/3};\ \ t_{8,fc} = \left(V_8\sin\gamma\cos^2\gamma\right)^{1/3}$$

$$t_{4,bc} = \left(V_{4,bc}\sin\beta\cos^2\beta\right)^{1/3};\ \ t_{8,bc} = \left(V_8\sin\beta\cos^2\beta\right)^{1/3}$$

$$R_{1,fc} = \frac{4\cos^2\gamma}{10.86\tan\gamma\ \sin\gamma t_4\lambda_s}$$

$$L_{\text{str,fc}} = \frac{h}{2\sin\gamma} - \frac{t_{8,fc}+t_{4,fc}}{2}\sqrt{\frac{2}{\cos^2\gamma}+\frac{1}{\sin^2\gamma}};\ \ R_{2,fc} = \frac{L_{\text{str,fc}}}{\pi r^2\lambda_s}$$

$$R_{3,fc} = \frac{\cos^2\gamma}{2.420\sin\gamma\, t_4\lambda_s}$$

$$R_{1,bc} = \frac{3\cos^2\beta}{10.86\tan\beta\ \sin\beta t_4\lambda_s}$$

$$L_{\text{str,bc}} = \frac{h}{2\sin\beta} - \frac{t_{8,bc}+t_{4,bc}}{2}\sqrt{\frac{2}{\cos^2\beta}+\frac{1}{\sin^2\beta}};\ \ R_{2,bc} = \frac{L_{\text{str,bc}}}{\pi r^2\lambda_s}$$

$$R_{3,bc} = \frac{2\cos^2\beta}{3.840\sin\beta\ t_4\lambda_s}$$

$$R_{\text{str,i}} = 2\left(R_1+R_2+R_3\right)$$

$$R_s = \left(\frac{2}{R_{\text{str,fc}}}+\frac{4}{R_{\text{str,bc}}}\right)$$

$$\lambda_{\text{f}_2\text{bcc,xy}} = \varepsilon\lambda_f + \frac{1}{hR_s}$$

$\mathbf{f_2}$bccz (z-direction)

$$\beta = \arctan\left(\tan(\gamma)/\sqrt{2}\right)$$

$$\varepsilon = 1 - 2\tan^2\beta\frac{r^2}{h^2}\left(\pi\left(1+\frac{4}{\sin\gamma}+\frac{4}{\sin\beta}\right)...\right.$$

$$\left. -\frac{16r}{3h}\left(\frac{3.741}{\sin(\pi-2\gamma)}+\frac{5.874}{\sin(\pi/2-\gamma)}+\frac{3.340}{\sin(\pi-2\beta)}+\frac{4.779}{\sin(\pi/2-\beta)}\right)\right)$$

$$V_{2,fc} = \frac{16}{3\sin(\pi-2\gamma)}r^3$$

$$V_{4,fc} = 2\frac{16}{3\sin(\pi-2\gamma)}r^3 - 12\left(\sqrt{8}-\sqrt{6}\right)r^3$$

$$V_{4,bc} = 2\frac{16}{3\sin(\pi-2\beta)}r^3 - 12\left(\sqrt{8}-\sqrt{6}\right)r^3$$

$$V_8 = V_{4,fc} + V_{4,bc} - \frac{16}{3}\left(3+\sqrt{12}-\sqrt{32}\right)r^3$$

$$t_{2,fc} = \left(V_{2,fc}\sin^2\gamma\cos\gamma\right)^{1/3};\ \ t_{8,fc} = \left(V_8\sin^2\gamma\cos\gamma\right)^{1/3}$$

$$t_{4,bc} = \left(V_{4,bc}\sin^2\beta\cos\beta\right)^{1/3};\ \ t_{8,bc} = \left(V_8\sin^2\beta\cos\beta\right)^{1/3}$$

$$R_{1,fc} = \frac{4\sin^2\gamma}{1.654\cos\gamma\, t_4\lambda_s}$$

$$L_{\text{str,fc}} = \frac{h}{2\sin\gamma} - \frac{t_{8,fc}+t_{4,fc}}{2}\sqrt{\frac{1}{\cos^2\gamma}+\frac{2}{\sin^2\gamma}};\ \ R_{2,fc} = \frac{L_{\text{str,fc}}}{\pi r^2\lambda_s}$$

$$R_{3,fc} = \frac{\sin^2\gamma}{1.185\cos\gamma\, t_4\lambda_s}$$

$$R_{1,bc} = \frac{4\sin^2\beta}{1.654\cos\beta\ t_4\lambda_s}$$

$$L_{\text{str,bc}} = \frac{h}{2\sin\beta} - \frac{t_{8,bc}+t_{4,bc}}{2}\sqrt{\frac{1}{\cos^2\beta}+\frac{2}{\sin^2\beta}};\ \ R_{2,bc} = \frac{L_{\text{str,bc}}}{\pi r^2\lambda_s}$$

$$R_{3,bc} = \frac{2\sin^2\beta}{1.133\cos\beta\ t_4\lambda_s}$$

$$R_{\text{str,i}} = 2\left(R_1+R_2+R_3\right)$$

$$R_z = \frac{h}{\pi r^2\lambda_s}$$

$$R_s = \left(\frac{1}{R_z}+\frac{4}{R_{\text{str,fc}}}+\frac{4}{R_{\text{str,bc}}}\right)$$

$$\lambda_{\mathrm{f_2bccz,z}} = \varepsilon\lambda_f + \frac{2\tan^2\beta}{hR_s}$$

$f_2$bccz (x,y-direction)

$$\beta = \arctan\left(\tan(\gamma)/\sqrt{2}\right)$$

$$\varepsilon = 1 - 2\tan^2\beta\frac{r^2}{h^2}\left(\pi\left(1+\frac{4}{\sin\gamma}+\frac{4}{\sin\beta}\right)...\right.$$

$$\left. -\frac{16r}{3h}\left(\frac{3.741}{\sin(\pi-2\gamma)}+\frac{5.874}{\sin(\pi/2-\gamma)}+\frac{3.340}{\sin(\pi-2\beta)}+\frac{4.779}{\sin(\pi/2-\beta)}\right)\right)$$

$$V_{2,fc} = \frac{16}{3\sin(\pi-2\gamma)}r^3$$

$$V_{4,fc} = 2\frac{16}{3\sin(\pi-2\gamma)}r^3 - 12\left(\sqrt{8}-\sqrt{6}\right)r^3$$

$$V_{4,bc} = 2\frac{16}{3\sin(\pi-2\beta)}r^3 - 12\left(\sqrt{8}-\sqrt{6}\right)r^3$$

$$V_8 = V_{4,fc} + V_{4,bc} - \frac{16}{3}\left(3+\sqrt{12}-\sqrt{32}\right)r^3$$

$$t_{2,fc} = \left(V_{2,fc}\sin\gamma\cos^2\gamma\right)^{1/3};\ t_{8,fc} = \left(V_8\sin\gamma\cos^2\gamma\right)^{1/3}$$

$$t_{4,bc} = \left(V_{4,bc}\sin\beta\cos^2\beta\right)^{1/3};\ t_{8,bc} = \left(V_8\sin\beta\cos^2\beta\right)^{1/3}$$

$$R_{1,fc} = \frac{4\cos^2\gamma}{9.576\tan\gamma\,\sin\gamma t_4\lambda_s}$$

$$L_{\text{str,fc}} = \frac{h}{2\sin\gamma} - \frac{t_{8,fc}+t_{4,fc}}{2}\sqrt{\frac{2}{\cos^2\gamma}+\frac{1}{\sin^2\gamma}};\ R_{2,fc} = \frac{L_{\text{str,fc}}}{\pi r^2\lambda_s}$$

$$R_{3,fc} = \frac{\cos^2\gamma}{3.468\sin\gamma\, t_4\lambda_s}$$

$$R_{1,bc} = \frac{3\cos^2\beta}{9.576\tan\beta\sin\beta\ t_4\lambda_s}$$

$$L_{\text{str,bc}} = \frac{h}{2\sin\beta} - \frac{t_{8,bc}+t_{4,bc}}{2}\sqrt{\frac{2}{\cos^2\beta}+\frac{1}{\sin^2\beta}};\ R_{2,bc} = \frac{L_{\text{str,bc}}}{\pi r^2\lambda_s}$$

$$R_{3,bc} = \frac{2\cos^2\beta}{4.564\sin\beta\ t_4\lambda_s}$$

$$R_{\text{str,i}} = 2\left(R_1+R_2+R_3\right)$$

$$R_s = \left(\frac{2}{R_{\text{str,fc}}}+\frac{4}{R_{\text{str,bc}}}\right)$$

$$\lambda_{f_2bccz,xy} = \varepsilon\lambda_f + \frac{1}{hR_s}$$

D Experimental setup of the thermal experiments

All specimens utilized in the experiment were additively manufactured by EOS GmbH, utilizing an AlSi10Mg aluminum alloy. They possess a cubic morphology with a 50 mm edge length and feature a periodic internal structure consisting of a single unit cell topology. These samples exhibit unit cells with uniform cell widths of 5 mm, 1 mm strut diameters, and a cubic shape. Owing to variations in the number and geometric arrangement of struts within each cell, the volume fraction differs among the tested specimens, and this information is detailed in Table 4.4. The available samples, shown in Figure 4.21, enable the investigation of how unit cell topology influences heat transfer, while keeping cell size, aspect ratio, and strut diameter constant. Two sides of the cube are sealed with 1 mm thick aluminium sheets that are additively manufactured along with the samples. Meanwhile, the remaining four sides remain open, facilitating the observation of the phase change phenomenon and the integration of temperature sensors.

The experimental configuration, as depicted in Figure 4.22, comprises the composite specimens, a heating system, a containment box, measurement instruments, and a data acquisition system. The heating system comprises a cartridge heater with a length of 50 mm and a diameter of 6.5 mm (100 W class from Horst GmbH, Germany). This cartridge heater is installed within an aluminum heat spreader measuring 15 mm x 50 mm x 50 mm. To maintain a consistent input power of 40 W, a PWM controller equipped with a solid-state relay (specifically, the CL240D05 by Crydom Inc., USA) is employed. To ensure effective thermal contact between the aluminum face sheet of the test sample and the heat spreader, a high-conductivity paste is utilized. As shown in Figure 4.22, a Germanium window is mounted on a flange and sealed on the test sample surface. Germanium is a semiconductor material with a narrow energy bandgap, which means it has excellent optical transmission properties in the infrared region of the electromagnetic spectrum. This property is crucial for IR visualization because it allows Germanium to transmit IR radiation efficiently without significant absorption. When using Germanium as an optical material, photons in the IR range can pass through it with minimal energy loss. Germanium is commonly used for IR imaging in the mid-infrared (MIR) region of the spectrum, which typically spans wavelengths from approximately 2.5 to 25 micrometers (μm). This is also known as thermal infrared, as it corresponds to the IR radiation emitted by objects at temperatures ranging from ca. -180°Cto ca. 900°C. Specifically, this range covers the wavelengths emitted by objects with temperatures in the hundreds of degrees Kelvin and higher. The relationship between temperature (T) and the peak wavelength (λ) of emitted thermal radiation is described by Wien's displacement law:

$$\lambda_{max} = \frac{2.898 \cdot 10^{-3}}{T} \tag{D.1}$$

where λ_{max} is the peak wavelength in micrometers (μm), and T is the temperature in Kelvin (K). In summary, Germanium is used for IR visualization in the mid-infrared (MIR) wavelength range due to its excellent optical transmission properties in this region. This allows infrared (IR) visualization of the melting front expansion. The Germanium window is circular with a diameter of 50 mm, manufactured by Edmund Optics Inc. It is mounted on, and bonded to, an aluminium plate. In order to avoid reflection issues related to the reflectivity of aluminium, a PTFE plate is added to the construction (see Figure 4.22b).

On the opposing side of the Germanium window, an expansion plate, known as the Backplate (as illustrated in Figure D.1) is affixed. This backplate contains 100 empty chambers with square holes measuring 1 mm in width. These holes serve the purpose of enabling a uniform volume expansion of the PCM of up to 10% during the melting process and help alleviate the potential risks associated with pressure buildup. The compact dimensions of the orifice in each chamber prevent significant disruption of both the melting front's shape and expansion. The backplate component is additively manufactured using a proprietary resin from Formlabs, Inc, and it is securely bolted to one side of the cubic specimen. An airtight seal is achieved using an O-ring. The measurement system consists of temperature sensors and infrared visualization.

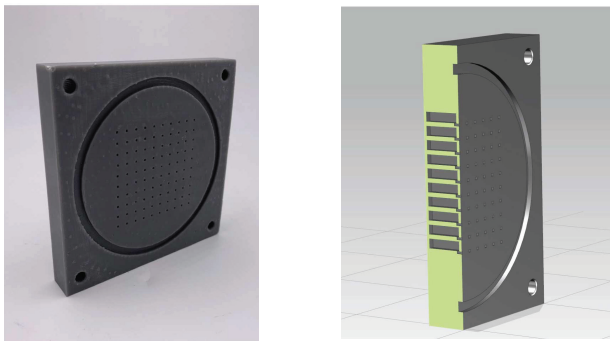

As manufactured CAD - section view

Fig. D.1: Epoxy resin-based backplate for the pressure compensation during melting of the PCM.

Ten four-wire PT100 temperature sensors are symmetrically positioned on two of the lateral sides of the cube, as depicted in Figure D.2. These sensors offer an accuracy of ±0.21 K at 40°C (tolerance class of F 0.15 A by Heraeus GmbH, Germany). The sensors are labeled in a progressive order as shown in Figure D.2. So, the sensor 2 and 7 are the closest to heating plate on each side, while the numbers 4 and 9 the furthest. The sides "A" and "B" represent the one that is facing the lower and upper orientation, respectively, when the test is conducted in "*side*" orientation. These PT100 sensors are connected through a PXI interface to a data logger (NI PXIe-1078 by National Instruments Corporation®), and the acquired data is processed and stored using the commercial software Dasylab® by measX GmbH. The sensors' casing is sealed with a bi-component epoxy glue on three of the six surfaces of the cubic specimen to create an airtight container for the PCM. Indeed, the cubic sample has one faces sealed during the manufacturing process, so that the heating plate can be thermally connected to the sample. One of the four orthogonal faces to the heater is enclosed from the Germanium window. The

opposite side is sealed with means of the Backplate, while the remaining faces are bonded to the Epoxy component shown in Figure D.2. Infrared inspection is conducted using a medium-wave-

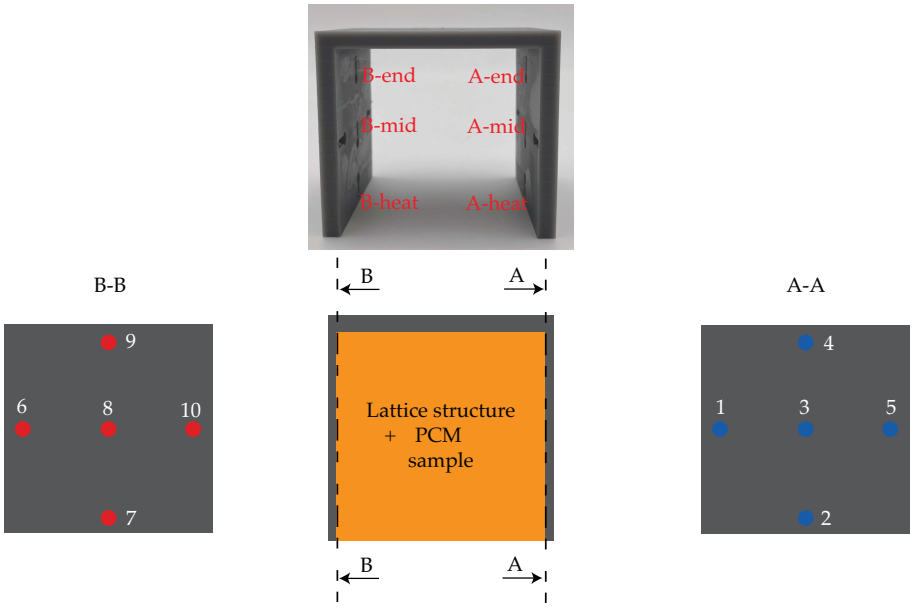

Fig. D.2: As manufactured casing for the PT100 sensor and schematics of the placement of the sensors.

cooled IR camera (ImageIR® 8300 from Infratec GmbH). The entire test cell is enclosed within a Polycarbonate box, accompanied by polystyrene foam (Styrodur®) that serves as insulation to isolate the test cell from the surrounding environment, as shown in Figure 4.22.

E Temperature profiles and Infrared frames

Temperature profiles for top heating

Results showing the temperature evolution on available PT100 sensors, plotted against experiment time for the top-heating orientation.

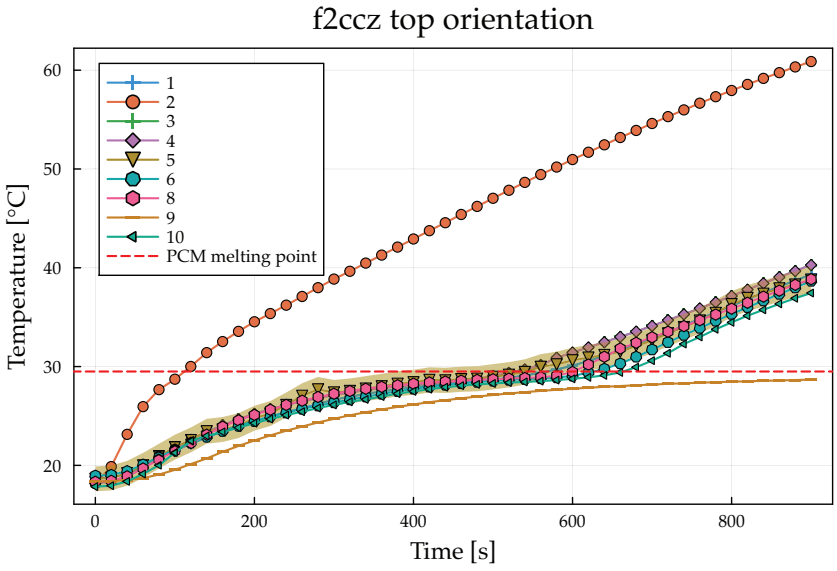

Fig. E.1: f_2ccz

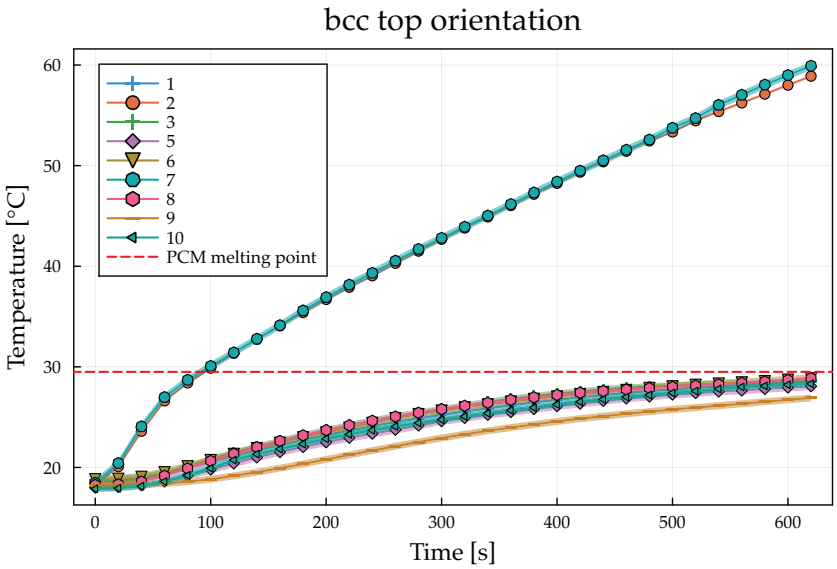

Fig. E.2: *bcc*

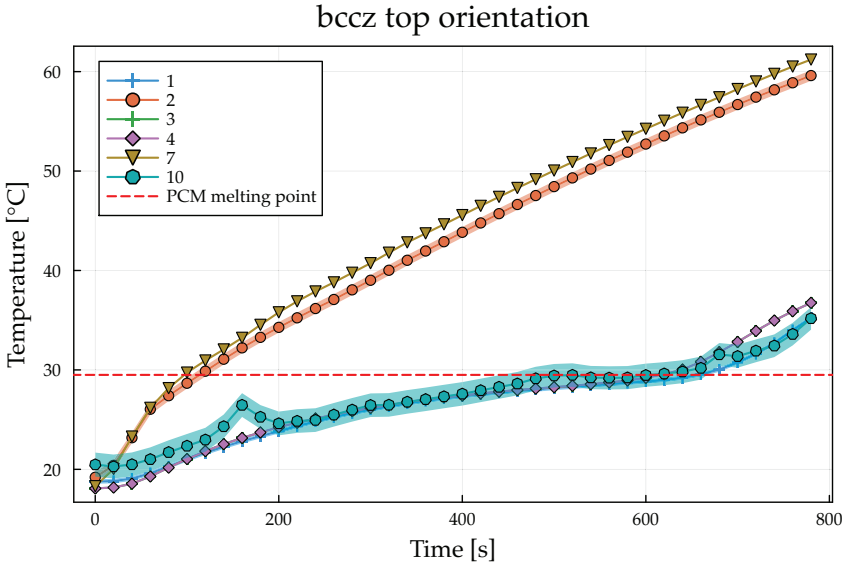

Fig. E.3: *bccz*

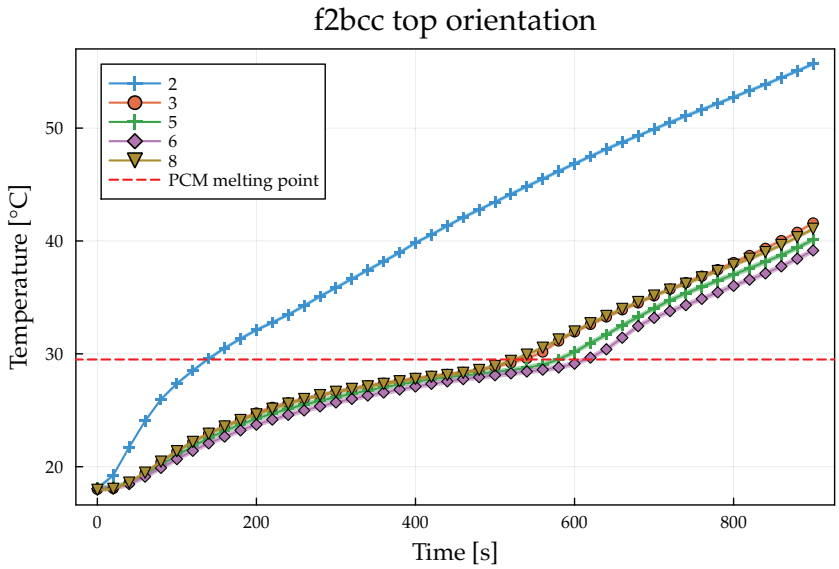

Fig. E.4: *f2bcc*

Temperature profiles for side heating

Results showing the temperature evolution on available PT100 sensors, plotted against experiment time for the side-heating orientation.

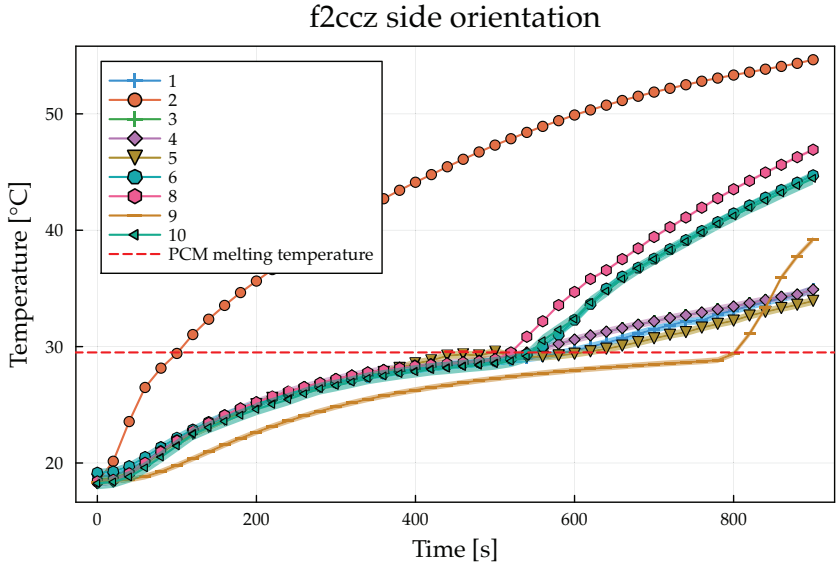

Fig. E.5: *f2ccz*

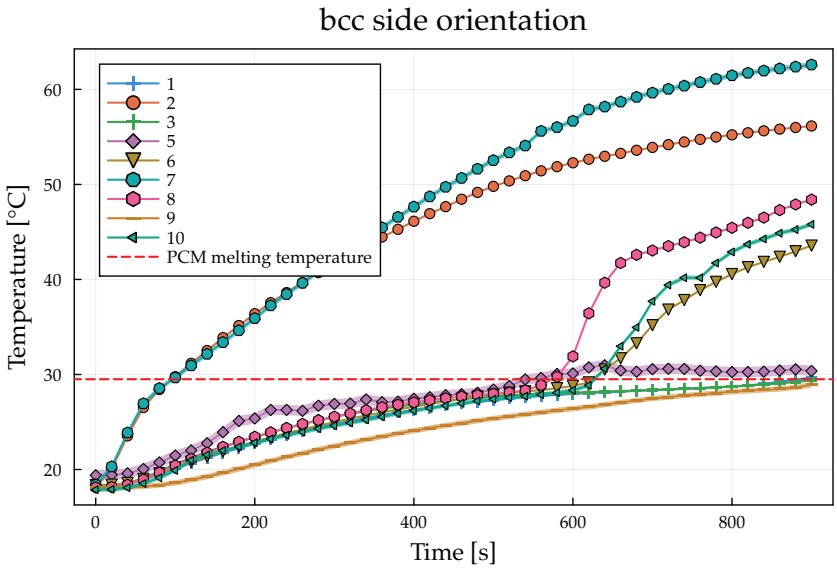

Fig. E.6: *bcc*

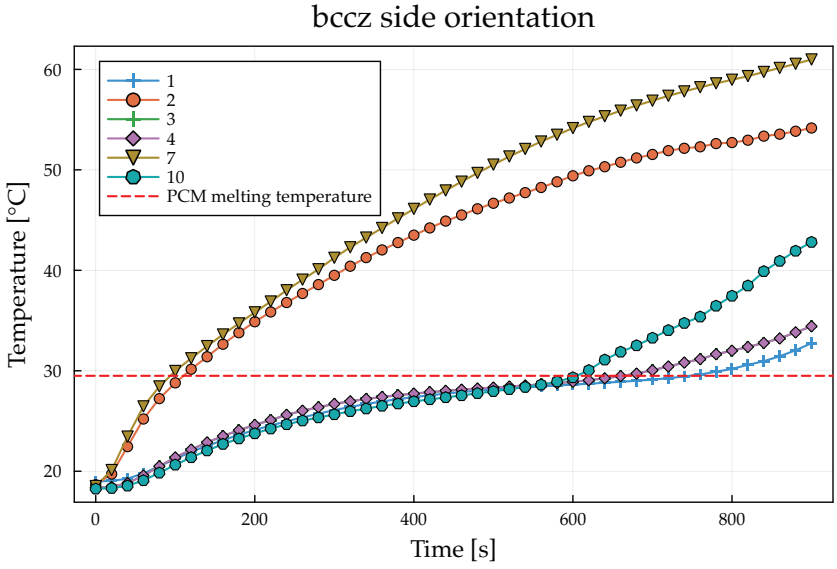

Fig. E.7: *bccz*

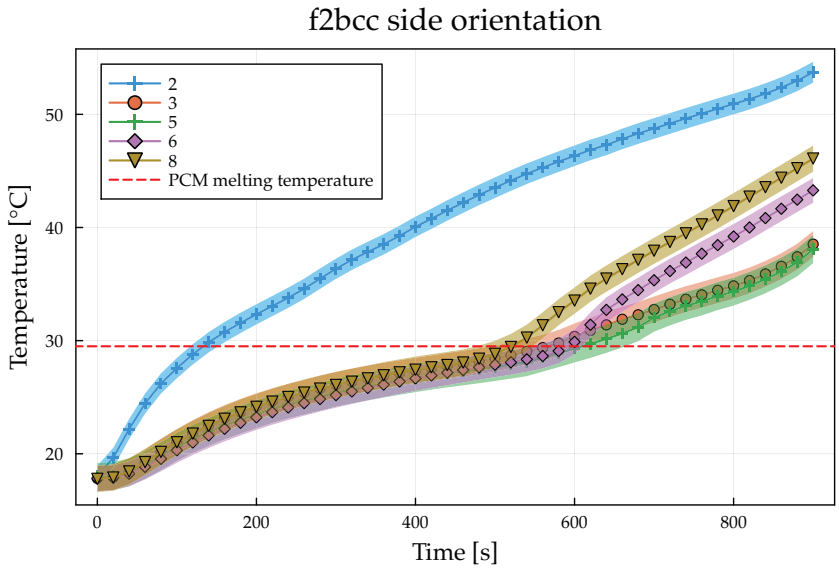

Fig. E.8: *f2bcc*

Temperature profiles for bottom heating

Results showing the temperature evolution on available PT100 sensors, plotted against experiment time for the bottom-heating orientation.

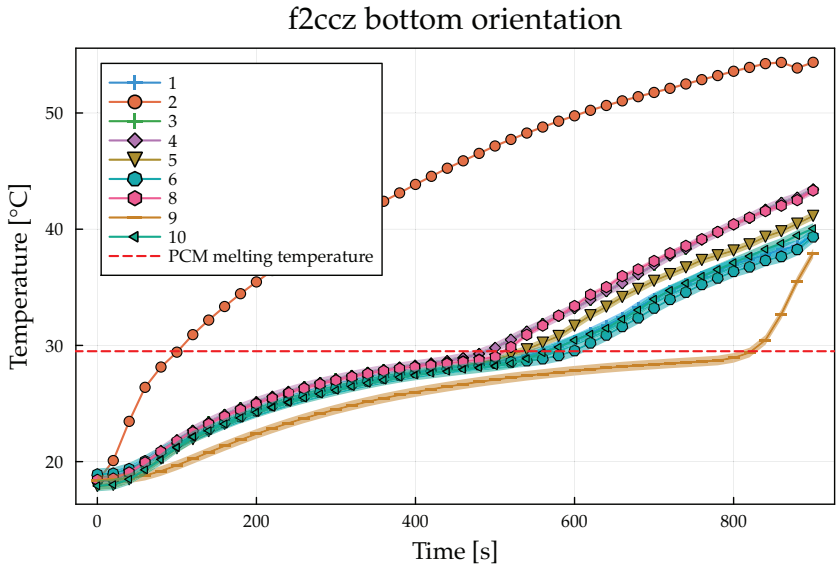

Fig. E.9: *f2ccz*

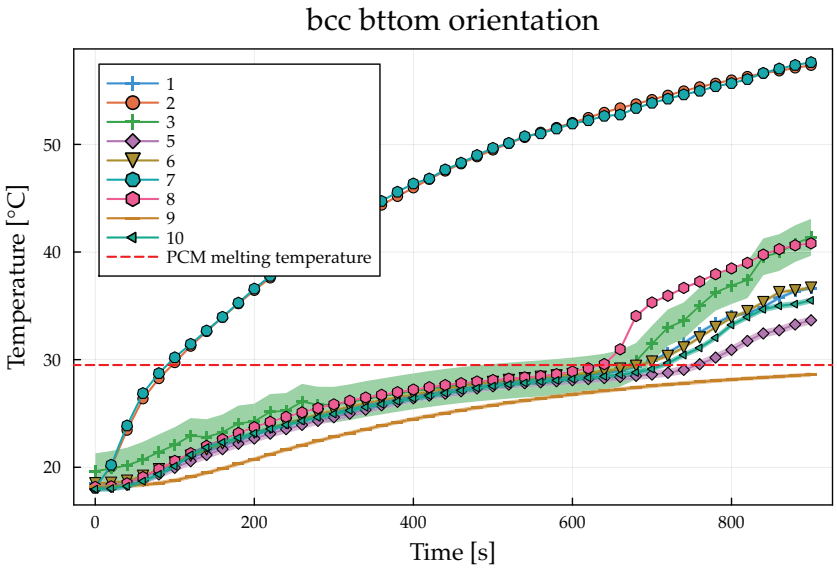

Fig. E.10: *bcc*

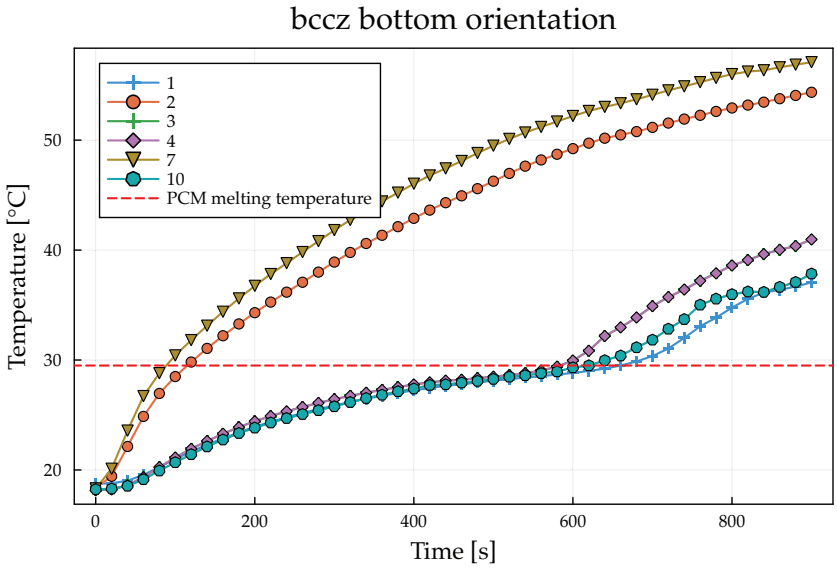

Fig. E.11: *bccz*

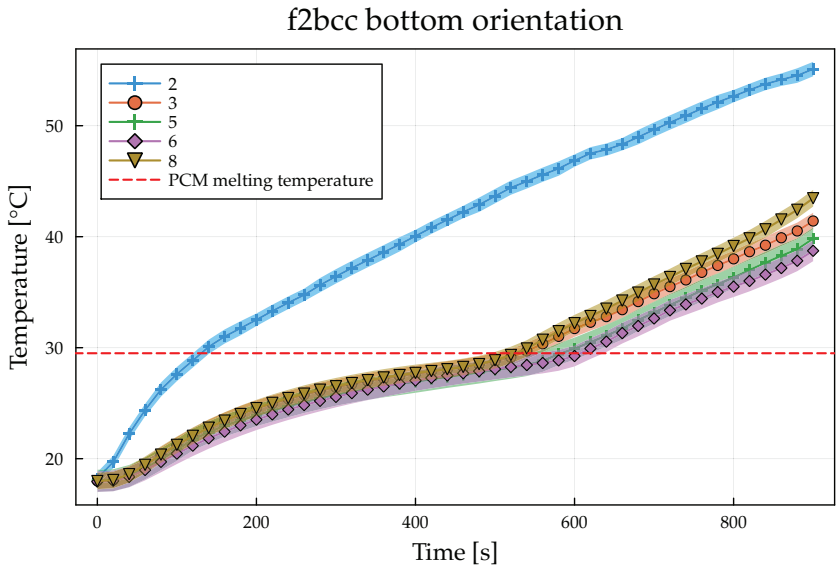

Fig. E.12: *f2bcc*

IR frames

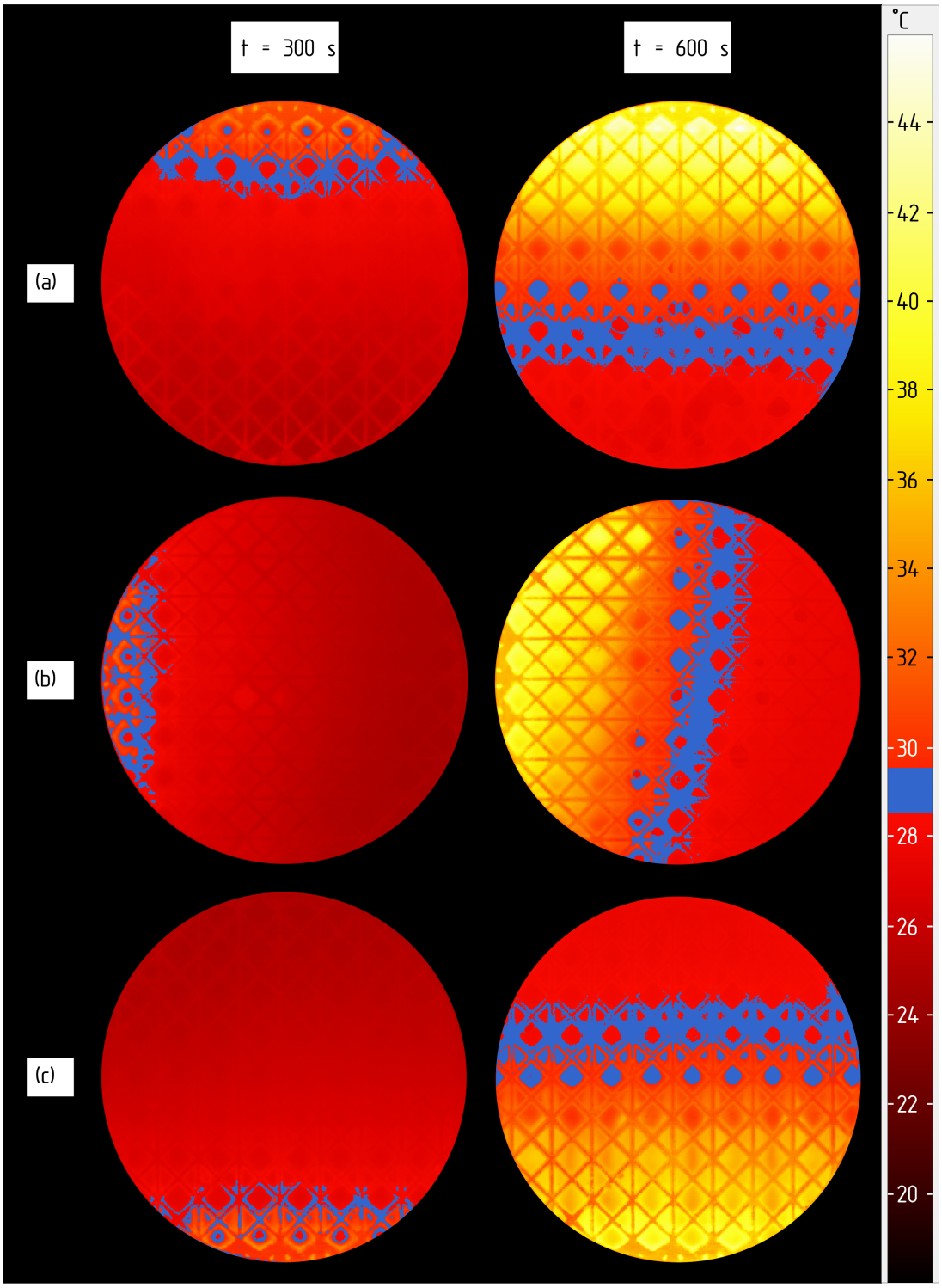

Fig. E.13: f_2ccz: (a) heating from top-orientation, (b) from side-orientation, (c) from bottom orientation.

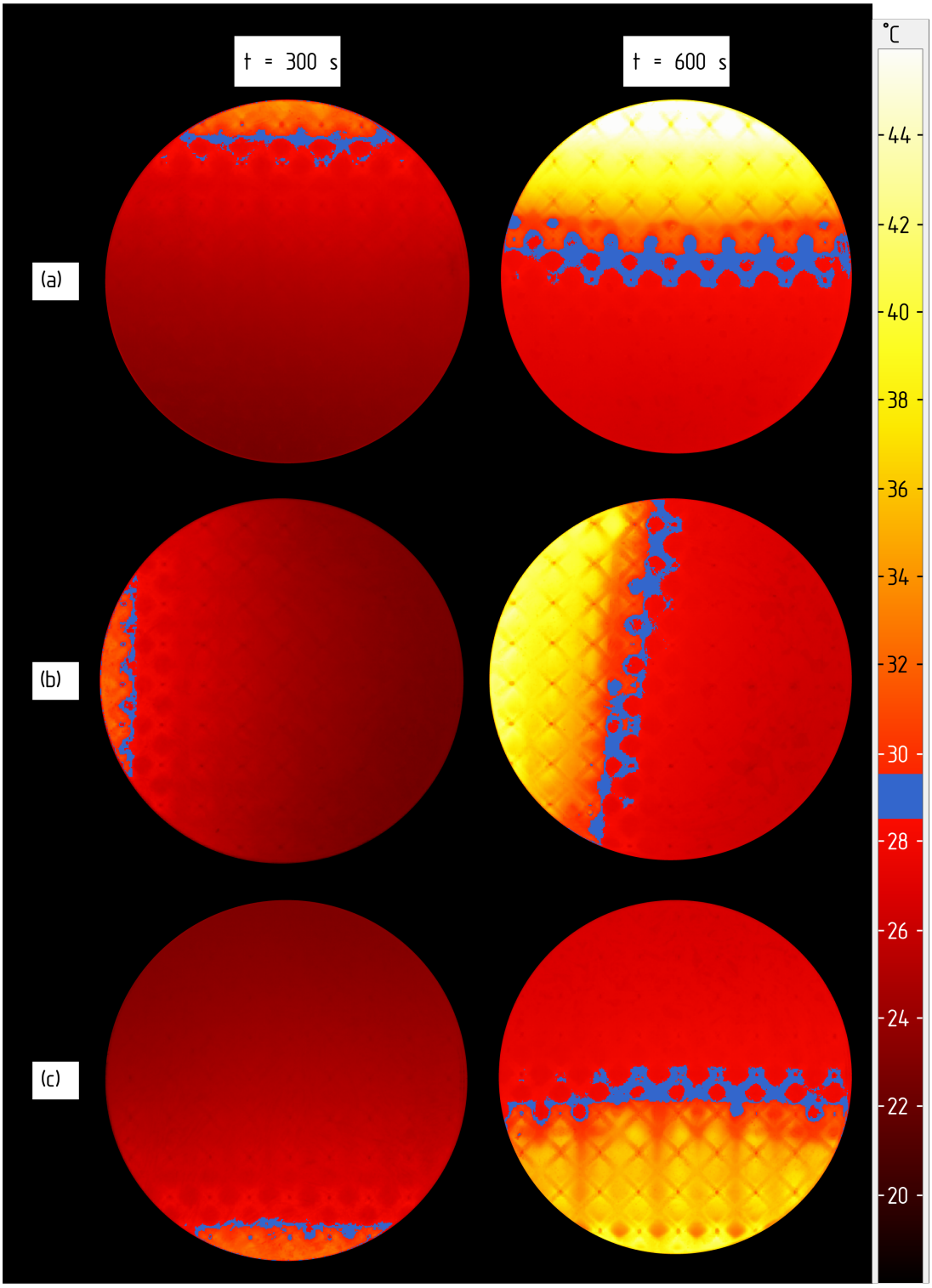

Fig. E.14: *bcc*: (a) heating from top-orientation, (b) from side-orientation, (c) from bottom orientation.

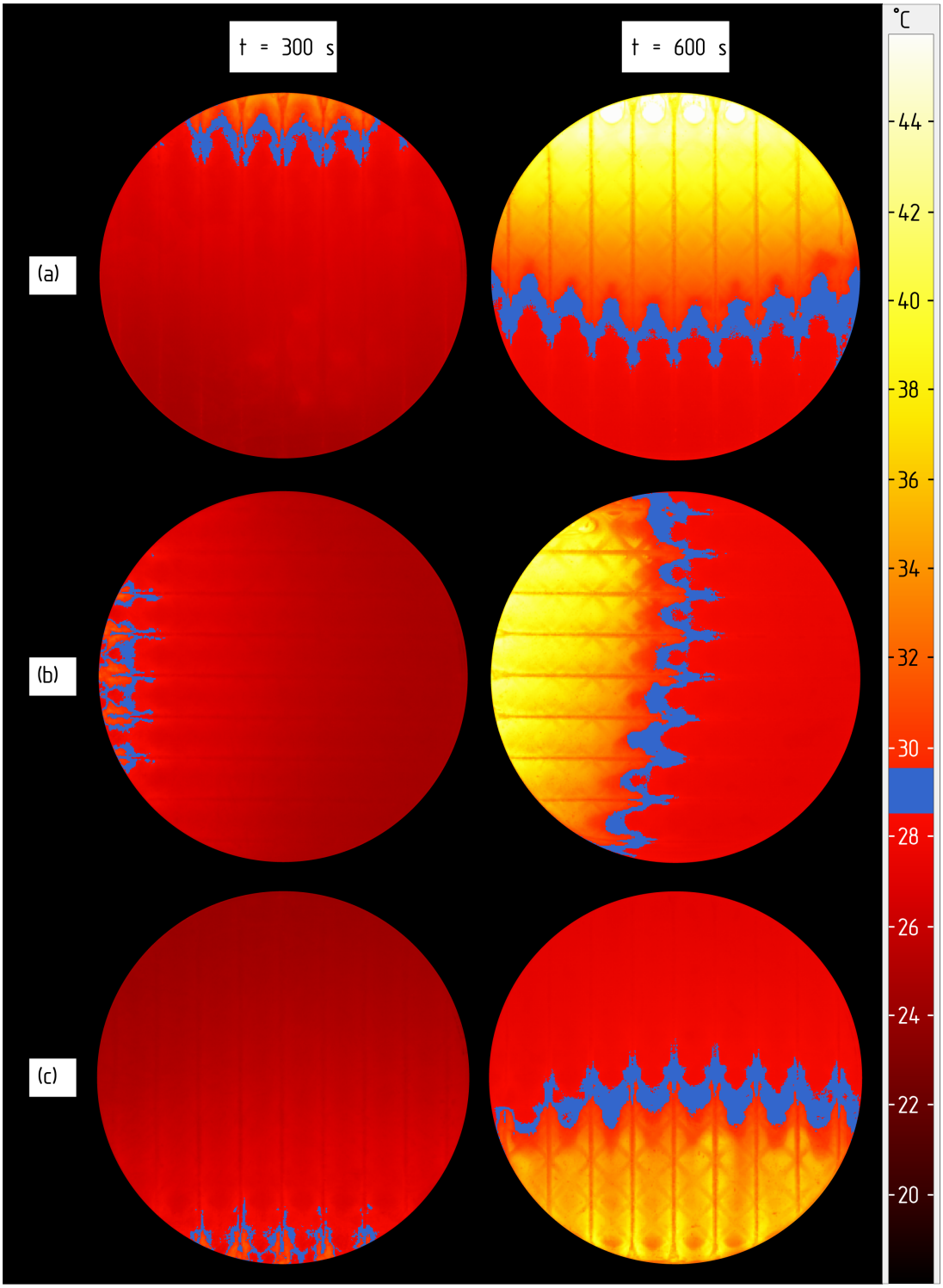

Fig. E.15: *bccz*: (a) heating from top-orientation, (b) from side-orientation, (c) from bottom orientation.

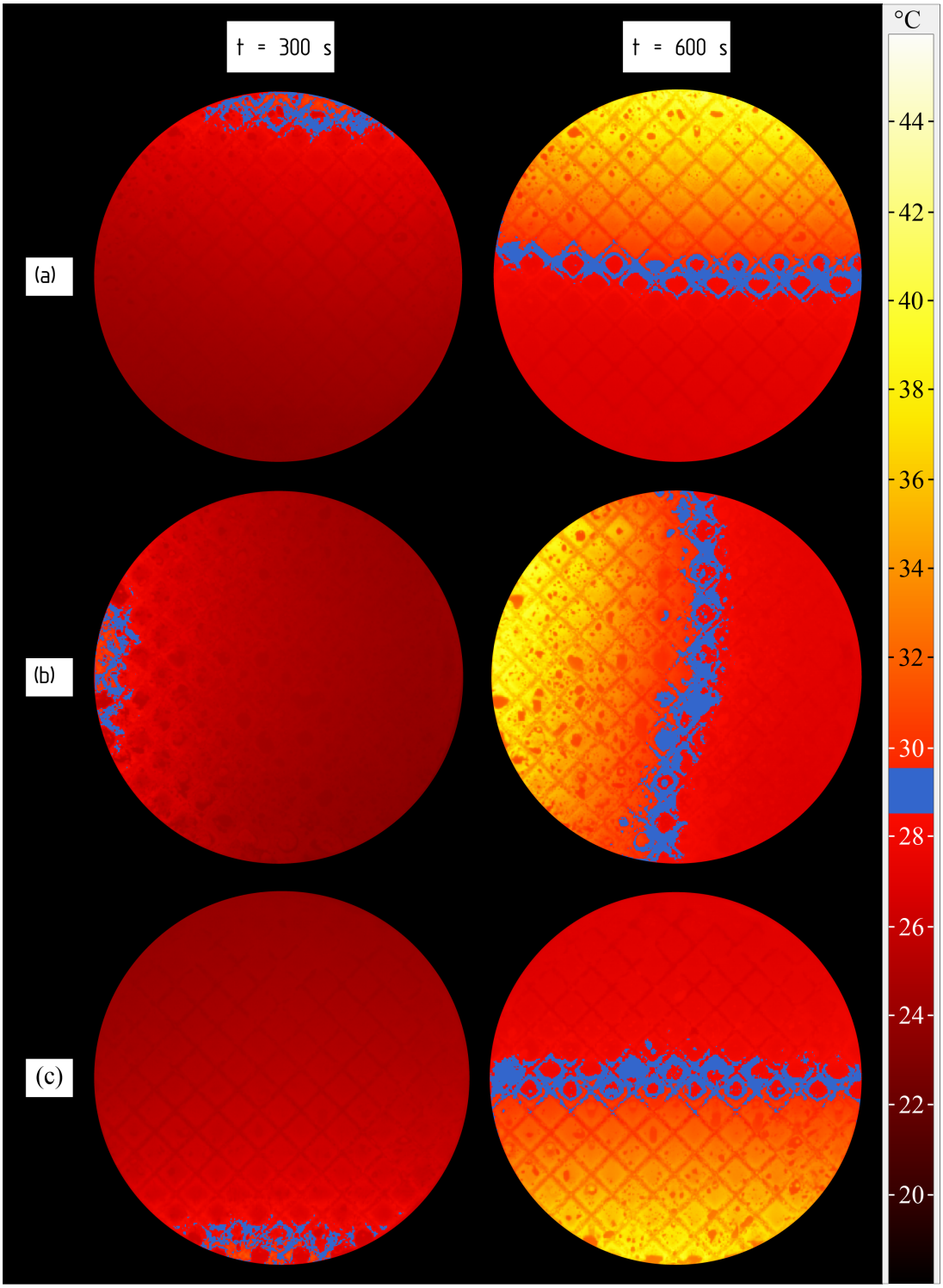

Fig. E.16: f_2bcc: (a) heating from top-orientation, (b) from side-orientation, (c) from bottom orientation.

F Algorithm Implementation Natural Convection

F.0.1 Algorithm implementation

Based on the *CoMeTFoam* solver from Schüller [158], a novel solver dedicated for PCMs embedded in orthotropic porous media is developed. The solver CoMeTFoam itself is based on the *buyont Boussinesq PimpleFoam solver*, implemented in OpenFoam version 5, and it makes use of the Enthalpy-Porosity method described in Chapter 2, and is capable to describe the behaviour of pure PCMs only. Therefore, the implementation of the conservation equations for porous media must be included. The following list of assumptions is made:

- The Boussinesq approximation is valid for the relevant physical cases;
- Local Thermal Equilibrium is valid;
- The flow is so slow that a Darcy-regime can be assumed a-priori.

The last assumption allows to write the momentum conservation equation with the Darcy-Forchheimer sink term, but without the need to calculate the Friction Coefficient, i.e. the sink term depends only on the permeability.
With reference to Figure F.1, the solver algorithm is described. Commencing from the prescribed initial and boundary conditions, the comprehensive characterization of the velocity, temperature, and pressure fields throughout the entire domain is established. Utilizing the temperature information, critical parameters such as the liquid fraction denoted as Φ, along with indispensable material properties encompassing density (ρ), heat capacity (Cp), kinematic viscosity (ν), the Boussinesq term (BT), and the Darcy term (DT), are computed. These calculated values serve as the foundation for the subsequent progression in the algorithm. The algorithm proceeds to the initial time increment, where the velocity equation is systematically resolved using the variables obtained from the preceding iteration or time step. Additionally, the unadjusted mass and pressure fluxes are determined.
Subsequent to the resolution of the corrected continuity equation, adjustments are made to the velocity, pressure, and mass flow parameters. The liquid fraction iteration process is then initiated. Within each iteration, material properties are initially computed using the liquid fraction at the current step. Subsequently, the energy equation is solved, and the liquid fraction is iterated utilizing a procedure involving a so-called source term.

It's imperative to note that due to the nonlinear characteristics of the phase change, the liquid fraction term necessitates linearization. This linearization of the term results in a situation where the temperature T^{n+1} may no longer be inherently consistent with the liquid fraction

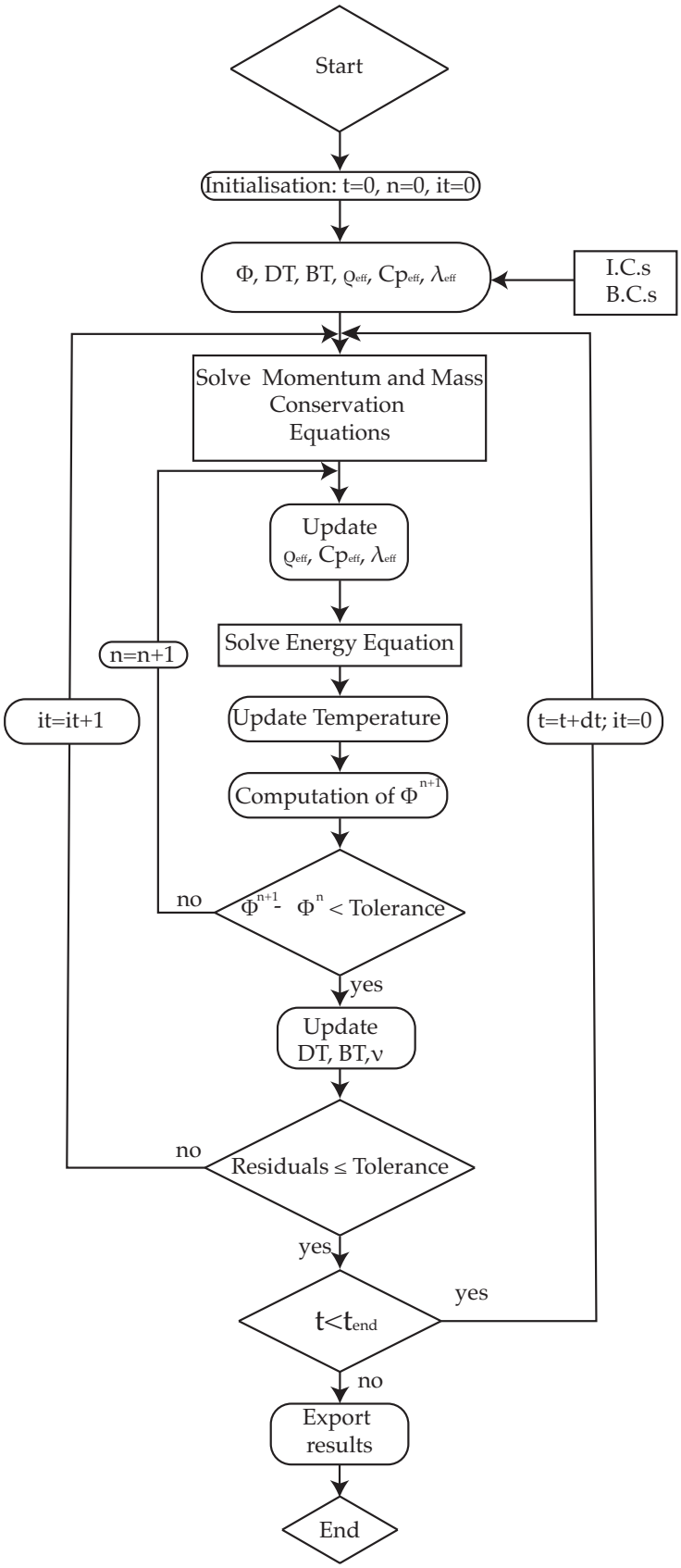

Fig. F.1: Solver flowchart

Φ^{n+1}, and, thus, not with the enthalpy H^{n+1}. Consequently, the enthalpy H^{pre}, determined as the mean of the inconsistent temperature T^{n+1}, must align with the consistent enthalpy H^{n+1} within the confines of this specific iteration step.

$$H^{\text{pre}} = H^{n+1} \tag{F.1}$$

which is equivalent to

$$Cp_{\text{eff}} T^{n+1} + \Phi^n h_m = Cp_{\text{eff}} T^{corr} + \Phi^{n+1} h_m \tag{F.2}$$

T^{corr} is related to the liquid fraction at the iteration step n, and it can be calculated via Equation F.3. The liquid fraction at the iteration step $n+1$ is calculated via Equation F.4.

$$T^{\text{corr}} = (T_l - T_s)\Phi^n + T_s. \tag{F.3}$$

$$\Phi^{n+1} = \left\{ \begin{array}{cc} 0, & T < T_s \\ \Phi^n + \Phi_{\text{relax}} \frac{c_p}{h_m} (T^{n+1} - T^{\text{corr}}), & T_s < T < T_l \\ 1, & T > T_l \end{array} \right\} \tag{F.4}$$

Φ_{relax} represents an underrelaxation term which is added to the iteration, and which influences the numerical stability and accuracy of the solution. The value shall lie between 0 and 1.
The computational procedure involves an iterative refinement of the liquid fraction until convergence is achieved between the temperature and liquid fraction fields. Once this convergence is attained, the computed values for the liquid fraction and temperature are employed to adjust the Darcy term (DT), the Boussinesq term (BT), and the fluid's viscosity (ν). Subsequently, the residuals arising from the continuity and momentum equations are scrutinized. Should these residuals fall below a predefined tolerance, the next time step is initiated. The simulation concludes upon the completion of the specified number of time steps.
As previously indicated, the PCM-lattice composite is simulated under the assumption of local thermal equilibrium. To achieve this, the effective thermophysical properties presented in section 4.1.3 are used, along with the permeability calculated in section 4.3.1. In addition to the standard equations for the enthalpy-porosity method presented in the literature by Brent et al. [159] and adjusted for several purposes by other authors [160, 161, 158], the momentum equation is corrected adding a Darcy-Brinkman-Forchheimer term. Given the assumption of low velocities the Forchheimer, i.e. the non-Darcy flow regime, part of this term is neglected.
Subsequent adjustments involve the inclusion of porosity, so that one obtains the equations 4.23,4.24,4.25. The lattice structures under investigation exhibit anisotropic topology, resulting in directionally dependent thermal conductivity and permeability. As a result, the developed solver treats these parameters as tensors. However, due to limitations in OpenFOAM, the implementation of the Darcy source term must be explicit, causing minor instabilities in the velocity field. To address this and improve stability, a relaxation factor of 0.7 is applied to the velocity calculation. To calculate the permeability, numerical investigations in the section 4.3.1 are proposed.

Validation of the PCM-lattice solver

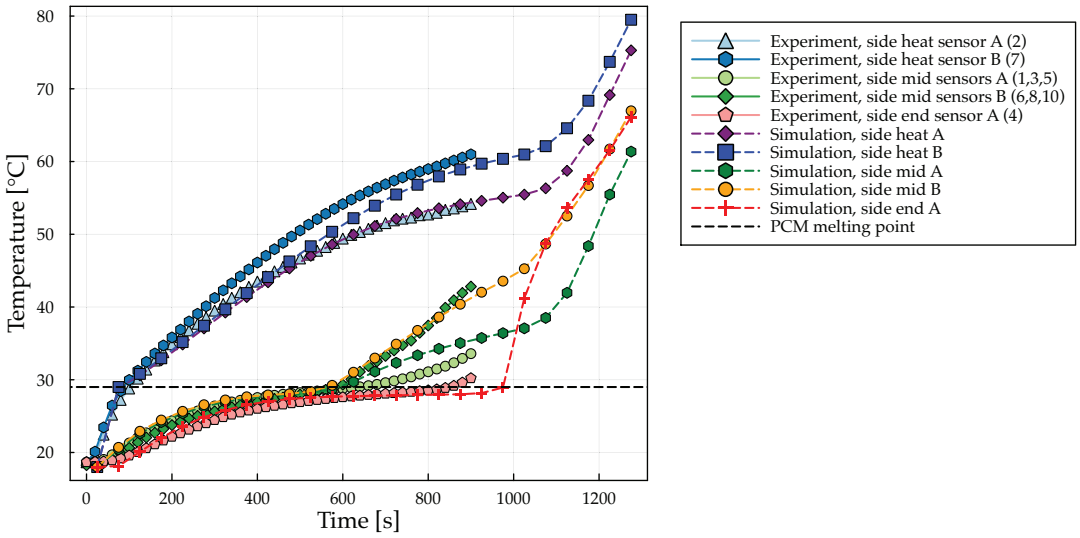

Fig. F.2: Validation of the PCM-lattice solver for the *bccz* sample, side orientation.

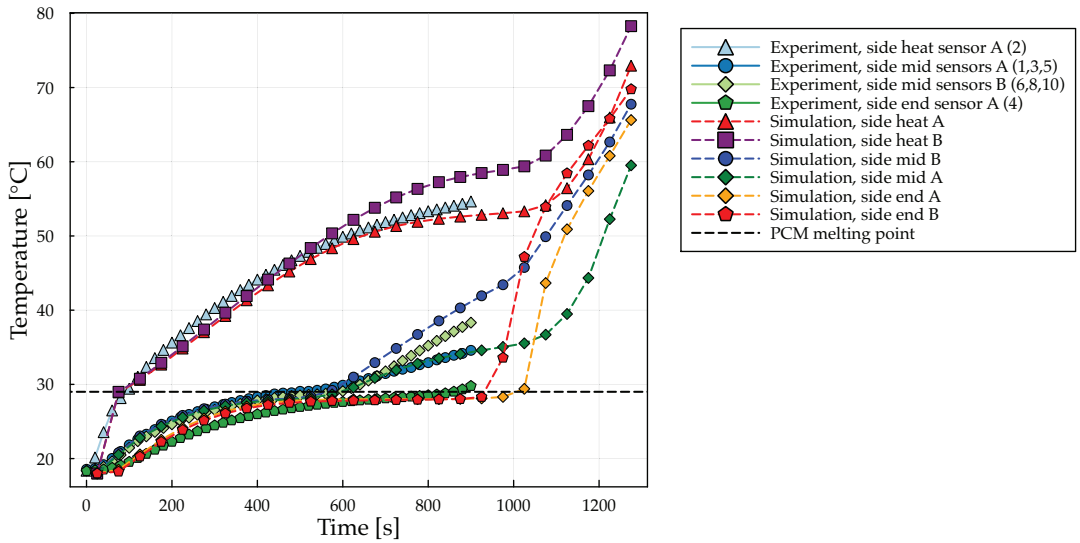

Fig. F.3: Validation of the PCM-lattice solver for the f_2ccz sample, side orientation.

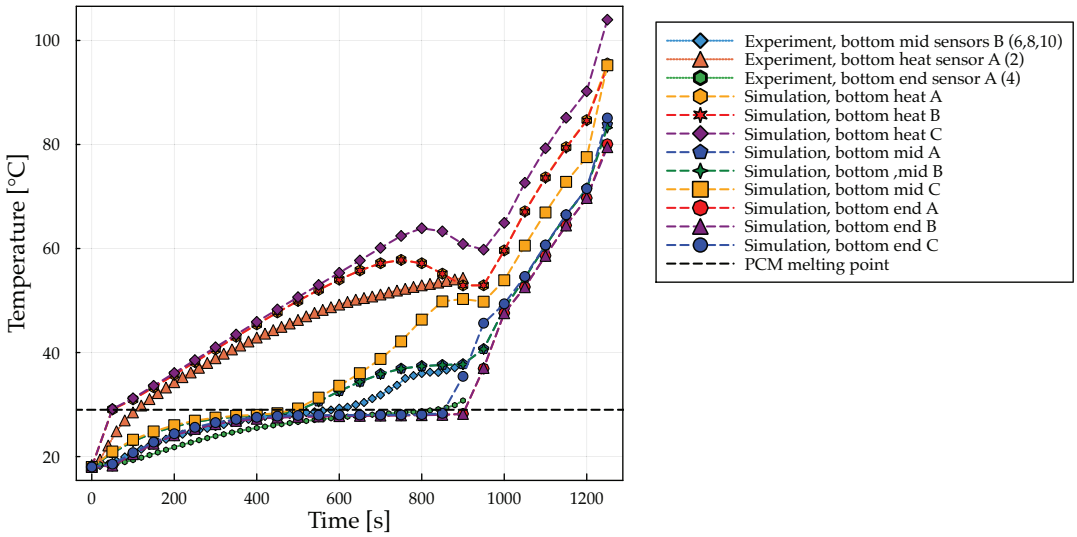

Fig. F.4: Validation of the PCM-lattice solver for the *bccz* sample, bottom orientation.

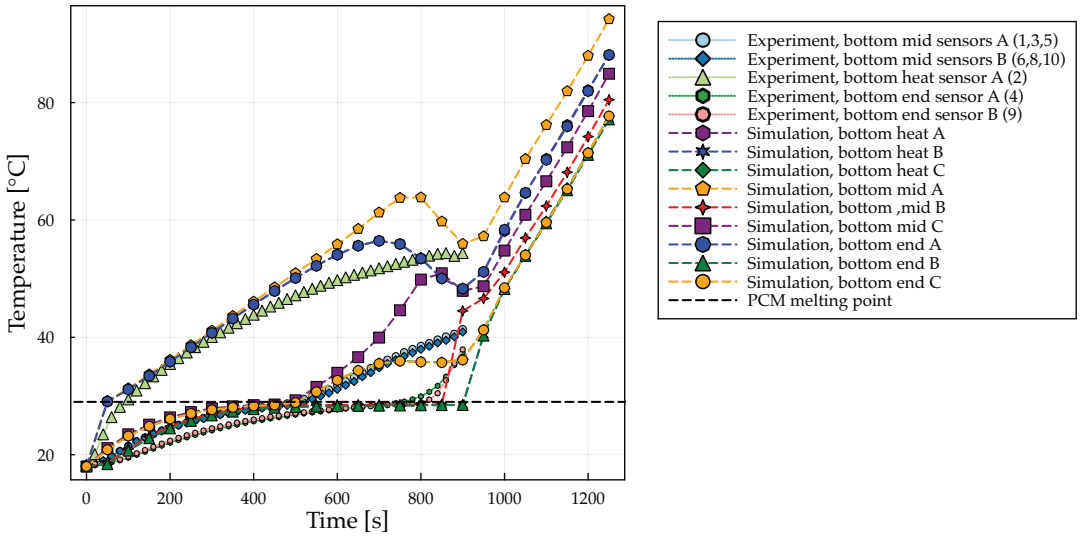

Fig. F.5: Validation of the PCM-lattice solver for the f_2ccz sample, bottom orientation.

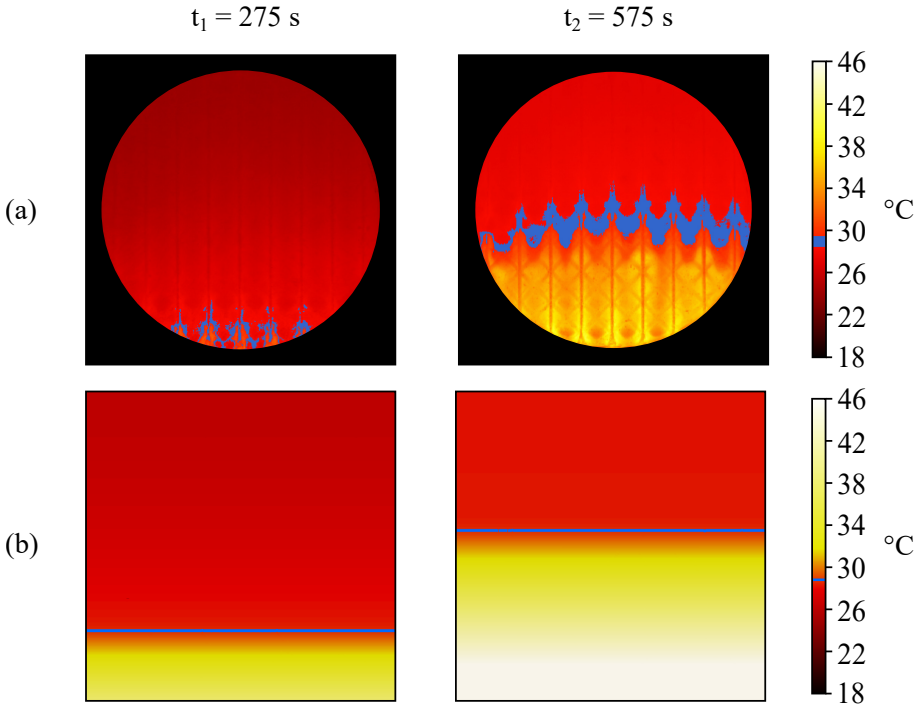

Fig. F.6: Melting front expansion: (a) experiments and (b) simulations for the *bccz* sample, bottom heating orientation.

G Derivations of the equations for the stability of beams

G.0.1 Derivation of Euler's critical load

This chapter derives the analytical solution for the critical buckling load of a beam as presented by Timoshenko and Gere [101]. The beam is considered to be ideal, meaning that it is perfectly straight and perfectly elastic, and is submitted to a centrally applied axial load P. It is modelled as a Euler-Bernoulli beam, without rotary inertia and shear deformations. The beam shall initially have hinged supports at both ends (fig. G.1). Before reaching the critical buckling load, the beam remains straight and is considered stable. This means that if a lateral force is applied and a small deflection produced, the deflection disappears after removing said lateral force. This is not the case when reaching the critical buckling load, as in this state small lateral forces will produce deflections that will remain even when removing the lateral load.

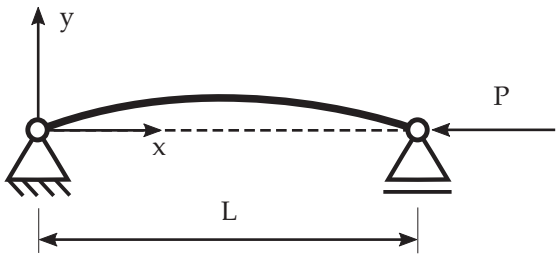

Fig. G.1: Buckling of a beam under an axial load.

To use beam theory, the beam must have a high slenderness. For a beam with circular cross-section, the slenderness is defined as the ratio between the beam's length L and its diameter D, and, typically, a slenderness of 10 or more is considered sufficiently slender. Additionally, assuming small deflections, the relationship between the curvature $\mathrm{d}^2y/\,\mathrm{d}x^2$ and the bending moment M at a specific section of the beam is

$$M = -EI\frac{\mathrm{d}^2y}{\mathrm{d}x^2} \tag{G.1}$$

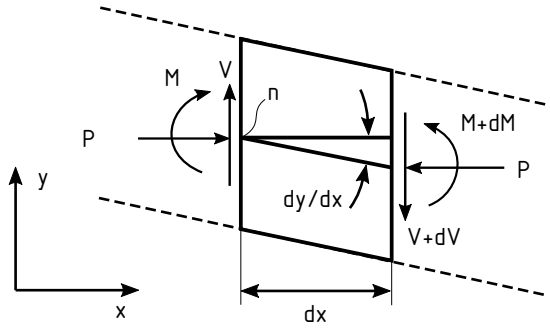

Fig. G.2: Forces and moments on the infinitesimal beam element.

where y is the deflection and EI the flexural rigidity of the beam. EI is the product of the Young's modulus E of the material and the bending moment of inertia I of the cross section, which are both assumed to be constant.

Another set of equations can be derived by considering the infinitesimal element of the beam from figure G.2. The angle $\mathrm{d}y/\mathrm{d}x$ is generally small, leading to $\tan(\mathrm{d}y/\mathrm{d}x) \approx \mathrm{d}y/\mathrm{d}x$. An equilibrium of moments around point n and an equilibrium of forces in y direction yield respectively

$$M + (V + \mathrm{d}V)\,\mathrm{d}x - (M + \mathrm{d}M) + P\frac{\mathrm{d}y}{\mathrm{d}x}\mathrm{d}x = 0 \tag{G.2}$$

$$V - (V + \mathrm{d}V) = 0 \tag{G.3}$$

Equation G.3 leads to $\mathrm{d}V = 0$, which shortens equation G.2 to

$$V\,\mathrm{d}x - \mathrm{d}M + P\,\mathrm{d}y = 0 \tag{G.4}$$

Dividing by $\mathrm{d}x$ and substituting M from equation G.1 yields

$$EI\frac{\mathrm{d}^3 y}{\mathrm{d}x^3} + P\frac{\mathrm{d}y}{\mathrm{d}x} = -V \tag{G.5}$$

or

$$EI\frac{\mathrm{d}^4 y}{\mathrm{d}x^4} + P\frac{\mathrm{d}^2 y}{\mathrm{d}x^2} = -\frac{\mathrm{d}V}{\mathrm{d}x} \tag{G.6}$$

Inserting $\mathrm{d}V = 0$ and defining $P/(EI) = \lambda^2$ leads to

$$\frac{\mathrm{d}^4 y}{\mathrm{d}x^4} + \lambda^2 \frac{\mathrm{d}^2 y}{\mathrm{d}x^2} = 0 \tag{G.7}$$

This differential equation has the following general solution

$$y = C_1 \sin(\lambda x) + C_2 \cos(\lambda x) + C_3 x + C_4 \tag{G.8}$$

with the derivatives

$$\begin{aligned} \frac{\mathrm{d}y}{\mathrm{d}x} &= C_1 \lambda \cos(\lambda x) - C_2 \lambda \sin(\lambda x) + C_3 \\ \frac{\mathrm{d}^2 y}{\mathrm{d}x^2} &= -C_1 \lambda^2 \sin(\lambda x) - C_2 \lambda^2 \cos(\lambda x) \end{aligned} \tag{G.9}$$

The constants of integration C_1 and C_2 can be determined by inserting known conditions at the beam's ends. For the beam with hinged ends, they are

$$y = \frac{\mathrm{d}^2 y}{\mathrm{d}x^2} = 0 \tag{G.10}$$

at both $x = 0$ and $x = L$. Applying these conditions to equation G.8 and its derivatives leads to $C_2 = C_3 = C_4 = 0$ and

$$\sin(\lambda L) = 0 \tag{G.11}$$

Here it is convenient to define $\eta = \lambda L$ as this parameter becomes significant later on (Timoshenko [101] uses the variable u instead of η but this conflicts with the notation of other variables in this work). Equation G.11 is fulfilled for $\eta = m\pi$ with $m \in \mathbb{N}^+$. The lowest possible value of λ that induces buckling is wanted, and $\lambda \sim \sqrt{P}$. Therefore, $m = 1$ and

$$\eta = \lambda L = \sqrt{\frac{P}{EI}} L = \pi \tag{G.12}$$

Hence, the critical buckling load is

$$P_{cr} = \frac{\pi^2 EI}{L^2} \tag{G.13}$$

This value for P_{cr} is known as Euler's critical load. The deflection curve is described by

$$y = A \sin \frac{m\pi x}{L} \tag{G.14}$$

where A is the amplitude of the deflection, which, due to the state of instability, cannot be determined. Taking $m > 1$ leads to higher critical buckling loads which correspond to higher modes of deflection. As can be seen in fig. G.3, m determines the number of half-sine waves of the deflection curve. The length of each half-sine wave is L/m.

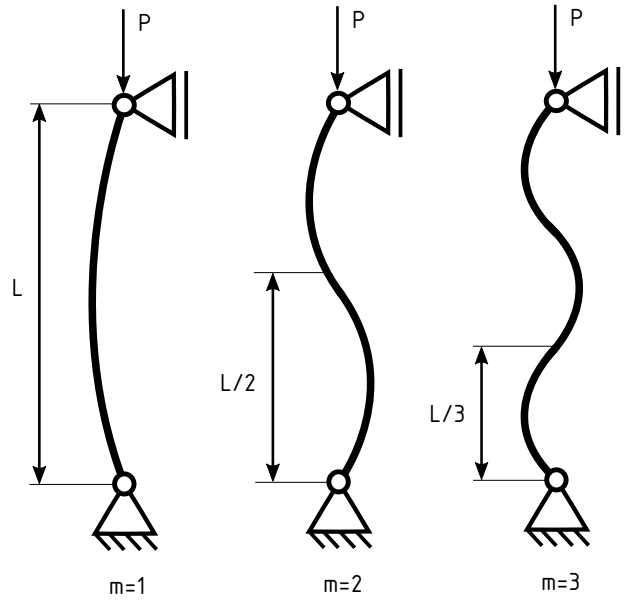

Fig. G.3: Deflection curves for different values of m.

The beam with hinged ends is called the fundamental case of buckling as it is assumed more frequently than any other case. The solutions for other end conditions of the beam is not derived here as they can be obtained simply by inserting their corresponding end conditions into the general solution (eq. G.8) and solving the system of equations. The most common combinations of boundary conditions are shown in figure G.4. Their critical buckling loads only differ by a factor n, which is called the end constraint factor. The end constraint factors for the different cases are also shown in figure G.4. Hence, the general equation for the critical buckling load is

$$P_{cr} = n^2 \frac{\pi^2 EI}{L^2} \tag{G.15}$$

The general equation may also be defined as

$$P_{cr} = \frac{\eta^2 EI}{L^2} \tag{G.16}$$

with $\eta = n\pi$. The end constraint factor is important for the lattice problem as the end conditions of the individual struts of the lattice structure do not belong to one of the basic configurations. Instead, they could be described by intermediate variants of the basic end conditions. For example, the end of a strut may be able to rotate, but there is also some rigidity against rotation provided by other struts that connect at that end. This means that the end condition of a beam in a lattice lies between the cases with $n = 1$ and $n = 2$, i.e., between the rigidly built-in end condition and the one which can rotate freely. A method to find the equivalent end constraint factor is presented in sections G.0.3 and further tools are introduced in H.0.2.

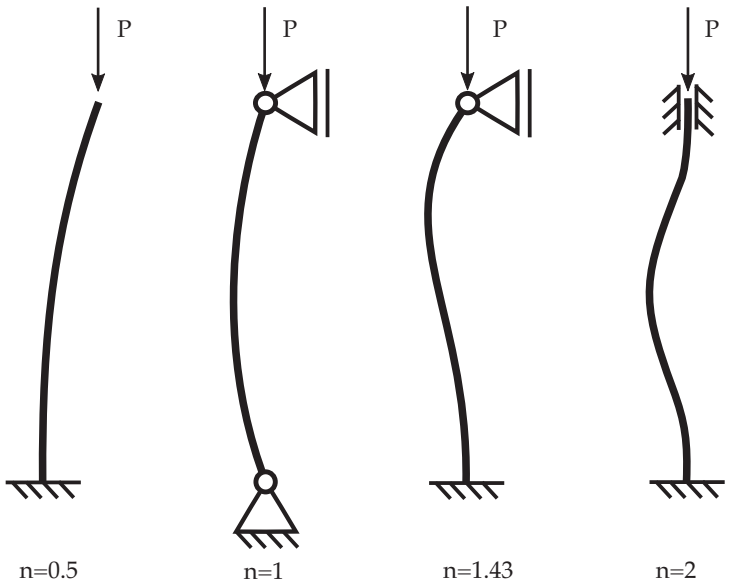

Fig. G.4: Different cases of buckling and their corresponding end constraint factor n.

G.0.2 Derivation by use of the energy method

An alternative way to calculate the buckling load is using the energy method. This method will be useful to calculate the solution for the elastically bedded beam in section H.0.1. The energy method, as presented by Timoshenko in [101], first requires assuming the deflection curve of the beam. With that, it's possible to derive the critical load. Unless the assumed deflection curve is exactly the correct one, the derived critical load will be larger than the true value. This problem can be bypassed by defining the assumed deflection curve with multiple parameters. Then, the parameters can be determined in such a way that they produce the lowest possible load, which will correspond to the most accurate critical load. For the case of the beam with hinged ends, such a parametric expression of the deflection curve is the following trigonometric series

$$y = a_1 \sin\frac{\pi x}{L} + a_2 \sin\frac{2\pi x}{L} + a_3 \sin\frac{3\pi x}{L} + ... = \sum_{m=1}^{m=\infty} a_m \sin\frac{m\pi x}{L} \tag{G.17}$$

For $x = 0$ and $x = L$, all terms of expression G.17 as well as the terms in its second derivative become zero. Therefore, the series satisfies the end condition of the beam from eq. G.10. The goal is now to find the parameters a_m that produce the deflection curve corresponding to the lowest load P.

The energy method works by assuming a small lateral displacement of the beam. This displacement will increase the strain energy of the system by an amount ΔU. Simultaneously, the load P will produce an external work ΔT on the system by moving a small distance. As long as $\Delta U > \Delta T$, the system will remain stable. However, if the external work surpasses the increase in strain energy, i.e., when $\Delta U < \Delta T$, the system is unstable. Thus, the critical load can be found when the condition

$$\Delta U = \Delta T \tag{G.18}$$

is fulfilled. For the buckled beam, the strain energy of bending is

$$\Delta U = \int_0^L \frac{M^2}{2EI}\,\mathrm{d}x = \frac{P^2}{2EI}\int_0^L y^2\,\mathrm{d}x \tag{G.19}$$

After inserting eq. G.17 and performing some operations it can be shown that the expression can be rewritten as

$$\Delta U = \frac{P^2 L}{4EI}\sum_{m=1}^{m=\infty} a_m^2 \tag{G.20}$$

The work produced by the load P during buckling is

$$\Delta W = \frac{P}{2}\int_0^L \left(\frac{\mathrm{d}y}{\mathrm{d}x}\right)^2 \mathrm{d}x \tag{G.21}$$

Again, eq. G.17 is inserted, and the integral can be replaced by a sum

$$\Delta W = \frac{\pi^2 P}{4L}\sum_{m=1}^{m=\infty} m^2 a_m^2 \tag{G.22}$$

Equating G.20 and G.22 leads to

$$\frac{P^2 L}{4EI}\sum_{m=1}^{m=\infty} a_m^2 = \frac{\pi^2 P}{4L}\sum_{m=1}^{m=\infty} m^2 a_m^2 \tag{G.23}$$

Solving for P:

$$P = \frac{\pi^2 EI}{L^2} \frac{\sum_{m=1}^{m=\infty} m^2 a_m^2}{\sum_{m=1}^{m=\infty} a_m^2} \tag{G.24}$$

Now the combination of parameters a_m that lead to the smallest value of P must be found. It can be shown that this minimum value of P is achieved by setting all parameters a_m equal to zero, except for one. The parameter that is different from zero must be a_1, as it is multiplied with the smallest value of m^2, i.e., $m^2 = m = 1$. This leads to

$$P_{cr} = \frac{\pi^2 EI}{L^2} \tag{G.25}$$

which is the same result that was derived previously.

G.0.3 Solution for a beam with rotational springs at the ends

Lattice structures present a more complex system where individual beams are combined into a three-dimensional structure. The points where two or more beams intersect is called a *vertex*. As stated in the previous chapter, when multiple beams are connected at their ends, a solution for the buckling load may be obtained by determining the end constraint factor of the critical beam and applying it to the general formula (eq. G.15). The critical beam is the one which buckles first. Local buckling of a lattice structure can thus be investigated by only considering the critical beam and introducing the combined effect of the beams connected at both vertices through the end constraint factor.

As the connected beams at a vertex will exert reactive moments on the critical beam and the vertex itself can rotate, the general end condition of the critical beam is a hinged support with an applied moment. This requires the assumption that the vertex is fixed regarding lateral translations. As the reactive moments are proportional to the rotation angle θ of the vertex, the applied moments can be replaced with rotational springs with the spring constant c (fig. G.5). The spring constant can be determined from the bending rigidity of the connected struts, and tools to calculate this bending rigidity will be presented in section H.0.2. This entire process of replacing the connecting beams at the vertices with equivalent elements, for example springs, is called the equivalent member method.

Assuming that the system is symmetrical and the same end-moment M_0 is applied at both ends, the boundary conditions are

$$y = 0 \tag{G.26}$$

$$\frac{\mathrm{d}^2 y}{\mathrm{d}x^2} = \frac{M_0}{EI} \tag{G.27}$$

at both $x = 0$ and $x = L$.

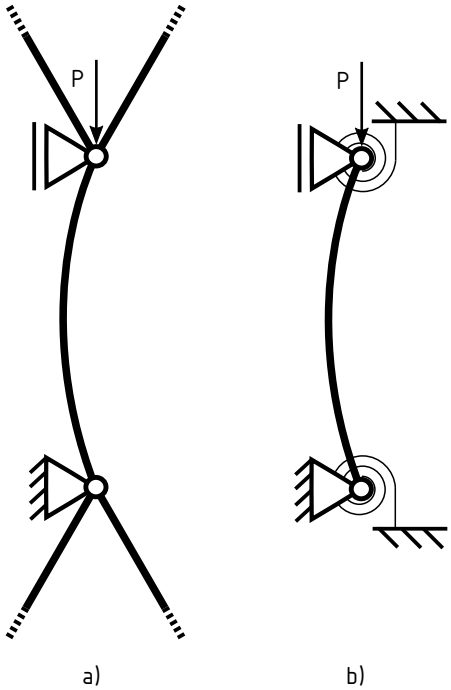

Fig. G.5: a) Critical beam inside a symmetrical lattice structure. b) Modelling of the critical beam by replacing the connected beams with rotational springs.

Taking advantage of the relation $M_0 = c\theta = c\,\mathrm{d}y/\,\mathrm{d}x$, equation G.27 becomes

$$\frac{\mathrm{d}^2 y}{\mathrm{d}x^2} = \frac{c}{EI}\frac{\mathrm{d}y}{\mathrm{d}x} \tag{G.28}$$

Inserting the boundary conditions into the general solution (eq. G.8) and its derivatives and solving the system of equations leads to

$$\cos(\lambda L) - \lambda \frac{EI}{c}\sin(\lambda L) = 1 \tag{G.29}$$

Introducing again the notation $\eta = \lambda L$ and defining $\zeta = EI/(cL)$ the equation becomes

$$\cos(\eta) - \eta\zeta\sin(\eta) = 1 \tag{G.30}$$

This equation must be solved for η as the end constraint factor is $n = \eta/\pi$. Note that $\eta = 0$ is already a solution, but the lowest possible value for $\eta > 0$ is required. It is not possible to solve equation G.30 for η, so the solution must be approximated. Newmark [157] provides an approximation with an error of less than 4%.

$$\eta = \pi \left(\frac{\pi^2 + 4/\zeta}{\pi^2 + 2/\zeta} \right) \tag{G.31}$$

After determining η, the buckling load can be calculated via equation G.16.

H Fundamentals on the modelling of beams on elastic foundations

Winkler presented in 1867 [96] the first fundamental work regarding beams on elastic foundations. His goal was describing the behaviour of rails, which are supported by soil. As schematically shown in Figure H.1, the foundation is represented by an infinite number of linear springs. The spring are independent from each other.

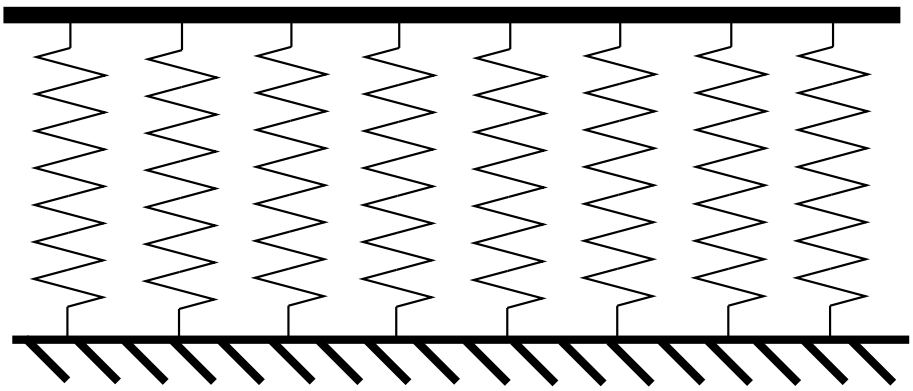

Fig. H.1: Beam on a Winkler foundation.

By representing the foundation through a configuration of uniformly distributed springs characterized by a consistent rigidity parameter denoted as α, their influence on the beam can be substituted with that of an elastic medium. This elastic medium, when considered at any given cross-sectional area, responds in proportion to the deflection experienced at that specific section. The assumed reaction forces are restricted to vertical directions aligned with the deflection of the beam. As elucidated by Timoshenko [101], the stiffness of the elastic medium can be quantified as follows.

$$k = k_{medium} = \frac{\alpha}{a} \tag{H.1}$$

where the variable a signifies the spacing between each spring. The parameter k is often denoted as the embedding coefficient, foundation modulus, modulus of subgrade reaction, or Winkler modulus, with the specific designation often dependent on the context of application. For the purposes of this study, it is termed the foundation modulus. This parameter possesses the dimensions of an elastic modulus (force divided by the square of length). It serves as the constant of proportionality connecting the deflection y and the foundation's response q (with dimensions of a line load in a 2D model) at any given point along the beam.

$$q = ky \tag{H.2}$$

As highlighted in the review conducted by Younesian et al. [100], a limitation of the Winkler model lies in the assumption that the springs are independent, whereas in reality, the deflection at a specific point is influenced not only by the pressure at that point but also by the pressure in adjacent points (see Figures H.2a and H.2b). The Winkler model, depicting a discontinuous pressure distribution, deviates from the continuous pressure distribution expected in reality. Therefore, a more accurate representation involves introducing interaction among the springs. Various models have been proposed to enhance the Winkler model by incorporating additional parameters. Typically, these models introduce a layer with specific properties between the beam and the springs, resulting in a continuous pressure distribution and a two-parameter model. One such model was developed by Pasternak in 1954 [97]. Pasternak postulates the existence of a layer deforming solely in transverse shear (refer to Figure H.2c), characterized by the shear stiffness G_P. Vertical deformation is restricted to the springs. The foundation's response is governed by

$$q = ky - G_P \frac{\mathrm{d}^2 y}{\mathrm{d}x^2} \tag{H.3}$$

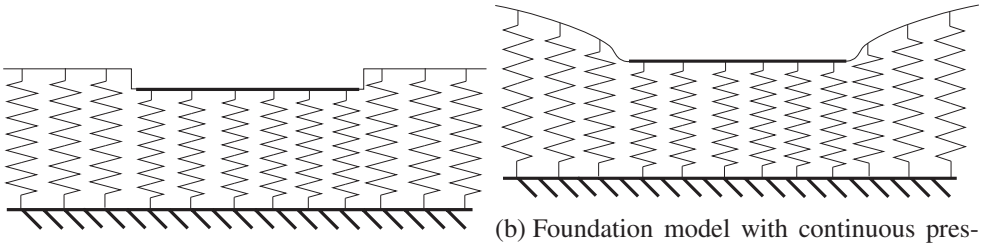

(a) Winkler model.

(b) Foundation model with continuous pressure distribution.

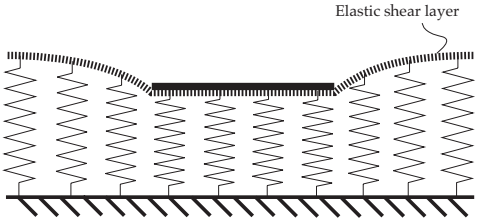

(c) Pasternak model.

Utilizing Winkler or Pasternak models presents a limitation as the foundation parameters, denoted as k or G_P, are often unknown. Given the scarcity of experimental data, it is preferable to have analytical equations that derive these parameters from the material properties of the foundation, specifically the elastic modulus E_f and Poisson's ratio ν_f. One solution involves modeling the medium as an elastic continuum and implementing certain simplifications or constraints. Vlasov's model [98] adopts this approach, assuming that the displacement distribution in the elastic medium can be represented by shape functions integrated over the entire depth of the foundation. Expressing k and G_P in terms of E_f, ν_f, and the shape functions, however, encounters a fundamental challenge due to the difficulty in determining these shape functions. The complexity of the problem is increased by considering its three-dimensional nature. Herrmann et al. [99] propose a solution for k and G_P in the context of a circular beam fully surrounded by a three-dimensional elastic continuum, employing a Vlasov model. The modeling of shape functions involves Bessel functions. In their study, both an exact solution and an approximate solution are presented. The approximate solution, neglecting tangential reactions of the elastic medium, does not yield a solution for G_P. It is, however, acknowledged that the approximate model achieves sufficient accuracy when the ratio between the shear moduli of the foundation and beam is less than approximately 0.03. The equation for the approximate solution of k is

$$k_{Herrmann} = \frac{16\pi G_f(1-\nu_f)}{2(3-4\nu_f)K_0(\psi)+\psi K_1(\psi)} \tag{H.4}$$

where G_f represents the shear modulus of the foundation, and the factor ψ is defined as $\psi = m\pi D/(2L)$. The functions $K_0()$ and $K_1()$ denote the modified Bessel functions of the second kind for orders 0 and 1, respectively. Notably, the parameter m signifies the number of half-sine waves characterizing the deflection curve. It is essential to have knowledge of or make assumptions about the shape of the deflection curve of the beam before applying the formula.
In seeking more straightforward, empirical, approximations for k within the context of modeling the medium as a Winkler foundation, challenges arise due to the three-dimensional nature of the beam against the two-dimensional nature of the Winkler model. Biot [162] proposed a solution by considering an infinitely long beam with finite width supported by a 3D, homogeneous, isotropic, semi-infinite (one-sided) elastic medium.
A relationship between these parameters can be established by equating the moments on the beam generated by an elastic medium with foundation modulus k to those of an elastic medium with material properties Ef and ν_f. The solution involves numerically solving various integrals for the bending moments, rendering it complex. Alternatively, Vesic [163] presented a simplified formula for k by aligning the maximum displacements produced by both models instead of focusing on the bending moments. Vesic's solution is expressed as

$$k_{Vesic} = \frac{0.65E_f}{1-\nu_f^2}\sqrt[12]{\frac{E_f b^4}{EI}} \tag{H.5}$$

where EI represents the bending stiffness of the beam, and b denotes the width of the contact between the beam and the foundation. It is noteworthy that the beam's diameter D can be employed as the foundation width b. Regrettably, empirical approximations for the shear modulus G_p of the shear layer in a Pasternak foundation for an embedded three-dimensional beam could not be located.

H.0.1 Mechanical stability of beams on elastic foundations

The foundational theories and current advancements outlined thus far provide a valuable framework for modeling an elastic foundation. The models described above can be effectively employed to delve deeper into the stability analysis of embedded lattice struts. To facilitate this analysis, a further abstraction is proposed. The individual strut can be reformulated as an embedded beam featuring simple supports. Subsequently, rotational springs are introduced at the hinged supports to incorporate more realistic boundary conditions. This modification enhances the model's capacity to represent realistic boundary conditions.

Solution for an embedded beam with rotational springs at the ends

The examination of buckling in more intricate structures necessitates an investigation into scenarios where moments are applied at the ends of the beam (see Figure H.3a). Aristizabal and Ochoa [164] developed the formulation for the problem of an elastically embedded beam with general end conditions, including rotational springs. This formulation builds upon the earlier work of Hetényi [102], who determined the buckling load of a beam on an elastic foundation using the differential equation of the deflection curve. Unfortunately, Hetényi's work only considers a pure Winkler foundation, thereby neglecting shear effects of the foundation. An analogous model incorporating shear effects (i.e., a Pasternak foundation) could not be found in the literature.

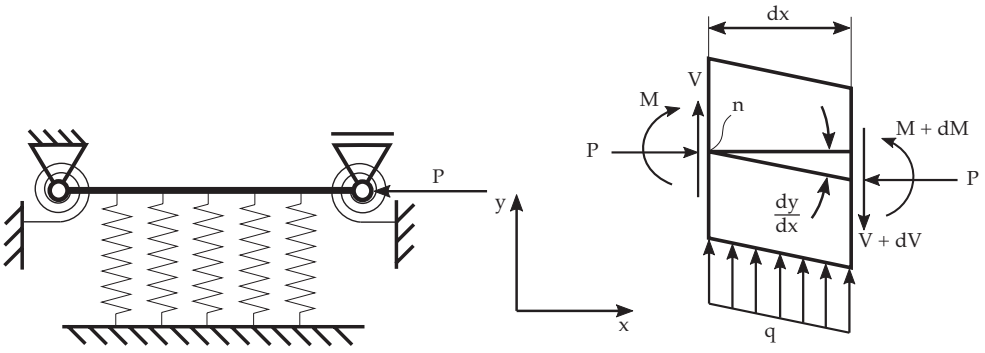

(a) Beam on elastic foundation under axial load and rotational springs at the supports.

(b) Forces and moments on the infinitesimal beam element.

Fig. H.3: Schematic representation of the system considered in the derivation.

Through the application of moment and force equilibriums on the infinitesimal beam element (see Figure. H.3b), it is possible to derive the differential equation governing the deflection curve. However, in contrast to equation G.7, an extra term ky is introduced, representing the pressure exerted by the elastic medium.

$$EI\frac{\mathrm{d}^4 y}{\mathrm{d}x^4} + P\frac{\mathrm{d}^2 y}{\mathrm{d}x^2} + ky = 0. \tag{H.6}$$

In accordance with Hetényi [102], the solution to this differential equation is contingent upon the relationship between P and $\sqrt{4kEI}$. Considering that a positive P indicates compression, it is imperative for P to be positive. When $0 < P < \sqrt{4kEI}$, the general solution to the differential equation is given by H.7.

$$y = (C_1 e^{\alpha x} + C_2 e^{-\alpha x})\cos(\beta x) + (C_3 e^{\alpha x} + C_4 e^{-\alpha x})\sin(\beta x), \tag{H.7}$$

with

$$\alpha = \sqrt{\sqrt{\frac{k}{4EI}} - \frac{P}{4EI}} \quad \text{and} \quad \beta = \sqrt{\sqrt{\frac{k}{4EI}} + \frac{P}{4EI}}. \tag{H.8}$$

For $P > \sqrt{4kEI}$, the solution to Equation H.6 is given by means of Equation H.9.

$$y = C_1\cos(\gamma x) + C_2\cos(\delta x) + C_3\sin(\gamma x) + C_4\sin(\delta x) \tag{H.9}$$

with

$$\gamma = \sqrt{\frac{P}{2EI} - \sqrt{\left(\frac{P}{2EI}\right)^2 - \frac{k}{EI}}} \quad \text{and} \quad \delta = \sqrt{\frac{P}{2EI} + \sqrt{\left(\frac{P}{2EI}\right)^2 - \frac{k}{EI}}}. \tag{H.10}$$

The solution for $P = \sqrt{4kEI}$ corresponds to the deflection curve of an infinitely long beam on an elastic foundation, which does not necessitate further analysis in this context. Hetényi [102] establishes that the general solution in the first case ($0 < P < \sqrt{4kEI}$) cannot be satisfied by real values of α and β. Consequently, buckling is only feasible for the case $P > \sqrt{4kEI}$.
The determination of the four constants $C_1 - C_4$ involves inserting the boundary conditions from Equations G.26 and G.27 into the general solution (Equation H.9) and its second derivative. This process results in a system of linear equations, which is expressed in a matricial form via Equation H.11. The buckling load of the system is then computed by setting the determinant of this matrix to zero.

$$\begin{vmatrix} A_{11}-A_{12} & A_{13} & A_{14} \\ A_{21}-A_{22} & A_{23} & A_{24} \\ \cos(\gamma L)-\cos(\delta L) & \sin(\gamma L) & \sin(\delta L) \end{vmatrix} = 0 \tag{H.11}$$

where the terms A_{ij} are

$$\begin{aligned} A_{11} &= -3\rho\gamma\sin(\gamma L) - L(1-\rho)\gamma^2\cos(\gamma L) \\ A_{12} &= -3\rho\delta\sin(\delta L) - L(1-\rho)\delta^2\cos(\delta L)] \\ A_{13} &= 3\rho\gamma\cos(\gamma L) - L(1-\rho)\gamma^2\sin(\gamma L) \\ A_{14} &= 3\rho\delta\cos(\delta L) - L(1-\rho)\delta^2\sin(\delta L)] \\ A_{21} &= L(1-\rho)\gamma^2 \\ A_{21} &= L(1-\rho)\delta^2 \\ A_{23} &= 3\rho\gamma \\ A_{24} &= 3\rho\delta \end{aligned} \tag{H.12}$$

Here, $\rho = 1/(1+3\zeta)$, and the coefficient $\zeta = EI/(cL)$ represents the ratio between the rigidity of the spring and the rigidity of the beam, as previously employed in equation G.30.
The critical buckling load is the smallest value of P that satisfies equation H.11.

H.0.2 Stiffness matrices of beams on elastic foundations

As discussed in section G.0.3, the examination of local buckling in a lattice structure involves employing the equivalent member method. In this approach, the beams connected at the vertices of the studied beam are substituted with a spring characterized by a spring constant c. This constant must be ascertained based on the rigidity of the adjacent beams. This can be addressed through the use of stiffness matrices. Therefore, a brief introduction to stiffness matrices will be provided here.
Cook et al. [144] in their book on finite element analysis, represent a beam as a structural element with a node at each end, the stiffness matrix establishes a relationship between the applied load on the nodes of the beam (expressed by a load vector **F**) and the resulting displacements of the nodes (expressed by a nodal displacement vector **d**). Assuming linear-elastic behavior, this relationship is expressed as $\mathbf{F} = \mathbf{Kd}$, where **K** represents the stiffness matrix of the beam element.
The dimensions of this matrix are contingent on the degrees of freedom of the element. In three-dimensional space, each node will have 6 degrees of freedom (three translational and three rotational). With two nodes, this results in a 12×12 matrix. Through the utilization of

symmetries and boundary conditions, the degrees of freedom can be reduced, leading to a simplified matrix.
The entries of the stiffness matrix can be determined using various methods. In the following, the potential energy approach as outlined by Zhaohua and Cook [165] will be discussed. This work also derives the stiffness matrix of the beam when it is placed on an elastic foundation. The following assumptions are considered:

- For the sake of simplification, each node of the beam is assumed to have only two degrees of freedom: lateral displacement v and cross-sectional rotation Θ_z.
- Shear deformations are neglected.
- The elastic foundation is represented by a two-parameter model. However, for the purpose of simplifying the derivation of the stiffness matrix, a one-parameter Winkler foundation is assumed. This implies that the elastic medium only generates radial reactions.

The approach commences by establishing an expression for the overall potential (strain) energy of the beam. The contributions from bending and the elastic foundation are extracted from equations 2.69 and 2.72, respectively, resulting in

$$\Delta U = \underbrace{\frac{1}{2}\int_0^L EI\frac{\mathrm{d}^2 v}{\mathrm{d}x^2}\,\mathrm{d}x}_{\text{Bending}} + \underbrace{\frac{1}{2}\int_0^L kv^2\,\mathrm{d}x}_{\text{Elastic Foundation}} \tag{H.13}$$

Subsequently, the process involves expressing the potential energy in relation to the nodal displacement vector $\mathbf{d}$. To interpolate the displacements along the length of the beam, a cubic polynomial is employed, following standard finite-element practices. Thus, at any point in the beam, v can be represented as

$$v = \begin{pmatrix} N_1 & N_2 & N_3 & N_4 \end{pmatrix} \begin{pmatrix} v_1 \\ \Theta_{z1} \\ v_2 \\ \Theta_{z2} \end{pmatrix} = \mathbf{Nd} \tag{H.14}$$

The cubic shape functions, denoted as N_i in Equation H.14, are expressed in terms of the local coordinate $\xi = x/L$. They are [144]

$$\begin{aligned} N_1 &= 1 - 3\xi^2 - 2\xi^3 \\ N_2 &= L(\xi - 2\xi^2 + \xi^3) \\ N_3 &= 3\xi^2 - 2\xi^3 \\ N_4 &= L(-\xi^2 + \xi^3) \end{aligned} \tag{H.15}$$

Since the derivative in Equation H.13 can be expressed as in Equation H.16, the notation expressed in Equation H.17 is introduced.

$$\frac{\mathrm{d}^2 v}{\mathrm{d}x^2} = \frac{\mathrm{d}^2}{\mathrm{d}x^2}\mathbf{N}\mathbf{d} \tag{H.16}$$

$$\mathbf{B} = \frac{\mathrm{d}^2}{\mathrm{d}x^2}\mathbf{N} = \begin{pmatrix} -\frac{6}{L^2} + \frac{12x}{L^3} & -\frac{4}{L} + \frac{6x}{L^2} & \frac{6}{L^2} - \frac{12x}{L^3} & -\frac{2}{L} + \frac{6x}{L^2} \end{pmatrix} \tag{H.17}$$

Thus, Equation H.13 can be modified as

$$\Delta U = \frac{1}{2}\mathbf{d}^T \mathbf{K_b}\mathbf{d} + \frac{1}{2}\mathbf{d}^T \mathbf{K_f}\mathbf{d} = \frac{1}{2}\mathbf{d}^T (\mathbf{K_b} + \mathbf{K_f})\mathbf{d} \tag{H.18}$$

where $\mathbf{K_b}$ is the bending stiffness matrix and $\mathbf{K_f}$ the stiffness matrix of the elastic foundation. These are defined in Equations H.19, and H.20.

$$\mathbf{K_b} = \int_0^L \mathbf{B}^T EI \mathbf{B}\,\mathrm{d}x = \frac{EI}{L^3}\begin{bmatrix} 12 & 6L & -12 & 6L \\ & 4L^2 & -6L & 2L^2 \\ & & 12 & -6L \\ sym. & & & 4L^2 \end{bmatrix} \tag{H.19}$$

$$\mathbf{K_f} = \int_0^L \mathbf{N}^T k \mathbf{N}\,\mathrm{d}x = k\begin{bmatrix} \frac{13}{35}L & \frac{11}{210}L^2 & \frac{9}{70}L & \frac{-13}{420}L^2 \\ & \frac{1}{105}L^3 & \frac{13}{420}L^2 & \frac{-1}{140}L^3 \\ & & \frac{13}{35}L & \frac{-11}{210}L^2 \\ sym. & & & \frac{1}{105}L^3 \end{bmatrix} \tag{H.20}$$

These solutions hold under the assumption of constant material properties and sections throughout the length of the beam. Combining these matrices yields the total element stiffness matrix $\mathbf{K} = \mathbf{K_b} + \mathbf{K_f}$.

While a similar approach can be used to derive an additional stiffness matrix for the elastic foundation, which shall account for shear effects in Pasternak-like models, it is not practical for this work. In the model discussed in section H.0.1, where rotational springs are implemented, a Winkler foundation is utilized. Consequently, introducing a Pasternak elastic foundation for the beams connected at the vertices would be inconsistent.

A more intricate solution for the stiffness matrix of embedded beams is presented by Yokohama [166]. In this model, the beam is treated as a Timoshenko beam, thus incorporating shear deformations. Additionally, the impact of axial load on transversal displacement is considered.

Consequently, the potential energy is given by:

$$\Delta U = \underbrace{\frac{EI}{2}\int_0^L \frac{\mathrm{d}^2 v}{\mathrm{d}x^2}\,\mathrm{d}x}_{\text{Bending}} + \underbrace{\frac{1}{2}\kappa GA\int_0^L \left(\frac{\mathrm{d}v}{\mathrm{d}x} - \Theta_z\right)^2 \mathrm{d}x}_{\text{Shear}} + \underbrace{\frac{k}{2}\int_0^L v^2\,\mathrm{d}x}_{\text{Foundation}} - \underbrace{\frac{F_x}{2}\int_0^L \frac{\mathrm{d}^2 v}{\mathrm{d}x^2}\,\mathrm{d}x}_{\text{Axial load}} \tag{H.21}$$

In the given expression, κ represents the shear coefficient, G is the shear modulus, and A denotes the cross-section. With respect to Equation H.13, two additional stiffness matrices can be derived from the corresponding terms in Equation H.21: the shear stiffness matrix $\mathbf{K_s}$, and the geometric matrix $\mathbf{K_g}$. The total element stiffness matrix can be obtained by summing up the individual contributions: $\mathbf{K} = \mathbf{K_b} + \mathbf{K_s} + \mathbf{K_f} + \mathbf{K_g}$.
Cook [144] points out that the stiffness matrix of the elastic foundation $\mathbf{K_f}$ is approximate due to the inexact nature of the shape functions in N. As established in earlier sections, the deflection of the beam in a Winkler foundation is described by exponential and trigonometric functions, not cubic polynomials. One approach to address this discrepancy is to increase the number of elements in the beam, although this falls under a numerical finite-element approach.
In this work, an assessment is presented, to determine if this more complex solution is necessary or if the simpler model with only bending and foundation stiffness matrices suffices. Specifically, the consideration of shear deformation may not be necessary for this study. Indeed, this work delves into stability investigations, which are relevant only for slender beams. Thus, the influence of shear deformation shall be minimal.
The first assumption, made to perform the derivation described above, was monodimensionality. For a three-dimensional beam with a total of 12 degrees of freedom, the stiffness matrix can be formulated with bearing in mind that [144]:

- Assuming a symmetrical cross-sectionn ($I_y = I_z = I$)and a foundation on all sides, the same stiffness matrix values can be applied to both the w and Θ_y degrees of freedom.
- The axial degree of freedom u, which describes the axial stretching, is characterised by the stiffness coefficient $a = AE/L$.
- Regarding the Θ_x degree of freedom, representing twisting around the x axis, the torsional stiffness coefficient $b = GI_t/L$ needs to be incorporated into the matrix. Here, I_t denotes the torsional constant, which, for a circular section, equates to the polar moment of inertia of the section.

For convenience, the entries of the 4×4 stiffness matrix of the beam with only two degrees of freedom are generalized

$$\mathbf{K} = \begin{bmatrix} K_1 & K_2 & K_3 & K_4 \\ & K_5 & -K_4 & K_6 \\ & & K_1 & -K_2 \\ \textit{sym.} & & & K_5 \end{bmatrix} \tag{H.22}$$

It is important to note that within the bending stiffness matrix, the entries K_2 and K_4 are equivalent, and K_3 is equal to $-K_1$. However, these equivalences do not extend to the stiffness matrix of the elastic foundation. Consequently, these relations cannot be employed to simplify the general stiffness matrix.
When employing the generalized matrix coefficients as per equation H.22 for a three-dimensional element, the expression $\mathbf{F} = \mathbf{Kd}$ can be developed as Equation H.23 [144].

$$\begin{pmatrix} F_{x1} \\ F_{y1} \\ F_{z1} \\ M_{x1} \\ M_{y1} \\ M_{z1} \\ \hline F_{x2} \\ F_{y2} \\ F_{z2} \\ M_{x2} \\ M_{y2} \\ M_{z2} \end{pmatrix} = \left[\begin{array}{cccccc|cccccc} a & 0 & 0 & 0 & 0 & 0 & -a & 0 & 0 & 0 & 0 & 0 \\ & K_1 & 0 & 0 & 0 & K_2 & 0 & K_3 & 0 & 0 & 0 & K_4 \\ & & K_1 & 0 & -K_2 & 0 & 0 & 0 & K_3 & 0 & -K_4 & 0 \\ & & & b & 0 & 0 & 0 & 0 & 0 & -b & 0 & 0 \\ & & & & K_5 & 0 & 0 & 0 & K_4 & 0 & K_6 & 0 \\ & & & & & K_5 & 0 & -K_4 & 0 & 0 & 0 & K_6 \\ \hline & & & & & & a & 0 & 0 & 0 & 0 & 0 \\ & & & & & & & K_1 & 0 & 0 & 0 & -K_2 \\ & & & & & & & & K_1 & 0 & K_2 & 0 \\ & & & & & & & & & b & 0 & 0 \\ & & & & & & & & & & K_5 & 0 \\ sym. & & & & & & & & & & & K_5 \end{array}\right] \begin{pmatrix} u_1 \\ v_1 \\ w_1 \\ \Theta_{x1} \\ \Theta_{y1} \\ \Theta_{z1} \\ \hline u_2 \\ v_2 \\ w_2 \\ \Theta_{x2} \\ \Theta_{y2} \\ \Theta_{z2} \end{pmatrix} \tag{H.23}$$

If the element coordinate system deviates from alignment with the global coordinate system, an adjustment is required for the stiffness matrix $\mathbf{K}$. This involves rotation using a rotation matrix $\mathbf{R}$ through an angle ϕ. The rotational operation is expressed as $\mathbf{R}^T\mathbf{KR}$. The rotation matrix applicable to the 12×12 stiffness matrix is defined as follows.

$$\mathbf{R} = \begin{bmatrix} \mathbf{R_0} & \mathbf{0} & \mathbf{0} & \mathbf{0} \\ \mathbf{0} & \mathbf{R_0} & \mathbf{0} & \mathbf{0} \\ \mathbf{0} & \mathbf{0} & \mathbf{R_0} & \mathbf{0} \\ \mathbf{0} & \mathbf{0} & \mathbf{0} & \mathbf{R_0} \end{bmatrix} \tag{H.24}$$

After establishing $\mathbf{R_0}$ as the fundamental 3×3 rotation matrix centered around the designated axis of rotation, the process of orienting beam elements ensues. Subsequently, the overall stiffness matrix for a specific structure, consisting of interconnected beams, is derived. This process, known as the assembly of elements, involves the summation of entries corresponding to each loaded degree of freedom within the local stiffness matrices of all beam elements sharing a

common node.

The stiffness matrices used by Yokohama [166] include the effects of shear deformation, i.e., the beams are modelled as Timoshenko beams. The effect of shear deformation is described by the factor $\Phi = 12EI/(\kappa L^2 GA)$. The stiffness matrices for Timoshenko beams on elastic foundations derived by Yokohama are:

$$\mathbf{K_b} = \frac{EI}{L^3(1+\Phi)^2}\begin{bmatrix} 12 & 6L & -12 & 6L \\ & (4+2\Phi+\Phi^2)L^2 & -6L & (2-2\Phi-\Phi^2)L^2 \\ & & 12 & -6L \\ sym. & & & (4+2\Phi+\Phi^2)L^2 \end{bmatrix}$$

$$\mathbf{K_s} = \frac{\kappa GA\Phi^2}{4L(1+\Phi)^2}\begin{bmatrix} 4 & 2L & -4 & 2L \\ & L^2 & -2L & L^2 \\ & & 4 & -2L \\ sym. & & & L^2 \end{bmatrix}$$

$$\mathbf{K_f} = \frac{kL}{(1+\Phi)^2}\begin{bmatrix} \frac{13}{35}+\frac{7\Phi}{10}+\frac{\Phi^2}{3} & (\frac{11}{210}+\frac{11\Phi}{120}+\frac{\Phi^2}{24})L & \frac{9}{70}+\frac{3\Phi}{10}+\frac{\Phi^2}{6} & -(\frac{13}{420}+\frac{3\Phi}{40}+\frac{\Phi^2}{24})L \\ & (\frac{1}{105}+\frac{\Phi}{60}+\frac{\Phi^2}{120})L^2 & (\frac{13}{420}+\frac{3\Phi}{40}+\frac{\Phi^2}{24})L & -(\frac{1}{140}+\frac{\Phi}{60}+\frac{\Phi^2}{120})L \\ & & \frac{13}{35}+\frac{7\Phi}{10}+\frac{\Phi^2}{3} & -(\frac{11}{210}+\frac{11\Phi}{120}+\frac{\Phi^2}{24})L \\ sym. & & & (\frac{1}{105}+\frac{\Phi}{60}+\frac{\Phi^2}{120})L^2 \end{bmatrix}$$

$$\mathbf{K_g} = \frac{P}{L(1+\Phi)^2}\begin{bmatrix} \frac{6}{5}+2\Phi+\Phi^2 & \frac{1}{10}L & -(\frac{6}{5}+2\Phi+\Phi^2) & \frac{1}{10}L \\ & (\frac{2}{15}+\frac{\Phi}{6}+\frac{\Phi^2}{12})L^2 & -\frac{1}{10}L & -(\frac{1}{30}+\frac{\Phi}{6}+\frac{\Phi^2}{12})L^2 \\ & & \frac{6}{5}+2\Phi+\Phi^2 & -\frac{1}{10}L \\ sym. & & & (\frac{2}{15}+\frac{\Phi}{6}+\frac{\Phi^2}{12})L^2 \end{bmatrix}$$

I Beam elements model implementation for embedded lattices

The implementation of this process is here briefly expounded upon, with a focus on one of the eight diagonal struts within a *bcc* cell. The same set of steps must be iterated for the remaining struts.

The coordinate system is established at the center of the cell volume. Firstly, a vector $\mathbf{T_{strut}}$ representing the strut direction is formulated. The entries, simplified to ± 1 for convenience, are determined based on the chosen diagonal strut. In the implemented code, these values are ascertained from the node coordinates of the first element in the strut.

Subsequently, three direction vectors for the springs are computed, each corresponding to one of the three springs attached to each node in the strut. The initial spring direction vector $\mathbf{T_{spr,1}}$ is chosen freely but must be orthogonal to the strut direction vector. A solution is attained through the dot product, which equals zero when the vectors are perpendicular. For simplicity, the 1- and 2-coordinates of the strut direction vector are identical, and the 3-coordinate is determined to satisfy the dot product's zero condition. For instance, with the direction vector $\mathbf{T_{strut}} = (1,1,-1)^T$ for a specific diagonal strut in a *bcc* cell, the equation to solve is

$$\mathbf{T_{strut}}\mathbf{T_{spr,1}} = \begin{pmatrix} 1 \\ 1 \\ -1 \end{pmatrix} \begin{pmatrix} 1 \\ 1 \\ t_{z,spr,1} \end{pmatrix} = 0, \tag{I.1}$$

whose solution yields $z = 2$. It can be demonstrated that the required z-coordinate, denoted as $t_{z,spr,1}$, is equal to $-2t_{z,strut}$ for all diagonal struts. Conversely, for a f_2cc cell, $t_{z,spr,1} = -t_{z,strut}$ is derived, signifying that altering the sign of the z-coordinate is sufficient to obtain a perpendicular vector. A visualization of the resulting vectors is depicted in Figure I.1.

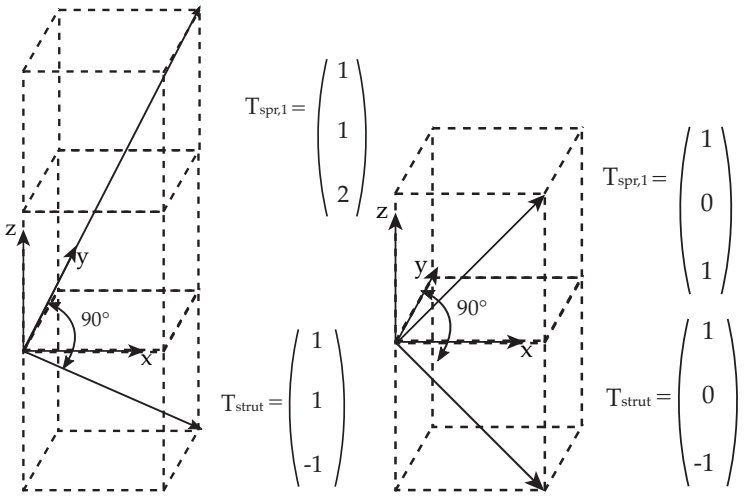

(a) for *bcc* unit cells, the perpendicular spring vector is obtained by multiplying the z-coordinate of the strut direction vector with -2

(b) for f_2cc unit cells, the perpendicular spring vector is obtained by multiplying the z-coordinate of the strut direction vector by -1.

Fig. I.1: The principle is applicable to all eight diagonal struts.

Subsequently, the vector $\mathbf{T_{spr,1}}$ undergoes normalization (division by its length) and is then multiplied by the desired length of the springs. The second and third spring direction vectors ($\mathbf{T_{spr,2}}$, $\mathbf{T_{spr,3}}$) are obtained via a rotation $\mathbf{T_{spr,1}}$ about $\mathbf{T_{strut}}$ with angle $\theta = 120°$ once and twice, respectively. This kind of rotation around an arbitrary axis requires 5 sub-steps, which get combined into a rotation matrix. With a normalised rotation axis, the matrix can be expressed as postulated by Cole [167],

$$\mathbf{R} = \begin{bmatrix} \cos\theta + t_x^2(1-\cos\theta) & t_x t_y(1-\cos\theta) - t_z\sin\theta & t_x t_z(1-\cos\theta) + t_y\sin\theta \\ t_y t_x(1-\cos\theta) + t_z\sin\theta & \cos\theta + t_y^2(1-\cos\theta) & t_y t_z(1-\cos\theta) - t_x\sin\theta \\ t_z t_x(1-\cos\theta) - t_y\sin\theta & t_z t_y(1-\cos\theta) + t_x\sin\theta & \cos\theta + t_z^2(1-\cos\theta) \end{bmatrix}, \quad \text{(I.2)}$$

with $\mathbf{T} = (t_x, t_y, t_z)^T$ being the normalized rotation axis vector, which is equal to $\mathbf{T_{strut}}$.
Ultimately, the determination of the three spring end nodes involves the addition of the spring direction vectors to the coordinates of the node where the three springs are attached. This process is iteratively carried out for each node along the diagonal beam and for all the beams within the structure.

I.1 Analytical solution for unit cells

The equivalent member method is applied here to obtain the analytical solution for the isolated case, and afterwards an analogous solution for the embedded case is derived.
To formulate the analytical solutions, it is instructive to consider the buckling shapes of the various cell types. As depicted in Figure 5.15, the critical strut in the f_2ccz and $bccz$ cells is consistently the vertical strut. The system can be decomposed into the vertical strut and an outer cell, which is a f_2cc cell for the f_2ccz system and a bcc cell for the $bccz$ system. Utilizing the equivalent member method, the outer cell is replaced by rotational springs acting at the lower and upper vertices. The equations required to calculate the critical buckling load for a strut with springs at the ends are derived in Appendix G.0.3 and H.0.1 for both the isolated and embedded cases.
The only missing parameter to apply these equations is the spring stiffness c. The spring stiffness is defined as $c = M/\theta$, where M is the end symmetric moment, and θ is the end slope of the bending curve. Consequently, as shown in Figure I.2a, for a given applied moment M at the cell ends, the angle θ is required. To determine the spring constant c, a moment is applied at the upper and lower vertex of the unit cell and the angle θ is determined from the assembled stiffness matrix of the unit cell itself.

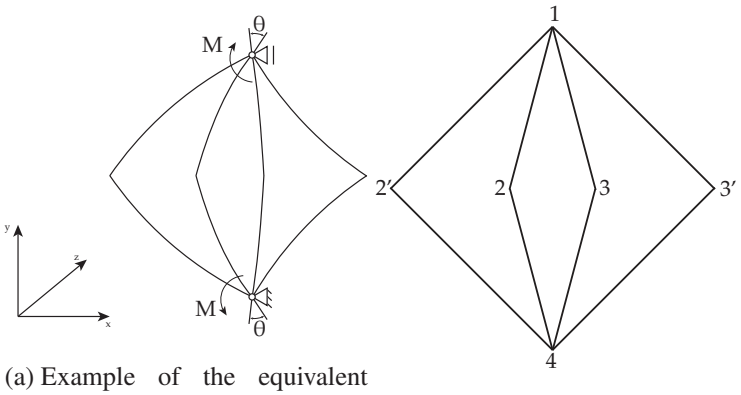

(a) Example of the equivalent model, based on a f_2cc unit cell.

(b) Naming convention for the vertices of a f_2cc cell.

Fig. I.2: Schematic representation of the equivalent model.

The relationship between loads and displacements is governed by the stiffness matrix of the cell, which can be formed from the stiffness matrices of its constituent beams. To obtain the stiffness matrices of the beams, the stiffness matrix of a horizontal beam (see Equation H.23), aligned with the x-axis, is rotated into the correct orientation. This rotation is accomplished by using $\phi_{d,bcc}$ for the bcc cell and ϕ_{d,f_2cc} for the f_2cc cell. To perform this rotation, the 12×12 rotation matrix (Equation H.24) is constructed, utilizing the basic 3×3 rotation matrix around the z-axis

$$\mathbf{R_0} = \begin{bmatrix} \cos(\phi) & \sin(\phi) & 0 \\ -\sin(\phi) & \cos(\phi) & 0 \\ 0 & 0 & 1 \end{bmatrix} \tag{I.3}$$

This basic rotation matrix is employed to build the 12×12 rotation matrix, which is used to orient the stiffness matrix of the horizontal beam to the desired orientation.
Exploiting symmetries within the stiffness matrices of the diagonal beams, where rotation angles are either ϕ or $180° - \phi$, enables simplifications such as $\cos(\phi) = -\cos(180° - \phi)$ and $\sin(\phi) = \sin(180° - \phi)$. Additionally, further symmetries exist among the displacements of the vertices in the specific loading case involving two applied moments about the z-axis at vertices 1 and 4. For the f_2cc cell, these symmetries can be expressed as in Equation I.4.

$$\begin{aligned} u_{2'} = u_{3'} &= 0 \\ v_2 = v_3 = v_{2'} = v_{3'} &= 0 \\ w_2 &= w_3 \\ w_{2'} &= w_{3'} \\ \Theta_{z,2'} &= \Theta_{z,3'} \\ \Theta_{y,2} = \Theta_{y,3} = \Theta_{y,2'} = \Theta_{y,3'} &= 0 \\ \Theta_{x,2} = \Theta_{x,3} = \Theta_{x,2'} = \Theta_{x,3'} &= 0 \end{aligned} \tag{I.4}$$

The subscripts denoted by indices 2, $2'$, 3, and $3'$ correspond to the respective vertices of the cell, following the naming convention illustrated in Figure I.2b. Considering the equations from I.4 along with the boundary conditions at vertices 1 and 4, the remaining displacements to be determined are $\Theta_{y,1}$, $\Theta_{z,2'}$, $w_{2'}$, and w_2. The equation $\mathbf{F} = \mathbf{K_{f_2cc}d}$ can thus be reduced to a four-dimensional problem, where $\mathbf{K_{f_2cc}}$ is the assembled stiffness matrix of the f_2cc cell

$$\begin{pmatrix} M_{z1} \\ M_{y2'} \\ F_{z2'} \\ F_{z2} \end{pmatrix} = \begin{bmatrix} 2K_{10,10} + 2K_{12,12} & 2K_{10,5} & 2K_{10,3} & 2K_{12,1} \\ 2K_{5,10} & 2K_{5,5} & 2K_{5,3} & 0 \\ 2K_{3,10} & 2K_{3,5} & 2K_{3,3} & 0 \\ 2K_{1,12} & 0 & 0 & 2K_{1,1} \end{bmatrix} \begin{pmatrix} \Theta_{z,1} \\ \Theta_{z,2'} \\ w_{2'} \\ w_2 \end{pmatrix} \tag{I.5}$$

Equation I.5 represents the relationship between the applied moments and displacements for the f_2cc cell under the condition of lateral fixing at the vertices. The stiffness matrix $\mathbf{K_{f_2cc}}$ is assembled from the stiffness matrices of the rotated (diagonal) beams. The stiffness matrix entries $K_{i,j}$ are determined based on the rotated beam's stiffness matrix, with i as the row index and j as the column index.
To solve for the slope $\Theta_{z,1}$ at vertex 1 when the load condition $\mathbf{F} = (M_{z1}, 0, 0, 0)^T$ is applied, the system is linear, and an arbitrary value of 1 *Nmm* can be used for the applied moment M_{z1} due to the problem's linearity.

For the f_2cc cell, symmetry implies equal bending rigidity around the x- and y-axes. However, for calculating the critical buckling loads of the vertical strut, only a rotational spring around the y-axis is needed, given that the buckling problem is addressed in a 2D-plane.
Equation I.5 is also applicable for determining the M/θ relation for the *bcc* cell, as indicated in [40]. The *bcc* cell can be considered as a f_2cc cell rotated 45° around the z-axis (with the exception of the longer struts), with the primary change being the use of $L_{d,\mathrm{bcc}}$ instead of $L_{d,\mathrm{f_2cc}}$ to calculate the stiffness matrix entries.
The stiffness matrix of an individual beam involves the combination of bending $\mathbf{K_b}$ and shear $\mathbf{K_s}$ stiffness matrices, as well as the foundation stiffness matrix $\mathbf{K_f}$ in the embedded case. A shear coefficient of $\kappa = 9/10$, corresponding to a circular cross-section, is applied for the beam. The geometric matrix $\mathbf{K_g}$, dependent on the axial load F_x acting on the beam element, requires an iterative process for determination. However, since the outer cell's axial load cannot be easily calculated, and previous work by [40] demonstrated that the geometric matrix is not crucial for cells with a vertical strut, it is omitted in this analysis.
In the isolated case, after obtaining the spring constant c, the end constraint factor n is determined through equation G.30 by solving for ζ, as the equation cannot be directly solved for η. As the equation cannot be solved for η, it is solved for ζ instead (Equation I.6). Figure I.3 shows the behaviour of the variable η, plotted against ζ.

$$\zeta = \frac{\cos(\eta) - 1}{\eta \sin(\eta)}. \tag{I.6}$$

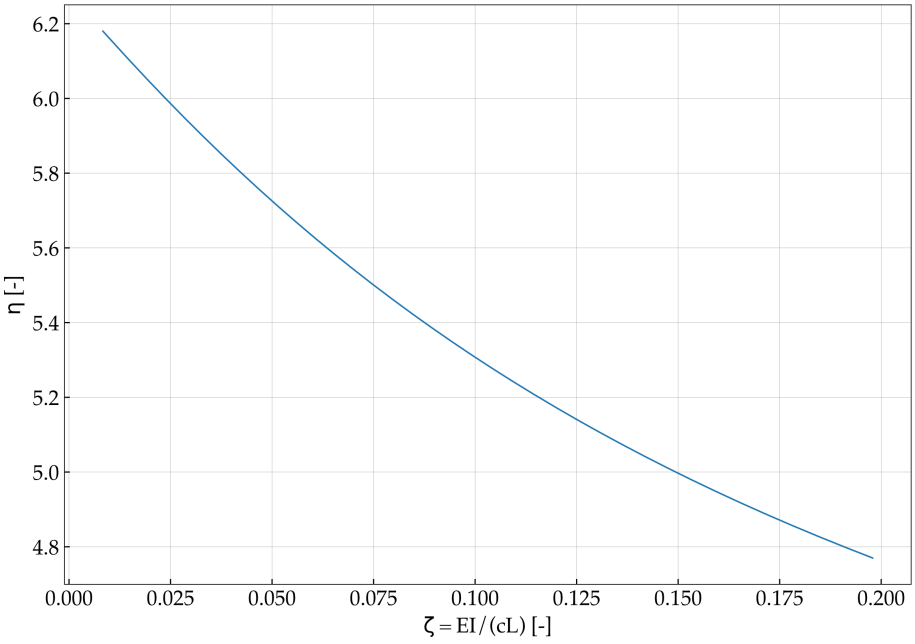

Fig. I.3: Relationship between η and ζ.

Via curve fitting, the following rational function can deliver a more useful inverse relationship between the two variables, with an error with a root mean square of less than 0.1% in the fitted interval. Equation I.7 provides a more exact fit than Newmark [157] (Equation G.31).

$$\eta = \frac{3.174\zeta^2 + 1.114\zeta + 2.486}{\zeta + 0.3952} \tag{I.7}$$

In the embedded case, the critical buckling load is determined using Equation H.11. As it is not feasible to solve this equation directly for P_{cr}, the following approach is employed:

- The determinant's value from Equation H.11 is computed for a range of loads, initiating with the smallest viable solution $P_{min} = \sqrt{4kEI}$ (as it has been established that the beam will not buckle at smaller values). Increments of $\Delta P = 1N$ are applied, with a maximum load of $P_{max} = 4P_{min}$ seeming sufficient.
- A curve is fitted to the data points employing a piecewise polynomial.
- The zeroes of the fitted curve are calculated using an iterative method. The critical load corresponds to the first zero greater than P_{min}. Higher-valued zeroes indicate higher modes of buckling for the beam.

The equivalent member method, as applied by Bühring does not yield satisfactory analytical solutions for the local buckling of bcc and f$_2$cc cells. Instead, an approximation for the critical buckling load is made by considering that one of the diagonal beams will buckle. Euler's formula for a beam on hinged supports, $P_{cr} = \pi^2 EI/(L^2)$, is then employed, ignoring the influence of surrounding beams. Bühring introduces a correction factor of $4\sin(\phi)$, reflecting the division of the applied force among the diagonal struts (see Figure I.4). In the embedded case, the same approximation is used, applying Equation 2.76 for a Winkler model or Equation 2.81 for a Pasternak model.

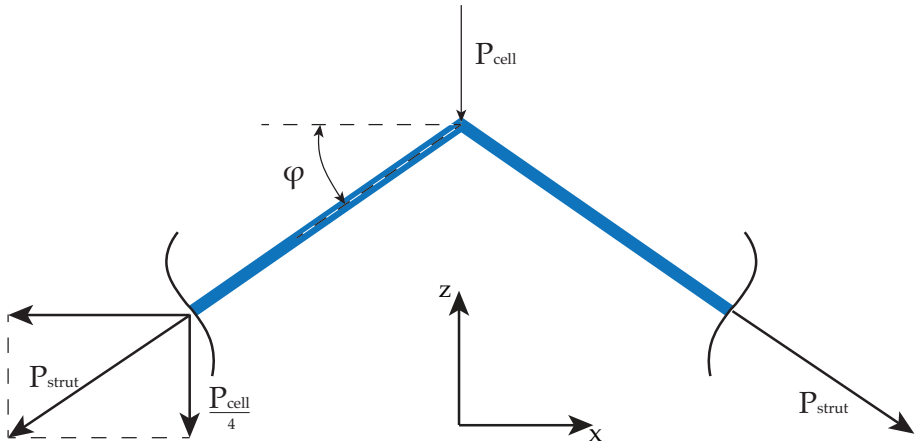

Fig. I.4: The load acting on the entire cell is distributed among the four struts. Force equilibrium dictates that $P_{cell} = 4\sin(\phi)P_{strut}$.

J Analysis of a lattice component

This section explores lattice components constructed from the individual unit cells examined in the previous section. The numerical models of lattice components can be generated by replicating the cell models in the three Cartesian coordinates. The size of the lattice component is defined by three parameters, denoted as $n_x \times n_y \times n_z$, representing the number of cells in the x-, y-, and z-directions, respectively. While numerical analyses using volumetric elements can become computationally expensive due to the high element count, they are employed for specific lattice configurations to validate results obtained with beam elements. Subsequently, the beam/spring model is utilized for a broader range of cell sizes, allowing for more extensive analyses. The section concludes with a comparison of the different geometries.
As observed in the analysis of individual unit cells, the chosen boundary conditions significantly impact the modes of buckling and, consequently, exert a substantial influence on the critical buckling load. Here, the selection of boundary conditions is tailored to emulate a compression test. Figure J.1 illustrates a fundamental configuration depicting how a compression test might be conducted by inserting the lattice component into a cuboid-shaped casing.

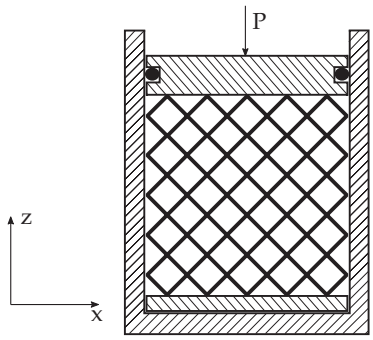

Fig. J.1: Schematic representation of a physical compression test, which is reproduced numerically in the following.

In the numerical model, the upper and lower faces of the component are connected to a plate, preventing transverse strain in those regions. This is simulated by establishing a rigid region between the upper nodes and replicating the same procedure for the lower nodes. For the lower master node, all translations and rotations are constrained. Conversely, at the upper master node, only translations in the x- and y-directions are restricted, as additional constraints would result in an over-constrained model, making a solution through eigenvalue analysis unattainable. Moreover, outward translations must be restricted for the nodes on the lateral faces of the lattice component. This restriction assumes that the nodes at the lateral vertices are in direct contact

with the inner faces of the case in the uncompressed state, necessitating a perfect fit between the lattice component and the case. For the two lateral faces of the lattice in the xz-plane, translations in the y-direction are constrained; for the lateral faces in the yz-plane, translations in the x-direction are restricted. It is important to note that these boundary conditions are approximate, as in the compressed state, the nodes are pushed outward, generating friction forces that also partially restrict translations in the other two directions. Determining the friction forces requires non-linear analysis, making it unclear how the other directions should be restrained. Here, two cases are examined separately: Case I, where only the outward direction is restrained, and Case II, where both x- and y-directions are restrained. A constraint in the z-direction is illogical, as movement in the direction of the load must be permitted. The numerical model based on beam elements is shown in Figure J.2.

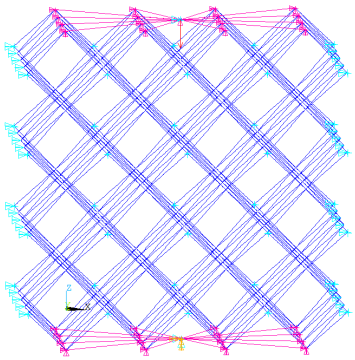

Fig. J.2: Numerical model with beam elements for a $4 \times 4 \times 4 - bcc$ lattice component in the isolated case. Cyan triangles denote translational restrictions, orange triangles rotational restrictions and pink triangles and lines constraint equations between nodes due to rigid regions.

If the entire component assumes the form of a slender column, global buckling of the component may occur. Bühring [142] offers a comprehensive method to analytically ascertain the critical buckling loads for global buckling of slender lattice components. However, the boundary conditions previously outlined for the lattice component in this work eliminate the possibility of global buckling. This is because the lateral restrictions and the restrained rotations at the ends of the structure leave no degrees of freedom for bending in the macrostructure.

Results comparison between beam model and volumetric model The beam/spring model is utilized for simulating the components. Here a comparison of the model outcomes is first made between beam/spring and volumetric model, with the scope of verification. To maintain analogous boundary conditions for this analysis, the lateral faces of the components are left unrestricted in both models.

The anticipated outcome of this analysis was that, for low strut slenderness ratios, the volumetric model would yield higher critical buckling loads due to volume overlap at the vertices, outperforming the beam model. Conversely, for high slenderness ratios, the beam model should

surpass the volumetric model, as the springs in the beam model are independent, while the volumetric foundation can move between cells, theoretically reducing the stability of the structure. However, this expectation proved to be partly incorrect. The results of the analysis are depicted in Figure J.3. It's worth noting that the embedded volumetric model could not be analyzed for slenderness ratios greater than $L/D = 20$ due to computational limitations.

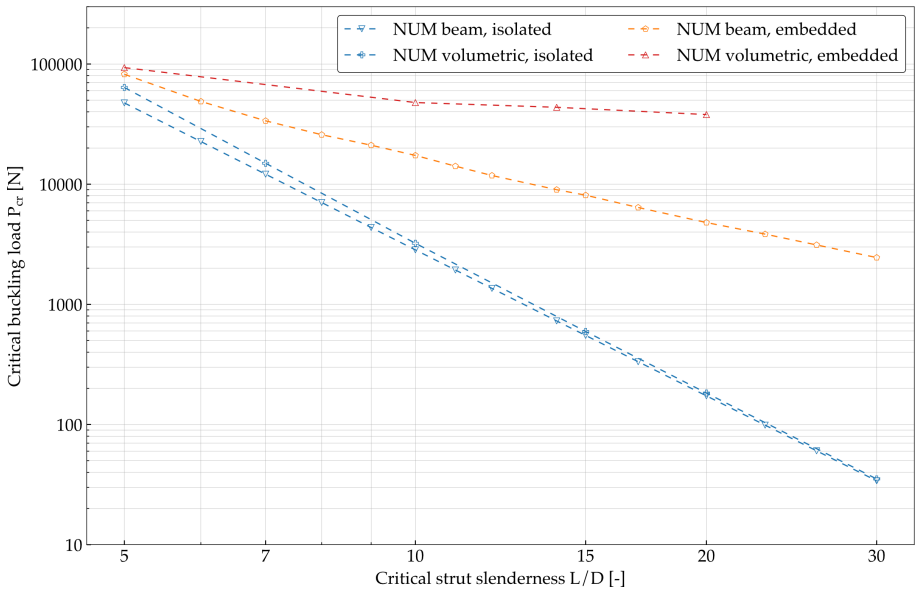

Fig. J.3: Critical buckling load comparison between the beam/spring and volumetric models for a $2 \times 2 \times 3 - bcc$ lattice.

In the isolated case, the results align with the studies conducted on individual cells. However, in the embedded case, the volumetric model yields high critical buckling loads, even at high slenderness ratios. This notable difference from the solutions of the beam/spring model was not observed when analyzing individual cells. A hypothesis is proposed that this discrepancy is related to the stiffness provided by the rigid regions at the top and bottom faces of the model. To investigate this, an individual *bcc* cell is studied where, instead of using a symmetry boundary condition on the side of the foundation model, the top and bottom faces of the foundation volume are part of the corresponding rigid region (see Fig. J.4). The results are displayed in Figure J.5, revealing that this boundary condition produces similarly high critical buckling loads. The difference from the solution curve of the embedded beam model even appears larger than with the $2 \times 2 \times 3$ component, likely because the rigid regions are closer to each other for the individual cell. The impact of this boundary condition should diminish for larger lattice components, as the distance to the rigid regions increases for most elements in the model. Unfortunately, this cannot be studied further, as a $2 \times 2 \times 3$ component is already near the limit of what can realistically be numerically analyzed with the available computational resources.

Figure J.6 illustrates the node displacement corresponding to the critical buckling load for a strut slenderness of $L/D = 20$. The observed displacements in the elastic medium are primarily loc-

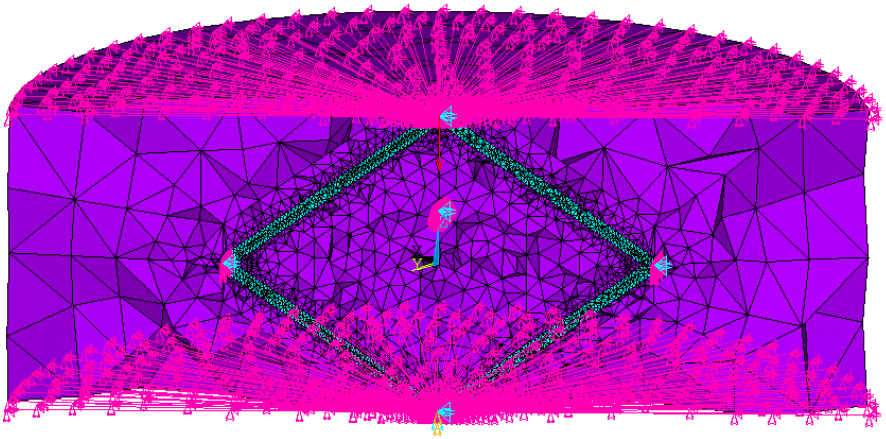

Fig. J.4: Section view of a volumetric model for a *bcc* unit-cell. The top and bottom faces of the foundation volume are part of the rigid region.

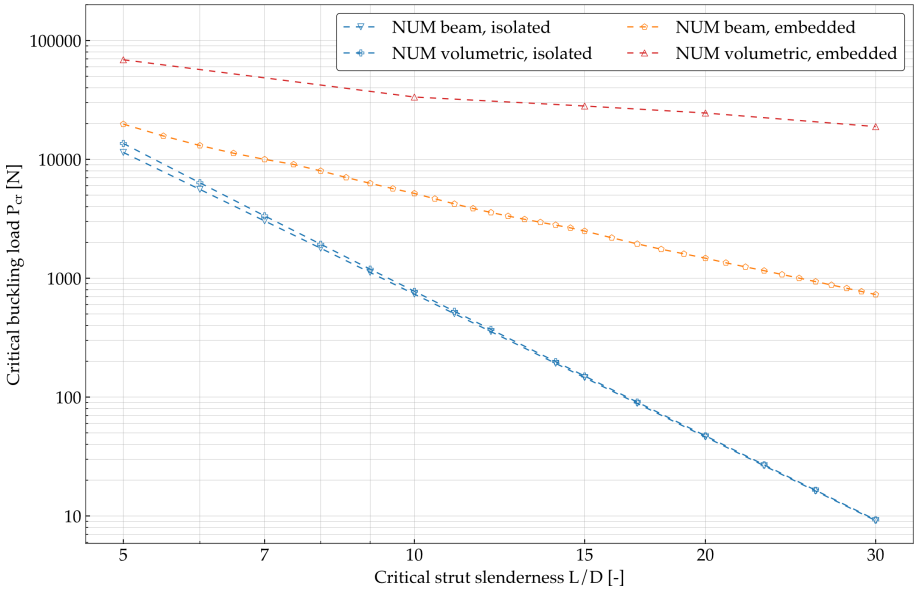

Fig. J.5: Critical buckling load for the case considered and shown in Figure J.4.

alized around the buckling strut, with minimal propagation to neighboring cells. Consequently, it appears that the stability reduction in the structure caused by the deformable elastic medium, when employing volumetric elements, has a negligible impact, as the deformations remain confined to the vicinity of the buckling strut. This finding lends additional support to the beam/spring model, wherein the foundation is treated independently for each strut.

It can be inferred that the imposed boundary conditions in the volumetric model, which include rigid top and bottom faces of the component, result in critical buckling loads significantly surpassing those obtained with the beam/spring model. While this conclusion holds true for lattice components with a small amount of unit-cells, it is anticipated that the impact diminishes for larger lattice components, where global buckling is the concern, rather than local

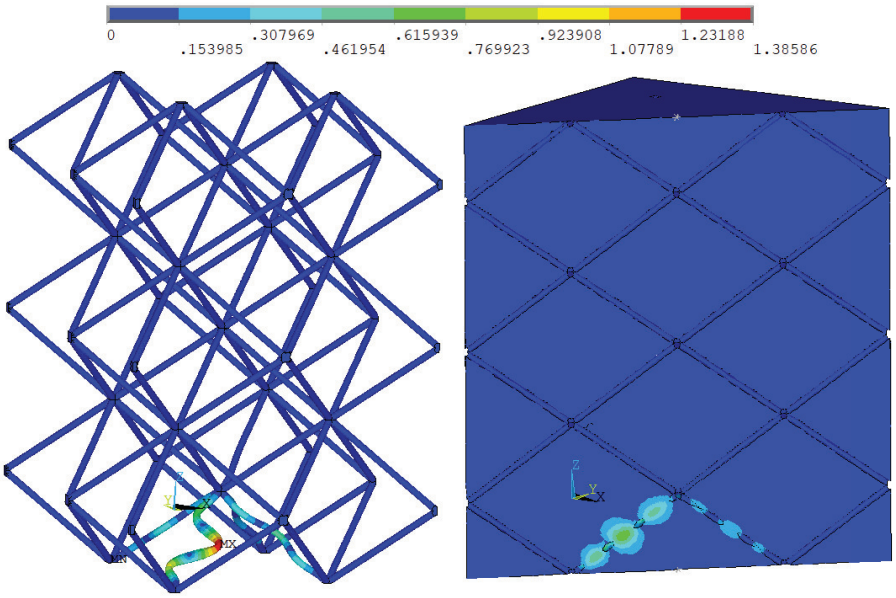

Fig. J.6: Nodal displacements within the lattice structure a) and elastic medium b) at critical buckling load for the $2 \times 2 \times 3 - bcc$ lattice with $L/D = 20$. Units in mm.

one. This assumption cannot be validated due to the computational expenses associated with volumetric models. The subsequent subsection explores lattice components using beam/spring elements, recognizing that the solution likely differs markedly from that derived using volumetric elements. Nevertheless, the investigations previously described suggest that the model based on beam/spring elements should yield conservative results, thus allowing valid qualitative (although not quantitative) considerations.

Component size variation using the beam model

To investigate the size effect, i.e. scale variance, on the critical buckling load, numerical analyses are conducted on lattice components of varying sizes using the beam/spring model, as mentioned above. Initially, cubic components with an equal number of cells in all three directions are examined to maintain a constant aspect ratio. When these lattice components are subjected to a compressive load, the force is distributed among the cells in the xy-plane. To facilitate a meaningful comparison across differently sized lattice components, the results of the critical buckling load are normalized dividing them by the number of cells in the xy-plane. For instance, in a lattice component based on a repetition of $3 \times 3 \times 3$ unit cells (i.e. three in each direction), the results are divided by 9. Figures J.7 to J.10 depict the critical buckling loads for the different unit-cells. The solutions are presented as functions of the component size for selected critical strut slenderness ratios of $L/D = 5, 15, 30$. The component sizes vary from 1

to 8 cells.

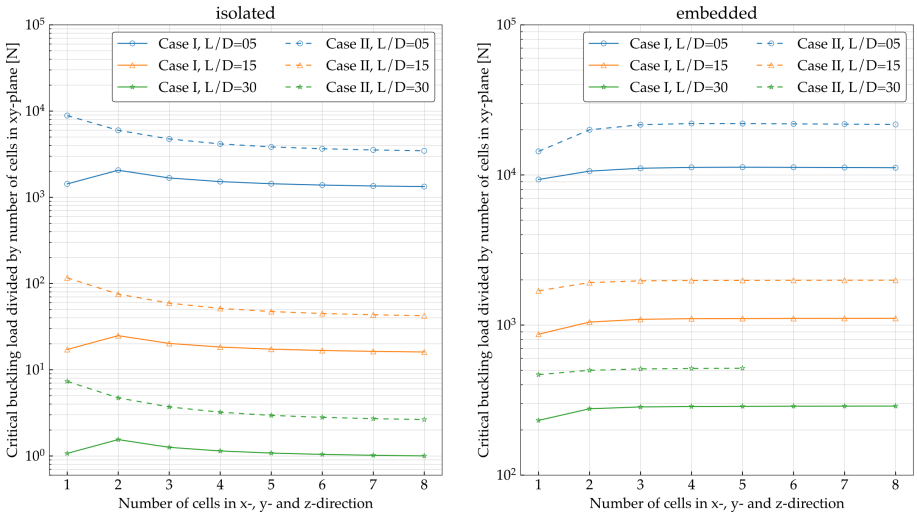

Fig. J.7: Critical buckling load variation for the f_2cc cell for Case I (only outward direction restrained), and Case II (both x- and y-directions restrained).

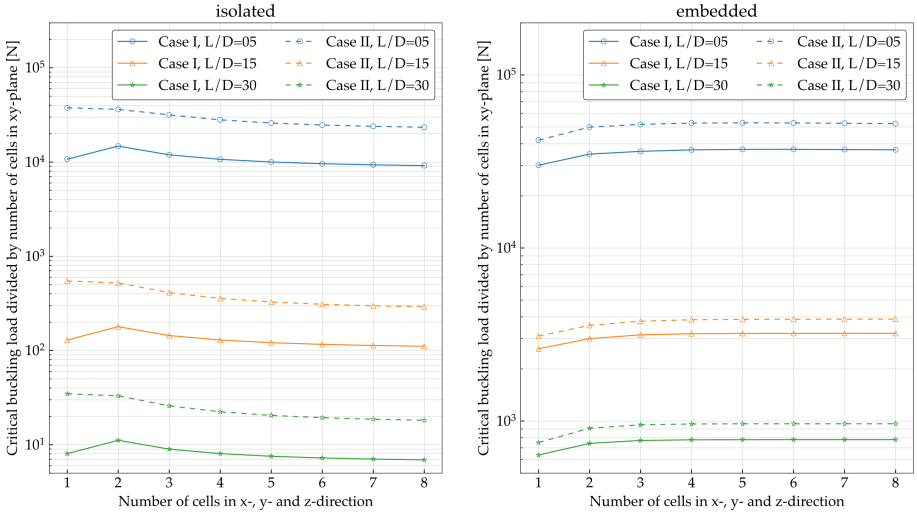

Fig. J.8: f_2ccz.

The lattice structures with f_2cc and f_2ccz unit-cells exhibit variations in critical buckling loads under different boundary conditions, specifically Cases I and II, as illustrated in Figures J.7 and J.8. Conversely, the *bcc* and *bccz* lattice structures demonstrate minimal discrepancies in critical buckling loads, with deviations on the order of approximately 1% in both boundary condition cases. The graphical representation in the figures exclusively displays the solution for Case I for clarity. This observed behavior can be ascribed to the stability of the lateral vertices inherent in the lattice structure.

Figure J.11a) portrays the buckling phenomenon in a f_2cc lattice under Case I, wherein the outer

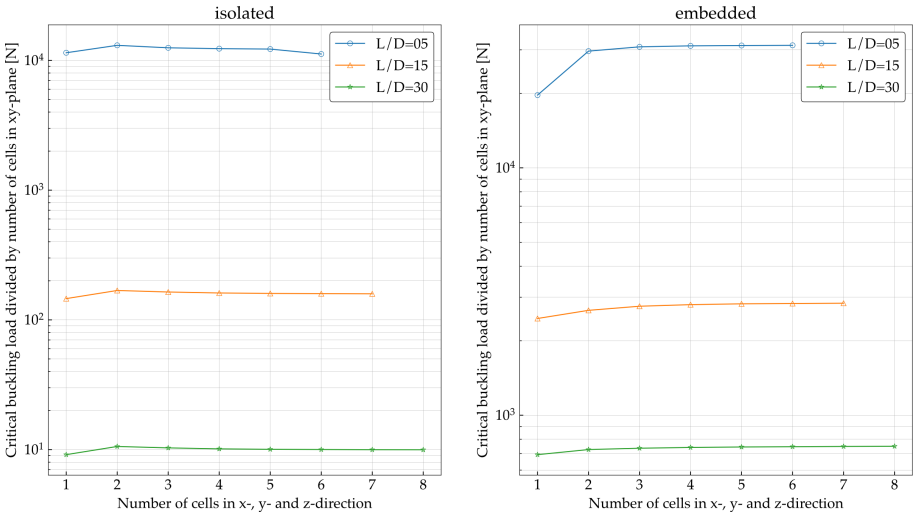

Fig. J.9: *bcc*.

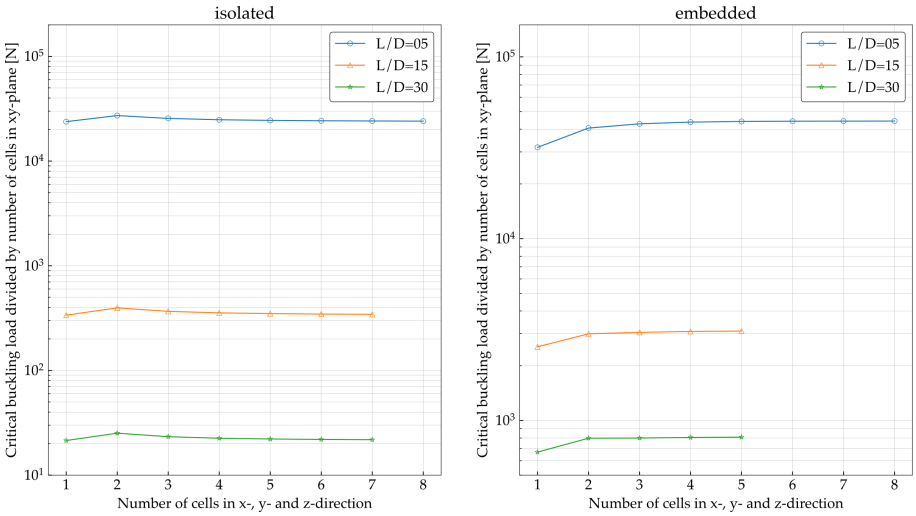

Fig. J.10: *bccz*.

struts of the outer cells exhibit sideways buckling. In contrast, in Case II (Figure J.11b), these outer struts are constrained, preventing lateral movement and leading to the buckling of inner struts. Consequently, distinct buckling modes emerge with different critical buckling loads. This principle is similarly applicable to the embedded case, as well as the lattices with f_2ccz unit-cells.

In contrast, the *bcc* lattice (Figure J.11c) presents a unique structural arrangement, where, when viewed from above, the struts align diagonally, and the diagonals connect at the outer vertices, impeding lateral translations along the boundary wall. As a result, for both *bcc* and *bccz* lattices, there is negligible disparity in critical buckling loads between the two boundary condition cases.

The resulting curves manifest a diminishing scale variance in the embedded scenario across all cell topologies, indicating a subtle augmentation in the critical buckling load concerning larger

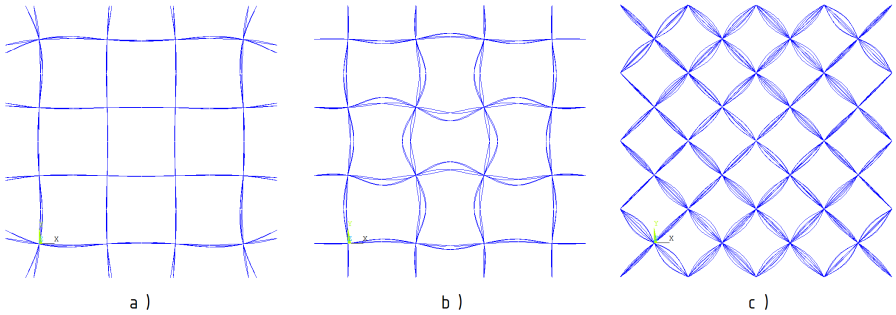

Fig. J.11: Top view of the buckled shape for lattices with a size $4 \times 4 \times 4$ and with $L/D = 15$. a) and b) show f_2cc lattices under both case I and case II, respectively. c) shows a *bcc* lattice under case I.

lattice components. This decreasing size effect is similarly discernible in isolated *bcc* and *bccz* lattices, suggesting that augmenting the number of cells in these instances reinforces the stiffness of the vertices. Conversely, isolated f_2cc and f_2ccz lattices exhibit a stiffening size effect in case II. An explicable rationale for this behavior emerges upon scrutinizing the buckling modes portrayed in Figure J.12, illustrating the buckled configuration of lattices sized $3 \times 3 \times 3$ for diverse cell types.

In the isolated setting, *bcc* and *bccz* types manifest simultaneous buckling of all cells, forming windmill-like structures characterized by point symmetry at the vertices. In contrast, for f_2cc and f_2ccz types, in case I, the outer cells of the xy-plane buckle, while in case II, the inner cells predominantly undergo buckling. Notably, in case II, rotational movement of the vertices in the outer cells is restricted. With an increase in lattice size, the number of inner cells experiences a more rapid increase than the number of outer cells, facilitating additional rotations of the vertices. This serves as a plausible explanation for the observed stiffening size effect in this particular case.

In the isolated scenario, the deflection curves of the struts display a singular half-sine wave, resulting in windmill-like structures with point symmetry at the vertices. Conversely, in the embedded scenario, cells do not buckle simultaneously; those situated at the top of the lattice (near the applied load) are the initial ones to buckle. The struts exhibit deflection curves characterized by multiple half-sine waves, as anticipated.

The investigation also delves into how the critical buckling load varies with the aspect ratio of the lattice component. Lattices with 5×5 cells in the xy-plane and a variable number of cells in the vertical direction are explored. The outcomes, depicted in Figure J.13 for a *bcc* lattice and Figure J.14 for an f_2ccz lattice, are not normalized by the number of cells in the xy-plane, as such normalization is unnecessary for result comparison within this context. In the isolated case, a stiffening size effect is apparent, whereas a consistent softening size effect is observed in the embedded case.

In summary, the imposed boundary conditions appear to induce a relatively modest size effect. Consequently, solutions obtained for individual cells closely align with those acquired for the

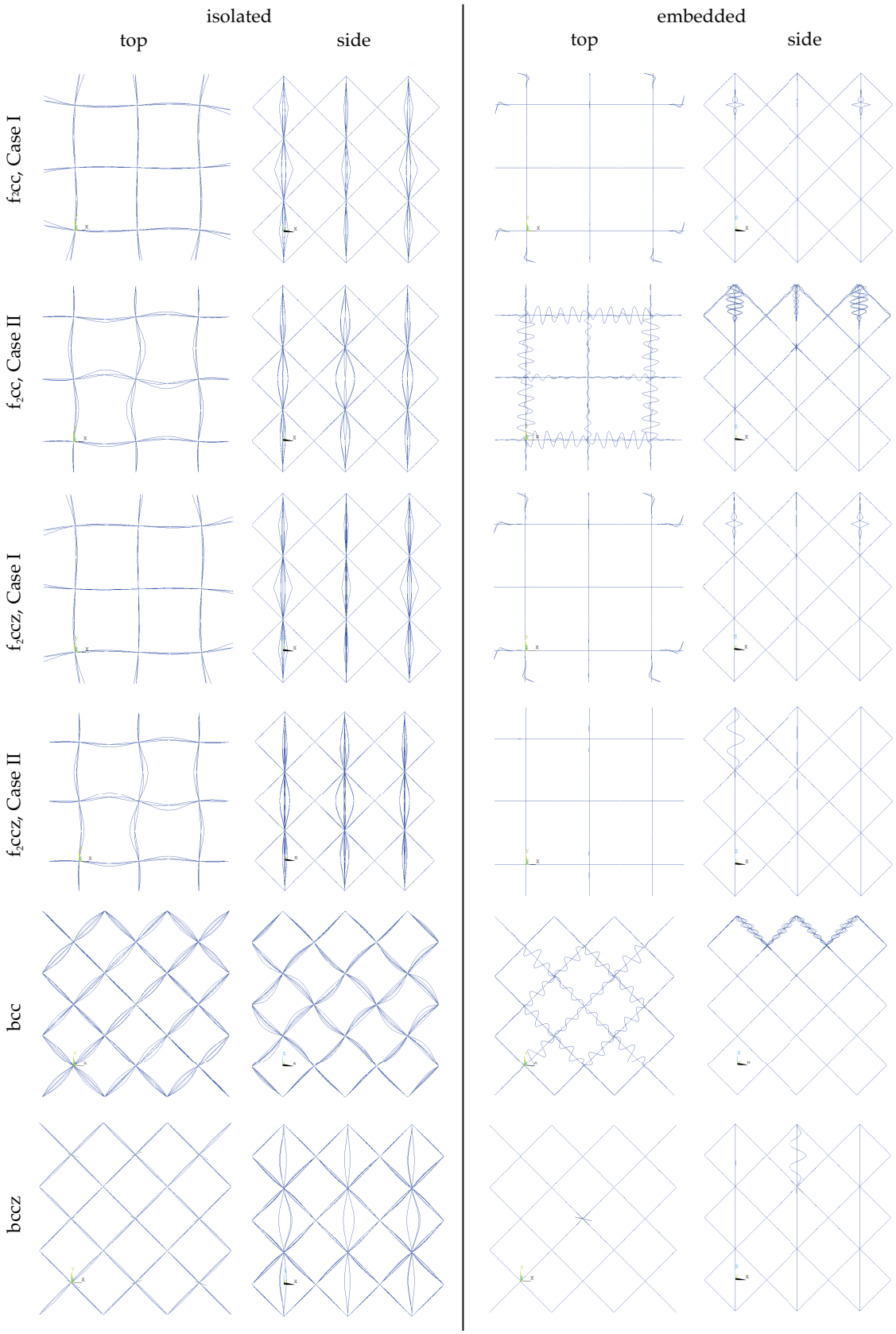

Fig. J.12: Buckled shapes for all lattices both in isolated and embedded conditions. Top and side columns describe two different views of the component. Size $3 \times 3 \times 3$ at $L/D = 30$.

components, necessitating straightforward multiplication by the number of cells in the xy-plane for conversion. It is imperative to underscore that this conclusion is contingent upon the specific nature of the provided boundary conditions.

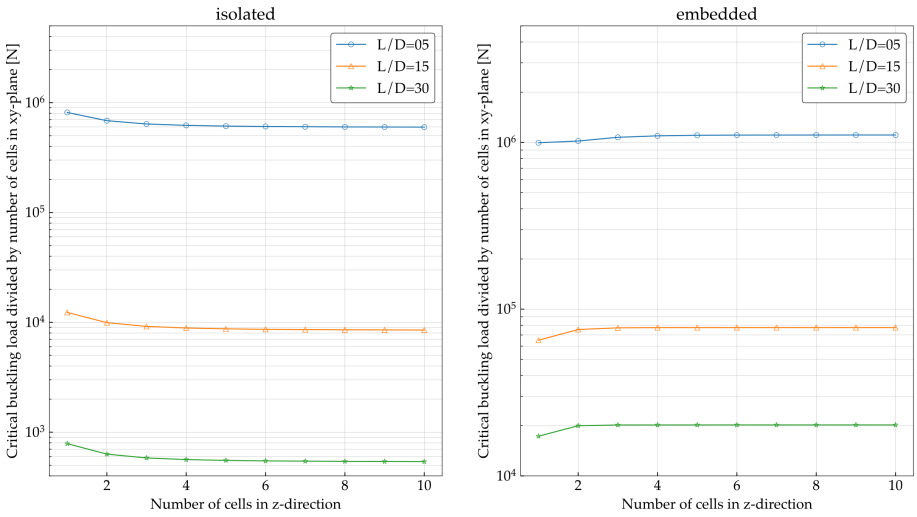

Fig. J.13: Critical buckling loads for a *bcc* lattice with 5×5 cells in the xy plane while varying the number of vertical cells (numerical analysis using beam/spring elements, for case I).

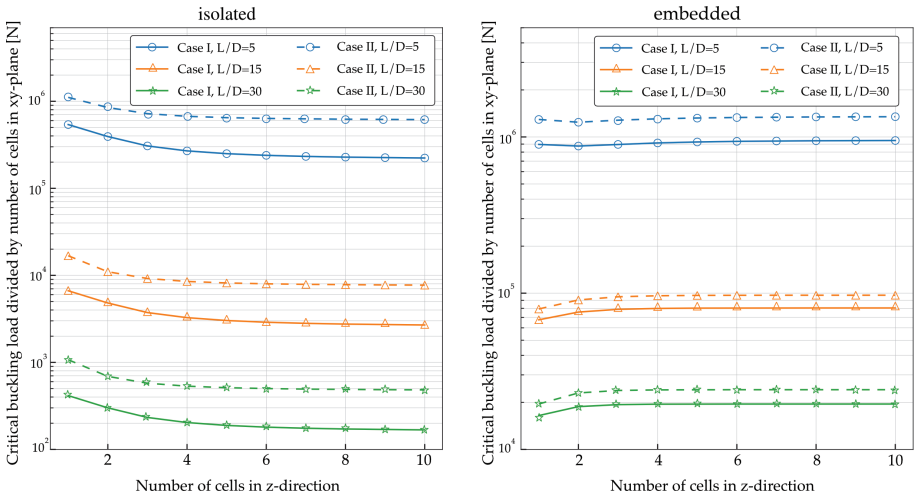

Fig. J.14: Critical buckling loads for a f_2ccz lattice with 5×5 cells in the xy plane while varying the number of vertical cells (numerical analysis using beam/spring elements, for case I and II).

K Automatic Differentiation

Automatic differentiation (AD) is a powerful numerical tool that is capable of computing exact derivatives (to machine precision) of computer programs. This is possible based on the idea that computer programs are made up of elementary operations such as multiplication, division, addition and subtraction [20]. The key to AD is the application of the chain rule [20], shown in equation K.1.

$$\frac{d}{dx}f(g(x)) = \frac{df}{dg}\frac{dg}{dx} \tag{K.1}$$

Automatic differentiation can be implemented through operator overloading and the use of dual numbers [20]. Dual numbers are similar to complex numbers, in that they are expressed as $a+b\varepsilon$. The variable ε^2 is defined to be 0 and the values a and b are both real numbers. The operations performed on dual numbers act as normal, as shown below in equation K.2 [20].

$$(a+b\varepsilon)+(c+d\varepsilon) = (a+c)+(b+d)\varepsilon \tag{K.2a}$$

$$(a+b\varepsilon)\times(c+d\varepsilon) = (ac)+(ad+bc)\varepsilon \tag{K.2b}$$

Dual numbers are powerful tools when passed into any smooth function f. By Taylor expansion, it can be shown that the function evaluation, as well as its derivative, can be found [20].

$$\begin{aligned} f(x) &= \sum_{k=0}^{\infty}\frac{f^{(k)}(a)}{k!}(x-a)^k \\ f(a+b\varepsilon) &= \sum_{k=0}^{\infty}\frac{f^{(k)}(a)}{k!}(a+b\varepsilon-a)^k \\ &= \sum_{k=0}^{\infty}\frac{f^{(k)}(a)b^k\varepsilon^k}{k!} \\ &= f(a)+bf'(a)\varepsilon+\varepsilon^2\sum_{k=2}^{\infty}\frac{f^{(k)}(a)b^k}{k!}\varepsilon^{(k-2)} \\ &= f(a)+bf'(a)\varepsilon \end{aligned} \tag{K.3}$$

Furthermore, AD can be used in either forward or reverse mode. Consider a generic problem where the Jacobian $\frac{df_i}{dx_j}$ is to be computed, where $i \in [1,2,\ldots,n]$ and $j \in [1,2,\ldots,m]$. Forward mode AD is capable of computing the Jacobian column-by-column $\frac{d\mathbf{f}}{dx_j}$. In reverse mode, the Jacobian is computed row-by-row $\frac{df_i}{d\mathbf{x}}$. How this is achieved will be discussed in the following sections. For the following examples, the derivative of the function in equation K.4 will be evaluated.

$$f(x_1,x_2) = x_1x_2 + x_1\sin(x_2) \tag{K.4}$$

Forward Mode

As was mentioned, forward mode AD computes a Jacobian column-by-column. This means it is more efficient to use forward mode when $n < m$. The evaluation of equation K.4 can be thought of visually as a directed acyclic graph (DAG), where each sub-evaluation is a vertex. The lines connecting each vertex can be thought of as where the derivatives are evaluated. The DAG for equation K.4 is shown in figure K.1. With forward mode AD, a function can be differentiated

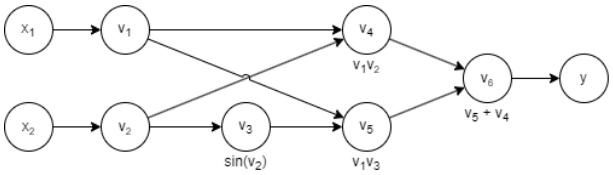

Fig. K.1: Graph of equation K.4

with respect to a single variable in each forward pass. A forward pass is simply computing the DAG from left to right. To achieve this using dual numbers, the dual number for only one variable is '*seeded*.' In this example $f(a,b)$, equation K.5. In this example, v_4 and v_5 using equation K.2b and v_6 used equation K.2a. To compute the full derivative, two forward passes are required.

$$\begin{aligned} v_1 &= a + 1\varepsilon & v_4 &= v_1v_2 = ab + b\varepsilon \\ v_2 &= b + 0\varepsilon & v_5 &= v_1v_3 = a\sin(b) + \sin(b)\varepsilon \\ v_3 &= \sin(b) + 0\varepsilon & v_6 &= v_4 + v_5 = ab + a\sin(b) + (b + \sin(b))\varepsilon \end{aligned} \tag{K.5}$$

Reverse Mode

Reverse mode AD computes a Jacobian row-by-row. This makes it more efficient when $m < n$. Reverse mode AD consists of a forward pass where the vertices and lines are computed, and a reverse accumulation pass. In this case, the lines are the derivatives of v_j w.r.t v_i rather than w.r.t the variable.

The reverse pass requires the evaluation of equation K.6. The parents (p) of vertex i are all the forward vertices connected to v_i. For this example, v_2 has v_3 and v_4 as parents. From equation K.6, it is clear that the entire DAG needs to be stored in memory to be able to compute the derivative. However, it is now also possible to compute the derivative w.r.t all the inputs.

$$\frac{\partial y}{\partial v_i} = \sum_{p \in \text{parent}(i)} \frac{\partial y}{\partial v_p} \frac{\partial v_p}{\partial v_i} \tag{K.6}$$

L Calculation of the Phase Change sensitivity

Recall that the residual form to solve the phase change problem is given as shown below. This was derived and given by [168]

$$R(T^{n+1}) = f\Delta t + \mathbf{C}T^n - (L^{n+1} - L^n) - (\mathbf{C} + \mathbf{K}\Delta t)T^{n+1}$$

Linear Gradient

When the system of equations is linear, the gradient can be computed as follows. Equation L.1 shows the simplified residual equation when the latent heat vectors are equal. The equation essentially becomes a linear system of equations that can be solved.

$$\begin{aligned} T^{n+1} &= (\mathbf{C} + \mathbf{K}\Delta t)^{-1}(f\Delta t + \mathbf{C}T^n) \\ T^{n+1} &= \mathbf{A}^{-1}b \end{aligned} \tag{L.1}$$

The gradient of this temperature vector can then be determined as follows in equation L.2. One thing to note from this derivative is that the derivative of the previous temperature vector is required. This means that the derivatives need to be tracked throughout each iteration. This has the effect of accumulating the transient effects throughout the entire simulation.

$$\begin{aligned} \frac{\partial T^{n+1}}{\partial \rho} &= \frac{\partial}{\partial \rho}\mathbf{A}^{-1}b \\ &= \frac{\partial \mathbf{A}^{-1}}{\partial \rho}b + \mathbf{A}^{-1}\frac{\partial b}{\partial \rho} \end{aligned} \tag{L.2a}$$

$$\begin{aligned} \frac{\partial \mathbf{A}^{-1}}{\partial \rho_i}b &= -\mathbf{A}^{-1}\frac{\partial \mathbf{A}}{\partial \rho_i}\mathbf{A}^{-1}b \\ &= -\mathbf{A}^{-1}\frac{\partial}{\partial \rho_i}(\mathbf{C} + \mathbf{K}\Delta t)\mathbf{A}^{-1}b \\ &= -\mathbf{A}^{-1}\left(\frac{\partial \mathbf{C}}{\partial \rho_i} + \Delta t\frac{\partial \mathbf{K}}{\partial \rho_i}\right)\mathbf{A}^{-1}b \end{aligned} \tag{L.2b}$$

$$\begin{aligned}\frac{\partial b}{\partial \rho} &= \frac{\partial}{\partial \rho}(f\Delta t + \mathbf{C}T^n) \\ &= \Delta t\frac{\partial f}{\partial \rho} + \frac{\partial}{\partial \rho}\mathbf{C}T^n \\ &= \frac{\partial \mathbf{C}}{\partial \rho}T^n + \mathbf{C}\frac{\partial T^n}{\partial \rho}\end{aligned} \tag{L.2c}$$

Non-Linear Gradient

The computation for the non-linear gradient needs to consider the latent heat vectors, as these are no longer equal and have a significant effect on the gradient. Due to the non-linearity, the temperature is iteratively determined using a Newton iteration, where the Jacobian, $\mathbf{J}$, of equation L is required. Using these, the temperature of the next time step can be determined.

$$\begin{aligned}T_{i+1}^{n+1} &= T_i^{n+1} + (\Delta T)_i \\ T_{i+1}^{n+1} &= T_0^{n+1} + \sum_{i=0}^{n}(\Delta T)_i\end{aligned} \tag{L.3a}$$

$$\text{Where: } T_0^{n+1} = T^n$$

$$(\Delta T)_i = [\mathbf{J}(T_i^{n+1})]^{-1} R(T_i^{n+1}) \tag{L.3b}$$

The gradient of the temperature vector can then be determined as shown in equation L.4. Some complications arise with the latent heat vector and matrix as the gradient of the previous temperature vector is required.

$$\frac{\partial T_{i+1}^{n+1}}{\partial \rho} = \frac{\partial T^n}{\partial \rho} + \frac{\partial}{\partial \rho}(\sum_{i=0}^{n}(\Delta T)_i) \tag{L.4a}$$

$$\begin{aligned}\frac{\partial}{\partial \rho}(\Delta T)_i &= \frac{\partial}{\partial \rho}\mathbf{J}^{-1}R \\ &= \frac{\partial \mathbf{J}^{-1}}{\partial \rho}R + \mathbf{J}^{-1}\frac{\partial R}{\partial \rho}\end{aligned} \tag{L.4b}$$

$$
\begin{aligned}
\frac{\partial \mathbf{J^{-1}}}{\partial \rho_e} R &= -\mathbf{J}^{-1} \frac{\partial \mathbf{J}}{\partial \rho_e} \mathbf{J}^{-1} R \\
&= -\mathbf{J}^{-1} \frac{\partial}{\partial \rho_e} \left(\mathbf{C} + \mathbf{K} \Delta t + \left. \frac{\partial L}{\partial T} \right|_i^{n+1} \right) \mathbf{J}^{-1} R \\
&= -\mathbf{J}^{-1} \left(\frac{\partial \mathbf{C}}{\partial \rho_e} + \Delta t \frac{\partial \mathbf{K}}{\partial \rho_e} + \frac{\partial}{\partial \rho_e} \left(\left. \frac{\partial L}{\partial T} \right|_i^{n+1} \right) \right) \mathbf{J}^{-1} R
\end{aligned}
\tag{L.4c}
$$

$$
\begin{aligned}
\frac{\partial R}{\partial \rho} &= \frac{\partial}{\partial \rho} (f \Delta t + \mathbf{C} T^n - (L^{n+1} - L^n) - \mathbf{A} T_i^{n+1}) \\
&= \Delta t \frac{\partial f}{\partial \rho} + \frac{\partial}{\partial \rho} \mathbf{C} T^n - \frac{\partial}{\partial \rho} (L^{n+1} - L^n) - \frac{\partial}{\partial \rho} (\mathbf{A} T_i^{n+1}) \\
&= \frac{\partial \mathbf{C}}{\partial \rho} T^n + \mathbf{C} \frac{\partial T^n}{\partial \rho} - \frac{\partial L^{n+1}}{\partial \rho} + \frac{\partial L^n}{\partial \rho} - \frac{\partial \mathbf{A}}{\partial \rho} T_i^{n+1} - \mathbf{A} \frac{\partial T_i^{n+1}}{\partial \rho}
\end{aligned}
\tag{L.4d}
$$